Plasma Physics Reports, Vol. 29, No. 10, 2003, pp. 803–815. Translated from Fizika Plazmy, Vol. 29, No. 10, 2003, pp. 867–879.

TOKAMAKS

A Possible Mechanism for the Generation and Motion of Blobs in Tokamaks

V. P. Vlasov and B. A. Trubnikov

Nuclear Fusion Institute, Russian Research Centre Kurchatov Institute, pl. Kurchatova 1, Moscow, 123182 Russia

Received January 15, 2003; in final form, March 7, 2003

Abstract—A possible mechanism for the generation and motion of so-called blobs—peculiar perturbations that are observed in a tokamak edge plasma—is proposed. It is suggested that blobs are self-contracting plasma filaments generated either by the thermal-radiative instability of a plasma with impurities or by the nonradiative resonant charge-exchange instability resulting from the presence of neutral hydrogen atoms near the tokamak wall. Instability occurs in a narrow temperature range in which pressure is a decreasing function of density. Under these conditions, the most typical perturbations are the local ones that originate spontaneously in the form of separate growing hills and wells in the density. The temperature at the centers of the hills is lower than that in the surrounding plasma, but they are denser and, consequently, brighter than the background. The (denser) hills should move ("sink") toward the separatrix, while the (less dense) wells should "rise" in the opposite direction, as is observed in experiments. It may even be said that they behave in accordance with a peculiar Archimedes' principle. © *2003 MAIK "Nauka/Interperiodica"*.

1. INTRODUCTION

Observations in some tokamaks have revealed filaments—commonly referred to as "blobs"—that appeared sporadically in the edge plasma, were stretched along the main magnetic field, and moved toward the chamber wall. Figure 1, borrowed from the paper by Marmar [1], presents six successive film frames of an individual blob that moved at a speed of 2 km/s toward the edge of the plasma column in the Alcator C-Mod tokamak (the frames were taken with an exposure time of 4 μs). Blobs have also been observed in the DIII-D tokamak, whose cross section is shown in Fig. 2, in which the arrow indicates the observation region.

From Fig. 1, we can see that, as a blob crosses the separatrix magnetic surface, it breaks into two parts, one of which stays inside the separatrix and the other passes through the separatrix and continues to move toward the wall. Blobs originate in the edge plasma, in which neutral impurities play an important role. In some papers, it was pointed out that the temperature at the center of a blob is close to 20 eV, which seems to be more than mere coincidence. The fact that a blob divides into two parts in crossing the separatrix likely provides evidence for its double structure.

The mechanism by which blobs move was considered by Krasheninnikov [2], who supposed that a blob is a magnetic tube that becomes polarized in a nonuniform peripheral tokamak magnetic field by the difference between the gradient drifts of the electrons and ions and then continues to move with the velocity $V = cE/B$ toward the wall, while at the same time being spread out by diffusion. However, in [2], nothing was said about the mechanism by which blobs originate.

In the present paper, we consider possible causes of the generation of blobs and the mechanism for their motion. Although the mechanism of motion to be considered here differs somewhat from that proposed in [2], it yields the same motion picture of the blobs.

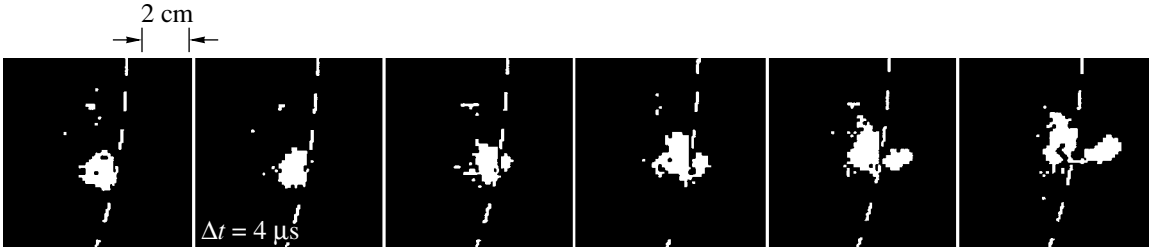

Fig. 1. Six successive frames of a blob in the Alcator C-Mod tokamak. The dashed curve shows the separatrix.

1063-780X/03/2910-0803$24.00

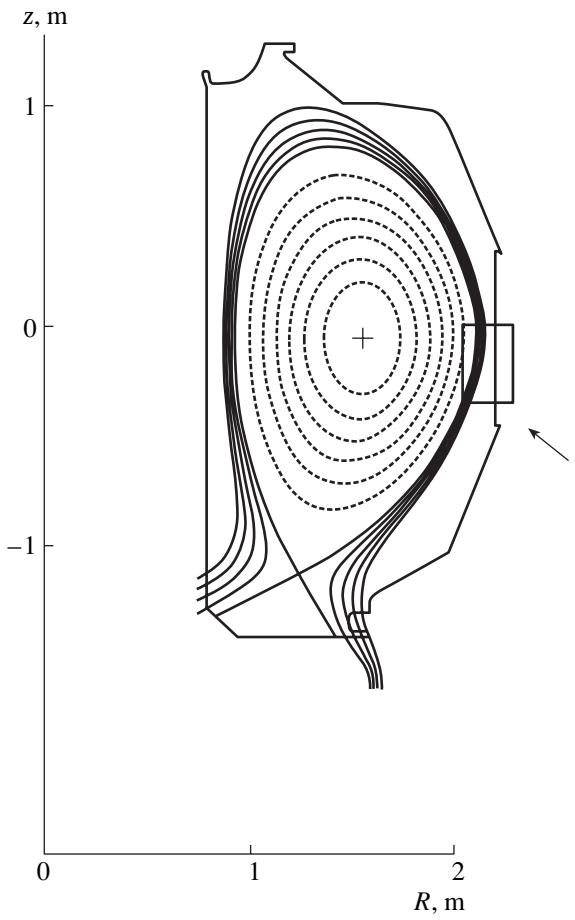

Fig. 2. Cross section of the DIII-D tokamak. The arrow indicates the region where the blobs are observed.

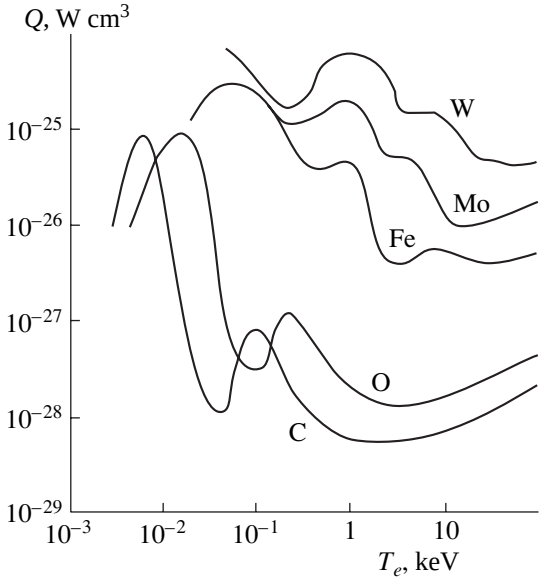

Fig. 3. Factor $Q(T)$ for C, O, Fe, Mo, and W impurities.

2. THERMAL-RADIATIVE INSTABILITY

We think that one of the possible mechanisms for the generation of blobs is thermal-radiative instability, during which the plasma heating power W is balanced by the power $W_{\rm rad}$ of radiative losses from impurities arriving from the chamber wall. In this case, the pressure p, as a rule, becomes a decreasing function of density, thereby giving rise to the instability.

It is important to note that, in such specific unstable media (in [3, 4], they were called "quasi-Chaplygin media"), there are no running waves that causally connect the neighboring regions. Consequently, more typical disturbances in these media are individual local perturbations that are spontaneously generated and grow until they reach their saturation level. These perturbations qualitatively resemble blobs. In addition, the blobs observed in experiments originate in a rather narrow temperature range around a value of ~20 eV. It is noteworthy that the model based on the thermal-radiative instability gives the same temperature value. Note that thermal-radiative instability is also referred to as radiative condensational instability and, in the particular case of Joule heating, is called thermal-ionizational instability [5].

Let us discuss this hypothesis in more detail. The inductive voltage around the circumference of the torus is approximately equal to $V\,[\mathrm{V}] \approx 3.6/B_\parallel\,[\mathrm{T}]$ [6], so that the longitudinal electric field can be assumed to be constant during the discharge, $E_\parallel = \mathrm{const}$. The Joule heating power $W_J = E^2\eta$ is deposited in the central plasma and heats it. However, blobs originate in the scrape-off layer (SOL) plasma, in which an important role is played by impurities arriving from the tokamak wall.

This is why, in considering the first illustrative example, we assume that the electrical conductivity in the peripheral plasma is created by collisions of electrons with neutral atoms and is described by the formulas

$$\eta = e^2 n_e/m_e\nu_{ea}, \quad \nu_{ea} = n_a\sigma_{ea}v_{Te}, \qquad \sigma_{ea} = \pi a^2, \quad v_{Te} = \sqrt{T_e/m_e}, \tag{2.1}$$

where σ_{ea} is the cross section for collisions and v_{Te} is the electron thermal velocity.

In the SOL plasma, impurity atoms are ionized and become ions with a certain density n_Z. The electrons recombine with impurity ions, emitting radiation with the specific power $W_{\rm rad} = n_e n_Z Q$. The dependence of the factor Q on the electron temperature T_e for typical impurities (such as C, O, Fe, Mo, and W) is shown in Fig. 3, borrowed from [7].

We can see that, for heavy impurities, this factor is nearly constant and is approximately equal to $Q \approx 10^{-17}$ [cm^3 erg/s]. In the simplest model at hand, the

equality $W_J = W_{\text{rad}}$ yields the dependence $n_Z\sqrt{T_e} = C_1 = E_\parallel^2 e^2/n_a\sigma_{ea}Q\sqrt{m_e} = \text{const}$.

If we introduce the ratio of the density of impurity ions to the electron density, $n_Z/n_e = \alpha$, and take into account the electron pressure $p = n_eT_e$, then we arrive at the following inverse dependence of the pressure of the electrons on their density:

$$p = \frac{C_2}{n_e}, \qquad C_2 = \left(\frac{C_1}{\alpha}\right)^2 = \text{const}. \tag{2.2}$$

It is this inverse dependence that leads to a peculiar kind of quasi-Chaplygin instability, which will be analyzed below.

3. THEORY OF QUASI-CHAPLYGIN INSTABILITIES

Here, the theory of quasi-Chaplygin instabilities, which was presented in detail in [3, 4], is described only briefly. We begin with the conventional hydrodynamic equations

$$\begin{aligned}\frac{\partial}{\partial t}\rho + \nabla\cdot(\rho\mathbf{v}) &= 0,\\ \frac{\partial}{\partial t}\mathbf{v} + (\mathbf{v}\cdot\nabla)\mathbf{v} &= -\frac{1}{\rho}\nabla p,\end{aligned} \tag{3.1}$$

but supplement them with an unusual equation of state in which the pressure decreases according to a power law as the density increases, $p = p_0(\rho/\rho_0)^{-|s|}$, where p_0 and ρ_0 are the unperturbed pressure and density of a homogeneous background medium, respectively. Introducing the dimensionless density $\rho_* = \rho/\rho_0$, we find it expedient to rewrite the equations as

$$\begin{aligned}\frac{\partial}{\partial t}\rho_* + \nabla\cdot(\rho_*\mathbf{v}) &= 0,\\ \frac{\partial}{\partial t}\mathbf{v} + (\mathbf{v}\cdot\nabla)\mathbf{v} &= \mu c_0^2\nabla\rho_*^{1/\mu},\end{aligned} \tag{3.2}$$

where $c_0 = \sqrt{|s|\,p_0/\rho_0}$ is the growth rate of the perturbations and the parameter $\mu = -1/(1 + |s|)$ will be referred to as the azimuthal number.

In a linear approximation such that $\rho_* = 1 + \Psi$ and $\Psi \ll 1$, the parameter μ drops out of Eqs. (3.2). If we pass over from the time t to the time $\tau = c_0t$ (having the dimensionality of length), then we reduce these two equations to the equation $\Delta\Psi + \Psi''_{\tau\tau} = 0$. As a result, in one-, two-, and three-dimensional geometries, the corresponding Laplace equations have the form

$$\begin{aligned}&\Psi''_{xx} + \Psi''_{\tau\tau} = 0, \quad \Psi''_{xx} + \Psi''_{yy} + \Psi''_{\tau\tau} = 0,\\ &\Psi''_{xx} + \Psi''_{yy} + \Psi''_{zz} + \Psi''_{\tau\tau} = 0.\end{aligned} \tag{3.3}$$

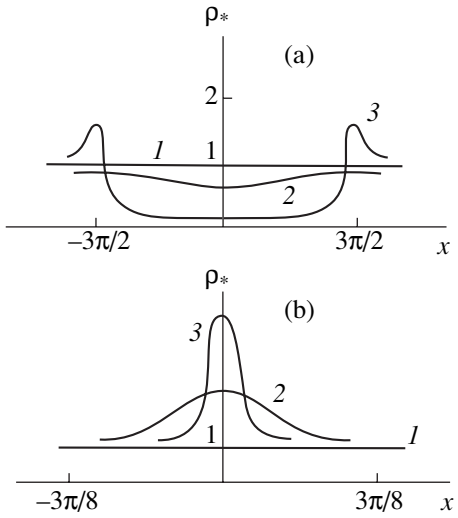

Fig. 4. Density profiles in an individual well and an individual hill that develop spontaneously against the background of an initially homogeneous medium (borrowed from [3, 4]). Curves *1* refer to $t = -\infty$. The evolution proceeds from curves *2* to curves *3*.

The simplest solutions to Eqs. (3.3) are those describing spatially periodic standing perturbations that grow exponentially in time: $\Psi(t, \mathbf{r}) \sim \exp(\gamma t + i\mathbf{kr})$. However, these perturbations can only originate from spatially periodic seeds, which, in turn, cannot appear for no reason whatever because, in such media, there are no running waves that causally connect the neighboring regions. That is why the most interesting solutions are those corresponding to spontaneous local perturbations. We require that these solutions vanish at an infinitely distant past ($t \longrightarrow -\infty$), thereby modeling the property of perturbations to originate spontaneously and grow progressively.

Thus, in three-dimensional spherical geometry, in which $\Psi(t, x, y, z) = \psi(R)\exp(\gamma t)$ (where $R = \sqrt{x^2 + y^2 + z^2}$), we obtain the following equation and local solution for $\psi(R)$:

$$\Delta_3\psi = \frac{1}{R}(R\psi)''_{RR} = -k^2\psi, \quad \psi = A\frac{\sin kR}{kR}, \tag{3.4}$$

where $k = \gamma/c_0 = 2\pi/\lambda$. At the center $R = 0$, the dimensionless density changes according to the law $\rho_* = 1 + \Psi \approx 1 + A\exp(\gamma t)$, so that there is no perturbation at $t \longrightarrow -\infty$. However, as time elapses, the perturbation grows progressively, forming either a hill (at $A > 0$) or a well (at $A < 0$) in the density.

In one-dimensional geometry, in which $\rho_* = \rho_*(t, x)$, nonlinear Eqs. (3.2) can be solved exactly. Figure 4 shows two examples of exact solutions in the form of a local density hill and a local density well, which develop against the background of an initially homogeneous medium.

In the next section, we will consider exact solutions typical of two- and three-dimensional geometries.

4. TWO- AND THREE-DIMENSIONAL MODELS OF THE BLOBLIKE OBJECTS

In the above illustrative example with Q = const, $|s| = 1$, and $\mu = -1/2$, we can construct a two-dimensional solution describing an object whose cross section partially resembles that of a blob. Specifically, we consider a solution of the form

$$\rho_* = \frac{\rho_0(t)}{\sqrt{1 + (x/a)^2 + (y/b)^2}}, \quad v_x = x\frac{\dot{a}}{a}, \quad v_y = y\frac{\dot{b}}{b}, \tag{4.1}$$

where the three functions a, b, and ρ_0 depend on the time t. We rewrite the continuity equation as

$$\frac{\partial}{\partial t}\ln\rho_* + (\mathbf{v}\cdot\nabla)\ln\rho_* = -\nabla\cdot\mathbf{v}, \tag{4.2}$$

in which we substitute expressions (4.1) to obtain the relationship $ab\rho_0 = M_*$ = const. The two components of the vector equation for the velocity $\mathbf{v}$ yield the following two equations for the functions $a(t)$ and $b(t)$:

$$\ddot{a} = F_a = -\frac{\partial}{\partial a}U_{\text{eff}}, \quad \ddot{b} = F_b = -\frac{\partial}{\partial b}U_{\text{eff}},$$
$$U_{\text{eff}} = \frac{1}{2}C_*(ab)^2 > 0, \quad C_* = \left(\frac{c_0}{M_*}\right)^2 = \text{const}. \tag{4.3}$$

Hence, the function U_{eff} might be considered as an effective potential energy for the motion of a "test particle" of unit mass ($m = 1$) in the (a, b) plane, in which case the "total energy" of the particle is conserved, $\dot{a}^2 + \dot{b}^2 + C_*(ab)^2 = \text{const}$.

Note that the two equations (4.3) can be solved only numerically. In the particular case $a = b$, we arrive at the equation $\dot{a} = -\sqrt{(C_*/2)(a_{\max}^4 - a^4)}$, whose solution is an elliptic cosine function.

For the elliptic solution, dimensionless density (4.1) becomes

$$\rho_* = \frac{M_*}{\sqrt{a^2b^2 + x^2b^2 + y^2a^2}}. \tag{4.4}$$

As may be seen, this density is maximum at the origin of the coordinates, $x = y = 0$. Since, in our model, the density is related to the temperature by $n = \text{const}/\sqrt{T}$, the temperature distribution has the form of a paraboloid with an elliptical cross section,

$$T = T(t, x, y) = C_T(a^2b^2 + x^2b^2 + y^2a^2), \tag{4.5}$$

where C_T = const. In the simplest model at hand, the contours of the same value of density, pressure, and temperature are ellipses $(x/a)^2 + (y/b)^2 = f(t)$. It is important to stress that, although the temperature in the central region of the ellipses is the lowest, radiation from this region is most intense because of the elevated density. This unusual situation is likely to take place in the observed blobs.

In three-dimensional geometry, we also can obtain an exact nonlinear ellipsoidal solution

$$\rho = \frac{A_0}{a_1a_2a_3\sqrt{1 + (x/a_1)^2 + (y/a_2)^2 + (z/a_3)^2}}, \quad A_0 = \text{const}, \tag{4.6}$$

in which the three semiaxes of the ellipsoid, a_i ($i = 1, 2, 3$), decrease with time according to the equations

$$\ddot{a}_i = -\frac{\partial}{\partial a_i}U_{\text{eff}}, \quad U_{\text{eff}} = C_*(a_1a_2a_3)^2 > 0, \quad C_* = \text{const}. \tag{4.7}$$

We can see that a test particle starting from a point with coordinates (a_1, a_2, a_3) should slide down the slope of the potential energy well and, at a certain time, should occur in the plane $a_1 = 0$, or in the plane $a_2 = 0$, or in the plane $a_3 = 0$. This indicates that the self-contraction of the ellipsoid parallel to one of its axes has come to an end. In attempting to apply this theoretical model to actual blobs, it is necessary to take into account additional dissipative effects that are capable of preventing the ellipsoid from being completely self-contracted.

Such dissipative effects are not incorporated into our model equations (3.1). However, for the case $|\gamma| = 1$ and $\mu = -1/2$, we can construct an even more general self-similar solution of the form $v_i = M_{ik}x_k$ (with summation over k), in which the off-diagonal elements of the matrix $M_{ik}(t)$ describe the rotation of the ellipsoid. In turn, the rotation may counteract the self-contraction and may even stop it.

We see that the above illustrative model with the Joule heating of neutrals, which leads to the Chaplygin adiabatic equation of state $p \sim 1/\rho$, reflects important features of the behavior of actual blobs in tokamaks, in particular, the spontaneity of the onset of individual local density hills and wells of different sizes λ and their growth on time scales of $\tau \sim \lambda/2\pi c_0$.

Near the tokamak wall, however, the current density is comparatively low and the SOL plasma is heated not by the Joule mechanism but by thermal conduction from the central region of the plasma column. Hence, a more complicated model is to be constructed, capable of explaining why the temperature at the centers of the blobs remains essentially constant in time. To do this, we consider the emission from impurities in tokamaks in more detail.

5. RESONANT EMISSION FROM CARBON ATOMS

The main impurity ions in a tokamak plasma are carbon ions with the atomic number $Z = 6$ and different charge numbers. Their density n_C is about $\alpha \approx 10^{-4}$ of the electron density n_e. Near the wall, however, the density of carbon ions can be markedly higher, although, their density at the wall is, of course, zero, while the density of the influx of neutral atoms from the wall is nonzero.

For the power $W_{rad} = n_e n_C Q$ radiated by carbon ions, the dependence of the factor $Q(T_e)$ on the electron temperature is already presented in Fig. 3; however, in order to provide a better insight into the subject, this dependence is also shown in Fig. 5, which is borrowed from the familiar paper by Post *et al.* [7].

The factor Q is seen to have a narrow resonance peak: it reaches a maximum, $Q_{max} \approx 10^{-18}$ [cm^3 erg/s], at $T_m = 7$ eV and is already two orders of magnitude smaller at $T \approx 20$ eV. These theoretical estimates were obtained in the average-ion approximation by using the coronal equilibrium model. However, as was pointed out, e.g., in [8], taking diffusive fluxes into account should lead to a deviation of the distribution of impurity ions from being coronal and to a corresponding change in the total radiation intensity. In this case, according to [8], the maximum value of the factor and the half-width of the peak both remain the same, but the maximum should occur at a temperature of $T_{max} = 20$ eV (see Fig. 7, curve *c*), which corresponds approximately to electron temperatures observed at the centers of blobs. Strictly speaking, in considering such rapidly moving objects as blobs, it is necessary to account for a delay in the formation of the distribution of impurity ions over the charge states, as was done, in particular, by Krasheninnikov *et al.* [9]. Also, radiative instabilities are known to be highly sensitive to the magnetic field strength. However, these effects are not expected to qualitatively change blob behavior.

If further experiments will confirm that it is indeed the manifestation of this strange "law of temperature conservation at the centers of blobs" that has been noticed in observations, then, in our opinion, its explanation lies just in the resonant nature of (i.e., the narrow peak in) the intensity of emission from carbon impurities (for oxygen ions, the dependence $Q(T)$ is also of a resonant nature, but these ions are practically absent in large tokamaks). In particular, the narrowness of the peak in the function $Q(T)$ allows us to rule out the above assumption that the radiation power $W_{rad} = n_e n_Z Q$ is balanced exclusively by the Joule heating power.

It would be more correct to assume that, in tokamaks, the power of radiative losses from impurities is balanced by the power of the heat flux from the central region of the plasma column. From the heat-conduction equation $(3n_eT)'_t = W_T = \nabla \cdot (k\nabla T) \approx kT''_{rr}$ we can see

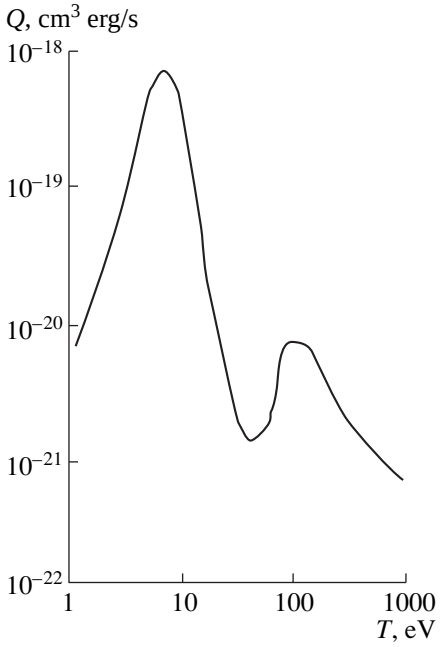

Fig. 5. Factor $Q(T)$ for carbon ion impurities (borrowed from [7]).

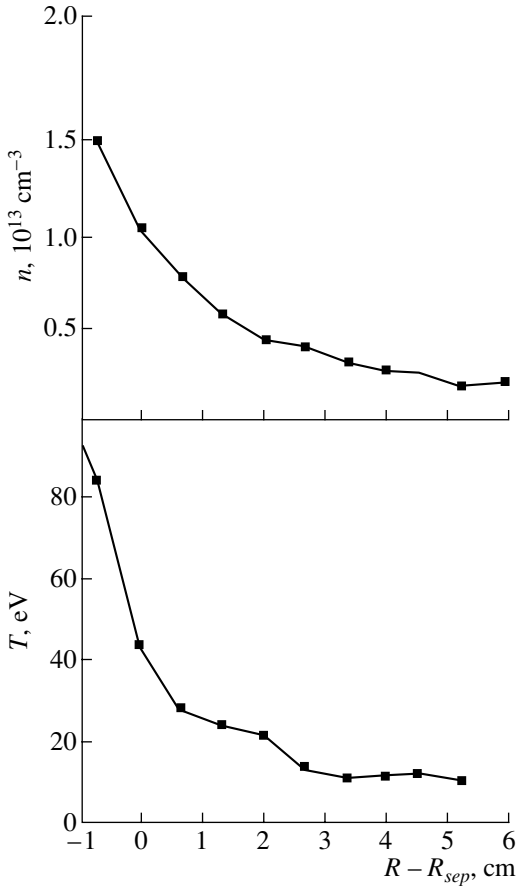

Fig. 6. Decrease in the density and temperature in the region around the separatrix and near the wall, where the blobs are observed in the DIII-D tokamak (borrowed from [10]).

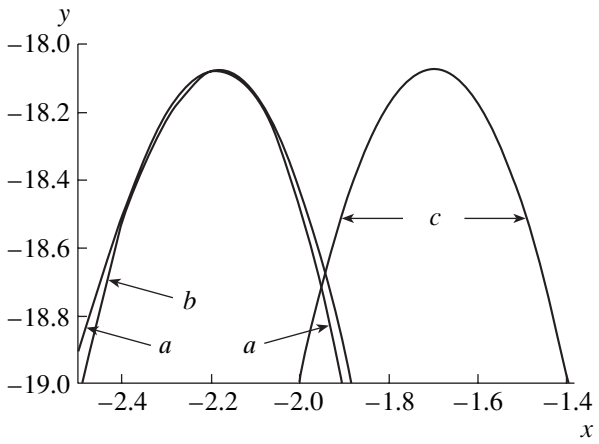

Fig. 7. Factor $Q(T)$: (*a*) Post's curve, (*b*) approximation by a parabola proposed here, and (*c*) shifted parabola.

that $W_T > 0$, provided that $T''_{rr} > 0$. Figure 6 presents the density (n_e) and temperature (T_e) profiles that were observed experimentally around the separatrix and near the wall in the DIII-D tokamak (see [10]). We can see that, in the separatrix region, $T''_{rr} > 0$; i.e., the heat is released there. In steady state, the power of the heat flux from the central region of the tokamak plasma should be balanced by the radiative loss power, indicating that the relationship $W_T = W_{\text{rad}}$, which is not associated with the electric conductivity η and currents, is satisfied.

In this model, blobs do not carry filamented currents; nevertheless, in a certain narrow temperature range δT around the peak in the function $Q(T)$, they may behave as unstable self-contracting objects.

6. A QUASI-CHAPLYGIN SITUATION AROUND THE EMISSION PEAK

It is important to point out the following circumstance. If we assume that the generation of blobs is associated with the presence of carbon ions that come from the wall, reach the separatrix, and penetrate the plasma to a certain depth, then a quasi-Chaplygin situation, which gives rise to the thermal-radiative instability, inevitably occurs in the emitting layer, regardless of the way in which heat is supplied to it. In this case, the heating power W may be pumped into the plasma by any means: by the injection of fast particle beams; by the electron-cyclotron, ion-cyclotron, or lower hybrid heating; etc.

In the quasi-Chaplygin situation, the equation for the local heat balance in the emitting layer, $W = W_{\text{rad}} = n_e n_Z Q(T)$, yields a certain relationship between the electron density n_e and the factor $Q(T)$, which should have the form

$$n_e = n_i = N(w, T)Q^s, \tag{6.1}$$

where the factor $N(w, T)$ depends on both the heating method, symbolized by the letter w, and temperature. Since the factor $Q(T)$ exhibits a sharp peak at $T = T_*$, we can insert this peak temperature into $N(w, T)$ and assume that $N = N_*$ is constant, which gives $n_e = N_* Q^s$, where s is a certain positive ($s = |s|$) or negative ($s = -|s|$) power index.

For example, for $s = 1$, the density and pressure are described by the parametric formulas $n = N_* Q(T)$ and $p = nT = N_* TQ(T)$. We can see that, as the temperature $T > T_*$ increases at the right slope of the peak, the density decreases but the pressure can increase in a certain narrow temperature range; this indicates that we are dealing with an unstable quasi-Chaplygin situation (symbolically, $p \sim 1/n$). In the opposite case ($s = -1$), we have $n = N_*/Q(T)$ and $p = N_* T/Q(T)$. We see that, as the temperature decreases from the peak value T_* leftward, the density increases, but the pressure can decrease in a certain temperature range, which again indicates an unstable quasi-Chaplygin situation.

Let us illustrate these general qualitative considerations about the role of the carbon peak by a specific example. In [7], the function $Q(T)$ for carbon ions near the first maximum in the temperature range 3–20 eV was approximated by the fifth-degree polynomial $y(x) = 10^3 \sum_{k=0}^{5} a_k x^k$, where $y = \log(Q\ [\text{cm}^3\ \text{erg/s}])$; $x = \log(T_e\ [\text{keV}])$; and the six coefficients are equal to $a_0 = 1.965300$, $a_1 = 4.572039$, $a_2 = 4.159590$, $a_3 = 1.871560$, $a_4 = 0.4173889$, and $a_5 = 0.03699382$.

The plot of the function $y(x)$ is shown by curve *a* in Fig. 7. Near the maximum, the function is well approximated by the parabola $y \approx y_{\max} - a(x - x_{\max})^2$; for the parameter values adjusted above, namely, $y_{\max} = -18.08$, $a = 9$, and $x_{\max} = \log(0.0065)$, the parabola is shown by curve *b* in Fig. 7.

In [7], numerical calculations were carried out in terms of the coronal equilibrium model. However, coronal equilibrium is distorted by anomalous diffusive fluxes. In [8], it was pointed out that, even when these fluxes are taken into account only approximately, the entire curve is shifted rightward so that its maximum occurs at $x_{\max} = \log(0.020)$, the values of the parameters $y_{\max}$ and a being unchanged. This shifted parabola is shown by curve *c* in Fig. 7. For $a = 9$, it corresponds to the following mutually inverse formulas:

$$Q = Q_{\max} \exp\left[-\beta\left(\ln\frac{T}{T_*}\right)^2\right],$$
$$T = T_* \exp\left[\pm\sqrt{\frac{1}{\beta}\ln\frac{Q_{\max}}{Q}}\right], \tag{6.2}$$

where $Q_{\max} = 10^{-18.08}$ [cm^3 erg/s], $\beta = 3.9$, and the peak temperature is set to be $T_* = 20$ eV. The plus and minus

signs refer to the right and left slopes of the peak, respectively.

We now can draw the following hypothetical scenario of the generation of blobs. Hot plasma diffuses from the center toward the periphery and progressively cools down. Close to the separatrix, this plasma enters the wall layer of carbon impurities. If the plasma temperature by that time has approached the peak value T_* from the right, the emission from this layer increases abruptly. Then, as was described above, the balance between the heating power and the radiative loss power will lead to a state characterized by a certain relationship $n = N_* Q^s$.

7. TWO REGIONS OF THE "CARBON" INSTABILITY

Next, we consider the following two cases: $s = |s| > 0$ and $s = -|s| < 0$. In the first case, we obtain the relationship $n = \text{const} \cdot \exp\left[-\beta_s\left(\ln\frac{T}{T_*}\right)^2\right]$ (where $\beta_s = |s|\beta > 0$), which indicates that taking into account the power index $|s|$ will merely change the parameter β. In other words, we are dealing with two situations: for $|s| > 1$, the half-width of the peak decreases and, for $|s| < 1$, the half-width of the peak increases. Presumably, the latter situation more closely corresponds to the experimental conditions, because blobs can originate at higher plasma temperatures, i.e., deeper within the plasma and, accordingly, farther from the separatrix. So, for the right slope of the peak ($T > T_*$), formulas (6.2) with $n \sim Q^{|s|}$ can be rewritten as

$$\nu = \frac{n}{n_{\max}} = \exp\left[-\beta_s\left(\ln\frac{T}{T_*}\right)^2\right] < 1, \qquad \frac{T}{T_*} = \exp\left[\sqrt{\frac{1}{\beta_s}\ln\frac{1}{\nu}}\right] > 1, \tag{7.1}$$

where $n_{\max}$ is a new constant. Then, setting, e.g., $|s| = 1/2$ and $\beta_s = |s|\beta = 3.9/2 = 1.95$, we arrive at the following dependence of the density on pressure:

$$p = 2nT = 2n_{\max}T_* P^{(1)}(\nu), \qquad P^{(1)}(\nu) = \nu\exp\left(0.71\sqrt{\ln\frac{1}{\nu}}\right). \tag{7.2}$$

The function $P^{(1)}(\nu)$ is plotted in Fig. 8a. We see that the pressure decreases with increasing density only at the right edge of the plot, in a narrow range of temperatures ($T(\nu) \sim 20$–25 eV), densities ($\nu \sim 0.9$–1), and pressures ($P^{(1)}(\nu) \sim 1.134$–1); it is in this range that the quasi-Chaplygin instability can develop.

We now analyze the second case, in which the power index is negative, $s = -|s| < 0$; i.e., $n \sim Q^{-|s|}$. In this case, instead of formulas (7.2), we deal with the formulas

$$\nu = \frac{n}{n_{\min}} = \exp\left[|\beta_s|\left(\ln\frac{T_*}{T}\right)^2\right] > 1, \qquad \frac{T}{T_*} = \exp\left[-\sqrt{(1/|\beta_s|)\ln\nu}\right] < 1, \tag{7.3}$$

where $n_{\min}$ is a new constant. In formulas (7.3), we have $n > n_{\min}$ and $T < T_*$, which corresponds to the left slope of the peak. This is why we have chosen the minus sign (–) in front of the square-root sign in the exponential function for the temperature. The dependence of the density on pressure has the form

$$p = 2nT = 2n_{\min}T_* P^{(2)}(\nu), \qquad P^{(2)}(\nu) = \nu\exp(-0.71\sqrt{\ln\nu}). \tag{7.4}$$

The function $P^{(2)}(\nu)$ is plotted in Fig. 8b. Again, we see that the pressure decreases with increasing density, but only at the left edge of the plot in a narrow range of temperatures ($T(\nu) = 16$–20 eV), densities ($\nu = 1$–1.1), and pressures ($P^{(2)}(\nu) = 0.88$–1), precisely where quasi-Chaplygin instability can develop. In the two cases at hand, we have $n^{(1)} \sim Q^{|s|}$ and $n^{(2)} \sim Q^{-|s|}$. This indicates that, if the parameters of the medium lie within the parameter range of the quasi-Chaplygin instability, then the thermal-radiative instability (which is also

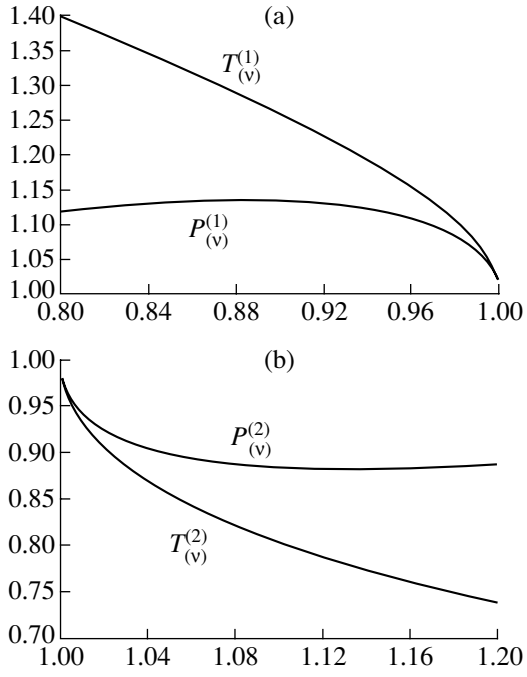

Fig. 8. Dependence of the pressure and temperature on the density: (a) at the right slope of the peak, $P^{(1)}(\nu)$, and (b) at the left slope of the peak, $P^{(2)}(\nu)$.

called radiative condensational instability) can occur. For both of the approximating profiles $P(\nu)$ obtained above, the nonlinear equations cannot be solved analytically, but it is easy to see that their solutions are unstable. Note that the above instability range near the peak is fairly narrow, which agrees well with observations of the distinctive properties of blobs. In some papers (see, e.g., [11]) devoted to radiative condensational instability, different heating models yielded a wider instability range, 7–50 eV, which agrees less closely with the observational data on blobs. However, in the range 30–50 eV, the instability is likely to be suppressed by plasma heat conduction.

It is also important to stress that the presence of a sharp peak in the emission intensity stops the self-contraction process and produces a peculiar effect—the flattening of perturbations. This effect is hard to calculate numerically but, at a qualitative level, it can be described as follows. If the temperature goes beyond the instability range, the perturbations stop growing and saturate at a certain level. However, the perturbations in the neighboring regions of the medium should continue to grow to this level and inevitably result in the formation of a flat-top hill in the density or a density well with a flat bottom, resembling lunar craters. The effect of flattening the perturbations is well illustrated by a number of numerical solutions given by Meerson in his review [12] on the radiative condensational instability. Although Meerson also presented some analytic solutions, he said nothing about our simplest bloblike ellipsoidal solutions (4.1), (4.6), and (9.3), which, however, were mentioned in [3, 4].

The fact that blobs can have different sizes (see [2]) provides indirect evidence that the flattening effect is indeed possible, provided that the blobs originate at different distances from the separatrix and thus differ in their "ages of formation."

Let us, however, consider another possible quasi-Chaplygin instability that is not associated with the emission of radiation.

8. NONRADIATIVE CHARGE-EXCHANGE INSTABILITY

We assume that there are no impurities and set $n_e = n_i$ and $T_e = T_i$. In this case, the thermal energy of a unit plasma volume is equal to $w = \frac{3}{2}(n_e + n_i)T$, and its time derivative obviously has the form

$$\frac{\partial}{\partial t}w = \frac{3}{2}(n_e + n_i)\frac{\partial}{\partial t}T + \frac{3}{2}T\left(\frac{\partial}{\partial t}n_e + \frac{\partial}{\partial t}n_i\right). \quad (8.1)$$

We also assume that, near the separatrix, the density n_0 of the neutral hydrogen (or deuterium) atoms that come from the wall and enter the plasma is sufficiently high. In this case, because of the resonant charge exchange of the plasma ions with neutrals, the density of the hot ions will decrease according to the equation

$$\frac{\partial}{\partial t}n_i = -\frac{n_i}{\tau_{cx}} = -n_i n_0 \sigma v_{Ti}, \quad (8.2)$$

where $\tau_{cx} = 1/n_0\sigma v_{Ti}$ is the charge-exchange time and σ is the cross section for resonant charge exchange. It is well known that this cross section is nearly constant: for ion temperatures of 10–100 eV, it decreases gradually from $\sigma = (3.6–2.6) \times 10^{-15}$ to 2.6×10^{-15} cm^2 (see [13]). Hence, instead of the power of recombination losses (i.e., the power of radiation emitted by the recombining carbon ions, $W_{\rm rad} = n_e n_Z Q_{\rm rad}(T)$), we can consider the power lost in nonradiative charge-exchange processes, $W_{cx} = n_e n_0 Q_{cx}(T)$, where the factor $Q_{cx} = \frac{3}{2}T\sigma v_{Ti}$ plays the same role as the factor $Q_{\rm rad}$ used above.

It has already been shown that the emission intensity exhibits a sharp peak, $Q_{\rm rad}^{\max} = 10^{-18}$ [cm^3 erg/s], at $T_* = 20$ eV. The charge exchange–related factor for hydrogen atoms can be expressed by the formula $Q_{cx} = 10^{-18}(T\ {\rm eV}/20)^{3/2}$ [cm^3 erg/s]. We can see that this factor exceeds the emission–related factor everywhere except at the peak, at which they are equal. We thus can conclude that hot charge-exchange neutrals produced near the separatrix fly away to the nearby wall almost instantaneously, thereby carrying energy outward from the plasma.

On the other hand, cold neutrals that are knocked out of the wall surface fly into the SOL plasma and become ionized in charge-exchange processes. The depth to which cold neutrals penetrate into the plasma can be estimated from the formula $L_0 = v_0\tau_{cx} = v_0/n_0\sigma v_{Ti}$, which can be rewritten as $L_0 n_0 \sigma = v_0/v_{Ti} = \sqrt{T_0/T_i}$. The temperature of the charge-exchanged ions is approximately equal to $T_i \sim 100–200$ eV and the temperature of the wall is about $T_0 \sim 1000$ K = 0.1 eV, so that we have $v_0/v_{Ti} \approx 1/45$. Setting $L_0 = 10$ cm and $\sigma = 3 \times 10^{-15}$ cm^2, we arrive at the estimate $n_0 \sim 7 \times 10^{11}$ cm^{-3} for the neutral density in the region in front of the separatrix, where blobs are thought to originate. At such a density of the neutrals, charge exchange–related heat losses from a unit volume would be equal to

$$W_{cx} = n_i n_0 Q_{cx} \approx 10^{13} \times (7 \times 10^{11}) \times 10^{-18}\ {\rm erg/cm^3\ s} = 0.7\ {\rm W/cm^3}. \quad (8.3)$$

Under the assumption that the thickness of the charge exchange–dominated wall layer is approximately equal to 10 cm, the heat flux to the entire wall surface can be estimated at 7 W/cm^2, which corresponds to a power flux of 700 W to a surface 10×10 cm in area (figuratively speaking, this is the power of an ordinary flatiron).

The above situation with charge exchange–related heat losses does not yet have features peculiar to the quasi-Chaplygin instability (specifically, the decrease in pressure with increasing density). There are also certain difficulties associated with the absence of a resonance peak analogous to the peak in the intensity of emission from carbon impurities. As was seen above, the presence of such a peak allows us to expect that a quasi-Chaplygin situation inevitably occurs in a certain narrow range of the parameters n_e and T_e of the background plasma, regardless of how heat is supplied to the emitting layer, provided that it is transported in such a way that the background parameters in question fall within the "dangerous" instability range.

For instance, at a high heating power in the JT-60U tokamak, the electron plasma density n_e is maintained at a fairly low level by injecting high-energy neutrals. As a result, the temperature at the center of the plasma column is approximately 40 keV and, even near the separatrix, the temperature is as high as about 4 keV. Under these conditions, blobs are not generated, presumably because the background parameters do not fall in the dangerous range.

At the same time, blobs are observed in the DIII-D tokamak, in which the plasma is also heated by neutral beam injection but the plasma density is extremely high (i.e., is close to the familiar Greenwald density limit; see [14]) and the temperature at the separatrix is equal to 40 eV (see Fig. 6). We think that it is these conditions that correspond to the quasi-Chaplygin instability range, in which blobs can originate.

In this section, however, we are assuming that the mechanism for generating blobs is associated not with emission from carbon impurities but with the power lost in nonradiative resonant charge-exchange processes, $W_{ex} = n_i n_0 Q_{cx}$, where the charge exchange–related factor is equal to $Q_{cx} = 10^{-18}\ (T\ [\text{eV}]/20)^{3/2}\ [\text{cm}^3\ \text{erg/s}]$. In this case, even in the absence of a narrow peak, we can nevertheless arrive at an unstable quasi-Chaplygin situation if we assume that the power of charge-exchange losses is balanced by a *constant* power continuously supplied to the plasma, $W_0 = \text{const}$, which depends neither on the plasma density nor on the plasma temperature.

In particular, this situation occurs in a plasma heated by neutral beam injection (as well as by any other means) in such a way that the power fed into the plasma is *constant* and is high enough to provide efficient operation of a tokamak in a steady mode. In the phenomenological approach at hand, we do not specify the mechanism by which heat is transported from the injection region to our hypothetical "charge-exchange layer" (it may be heat conduction, diffusion, convection, or some other mechanism) and merely assume that $W_{cx} = W_0 = \text{const}$. If we further assume that $\alpha = n_0/n_e = \text{const}$, then we obtain the desired quasi-Chaplygin relationships

$$W_0 = W_{cx} \sim \alpha n_i^2 T^{3/2} = \text{const},$$
$$n_i \sim \text{const}\, T^{-3/4}, \quad p = 2nT \sim T^{1/4} \sim \frac{\text{const}}{n^{1/3}}, \tag{8.4}$$

in which the pressure decreases with increasing density, and thus again arrive at instability, as will be clear later.

9. NONLINEAR SOLUTIONS FOR ARBITRARY μ VALUES

If, as before, we introduce the dimensionless density $\rho_* = n/n_0$, then we can write the equations of motion in the standard quasi-Chaplygin form:

$$\frac{\partial}{\partial t}\rho_* + \nabla\cdot(\rho_*\mathbf{v}) = 0,$$
$$\frac{\partial}{\partial t}\mathbf{v} + (\mathbf{v}\cdot\nabla)\mathbf{v} = -\frac{1}{\rho}\nabla p = \mu c_0^2 \nabla \rho_*^{1/\mu}, \tag{9.1}$$

where $c_0^2 = p_0/3\rho_0 > 0$. The azimuthal number is equal to $\mu = -3/4 < 0$, which is close to the value of this parameter in the first example with Joule-heated neutrals, $\mu = -1/2 < 0$. Consequently, the overall pattern of the instability due to charge-exchange losses is qualitatively very similar to that of the instability in the first example.

In a linear approximation such that $\rho_* = 1 + \Psi$ with $\Psi \ll 1$, the azimuthal number drops out, leaving the equations

$$\frac{\partial}{\partial t}\Psi = -\nabla\cdot\mathbf{v}, \quad \frac{\partial}{\partial t}\mathbf{v} = c_0^2\nabla\Psi,$$
$$\Delta\Psi + \frac{1}{c_0^2}\Psi_{tt}'' = 0 \tag{9.2}$$

to describe the growing standing perturbations. In a nonlinear approximation with $\mu = -3/4 < 0$, we can, as before, construct a self-similar two-dimensional ellipsoidal solution. Moreover, as will be shown below, such a solution can also be constructed for arbitrary values of the azimuthal number μ.

To do this, we seek a self-similar solution in the form

$$\rho_* = \left[A(t)\left(1 + \frac{x^2}{a^2} + \frac{y^2}{b^2}\right)\right]^\mu, \quad v_x = x\frac{\dot a}{a},$$
$$v_y = \frac{\dot b}{b}. \tag{9.3}$$

In this case, the first of Eqs. (9.1), namely, the continuity equation, gives the relationship $A(t) = C_*(ab)^{-1/\mu}$,

where $C_* > 0$ is a constant, and the second of Eqs. (9.1) yields the equations

$$\ddot{a} = -\frac{\partial}{\partial a}U_{\text{eff}}, \quad \ddot{b} = -\frac{\partial}{\partial b}U_{\text{eff}},$$
$$U_{\text{eff}} = 2\mu^2 c_0^2 C_*(ab)^{-1/\mu}, \tag{9.4}$$

where the function $U_{\text{eff}} = U(a, b)$ plays the role of the potential energy of a "test" particle of unit mass moving in the (a, b) plane. For negative azimuthal numbers ($\mu < 0$), this energy is maximum at the lines $a = b = 0$, toward which the test particle should tend during the self-contraction of the ellipsoid.

By analogy, it is easy to construct a solution describing the self-contraction of a three-dimensional ellipsoid parallel to one of its axes. We thus see that solutions describing self-contracting blobs can also be constructed in the model with nonradiative charge exchange losses.

We now consider the motion of the blobs.

10. POSSIBLE MECHANISM FOR BLOB MOTION

As has already been noted, the mechanism for blob motion was described by Krasheninnikov [2] (see also [14]), who considered a blob as a magnetic tube in a magnetic field B_φ decreasing toward the plasma edge. The difference between the gradient drifts of the electrons and ions polarizes the magnetic tube and produces a polarization electric field $\mathbf{E}$, in which charged particles drift with the velocity $\mathbf{V} = c\mathbf{E} \times \mathbf{B}/B^2$.

Our quasi-Chaplygin model is also capable of describing blob motion; moreover, it provides a simpler motion pattern than do the models developed in [2, 14], because it is based on the one-fluid MHD approximation, which makes no distinction between plasma ions and electrons. The equation of blob motion obtained in our model makes it possible to draw an analogy with Archimedes' principle: the (denser) hills in the plasma density "sink toward the bottom" (i.e., toward the tokamak chamber wall), while the (less dense) wells "rise upward" (from the wall toward the plasma center). The same effect was captured in [2, 14] and was also observed experimentally. In this respect, the two approaches are equivalent. There is, however, preliminary information that blobs were observed both on the inner and outer sides of the torus. If this information finds further confirmation in experiments, then the models developed by Krasheninnikov and others need to be improved.

We now describe the motion of blobs in our model in more detail. The plasma motion in a tokamak can be divided into three stages. First, the plasma diffuses from the central regions toward the periphery and cools down. Near the separatrix, the plasma parameters fall in the dangerous instability range; this is followed by the second stage—the generation of blobs. In this stage, the density $n_e = n_i$ of the plasma and its temperature $T_e = T_i$ are such that the growing perturbations of the plasma density in the form of hills and wells of different sizes (which depend on the sizes of the initial spontaneous seed perturbations) can be generated. The perturbations continue to grow and develop until the plasma within them behaves in accordance with the quasi-Chaplygin equation of state $p \sim \rho^{-|\gamma|}$. However, at a certain time, the temperature of the blobs goes beyond the dangerous range and the plasma enters a third stage.

In this final stage, a blob that has already been formed can be regarded as a small ball (in a three-dimensional model) or a thin magnetic tube (in a two-dimensional model) whose interior is fully ionized plasma obeying the conventional adiabatic equation of state with a positive power index, $p \sim \rho^{5/3}$.

The motion of this (perfectly conducting) plasma in a magnetic field is described by the standard equation of motion

$$\rho\frac{d}{dt}\mathbf{v} = -\nabla p + \mathbf{f}_m, \quad \mathbf{f}_m = \frac{1}{c}[\mathbf{j} \times \mathbf{B}], \tag{10.1}$$

where $\mathbf{f}_m$ is the magnetic Ampère force. In the equatorial plane $z = 0$ of a tokamak, the radial component of the Ampère force is equal to

$$f_r = \frac{1}{c}(j_\varphi B_z - j_z B_\varphi) = -\frac{\partial}{\partial r}\frac{B_z^2}{8\pi} - \frac{1}{r^2}\frac{\partial}{\partial r}\frac{r^2 B_\varphi^2}{8\pi}. \tag{10.2}$$

It should be mentioned parenthetically that $j_z = (c/4\pi r)\partial(rB_\varphi)/\partial r$ at $z = 0$. In equilibrium, we obviously have $dp/dr = f_r$. Let us, however, consider a two-dimensional, fully developed blob as a magnetic tube that has a small cross-sectional area S and is stretched along the tokamak magnetic field. The mass $m_1 = S\rho$ per unit length of the tube should be regarded as being conserved during its small displacements near the separatrix.

Then, multiplying Eq. (10.1) by S, we write the following equation for radial motion of the tube in the separatrix region:

$$m_1\ddot{r} = -m_1\frac{\partial}{\partial r}\frac{5T}{m_i} + F_r, \tag{10.3}$$

where m_i is the mass of an ion. On the right-hand side of the equation, the first term, which is the gradient of the enthalpy, describes the force that pushes the tube toward the separatrix (toward the bottom). The second term describes the magnetic force

$$F_r = Sf_r = \frac{1}{c}(J_\varphi B_z - j_z \Psi_\varphi) \tag{10.4}$$

(where $J_\varphi = j_\varphi S$ and $\Psi_\varphi = B_\varphi S$), which pushes the tube away from the separatrix. On the one hand, the magnetic flux $\Psi_\varphi = B_\varphi S$ through the cross section of the tube is frozen in the plasma and, therefore, does not change

during displacements of the tube. On the other hand, the current $J_\varphi = j_\varphi S$ flowing in the tube can also be regarded as being conserved. Consequently, we can assume that the net magnetic force F_r is constant. It is also important to note that this net force is independent of the mass per unit length of the blob, $m_1 = \rho S$, but depends on its cross-sectional area S.

It is easy to see that Eq. (10.3) is equivalent to Archimedes' principle. In a coordinate system in which the z axis points downward along the gravity force g, the motion of a massive cylinder of mass m_1, cross-sectional area S, and length L_1 in water is obviously described by the equation

$$m_1\ddot{z} = m_1|g| - F_A, \quad F_A = (SL_1\rho_w)|g|, \qquad (10.5)$$

where ρ_w is the water mass density and F_A is the buoyancy force. This analogy implies that the denser blobs (hills) should "sink toward the bottom" (i.e., toward the separatrix and farther toward the wall or the divertor), while the less dense blobs (wells) should "rise upward" (from the separatrix toward the plasma center).

This motion pattern can apparently provide a realistic interpretation of Fig. 1, which presents six successive film frames of a moving blob. It is reasonable to assume that the blob shown in the frames in Fig. 1 is a hill (rather than a well) approaching the separatrix. When the separatrix is reached, the blob breaks into two parts. The lighter (substantially depleted) part, which is more likely to be a well (rather than a hill) in the plasma density, stops moving inside the separatrix and gradually dissipates. The heavier (far more massive) part, which is more likely to be a hill, passes through the separatrix and continues to move toward the wall, in which case, however, it is dissipated by the divertor and, accordingly, is progressively slowed down.

11. ROTATION OF DENSER BLOBS

Our nonlinear quasi-Chaplygin model is also capable of describing the rotation of blobs that has been observed in some tokamak experiments. This can be done by taking into account the off-diagonal elements of the matrix $M_{ik}(t)$ in the self-similar solutions $v_i = M_{ik}x_k$. In this case, the equation of motion with $\gamma = -1$ yields the relationships

$$\frac{d}{dt}v_i = (\dot{M}_{ij} + M_{ik}M_{kj})x_j = -\frac{1}{\rho}\nabla_i p = -\frac{1}{2}c_0^2\nabla_i\rho_*^{-2}, \qquad (11.1)$$

which allow us to look for an ellipsoidal solution such that

$$\rho_* = \frac{A(t)}{\sqrt{1+S}}, \quad S = B_{jk}(t)x_jx_k, \qquad -\frac{1}{\rho}\nabla_i p = -\frac{c_0^2}{A^2(t)}B_{ik}x_k. \qquad (11.2)$$

Using relationships (11.2), we can express the matrix $\hat{B}$ in terms of the matrix $\hat{M}$, $B_{ij} = -(A(t)/c_0)^2(\dot{M}_{ij} + M_{ik}M_{kj})$. In this way, the continuity equation leads to the following two equations:

$$\frac{\partial}{\partial t}\ln\rho_* + (\mathbf{v}\cdot\nabla)\ln\rho_* = -\nabla\cdot\mathbf{v} = -M_{ii} = \frac{\dot{A}}{A}, \qquad \dot{B}_{ik} = -2M_{ij}B_{jk}, \qquad (11.3)$$

in which summation is implied over the repeated indices.

To illustrate this point, we consider a simple two-dimensional cylinder rotating as a solid body. In this case, we have

$$x = r\cos\varphi, \quad y = r\sin\varphi, \quad \varphi = \omega t, \qquad \dot{x} = -\omega y, \quad \dot{y} = \omega x, \qquad (11.4)$$

and, therefore, $M_{11} = M_{22} = 0$, $M_{12} = -\omega$, and $M_{21} = \omega$. The first of Eqs. (11.3) yields $\dot{A} = 0$ and $A = A_0 = \text{const}$, and the second gives $B_{ik} \sim \delta_{ik}$ and, consequently, $S = B_{ik}x_ix_k \sim r^2$. If we write the final solution in the form of a hill in the density,

$$\rho_* = \frac{A_0}{\sqrt{1+(r/a)^2}}, \qquad (11.5)$$

then we can readily see that this hill can be in equilibrium only when it rotates as a solid body with a certain angular frequency, $\omega = c_0/aA_0$, such that centrifugal forces prevent its quasi-Chaplygin self-contraction. At large radial distances r, however, this exact nonlinear solution decreases too gradually (as $\rho^* \approx c_0/\omega_r$) and, therefore, can hardly be said to correspond to actual blobs. This remark also applies to all of the above exact nonlinear solutions in the form of collapsing ellipsoids.

In real situations, the rotation of blobs can be attributed to the fact that, outside the separatrix, their edges are in contact with the limiters or with the divertor plates, which primarily absorb electrons. The remaining (excess) ions create a positive space charge within the blob filament, so that it begins to rotate about its axis because of the electric drift in the toroidal magnetic field $B_\parallel$.

Experiments show that blobs moving in the radial direction and approaching the wall are also displaced poloidally just downward from the equatorial plane $z = 0$, i.e., in a direction opposite to that of the gradient drift

of the ions (see Fig. 2). That the blobs move in this direction may be qualitatively explained by assuming that, near the wall, the blob filament, rotating counterclockwise, interacts directly with the SOL plasma and rolls down the layer like a toothed wheel, clinging to the wall but with a certain sliding factor $k_{sl} < 1$.

This vivid picture, which is illustrative in character, makes it possible to obtain a rough estimate for the poloidal velocity of blobs. Thus, if the radial electric field within a blob filament is 100 V/cm, then, in the magnetic field $B = 20$ kG, the filament rotates about its axis with the angular velocity $V_{\rm rot} = cE/B = 5$ km/s and slides down the wall with the poloidal velocity $v_p = k_{sl}V_{\rm rot}$. The experimentally observed values of the poloidal velocities, $v_p \sim 500$ m/s [10], show that, in this case, the sliding factor is approximately equal to $k_{sl} \sim 1/10$. The development of a more exact theory of the poloidal motion of rotating charged blobs may require the inclusion of the transverse viscosity of the SOL plasma, in the spirit of the formulas that were used in the cited papers by Krasheninnikov *et al.* to describe nonrotating blobs.

12. CONCLUSIONS

In conclusion, we summarize the results obtained. We have discussed the following distinctive features of observed blobs:

(i) the randomness (spontaneity) of their onset,

(ii) their local nature (blobs are individual local perturbations),

(iii) the presence of wells and hills in the plasma density,

(iv) great diversity in size (0.3–3 cm), and

(v) motion in accordance with Archimedes' principle (the hills sink to the separatrix, while the wells rise in the opposite direction).

These features allow us to conclude that blobs may be thought of as a kind of so-called quasi-Chaplygin medium and thus should be described by the corresponding equations. In our model, blobs are considered as self-contracting plasma objects. In order for the self-contraction of local blobs to occur, certain conditions must be met, specifically, the equation of state of the blob matter should describe such a situation that, as the density n increases, the pressure $p = nT$ decreases because of an even faster decrease in the blob temperature due to some particular mechanism for heat removal from the blob.

In our opinion, a mechanism for the self-contraction of blobs may be associated either with the nonradiative resonant charge-exchange instability, resulting from the presence of cold neutral hydrogen (deuterium) atoms near the tokamak wall, or with thermal-radiative instability, driven by the presence of carbon or oxygen impurities in the plasma. Note that thermal-radiative instability is also referred to as radiative condensational instability, the theory for which was formulated in [3, 4] and in [11, 12, 15, 16].

A characteristic feature of carbon and oxygen impurities is that their emission spectra exhibit sharp peaks (maxima) at certain (comparatively low) temperatures near the tokamak wall. Of course, additional experimental investigations are needed to make the final choice between the above two possible self-contraction mechanisms—nonradiative charge exchange with neutrals and radiation from impurities.

In this context, we should mention tokamak experiments performed by Lazarev *et al.* [17], who observed the sporadic appearance of small plasma bunches that were carried away from the plates of a lithium divertor and manifested themselves as individual small bright spots at the plates. These plasma bunches might have developed from lithium blobs.

If future experiments on different tokamaks will confirm that such impurities as carbon and oxygen (with the corresponding spectral lines) are indeed present in a blob, then the phenomenon of blobs may turn out to be closely akin to the MARFE phenomenon, since it is commonly accepted that MARFEs originate from the thermal-radiative instability of carbon impurities. Note, however, that MARFEs have been observed to be comparatively long-lived (on time scales of about $\tau \sim 1000$ μs) immobile bright formations occurring on the inner side of the torus. As for blobs, they rapidly (at a velocity of about several kilometers per second) move through the SOL plasma toward the wall and last for much shorter times ($\tau \sim 50$–100 μs). In most of the papers on the subject, it is reported that blobs are observed on the outer side of the torus; however, some papers reported the occurrence of blobs on the inner side. We thus can conclude that MARFEs and blobs are likely to have very different properties.

ACKNOWLEDGMENTS

We would like to thank V.I. Ilgisonis, V.S. Lisitsa, V.G. Merezhkin, S.V. Mirnov, and D.A. Shuvaev for their valuable advice in connection with our work. We are especially grateful to V.A. Vershkov and G.I. Kirnev for discussing the experimental results and to D.Kh. Morozov for bringing to our attention the possible relationship between the blobs and MARFE phenomena and for useful critical comments. This work was supported in part by the RF Presidential Council on Scientific Grants and the Federal Program for Government Support of Leading Scientific Schools, project no. 00-15-96526.

REFERENCES

1. E. S. Marmar, in *Proceedings of the 19th IAEA Fusion Energy Conference, Lyon, 2002*, Paper OV/4-1.
2. S. I. Krasheninnikov, Phys. Lett. A **283**, 368 (2001).
3. S. K. Zhdanov and B. A. Trubnikov, *Quasi-Gaseous Unstable Media* (Nauka, Moscow, 1991).

4. D. A. Trubnikov, S. K. Zhdanov, and S. M. Zverev, *Hydrodynamics of Unstable Media* (CRC, Boca Raton, FL, 1996).
5. B. B. Kadomtsev, *Reviews of Plasma Physics*, Ed. by M. A. Leontovich (Atomizdat, Moscow, 1963; Consultants Bureau, 1966), Vol. 2.
6. M. M. Stepanenko, private communication.
7. D. E. Post, R. V. Jensen, C. B. Tarter, *et al.*, At. Data Nucl. Data Tables **20**, 397 (1977).
8. Yu. N. Dnestrovskii and D. P. Kostomarov, *Numerical Simulations of Plasmas* (Nauka, Moscow, 1982; Springer-Verlag, New York, 1986).
9. S. I. Krasheninnikov, D. J. Sigmar, D. Kh. Morozov, *et al.*, Contrib. Plasma Phys. **36**, 271 (1996).
10. J. A. Boedo, D. Rudakov, R. Moyer, *et al.*, Phys. Plasmas **8**, 4826 (2001).
11. D. Kh. Morozov and Kh. Érrera, Fiz. Plazmy **24**, 379 (1998) [Plasma Phys. Rep. **24**, 347 (1998)].
12. B. I. Meerson, Rev. Mod. Phys. **68**, 215 (1996).
13. *Handbook of Physical Quantities*, Ed. by I. S. Grigoriev and E. Z. Meilikhov (Énergoatomizdat, Moscow, 1991; CRC, Boca Raton, FL, 1997).
14. S. I. Krasheninnikov, A. Yu. Pigarov, S. A. Galkin, *et al.*, in *Proceedings of the 19th IAEA Conference on Fusion Energy, Lyon, 2002*, Paper IAEA-CN-94/TH/-1.
15. B. J. Lipshultz, J. Nucl. Math. **145–147**, 15 (1987).
16. V. I. Gervids, V. I. Kogan, and D. Kh. Morozov, Fiz. Plazmy **27**, 994 (2001) [Plasma Phys. Rep. **27**, 938 (2001)].
17. V. B. Lazarev, E. A. Azizov, A. G. Alekseev, *et al.*, in *Proceedings of the 30th Zvenigorod Conference on Plasma Physics and Controlled Fusion Research, Zvenigorod, 2003*, Abstracts of Papers, p. 50.

Translated by O.E. Khadin

Plasma Physics Reports, Vol. 29, No. 10, 2003, pp. 816–825. Translated from Fizika Plazmy, Vol. 29, No. 10, 2003, pp. 880–890.

TOKAMAKS

Beta-Limiting MHD Phenomena in Toroidal Systems

V. D. Pustovitov

Nuclear Fusion Institute, Russian Research Centre Kurchatov Institute, pl. Kurchatova 1, Moscow, 123182 Russia

Received December 26, 2002; in final form, April 17, 2003

Abstract—Equilibrium effects, neoclassical tearing modes, and resistive wall modes are discussed as phenomena limiting attainable plasma pressure, with emphasis on the current progress in theoretical studies at the Kurchatov Institute. The review is based on the results presented at the 11th International Congress on Plasma Physics (Sydney, 2002). © *2003 MAIK "Nauka/Interperiodica".*

1. INTRODUCTION

High-β steady-state operation is a long-run objective of fusion research (here, $\beta \equiv 2\bar{p}/\mathbf{B}^2$ is the ratio of the averaged plasma pressure $\bar{p}$ to the magnetic field pressure $\mathbf{B}^2/2$). There are two distinct mechanisms of β limitation in toroidal systems: those related to MHD equilibrium and MHD stability. In general, equilibrium issues can be more easily resolved. However, the stability problem remains critical for toroidal systems, though considerable progress has been gained in tokamak operation [1]. The range of MHD phenomena that can result in β limitation in toroidal systems is rather wide. This topic was thoroughly discussed in the fundamental work [1], which gives an excellent review of the today's physics of tokamaks. Here, we discuss the equilibrium and stability effects that can influence the β limit, with emphasis on recent theoretical results, in particular, on neoclassical tearing modes (NTMs) and resistive wall modes (RWMs), since they can put the most severe β limitations for large long-pulse ITER-like tokamaks. One goal of these theoretical studies is a more precise calculation of the balance between stabilizing and destabilizing effects for NTMs, the contributions from the bootstrap current and the polarization current in the generalized Rutherford equation. Another goal is the analysis of the feedback suppression of RWMs. This includes the study of double-wall effects on RWMs, the modeling of ideal and conventional feedback systems, and the comparison between feedback algorithms with different input signals.

2. EQUILIBRIUM

The plasma equilibrium in magnetic confinement systems is described by the equations

$$0 = -\nabla p + \mathbf{j} \times \mathbf{B}, \tag{1}$$

$$\mathbf{j} = \nabla \times \mathbf{B}, \quad \nabla \cdot \mathbf{B} = 0. \tag{2}$$

Here, p is the plasma pressure, $\mathbf{j}$ is the current density, and $\mathbf{B}$ is the magnetic field.

Equation (1) multiplied by ∇r and integrated over the plasma volume (assuming $p = 0$ at the boundary) gives

$$\int \frac{p}{r} dV + \int (\mathbf{j} \times \mathbf{B}) \cdot \nabla r dV = 0, \tag{3}$$

where r is the radius in the cylindrical coordinates r, ζ, and z, attached to the main axis of the system. The first term in this integral equilibrium condition describes the ballooning force, which increases with plasma pressure. The equilibrium limit is the maximum pressure at which the electromagnetic force $\mathbf{j} \times \mathbf{B}$ is still able to oppose this ballooning force.

Analytical estimates lead to the following scaling for the equilibrium β limit for a large-aspect-ratio ($R/b \gg 1$) circular plasma in tokamaks and stellarators [2, 3]:

$$\beta_{eq} \propto \mu^2 \frac{b}{R}. \tag{4}$$

Here, μ is the rotational transform and b and R are the minor and major radii, respectively.

This formula shows that β_{eq} is larger in systems with a smaller aspect ratio R/b (compact systems) and/or with a larger rotational transform. However, the range $\mu > 1$ is a dangerous area because the $\mu = 1$ surface in the plasma makes it unstable against the $m/n = 1/1$ mode, which strongly affects the overall performance. This is equally true for tokamaks [1, 4, 5] and stellarators [6–8].

In addition to high β_{eq}, compact systems have other advantages and are attracting increased interest [9–15]. Spherical tokamaks have already demonstrated their ability to operate with β up to 20 and even 30% [10–12]. Recent results from the NSTX spherical torus were presented by Maingi at the 11th International Congress on Plasma Physics (Sydney, 2002) [16]. Here, we discuss only conventional tokamaks and stellarators.

Another way of increasing β_{eq} in toroidal systems is plasma shaping, mainly the vertical elongation of the plasma cross section. It is known that, besides increas-

ing β_{eq}, the plasma shaping in tokamaks has great many other advantages. Proper shaping improves plasma stability and energy confinement [1, 17–26]. The benefits of plasma shaping were widely recognized long ago, and tokamaks (including the mentioned spherical tokamaks) now operate with noncircular (D-shaped) plasma.

In conventional stellarators, similar shaping allows the increase in β_{eq} by a factor of 1.5–2, depending on the rotational transform [27, 28]. Estimates for large-aspect-ratio configurations with K = const show that [27]

$$\frac{\beta_{eq}(K)}{\beta_{eq}(1)} = \frac{3K^2+1}{4}\left(\frac{2K}{K^2+1}\right)^2, \quad (5)$$

where K is the toroidally averaged plasma elongation. The formula can be applied to tokamak and stellarator configurations without shear. It shows that a double increase in β_{eq} is achieved at $K = 2$. This value is quite reasonable. For comparison, $K = 1.7$ in JET [29], $K \leq 1.8$ in ASDEX Upgrade [30] and JT-60U [31], $K = 1.85$ in DIII-D [32], $1.1 < K < 2.8$ in the TCV tokamak [23, 26], and $K = 1.7$–2.0 in ITER [33]. A remarkable feature of stellarators with shear is a much stronger dependence of β_{eq} on the plasma elongation than that described by formula (5). Therefore, the elongation $K = 1.2$–1.3 may be sufficient to double β_{eq} in stellarators [27]. This conclusion is valid for conventional stellarators with planar circular axis; typical representatives of this family are CHS [34] and LHD [35].

In contrast to tokamaks, conventional stellarators have not yet used the tokamak-like plasma shaping as a standard technique. However, this possibility was analyzed and even tested in experiments in the ATF torsatron [36–38]. When stellarators face the problem of achieving β several times higher than values typical for present-day experiments, plasma shaping must be accepted as a natural way of expanding the capabilities of stellarators.

Plasma shaping allows the combined improvement of several important properties, whereas some other means of increasing β_{eq} can actually bring severe limitations on β due to the deterioration of plasma stability. An example is the inward (high-field-side) shift of the plasma column in conventional stellarators. In principle, this method allows the suppression of the Pfirsch–Schlüter current [39] to such an extent that the configuration can become almost independent of the plasma pressure (in some cases, theoretically, completely independent) [40, 41]. Such a configuration was first described by Greene and Johnson in 1961 [42], and another example was given in 1966 [43]. The described configurations looked rather exotic ($R/b = 100$ and 100 periods of the helical field in [43]), independence from the plasma pressure was never observed in conventional stellarators, and there was no convincing theory explaining the underlying physics and relations between the main parameters. That is why the unusual predictions of [42, 43] remained unnoticed and unexplained for a long time. Interest revived when experiments on Heliotron E produced some results [44, 45] that contradicted the expectations based on customary notions. It was proved later [40, 41] that these results were a manifestation of the same mechanism that was responsible for the pressure independence in [42, 43]. Theory [40, 41] also explained why the pressure independence was never observed experimentally and predicted that it could be achieved in Heliotron E, though in a regime rather far from the standard operation. It was a real success that, afterwards, the experiment [46] indeed demonstrated the predicted phenomenon. Later, the analytical predictions [40, 41] and the experimental results [46] were confirmed by precise numerical calculations [47, 48]. Complete agreement between different theoretical approaches and experimental results was an impressive demonstration of the predictive power of the MHD equilibrium theory.

It is known that inward shifting also improves the neoclassical transport and confinement of high-energy particles in stellarators. On the other hand, the inward shift deteriorates MHD stability [49–53]. The very low stability limit in strongly inward-shifted stellarator configurations makes them unpractical. To be precise, we should note that these statements about stability are primarily based on theoretical knowledge. At the same time, some experimental results from LHD seem to demonstrate a better stability of inward-shifted configurations than was expected from theory.

Stellarators are inherently three-dimensional systems. When 3D shaping is allowed, it is possible to optimize a system in such a way that the Pfirsch–Schlüter current is much lower than that in conventional stellarators. Accordingly, β_{eq} becomes very large. For example, Nührenberg and Zille numerically found a configuration [54] that was almost insensitive to the plasma pressure even at $\beta = 50\%$ (which implies that $\beta_{eq} > 50\%$). The reduction of the Pfirsch–Schlüter current became one of the key elements in the concept of the W7-X stellarator [55, 56].

High β_{eq} has many advantages: the Shafranov shift and variations in the rotational transform profile are small, and the plasma pressure affects the shape of the plasma boundary only slightly. It seems, however, that high β_{eq} is always related to a relatively low stability limit. Even in the perfectly optimized W7-X stellarator, this limit is below 5% [55, 56].

The above is true for the static equilibrium described by Eqs. (1) and (2). However, tokamaks and stellarators sometimes operate with rotating plasma. For example, in the DIII-D tokamak, the toroidal velocity reaches 300 km/s [57]. The related centrifugal force increases the ballooning expansion of the plasma. Therefore, one could expect that the rotation would lower the equilibrium β limit. This can be analyzed

using the formula of [58] for the Shafranov shift [2, 59] with plasma rotation taken into account,

$$\Delta' = \Delta'_S - \frac{a}{R}\frac{\overline{\rho v_t^2} - \rho v_t^2}{B_\theta^2}, \quad (6)$$

where

$$\Delta'_S = -\frac{a}{R}\left[\frac{l_i}{2} + 2\frac{\bar{p} - p}{B_\theta^2}\right] \quad (7)$$

is a "static" part of Δ' [2, 59], the prime denotes d/da, a is the minor radius of a magnetic surface, R is the major radius of the torus, $B_\theta(a) = J/(2\pi a)$ is the field produced by the longitudinal current J flowing through the tube a = const, the bar stands for cross-sectional averaging, ρ is the plasma mass density, v_t is the toroidal velocity, and

$$l_i \equiv \overline{B_\theta^2}/B_\theta^2 \quad (8)$$

is the internal inductance of the plasma tube a = const per unit length.

It is clear that Δ'_S is negative for radially decreasing $p(a)$. Equation (6) shows that the rotation with a decreasing profile of ρv_t^2 increases $|\Delta'|$; consequently, the shift Δ becomes larger. On the other hand, one can reduce $|\Delta'|$ by making ρv_t^2 a growing function of a so that $\overline{\rho v_t^2} < \rho v_t^2$. Both of these conclusions were clearly formulated in [58]. However, the reduction of $|\Delta'|$ in the central part of the plasma column does not yet guarantee an increase in the equilibrium pressure limit. A complete solution of the equilibrium problem must include integration of Δ' with proper boundary conditions. Finally, for a free-boundary equilibrium with p and ρv_t^2 vanishing at the boundary, the effect of toroidal plasma rotation on the equilibrium β limit can be estimated as [60, 61]

$$\beta_{\rm rot} = \beta_{\rm static} - \frac{\overline{\rho v_t^2}}{B_0^2}, \quad (9)$$

where B_0 is the toroidal field at the axis. The last term here is small, so that the decrease in the equilibrium β limit due to the toroidal plasma flow is negligible for typical plasma parameters [61]. Therefore, for fusion plasmas, the plasma rotation effects in global equilibrium can be ignored. The same is true for poloidal rotation under reasonable conditions. Note that Eqs. (6) and (7) show a simple way to generalize the results of the classical theory of plasma equilibrium in tokamaks to the case with a toroidal rotation: in expressions obtained with the use of Shafranov's formula (7), it is sufficient to replace $2p$ by $2p + \rho v_t^2$.

One may conclude that toroidal magnetic configurations can be optimized in such a way that plasma equilibrium is possible, theoretically, up to rather high β. However, only stable equilibria can be realized. There are a lot of instabilities that can destroy equilibrium at $\beta < \beta_{\rm eq}$ [1, 4, 5, 39, 62, 63]. We consider here the stability limitations related to NTMs and RWMs. A potential danger of these instabilities was recognized quite recently, and these fields are now being extensively studied.

3. NEOCLASSICAL TEARING MODES

During the past decade, NTMs have been identified as one of the most serious potential limitations on the attainable plasma pressure in long-pulse tokamak discharges [1, 64, 65]. It was found that the critical β for the onset of the $m/n = 3/2$ mode (often called a soft beta limit) is

$\beta_N < 2$ in TFTR (supershot) [66],

$\beta_N = 2.3$ in DIII-D (long-pulse ELMy H-mode) [67],

$\beta_N = 2.5$ in JT-60U (long-pulse ELMy H-mode) [68],

$\beta_N = 2.2$–2.6, depending on the plasma shape, in ASDEX Upgrade (ELMy H-mode) [69, 70], and

$\beta_N = 2.5$–2.6 in JET (ITER-like discharges, ELMy H-mode) [71].

The normalized beta, sometimes called Troyon β, is defined as

$$\beta_N = \beta[\%]\frac{b\ [\mathrm{m}]\ B\ [\mathrm{T}]}{I\ [\mathrm{MA}]},$$

where I is the plasma current and B is the magnetic field.

For a tokamak-reactor, the attractive range is $3 < \beta_N < 4$ [1]. Sometimes, even higher β_N (up to $\beta_N = 6$ [72]) are mentioned. That is why NTMs, which have a relatively low onset limit, became a concern for the fusion community. The problem is aggravated by the fact that, in experiments, the dependence of the onset β_N on ρ^* (the ion gyroradius normalized to the plasma column radius) is unfavorable for large tokamaks. Earlier observations provided the following scalings for the onset of the $m/n = 3/2$ mode:

$\beta_N \propto \rho^*$ in ASDEX Upgrade [73],

$\beta_N \propto (\rho^*)^{0.13}(\nu^*)^{0.32}$ in DIII-D [64], and

$\beta_N \propto (\rho^*)^{0.64}(\nu^*)^{-0.1}$ in JET [74].

Here, ν^* is the collision frequency normalized to the bounce frequency (see [1], p. 2144). These scalings are clearly incompatible. However, experimental progress, the accumulation of data, and their comparison and analysis have recently led to the opinion [75] (in contrast to earlier conclusions) that the NTM data from DIII-D and JET are, nevertheless, consistent with the linear scaling of the onset β_N on ρ^* observed in ASDEX Upgrade. Although there is a substantial scat-

ter in the JET data in the plot β_N vs. ρ^*, the correlation and scatter are substantially improved when using local parameters [76]. A linear scaling was also observed in JT-60U [77]: $\beta_N \propto \rho^*(\nu^*)^{0.36}$.

If the linear scaling could be valid for much smaller ρ^* than that in the existing devices (e.g., by factor of 3), the critical β_N in ITER with $\rho^* \approx 2 \times 10^{-3}$ might be about 0.5 [65], which is far below the acceptable level.

This number is just an estimate based on an incomplete theory and insufficient data. NTMs are a rather complicated phenomenon involving several competing processes. Therefore, all theoretical predictions remain uncertain and somewhat restricted even for present-day tokamaks. A great deal of work is needed to develop a reliable predictive theory.

The existing theory of NTMs is based on the generalized Rutherford equation for the time evolution of the width W of a magnetic island (see, e.g., [64, 78, 79]):

$$\frac{\tau_s}{r_s}\frac{dW}{dt} = r_s\Delta'(W) + \beta_p\left[\frac{C_b W}{W^2 + W_0^2} - \frac{C_{mw}}{W} - \frac{C_p}{W^3}\right] - \frac{C_{CD}}{W}. \quad (10)$$

Here $\tau_s = \mu_0 r_s^2/(1.22\eta)$ is the resistive time at the resonant surface of radius r_s, η is the neoclassical resistivity, Δ' is the conventional tearing parameter (do not confuse this with equilibrium Δ' in the previous section), β_p is the poloidal beta at the resonant surface, W_0 is the characteristic island width below which the cross-field transport dominates over parallel transport and equalizes the plasma pressure along the island, the term with C_b accounts for the destabilizing neoclassical bootstrap drive, the term with C_{mw} is related to the stabilizing effect of the magnetic well, the term with C_p describes the effect of the so-called polarization currents induced by the diamagnetic motion of the island through the plasma, and the last term with C_{CD} is associated with the stabilizing effect of a properly localized current drive.

The term with C_p is usually considered to be stabilizing: $C_p > 0$. A model based on this assumption with $C_p \propto (\rho^*)^2$, which is known as the ion polarization current model, is frequently used to estimate β_N. It was asserted that experimental observations of tearing modes in ASDEX Upgrade could be satisfactorily explained by the ion polarization current model [73, 80]. However, some data from other devices demonstrated somewhat different behavior [81]. Also, there is an obvious disagreement between the semiempirical models and the theoretical predictions [82]. Nevertheless, there is a general tendency to accept the polarization current model as superior in predicting the scaling and magnitude of the critical β [75].

Waelbroeck and Fitzpatrick pointed out [83] that the true value and even the sign of C_p may differ from the generally accepted ones. Evident theoretical contradictions stimulated further studies [84] that led to the conclusion [85] that, although the analysis of [83], which was based on a simplified model, is somewhat ambiguous, the statement that the polarization current in the absence of drift effects is destabilizing ($C_p < 0$) is correct. However, the question remained as to whether the models used were adequate.

The dilemma whether the effect of the polarization current on NTMs is stabilizing or destabilizing and the origin of these contradictions were discussed in [86, 87], where it was shown that a less restrictive model gives a stabilizing polarization current. Favorable predictions about the role of the polarization current were obtained in [87, 88], where different profile functions were used to describe the electrostatic potential and density perturbations instead of the common profile function used in the existing theory. For example, with an assumption; drift effects taken into account, the result is [88]

$$C_p \propto (\omega_{*i} - \omega)(\omega + k_*\omega_{*i}), \quad (11)$$

where ω is the island rotation frequency in the reference frame with a vanishing equilibrium radial electric field, ω_{*i} is the ion drift (diamagnetic) frequency, and k_* is a positive number.

One can see that $C_p < 0$ when the ratio ω_{*i}/ω is small, which agrees with the results of [83, 89]. It is known, however, that in DIII-D [75] and JT-60U [90], the mode rotates in the ion diamagnetic direction. In the DIII-D tokamak, the observed island rotation frequency lies in the range $0 < \omega < \omega_{*i}$ [75]. Under this condition, $C_p > 0$ and the term with C_p is stabilizing. Recent theory shows that it can also be stabilizing even in the absence of the ion drift effects due to the shear of the plasma flow [87].

The discussion about the sign of C_p reflects the fact that C_p "oscillates" around zero. Since the sign of C_p can be easily changed in a narrow range of ω, one can conclude that C_p should be small. If so, its stabilizing role cannot be substantial. This is however, it is also supported by the detailed NTM analysis that takes into account the finite ratio of the ion gyroradius to the magnetic island width, ρ_i/W [91]. It is shown in that paper that both C_b and C_p are actually smaller than the values used in the existing theory, developed in the approximation $\rho_i/W \longrightarrow 0$. What is surprising is that, according to [91], the dependence of C_p on ρ_i/W cannot be ignored even at $\rho_i/W = 10^{-1}$–10^{-2} (remember that $\rho_i = 1$ cm at $T = 10$ keV and $B = 1$ T). The conclusion is that the onset β can be one-half of the traditionally estimated NTM limit. This result of [91] is most unfavorable for large tokamaks, which again demonstrates that the problem is rather complicated and challenging.

The destabilizing effect of the bootstrap current depends not only on C_b in Eq. (10), but also on the value of W_0. The larger the W_0, the smaller the destabilizing term. In the generally accepted model [64], W_0 is related to the competition of the perpendicular and parallel heat transport inside the island, which results in the weakening of the perturbed bootstrap current. Recently, a generalized transport threshold model of NTMs in tokamaks was proposed in [92, 93]. In addition to transverse and parallel heat transports, the model takes into account several other mechanisms opposing the instability drive. According to [92, 93], with account taken of the parallel convection and magnetic island rotation, the equation for the island width evolution has the same form as Eq. (10). However, in these cases, the value of W_0 may be different, since it is determined by the smallest value of the characteristic scales related to the above three mechanisms. This means that W_0 may sometimes be smaller than the value used in the existing theory. Accordingly, the stability β limit must again be lower.

Incorporation of the perpendicular viscosity changes the structure of the equation for W. It is shown in [93] that, in this case, one should make a substitution in Eq. (10):

$$\frac{C_b W}{W^2 + W_0^2} \longrightarrow C_b\left[\frac{W}{W^2 + W_0^2} - \frac{C_\mu W_\mu^2}{W(W^2 + W_\mu^2)}\frac{\omega}{\omega_{*i}}\right], \quad (12)$$

where W_μ is the characteristic length related to the ion perpendicular viscosity coefficient $\mu_{\perp i}$, $W_\mu^2 \approx \mu_{\perp i}/(\sqrt{\varepsilon}\nu_i)$, $\varepsilon = r_s/R$, ν_i is the ion collision frequency, and C_μ is a positive coefficient on the order of unity.

The authors of [93] pointed out that, for $W < (W_0, W_\mu)$, the right-hand side of expression (12) becomes

$$-\frac{C_b C_\mu}{W}\frac{\omega}{\omega_{*i}}. \quad (13)$$

This value is negative for $\omega/\omega_{*i} > 0$.

If so, the perturbed bootstrap current is stabilizing. This seems too good to be true, and this prediction will certainly be analyzed in more detail because any chance to suppress NTMs must be utilized in tokamaks. In any case, the above results are certainly valuable as a first theoretical comparison of various relevant effects.

The term with C_{mw} in Eq. (10), which is often called Glasser–Greene–Johnson (GGJ) term, is frequently ignored in calculations because, according to some estimates, it is two to three times smaller than the term with C_b [64]. It can be argued, however, that this term must be retained, especially in view of the fact that the stability or instability of NTMs is determined by the rather delicate balance of the opposing terms in Eq. (10).

It is known that toroidicity, which determines the value of C_{mw}, may produce a stabilizing effect on tearing modes [94, 95]. Plasma shaping can be used to reinforce this effect. The influence of plasma geometry on NTMs was studied numerically by Kruger *et al*. [96]. Three tokamaks were considered: TFTR (large aspect ratio, circular cross section), DIII-D (slightly smaller aspect ratio, D-shaped cross section), and Pegasus ELART (extremely low-aspect-ratio tokamak with $A \leq 1.2$, stronger shaping). The conclusion was that the GGJ term is negligible for TFTR, but is more significant for shaped tokamaks, though it would play little role in the efforts to stabilize NTMs in DIII-D (if the shear is not very small). Another conclusion was that, in low-aspect-ratio devices, where the shear is low and beta is high, it might be possible to stabilize NTMs by flattening the profile of the safety factor q near low-order rational magnetic surfaces using a combination of shaping and localized current drive.

The latter conclusion was supported by analytical theory [97]. It was shown that the stabilizing GGJ term could be stronger than the bootstrap terms when

$$0.81\frac{\varepsilon^{3/2}}{S}\frac{1 + \tau_i + \eta_e + \tau_i\eta_i}{1 + \tau_i + 0.4\eta_e - 0.17\tau_i\eta_i}\left[1 - \frac{1}{q^2} + 6\frac{e\delta}{\varepsilon}\right] \geq 1. \quad (14)$$

This formula shows that the combination of the three factors can make the GGJ term large: small shear S at the resonant surface, large ellipticity e (related to the elongation K by $e = (K^2 - 1)/(K^2 + 1)$), and large triangularity δ. Also, formula (14) explicitly shows the sensitivity of NTMs to the equilibrium profiles: $\tau_i \equiv T_i/T_e$ and $\eta_{i,e} \equiv \partial \ln T_{i,e}/\partial \ln n_0$, where T_i and T_e are the ion and electron temperatures, respectively, and n_0 the equilibrium plasma density.

These optimistic predictions of the theory agree well with the experimental observations in ASDEX Upgrade [69, 70] that an increase in the plasma triangularity resulted in an increase in β_N from $\beta_N = 2.2$–2.4 for discharges with a low triangularity to $\beta_N = 2.5$–2.6 for a larger triangularity ($\delta_{top} \approx 0.2$ in the notation of [69, 70]). Also, there is a qualitative agreement with observations in DIII-D that a combination of plasma shaping and q profile modification allows one to substantially increase the NTM beta limit [98]. Finally, this theory gives a reasonable explanation why the onset β_N in shaped tokamaks ($\beta_N = 2.2$–3.0) is larger than in TFTR with circular plasma ($\beta_N < 2$). It should be remembered, however, that a recent interpretation of JET results, stating that an increase in the triangularity raises the NTM β limit while an increase in the elongation makes it lower [99], shows that the problem still remains open.

Favorable theoretical predictions and (in general, promising) experimental results justify the conclusion that all studies related to the stabilizing effect of plasma shaping are to be encouraged. It is known that plasma shaping affects the bootstrap current [17, 38, 100]. Therefore, it might be interesting to optimize shaping

in order to minimize C_b and simultaneously maximize C_{mw}.

4. RESISTIVE WALL MODES

Several years ago, it was demonstrated in DIII-D experiments that at high β near the beta limit, the stability of ideal MHD global kink modes is strongly influenced by the vacuum vessel [101, 102]. It is now a well established fact that the stabilization of low-n kink modes by a conducting wall is crucial for high-β steady-state advanced tokamak scenarios [103]. However, a real wall with a finite conductivity can stabilize the mode only over the time of magnetic diffusion through the wall, τ_w, which can be estimated in cylindrical approximation as $\tau_w = \mu_0 \sigma_w d_w r_w$, where σ_w, r_w, and d_w are the conductivity, minor radius, and thickness of the wall, respectively. On a larger time scale, eddy currents that are induced in the wall and oppose the growth of the mode decay and the kink modes can become unstable. Since their growth rates are determined by τ_w, the modes are called resistive wall modes (RWMs).

Experiments in the DIII-D tokamak [104] have shown that the RWMs limit the attainable β_N at the level

$$\beta_N \approx 4 l_i, \tag{15}$$

where l_i is the internal inductance (it was found later that the RWM stability limit can sometimes be even lower). This value is known as the Troyon limit, representing the ideal MHD beta limit for tokamak discharges without wall stabilization and sawtooth instability [1, 105]. Definition (8) (for circular plasmas) shows that larger l_i values are obtained for more peaked toroidal currents. However, advanced tokamak operation [22, 24, 31, 100, 106–108] with a low or negative shear in the plasma center and a high bootstrap current fraction, on the contrary, demands broad current profiles. Sometimes, the advanced operation even leads to the formation of a so-called "current hole" [109–111]. In the JT-60U tokamak, a current hole, extended up to 40% of the plasma minor radius, existed stably for several seconds [110]. Such distributions have a relatively small l_i (say, smaller than $l_i = 0.5$, which corresponds to a uniform current density). In principle, the tokamak configuration and discharge operation could be optimized to maximize l_i at advanced operation with a bootstrap current fraction as high as 50–70% [112]. However, even in this case, $l_i \cong 1$, which is a rather moderate value.

Keeping l_i as high as possible, as proposed in [112], could be a good way to increase the RWM instability beta limit. However, it is not yet clear whether this idea can be successfully realized with a desired result. Also, even with $l_i = 1$, Troyon limit (15) is not high enough to satisfy the reactor demands. In any case, one must look for the possibility of stationary tokamak operation with β above limit (15).

In recent years, the physics of RWMs and their stabilization have been extensively studied in the DIII-D tokamak (see [57, 103, 104, 113, 114] and references therein). Two approaches to stabilizing RWMs have been tested: plasma rotation and active feedback control. The latter approach was considered to be relatively simple, reliable, and efficient. In reality, however, a great deal of effort has been spent to demonstrate that it works as expected. Finally, reported result [114] was impressive: the feedback system allowed RWMs in DIII-D to be suppressed and the discharge to be sustained for almost a second at pressures approaching twice the no-wall limit.

Feedback stabilization is, in essence, based on conventional electrodynamics, electrical engineering, and control theory. When a particular feedback algorithm is assumed, the results of analysis may depend strongly on the circuit characteristics and the location and properties of the probes. However, the comparison and understanding of the results on RWM feedback stabilization can be greatly eased when the simple formula [115]

$$\gamma \tau_w = \Gamma_0 + 2m \frac{B_{\text{ext}}}{B_\Sigma} \tag{16}$$

is used to explain what is required from the feedback system. Here, γ is the RWM growth rate; $\Gamma_0 = \gamma_0 \tau_w$, with γ_0 being the open-loop growth rate of the same mode; B_{ext} is the amplitude of the radial magnetic field perturbation produced by all sources outside the first wall, including the feedback field ($B_{\text{ext}} = 0$ when the mode is affected by the first wall only); B_Σ is the amplitude of the total radial field perturbation at the first wall; and m is the poloidal mode number. Stabilization is achieved when $\gamma < 0$. Therefore, irrespective of the algorithm, the feedback system must guarantee that the external (with respect to the first wall) field B_{ext} satisfies the criterion

$$\frac{B_{\text{ext}}}{B_\Sigma} < -\frac{\Gamma_0}{2m}. \tag{17}$$

These expressions are derived for a single-mode perturbation in the cylindrical approximation. Such an approach is widely used in theory, which is justified by a comparison of the analytic results with numerical simulations [113, 116].

The analysis of the feedback stabilization of RWMs is simplified by the fact that Γ_0 in Eq. (16) can be considered fixed and independent of B_{ext}. This quantity is determined by the behavior of the perturbed radial field $B_r(r)$ inside the plasma. Toroidal calculations [117, 118] show that the feedback does not strongly modify the $B_r(r)$ profile in the plasma. This is also confirmed by DIII-D experiments and related numerical analysis [113].

In configuration with one resistive wall, B_{ext} is a field produced by the feedback system: $B_{\text{ext}} = B_f$. Then, criterion (17) explicitly gives the necessary stabilizing

field B_f in terms of B_Σ. By definition, B_Σ is the radial component of a magnetic perturbation, which can be measured by "radial" probes. Criterion (17) shows that knowledge of B_Σ is sufficient for determining B_f that is needed to suppress the mode. In other words, RWMs can be easily stabilized by a feedback system with radial magnetic probes. A comparison of RWM feedback systems with different input signals shows that using poloidal probes allows RWM suppression at a lower gain of the system [119]. In all other respects, poloidal probes are no better than radial ones.

These conclusions, however, contradict the common opinion that a feedback system with sensors measuring the poloidal field is much better than one with radial-field sensors. This opinion is based on the solid foundation of numerical calculations and experimental results from DIII-D [113, 114, 117, 118] and cannot be impugned.

This contradiction was resolved in [120] by noting that analytical theory deals with a single harmonic in poloidal and toroidal angles θ and ζ, $\tilde{B}_r = B_r(r)\exp[i(m\theta - n\zeta) + \gamma t]$, while the frame-like correction coils used in DIII-D [5, 7, 104, 113, 114] and assumed in numerical calculations [116–118, 121] produce additional side-band harmonics affecting the measured signal. The radial component of the magnetic field calculated with account taken of these harmonics can vanish at the probe position (equatorial plane) when an RWM is not yet suppressed, thus breaking the feedback loop. This never happens with the poloidal component at this position.

This analysis not only explains the observed difference between feedback systems with radial and poloidal probes, but also shows the great difference between "ideal" and "conventional" systems. It seems that helical correction coils could be better than those presently used in DIII-D. Their comparison is an open issue, perhaps, for a theoretical study only, because the experimental success of DIII-D [114] is sufficient proof of the efficiency of the existing feedback system. In any case, the problem of the "purity" of the feedback-produced magnetic field must be examined.

Feedback "helps" the wall to sustain the induced currents that otherwise would decay because of the wall resistivity. A second wall placed between the plasma-facing (first) wall and the correction coils acts as a screen distorting the feedback-produced field. When the coupling of the feedback with the first wall becomes weak, a slow mode can grow unstabilized [115]. This problem first appeared because ITER has a double wall [1] and the correction coils must be located on the outside. Numerical simulations [116] show that, indeed, the double-wall structure of ITER makes the active control of RWMs somewhat more demanding than in tokamaks with a single wall. The problem can become even more serious in future designs, as the need is to keep the correction coils closer to the first wall if the first wall is resistive.

5. CONCLUSIONS

In the early stages of tokamak and stellarator research, plasma equilibrium was one of the most serious problems [2–5, 39, 42, 43, 60, 122, 123] responsible for β limitation. Now, all major equilibrium issues have been resolved or, at least, thoroughly investigated. It is known that equilibrium limit in toroidal systems can be practically removed by properly optimizing the configuration geometry. Axisymmetric plasma shaping has become a natural element of tokamak operation and remains a potentially useful tool for conventional stellarators. With more complicated 3D shaping, including spatial deformations of the magnetic axis, stellarator configurations can be made almost insensitive to plasma pressure. It seems, however, that optimizing stellarators to very high β_{eq} generally leads to a rather low stability limit. It is not yet clear what kind of stellarators might be able to combine high β_{eq}, good confinement and high stability limit so that stellarators would be competitive with the best modern tokamaks. In general, stellarators have made great progress in recent years; e.g., LHD operates now with β up to 3% [51–53].

Tokamaks are certainly ahead of stellarators on the road to fusion reactors. To satisfy reactor needs, tokamaks must finally demonstrate their capability for high-β steady-state operation. This requires, in particular, preventing NTMs and RWMs that act as factors limiting β. There have been successful experiments on their suppression [30, 31, 114, 124–126]. At the same time, there is great uncertainty in extrapolating the existing data to ITER-scale devices. For example, it is not clear to what extent NTM behavior will be governed by the mentioned unfavorable gyroradius dependence of the onset β and what would be the final form of the generalized Rutherford equation for NTMs. One very important problem is the recovery of β after stabilizing NTMs. A more general question is what the upper limit for β is with active NTM stabilization. A similar question for RWMs has recently been answered: calculations for high-β advanced tokamak equilibria with an ITER shape have shown that the feedback control of RWMs is possible for β_N up to 5, which is twice the no-wall limit [118]. Experiment [114] confirmed this possibility, although at a lower β_N. On the other hand, the influence of plasma rotation and error fields on RWMs [57, 114] still remains an open issue for theorists.

The step from the existing tokamaks to ITER is too big for confident extrapolations based on the available data. This is a typical rather than dramatic situation in science. Perhaps, JET is a good example of such a step in fusion. In this case, a reliable theory is needed to reduce the uncertainty. The rapid development of the MHD theory of NTMs and RWMs reflects the importance of the subjects and the scope of this problem.

ACKNOWLEDGMENTS

The author is grateful to Yu.V. Gribov, V.S. Mukhovatov, A.B. Mikhailovskii, S.V. Konovalov, M. Shimada, and N.V. Ivanov for the continuous support.

REFERENCES

1. ITER Physics Basis, Nucl. Fusion **39**, 2137 (1999).
2. L. E. Zakharov and V. D. Shafranov, *Reviews of Plasma Physics*, Ed. by M. A. Leontovich and B. B. Kadomtsev (Énergoizdat, Moscow, 1982; Consultants Bureau, New York, 1986), Vol. 11.
3. V. D. Pustovitov, *Reviews of Plasma Physics*, Ed. by B. B. Kadomtsev and V. D. Shafranov (Consultants Bureau, New York, 2000), Vol. 21, p. 1.
4. G. Bateman, *MHD Instabilities* (MIT Press, Cambridge, 1978; Énergoizdat, Moscow, 1982).
5. J. Wesson, *Tokamaks* (Clarendon, Oxford, 1987).
6. B. A. Carreras, L. Garcia, and V. E. Lynch, Phys. Fluids **29**, 3356 (1986).
7. M. Wakatani, K. Ichiguchi, F. Bauer, *et al.*, Nucl. Fusion **26**, 1359 (1986).
8. T. Matsumoto, Y. Nakamura, and M. Wakatani, Nucl. Fusion **36**, 1571 (1996).
9. Y.-K. M. Peng and D. J. Strickler, Nucl. Fusion **26**, 769 (1986).
10. S. M. Kaye, M. G. Bell, R. E. Bell, *et al.*, Phys. Plasmas **8**, 1977 (2001).
11. A. Sykes, Plasma Phys. Controlled Fusion **43**, A127 (2001).
12. S. M. Kaye, M. Bell, R. Bell, *et al.*, in *Proceedings of the ITPA Meeting on CDs and Modeling, Princeton, 2002*.
13. S. Okamura, K. Matsuoka, S. Nishimura, *et al.*, Nucl. Fusion **41**, 1865 (2001).
14. M. C. Zarnstorff, L. A. Berry, A. Brooks, *et al.*, Plasma Phys. Controlled Fusion **43**, A237 (2001).
15. P. R. Garabedian, Phys. Plasmas **9**, 137 (2002).
16. R. Maingi, M. G. Bell, R. E. Bell, *et al.*, Plasma Phys. Controlled Fusion **45**, 657 (2003).
17. C. O. Beastly and J. T. Hogan, Nucl. Fusion **28**, 1923 (1988).
18. R. E. Bell, N. Asakura, S. Bernabei, *et al.*, Phys. Fluids B **2**, 1271 (1990).
19. C. S. Chang and S. M. Kaye, Phys. Fluids B **3**, 395 (1991).
20. A. Bondeson, M. Benda, M. Persson, and M. S. Chu, Nucl. Fusion **37**, 1419 (1997).
21. A. C. England, R. E. Bell, S. P. Hirshman, *et al.*, Plasma Phys. Controlled Fusion **39**, 1373 (1997).
22. A. D. Turnbull, T. S. Taylor, M. S. Chu, *et al.*, Nucl. Fusion **38**, 1467 (1998).
23. A. Pochelon, T. P. Goodman, M. Henderson, *et al.*, Nucl. Fusion **39**, 1807 (1999).
24. O. Gruber, R. Wolf, H.-S. Bosch, *et al.*, Nucl. Fusion **40**, 1145 (2000).
25. L. L. Lao, Y. Kamada, T. Oikawa, *et al.*, Nucl. Fusion **41**, 295 (2001).
26. F. Hofmann, R. Behn, S. Coda, *et al.*, Plasma Phys. Controlled Fusion **43**, A161 (2001).
27. V. D. Pustovitov, J. Plasma Fusion Res. **70**, 943 (1994).
28. V. D. Pustovitov, J. Plasma Fusion Res. SERIES **3**, 571 (2000).
29. M. Keilhacker, A. Gibson, C. Gormezano, and P. H. Rebut, Nucl. Fusion **41**, 1925 (2001).
30. O. Gruber, R. Arslanbekov, C. Atanasiu, *et al.*, Nucl. Fusion **41**, 1369 (2001).
31. Y. Kamada and JT-60 Team, Nucl. Fusion **41**, 1311 (2001).
32. B. W. Rice, K. H. Burrel, J. R. Ferron, *et al.*, Nucl. Fusion **39**, 1855 (1999).
33. Y. Shimomura, Y. Murakami, A. R. Polevoi, *et al.*, Plasma Phys. Controlled Fusion **43**, A385 (2001).
34. S. Okamura, K. Matsuoka, R. Akiyama, *et al.*, Nucl. Fusion **39**, 1337 (1999).
35. A. Iiyoshi, A. Komori, A. Ejiri, *et al.*, Nucl. Fusion **39**, 1245 (1999).
36. J. F. Lyon, B. A. Carreras, K. K. Chipley, *et al.*, Fusion Technol. **10**, 179 (1986).
37. B. A. Carreras, H. R. Hicks, J. A. Holmes, *et al.*, Nucl. Fusion **24**, 1347 (1984).
38. R. J. Colchin, M. Murakami, E. Anabitarte, *et al.*, Phys. Fluids B **2**, 1347 (1990).
39. K. Miyamoto, *Fundamentals of Plasma Physics for Controlled Fusion* (Iwanami, Tokyo, 1997).
40. V. D. Pustovitov, Nucl. Fusion **36**, 583 (1996).
41. V. D. Pustovitov, Nucl. Fusion **36**, 1281 (1996).
42. J. M. Greene and J. L. Johnson, Phys. Fluids **4**, 875 (1961).
43. J. M. Greene, J. L. Johnson, and K. E. Weimer, Plasma Phys. **8**, 145 (1966).
44. S. Besshou, K. Ogata, K. Kondo, *et al.*, Nucl. Fusion **35**, 173 (1995).
45. S. Besshou, K. Ogata, K. Kondo, *et al.*, Trans. Fusion Technol. **27**, 219 (1995).
46. S. Besshou, V. D. Pustovitov, N. Fujita, *et al.*, Phys. Plasmas **5**, 481 (1998).
47. Y. Sato, M. Yokoyama, M. Wakatani, and V. D. Pustovitov, Nucl. Fusion **40**, 1627 (2000).
48. M. Yokoyama, K. Itoh, K. Nagasaki, *et al.*, Nucl. Fusion **40**, 1909 (2000).
49. N. Yanagi, S. Morimoto, K. Ichiguchi, *et al.*, Nucl. Fusion **32**, 1264 (1992).
50. K. Ichiguchi, N. Nakajima, M. Okamoto, *et al.*, Nucl. Fusion **33**, 481 (1993).
51. S. Sakakibara, H. Yamada, K. Y. Watanabe, *et al.*, Nucl. Fusion **41**, 1177 (2001).
52. H. Yamada, A. Komori, N. Ohyabu, *et al.*, Plasma Phys. Controlled Fusion **43**, A55 (2001).
53. S. Sakakibara, H. Yamada, K. Y. Watanabe, *et al.*, Plasma Phys. Controlled Fusion **44**, A217 (2002).
54. J. Nührenberg and R. Zille, Phys. Lett. A **129**, 113 (1988).
55. C. Beidler, G. Grieger, F. Herrnegger, *et al.*, Fusion Technol. **17**, 148 (1990).
56. G. Grieger, W. Lotz, P. Merkel, *et al.*, Phys. Fluids B **4**, 2081 (1992).

57. A. M. Garofalo, M. S. Chu, E. D. Fredrickson, *et al.*, Nucl. Fusion **41**, 1171 (2001).
58. H. P. Zehrfeld and B. J. Green, Nucl. Fusion **13**, 750 (1973).
59. V. D. Shafranov, *Reviews of Plasma Physics*, Ed. by M. A. Leontovich (Gosatomizdat, Moscow, 1963; Consultants Bureau, New York, 1966), Vol. 2.
60. V. D. Pustovitov, in *Proceedings of the 29th EPS Conference on Controlled Fusion and Plasma Physics, Montreux, 2002*, Paper P-2.107.
61. V. D. Pustovitov, Fiz. Plazmy **29**, 124 (2003) [Plasma Phys. Rep. **29**, 105 (2003)].
62. M. Wakatani, Y. Nakamura, and K. Ichiguchi, Nucl. Eng. Des. Fusion **15**, 395 (1992).
63. A. B. Mikhailovskii, *Instabilities in a Confined Plasma* (Inst. Phys., Bristol, 1998).
64. O. Sauter, R. J. La Haye, Z. Chang, *et al.*, Phys. Plasmas **4**, 1654 (1997).
65. R. J. Buttery, S. Günter, G. Giruzzi, *et al.*, Plasma Phys. Controlled Fusion **42**, B61 (2000).
66. Z. Chang, E. D. Fredrickson, S. H. Batha, *et al.*, Phys. Plasmas **5**, 1076 (1998).
67. R. J. La Haye, L. L. Lao, E. J. Strait, and T. S. Taylor, Nucl. Fusion **37**, 397 (1997).
68. A. Isayama, Y. Kamada, T. Ozeki, and N. Isei, Plasma Phys. Controlled Fusion **41**, 35 (1999).
69. M. Maraschek, S. Günter, R. C. Wolf, and ASDEX Upgrade Team, in *Proceedings of the 26th EPS Conference on Controlled Fusion and Plasma Physics, Maastricht, 1999*; ECA **23J**, 1393 (1999).
70. R. C. Wolf, O. Gruber, M. Maraschek, *et al.*, Plasma Phys. Controlled Fusion **41**, B93 (1999).
71. JET Team, Nucl. Fusion **39**, 1965 (1999).
72. J. D. Galambos, L. J. Perkins, S. W. Haney, and J. Mandrekas, Nucl. Fusion **35**, 551 (1995).
73. S. Günter, A. Gude, M. Maraschek, *et al.*, Nucl. Fusion **38**, 1431 (1998).
74. R. J. Buttery, T. C. Hender, G. T. A. Huysmans, *et al.*, in *Proceedings of the 26th EPS Conference on Controlled Fusion and Plasma Physics, Maastricht, 1999*; ECA **23J**, 121 (1999).
75. R. J. La Haye, R. J. Buttery, S. Guenter, *et al.*, in *Proceedings of the 18th IAEA Fusion Energy Conference, Sorrento, 2000*, Paper IAEA-CN-77/EXP3/05.
76. JET Team, in *Proceedings of the 18th IAEA Fusion Energy Conference, Sorrento, 2000*, Paper IAEA-CN-77/OV1/2.
77. A. Isayama, Y. Kamada, T. Ozeki, *et al.*, in *Proceedings of the 18th IAEA Fusion Energy Conference, Sorrento, 2000*, Paper IAEA-CN-77/EXP3/03.
78. H. R. Wilson, M. Alexander, J. W. Connor, *et al.*, Plasma Phys. Controlled Fusion **38**, A149 (1996).
79. H. Zohm, Phys. Plasmas **4**, 3433 (1997).
80. S. Günter, G. Giruzzi, A. Gude, *et al.*, Plasma Phys. Controlled Fusion **41**, B231 (1999).
81. R. J. La Haye, R. J. Buttery, S. Guenter, *et al.*, Phys. Plasmas **7**, 3349 (2000).
82. A. B. Mikhailovskii, V. D. Pustovitov, and A. I. Smolyakov, Plasma Phys. Controlled Fusion **42**, 309 (2000).
83. F. L. Waelbroeck and R. Fitzpatrick, Phys. Rev. Lett. **78**, 1703 (1997).
84. A. B. Mikhailovskii, V. D. Pustovitov, V. S. Tsypin, and A. I. Smolyakov, Phys. Plasmas **7**, 1204 (2000).
85. A. B. Mikhailovskii, V. D. Pustovitov, A. I. Smolyakov, and V. S. Tsypin, Phys. Plasmas **7**, 1214 (2000).
86. A. B. Mikhailovskii, V. S. Tsypin, I. C. Nascimento, and R. M. Galvão, Phys. Plasmas **7**, 3474 (2000).
87. A. I. Smolyakov, E. Lazzaro, R. Coelho, and T. Ozeki, Phys. Plasmas **9**, 371 (2002).
88. A. B. Mikhailovskii, S. V. Konovalov, V. S. Tsypin, *et al.*, Phys. Plasmas **7**, 4763 (2000).
89. R. Fitzpatrick and F. L. Waelbroeck, Phys. Plasmas **7**, 4983 (2000).
90. T. Ozeki, A. I. Smolyakov, A. Isayama, *et al.*, in *Proceedings of the 28th EPS Conference on Controlled Fusion and Plasma Physics, Funchal, 2001*; ECA **25A**, 1345 (2001).
91. S. V. Konovalov and A. B. Mikhailovskii, Plasma Phys. Controlled Fusion **43**, 1149 (2001).
92. S. V. Konovalov, A. B. Mikhailovskii, M. S. Shirokov, and V. S. Tsypin, Plasma Phys. Controlled Fusion **44**, 579 (2002).
93. S. V. Konovalov, A. B. Mikhailovskii, M. S. Shirokov, and V. S. Tsypin, in *Proceedings of the 29th EPS Conference on Controlled Fusion and Plasma Physics, Montreux, 2002*, Paper P-4.063.
94. M. Kotschenreuther, R. D. Hazeltine, and P. J. Morrison, Phys. Fluids **19**, 249 (1985).
95. H. Lütjens, J.-F. Luciani, and X. Garbet, Phys. Plasmas **8**, 4267 (2001).
96. S. E. Kruger, C. C. Hegna, and J. D. Callen, Phys. Plasmas **5**, 455 (1998).
97. A. B. Mikhailovskii, B. N. Kuvshinov, V. D. Pustovitov, and S. E. Sharapov, Fiz. Plazmy **26**, 403 (2000) [Plasma Phys. Rep. **26**, 375 (2000)].
98. R. J. La Haye, B. W. Rice, and E. J. Strait, Nucl. Fusion **40**, 53 (2000).
99. T. C. Hender, D. N. Borba, R. J. Buttery, *et al.*, in *Proceedings of the 18th IAEA Fusion Energy Conference, Sorrento, 2000*, Paper IAEA-CN-77/EXP3/02.
100. A. Bondeson, D.-H. Liu, F. X. Söldner, *et al.*, Nucl. Fusion **39**, 1523 (1999).
101. E. J. Strait, T. S. Taylor, A. D. Turnbull, *et al.*, Phys. Rev. Lett. **74**, 2483 (1995).
102. T. Taylor, E. J. Strait, L. L. Lao, *et al.*, Phys. Plasmas **2**, 2390 (1995).
103. T. C. Luce, M. R. Wade, P. A. Politzer, *et al.*, Nucl. Fusion **41**, 1585 (2001).
104. A. M. Garofalo, E. J. Strait, J. M. Bialek, *et al.*, Nucl. Fusion **40**, 1491 (2000).
105. F. Troyon, R. Gruber, H. Saurenmann, *et al.*, Plasma Phys. Controlled Fusion **26**, 209 (1984).
106. T. S. Taylor, H. St. John, A. D. Turnbull, *et al.*, Plasma Phys. Controlled Fusion **36**, B229 (1994).
107. C. Gormezano, Plasma Phys. Controlled Fusion **41**, B367 (1999).
108. T. Fujita, Y. Kamada, S. Ishida, *et al.*, Nucl. Fusion **39**, 1627 (1999).

109. N. C. Hawkes, B. C. Stratton, T. Tala, *et al.*, Phys. Rev. Lett. **87**, 115001 (2001).
110. T. Fujita, T. Oikawa, T. Suzuki, *et al.*, Phys. Rev. Lett. **87**, 245001 (2001).
111. G. T. A. Huysmans, T. C. Hender, N. C. Hawkes, and X. Litaudon, Phys. Rev. Lett. **87**, 245002 (2001).
112. Y. R. Lin-Liu, A. D. Turnbull, M. S. Chu, *et al.*, Phys. Plasmas **6**, 3934 (1999).
113. M. Okabayashi, J. Bialek, M. S. Chance, *et al.*, Phys. Plasmas **8**, 2071 (2001).
114. L. C. Johnson, M. Okabayashi, A. M. Garofalo, *et al.*, in *Proceedings of the 28th EPS Conference on Controlled Fusion and Plasma Physics, Funchal, 2001*; ECA **25A**, 1361 (2001); http://www.cfn.ist.utl.pt/EPS2001/fin/pdf/P4.008.pdf.
115. V. D. Pustovitov, Fiz. Plazmy **27**, 209 (2001) [Plasma Phys. Rep. **27**, 195 (2001)].
116. A. Bondeson, Yueqiang Liu, D. Gregoratto, *et al.*, Nucl. Fusion **42**, 768 (2002).
117. Y. Q. Liu, A. Bondeson, C. M. Fransson, *et al.*, Phys. Plasmas **7**, 3681 (2000).
118. A. Bondeson, Y. Q. Liu, C. M. Fransson, *et al.*, Nucl. Fusion **41**, 455 (2001).
119. V. D. Pustovitov, Plasma Phys. Controlled Fusion **44**, 295 (2002).
120. V. D. Pustovitov, Rep. No. NIFS-723 (Nat. Inst. Fusion Sci., Toki, 2002).
121. M. S. Chance, M. S. Chu, M. Okabayashi, and A. D. Turnbull, Nucl. Fusion **42**, 295 (2002).
122. V. S. Mukhovatov and V. D. Shafranov, Nucl. Fusion **11**, 605 (1971).
123. B. A. Carreras, G. Grieger, J. H. Harris, *et al.*, Nucl. Fusion **28**, 1613 (1988).
124. C. D. Warrick, R. J. Buttery, G. Cunningham, *et al.*, Phys. Rev. Lett. **85**, 574 (2000).
125. G. Gantenbein, H. Zohm, G. Giruzzi, *et al.*, Phys. Rev. Lett. **85**, 1242 (2000).
126. H. Zohm, G. Gantenbein, A. Gude, *et al.*, Nucl. Fusion **41**, 197 (2001).

Translated by the author

Plasma Physics Reports, Vol. 29, No. 10, 2003, pp. 826–830. Translated from Fizika Plazmy, Vol. 29, No. 10, 2003, pp. 891–895.

TOKAMAKS

Identification of the Structure of Large-Scale MHD Perturbations in a Tokamak from Mirnov Signals

A. M. Kakurin and I. I. Orlovsky

Russian Research Centre Kurchatov Institute, pl. Kurchatova 1, Moscow, 123182 Russia

Received February 18, 2003; in final form, March 31, 2003

Abstract—An algorithm is proposed that allows one to identify the MHD mode structure in toroidal plasmas by processing signals from Mirnov probes measuring plasma MHD activity. The algorithm differs fundamentally from the diagnostic methods presently used in tokamaks, being simpler and more efficient. The algorithm is based on constructing an analytic signal using the Hilbert transformation of the Mirnov signals at a given instant. The phase and amplitude dependences obtained take into account the toroidal effects and allow one to determine the number and amplitude of the excited MHD mode. The algorithm was approbated with both test signals and actual signals from MHD diagnostics in the T-10 tokamak. It is demonstrated that the algorithm can be used to analyze single-mode MHD instabilities in toroidal plasmas. © *2003 MAIK "Nauka/Interperiodica".*

1. INTRODUCTION

Conventional methods for studying MHD instabilities in tokamaks are based on analyzing the spatial and temporal evolutions of the perturbations of the poloidal magnetic field in the plasma column [1]. These perturbations have the form of waves propagating in the poloidal and toroidal directions and are usually detected by a set of local magnetic pick-up coils (Mirnov probes) located near the plasma surface. The Mirnov signals are oscillations whose frequencies and amplitudes vary in time. The MHD instability that is responsible for the poloidal field perturbations and is termed "tearing-mode instability" leads to the rearrangement of the magnetic surfaces, which is accompanied by the formation of magnetic islands rotating in the poloidal and toroidal directions.

The island structure is uniquely identified by analyzing the spatial structure of the poloidal field perturbations, which can be expanded in spatial components, each corresponding to a specific magnetic-island structure (i.e., an MHD eigenmode).

The island structure in the toroidal direction can be identified by applying the expansion in Fourier series in spatial harmonics $\exp(n\phi)$, where n is the harmonic number (the toroidal wavenumber) and ϕ is the angular coordinate in the toroidal direction.

The identification of the island structure in the poloidal direction is complicated by the toroidal effects, which distort the poloidal structure of the field perturbations. This is clearly demonstrated in Fig. 8. This figure shows an instantaneous distribution of the poloidal field perturbations $B_\theta(\theta)$ in polar coordinates, which is obtained by interpolating the signals from 24 Mirnov probes arranged uniformly in the poloidal direction. The distribution has the shape of a rosette with petals of different width, which are spaced at irregular intervals. The number of petals corresponds to the poloidal wavenumber m of the excited MHD mode.

For a tokamak plasma with a circular cross section, Merezhkin [2] proposed switching from the poloidal coordinate θ, in which the spatial phase structure of a perturbation is distorted by toroidal effects (the perturbation wavelength is not constant along the poloidal angle θ), to the coordinate θ^*,

$$\theta^* = \theta - \lambda\sin\theta, \tag{1}$$

with

$$\lambda = \frac{r}{R}\left(\beta_p + \frac{l_i}{2} + 1\right),$$

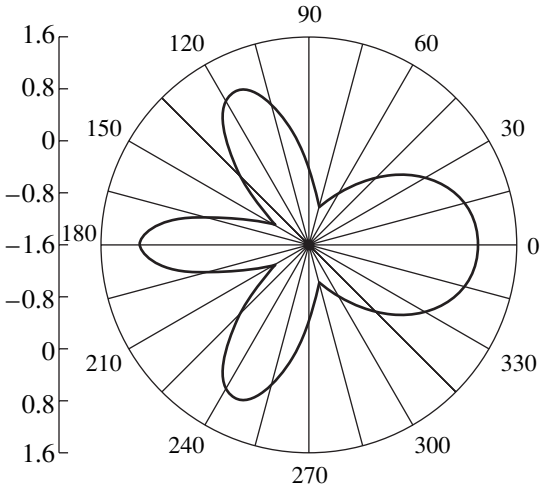

Fig. 1. Spatial distribution of the poloidal field perturbations $B_\theta(\theta) = \cos(m\theta^*)$ with $\theta^* = \theta - \lambda\sin(\theta)$, $m = 4$, and $\lambda = 0.5$ (the phase modulation of the fourth mode).

1063-780X/03/2910-0826$24.00 © 2003 MAIK "Nauka/Interperiodica"

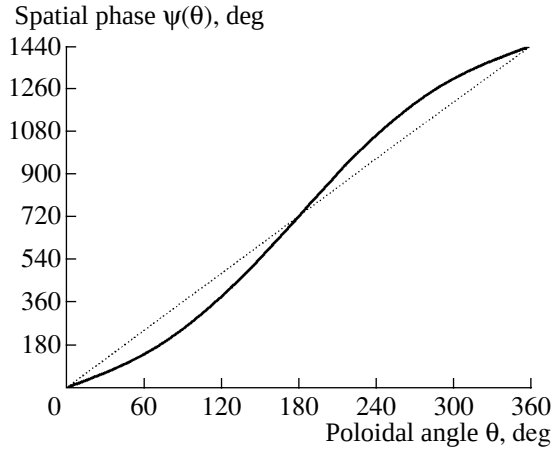

Fig. 2. Spatial phase ψ vs. poloidal angle θ for the distribution shown in Fig. 1.

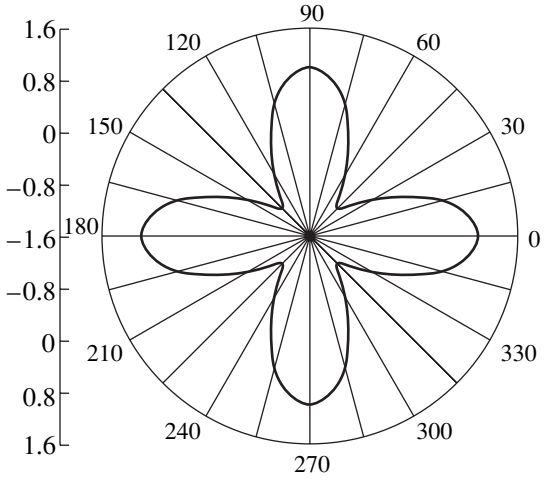

Fig. 3. Spline interpolation of the dependence $B(4\psi)$, where $\psi(\theta)$ is the phase dependence shown in Fig. 2.

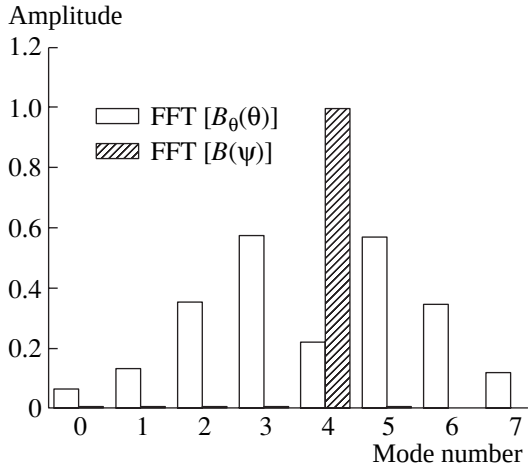

Fig. 4. Amplitudes of the Fourier harmonics for the distributions $B_\theta(\theta)$ and $B(\psi)$.

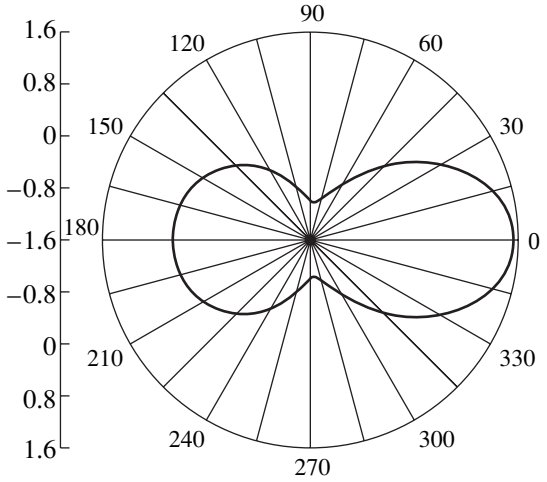

Fig. 5. Spatial distribution of the poloidal field perturbation $B_\theta(\theta) = (1 + 0.5\cos(\theta))\cos(2\theta)$ (the amplitude modulation of the second mode).

in which the toroidal distortions are absent to first order (the wavelength is constant along the coordinate θ*). Here, R is the tokamak major radius, r is the radius of the magnetic surface on which magnetic islands arise, β_p is the poloidal beta, and l_i is the internal inductance. The angle θ is counted from the low-field side of the equatorial plane.

Expression (1) is complicated to use in practice because λ is difficult to determine from the experimental data. One of the versions of employing this expression is to fit the experimental data by a model MHD perturbation with a spatial phase $\varphi_i = m(\theta_i - \lambda\sin\theta_i) + \delta$, where θ_i is the coordinate of the ith probe and λ, δ, and m are free parameters [3].

A new approach to the identification of the mode structure of MHD perturbations is to process the Mirnov signals by using a singular value decomposition (SVD) method or a similar biorthogonal decomposition method [5]. These methods are based on the construction of a covariance matrix (see [4]) with elements in the form of expressions composed of the signals from different Mirnov probes at different instants. A subsequent analysis of the covariance matrix allows one to identify the mode structure of a perturbation. The disadvantage of the SVD method is the assumption that the mode structure does not change within the time sample (up to several milliseconds) that is used to construct the covariance matrix.

Thus, an important problem is to develop an easy to implement and physically explicit numerical algorithm

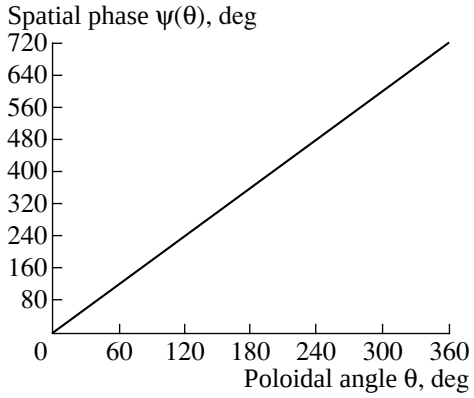

Fig. 6. Spatial phase ψ vs. poloidal angle θ for the distribution shown in Fig. 5.

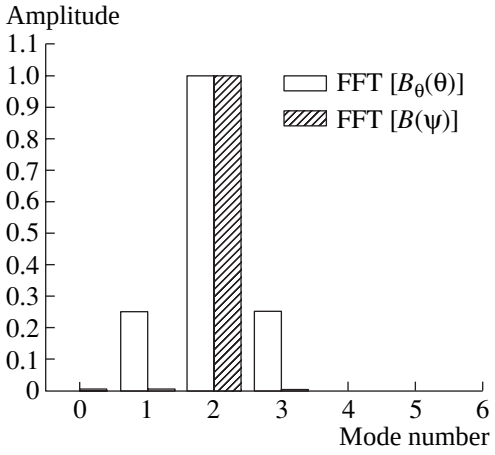

Fig. 7. Amplitudes of the Fourier harmonics of the distributions $B_\theta(\theta)$ and $B(\psi)$ in the case of amplitude modulation (Fig. 5).

for the identification of the instantaneous poloidal structure of an MHD mode by using only Mirnov signals, without invoking the data on λ.

2. MODE-IDENTIFICATION ALGORITHM

We consider a case with a single MHD mode. At a given instant of time, its magnetic field $B_\theta(\theta)$ is an oscillating function of the poloidal angle θ with spatially varying period and amplitude. It is necessary to find a function $\psi(\theta)$ such that the period of $B_\theta(\psi)$ will be constant over the coordinate ψ. It is also required that the transformation does not change the number of maxima, minima, and zeros, which means that the number of petals of the spatial distribution in the new variables should be the same as that in polar coordinates (Fig. 1).

We represent the initial function as a product $B_\theta(\theta) = A(\theta)\cos(\psi(\theta))$, where $A(\theta)$ and $\cos(\psi(\theta))$ are the amplitude and phase factors, respectively. Generally, this representation is ambiguous; however, there is a mathematically rigorous and physically correct method for determining the amplitude and phase of an oscillating function by constructing the so-called analytic signal. This method is reduced to the following procedure. From the given dependence $B_\theta(\theta)$, by using the Hilbert transformation [6, 7], we construct the complex function (the analytic signal)

$$Z(\theta) = A(\theta)\exp(i\psi(\theta)) = B_\theta(\theta) + iH[B_\theta(\theta)], \quad (2)$$

where $A(\theta)$ is the amplitude of the analytic signal and $\psi(\theta)$ is the generalized phase. The Hilbert transformation is given by

$$H(B_\theta(\theta)) = \frac{1}{\pi}\text{v.p.}\int_{-\infty}^{+\infty}\frac{B_\theta(\tau)}{\theta-\tau}d\tau, \quad (3)$$

where v.p. is the Cauchy principal value.

Thus, we have found the function $Z(\theta)$, which satisfies the above requirements; in particular, it has a constant period over the variable ψ. As θ varies within the range $0 \le \theta \le 2\pi$, the generalized phase ψ varies within the range $0 \le \psi(\theta) \le 2\pi m$, where $m > 0$ is an integer. Hereinafter, m is identified with the poloidal wavenumber of the MHD mode.

Let us consider the algorithm for processing a set of the experimental data. Let there be a set of the values of the poloidal magnetic field perturbations $B_\theta(\theta_i)$ for a given MHD mode at a given instant of time that are obtained from Mirnov probes with coordinates θ_i.

By constructing a spatial analytic signal, we change from the set $\{\theta_i\}$ to the new set $\{\psi_i = \psi(\theta_i)\}$.

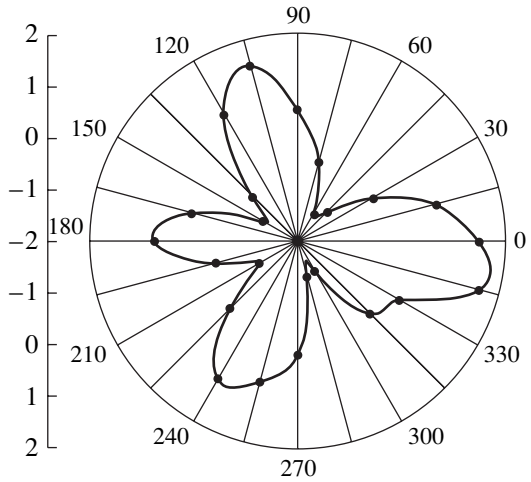

Fig. 8. Spatial distribution of the poloidal field perturbation $B_\theta(\theta)$ in the T-10 tokamak (spline interpolation over signals from 24 probes taken at the 276th millisecond of shot no. 34669).

Using the amplitude factor of the analytic signal $A(\theta_i)$, we correct the perturbation values of the poloidal magnetic field to obtain the set

$$B(\theta_i) = \frac{B_\theta(\theta_i)}{A(\theta_i)}\langle A(\theta_i)\rangle, \quad (4)$$

where $\langle A(\theta_i)\rangle$ is the average value of $A(\theta_i)$ over the interval $0 \le \theta_i \le 2\pi$. Using a one-to-one correspondence between the sets $\{B(\theta_i)\}$ and $\{\psi_i\}$, we obtain the dependence $B(\psi)$. In new variables, the corrected field perturbations have the form of oscillations with a constant amplitude and period.

3. APPLICATIONS OF THE METHOD

The efficiency of the algorithm proposed was tested by applying it to a field with a given spatial mode structure. The field was modeled by a harmonic distribution $B_\theta(\theta^*) = \cos(m\theta^*)$ with a toroidal correction described by formula (1). By varying the parameter λ, we introduced a toroidal distortion (spatial phase modulation) of the resulting distribution $B_\theta(\theta)$, which was no longer a harmonic function but contained a set of spatial harmonics in θ. Figure 1 shows the model distribution $B_\theta(\theta)$ for $m = 4$ and $\lambda = 0.5$, which clearly demonstrates the difference in the petal shapes. The phase of the analytic signal $\psi(\theta)$ (Fig. 2) that corresponds to this distribution is nonlinear. In the distribution $B(m\psi)$ calculated by the algorithm proposed (for a better visualization of the effect, the distribution $B(\psi)$ is scaled down by a factor of $m = 4$), the petals are identical in shape (Fig. 3). Figure 4 shows the Fourier transforms of the distributions $B_\theta(\theta)$ and $B(\psi)$. It can be seen that the Fourier transform of $B_\theta(\theta)$ contains additional harmonics with amplitudes of up to 60% of the fundamental harmonic, whereas the distribution processed by the proposed algorithm contains a single mode with a correctly determined mode number and amplitude (the error in determining the mode amplitude is less than 0.5%, and the amplitude of the "false" harmonics does not exceed 1%). When applying the algorithm to distributions with different λ values (from 0 to 1), the results differed by no more than 1%.

The applicability of this algorithm to a case with an amplitude modulation of the signal was verified by a model signal $B_\theta(\theta) = (1 + 0.5\cos\theta)\cos(2\theta)$, which corresponds to the amplitude modulation of the second mode (Fig. 5). The phase dependence $\psi(\theta)$ in this case is linear (Fig. 6). Figure 7 shows the Fourier transforms of the initial function $B_\theta(\theta)$ and the function $B(\psi)$ constructed using the algorithm proposed. In both cases, the amplitude of the second mode is described correctly; however, the Fourier transform of $B_\theta(\theta)$ contains satellite harmonics with amplitudes that amount to ~25% of the second-mode amplitude.

The figures clearly demonstrate that the proposed algorithm for the identification of the perturbation

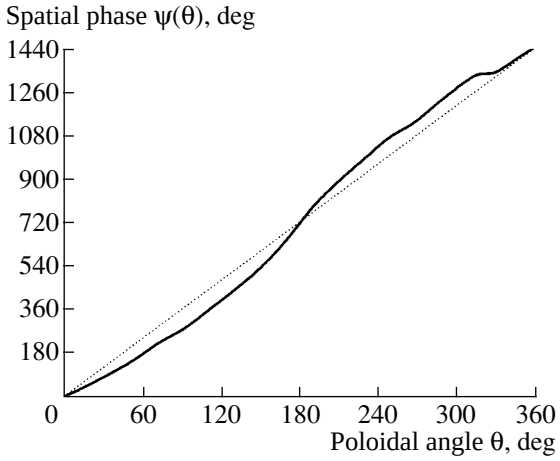

Fig. 9. Spatial phase ψ vs. poloidal angle θ for the experimental distribution shown in Fig. 8.

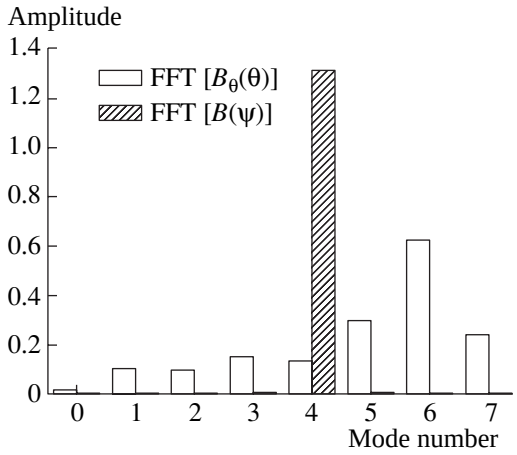

Fig. 10. Amplitudes of the Fourier harmonics of the experimental distributions $B_\theta(\theta)$ and $B(\psi)$.

mode structure is more efficient in comparison with a direct expansion in a Fourier series. The total error defined as

$$\delta_s = \sqrt{\sum_{i \neq m}\left(\frac{b_i}{b_m}\right)^2}, \quad (5)$$

where b_i is the amplitude of the ith Fourier harmonic and m is the mode number, is less than 0.01 for this algorithm, whereas δ_s may be larger than unity for a direct expansion in a Fourier series (see Fig. 4). The accuracy of this method can be enhanced by increasing the number of interpolation points when constructing the analytic signal (in the calculations described in this paper, we used interpolation over 512 points).

The algorithm was also tested by processing the experimental data from the T-10 tokamak (Fig. 8). The results of the test are presented in Figs. 9 and 10, which show the dependence $\psi(\theta)$ and the spatial spectrum of

the poloidal field perturbations. One can see that the algorithm yields a nonlinear dependence $\psi(\theta)$, which complies well with the dependence $\theta^*(\theta)$ given by expression (1). Some deviations (in particular, near $\theta = 330°$) can be attributed to the influence of the currents that are induced in the elements of the chamber and distort the probe signal. The results of applying the algorithm clearly demonstrate that the perturbation is associated with the $m = 4$ mode.

4. CONCLUSIONS

The proposed algorithm, although limited to a single mode, significantly simplifies the analysis of MHD signals, reduces the role of the human factor, and substantially improves the reliability of the results obtained. The algorithm can be extended to cases in which the spatial structure of the poloidal magnetic field is distorted not only by the toroidal effects, but also by such factors as the displacement of the plasma column from the center of the chamber and the deviations of the plasma column cross section from the circular. The algorithm can be used to analyze large-scale MHD perturbations of the magnetic field, such as tearing, kink, and the resistive wall modes.

An analysis of the multimode perturbations requires the development of additional algorithms for mode separation. These could be methods of wavelet analysis adapted for the poloidal angle–wavenumber coordinates.

ACKNOWLEDGMENTS

This work was supported in part by the Department of Atomic Science and Technology of the Ministry of Atomic Industry of the Russian Federation, the Russian Foundation for Basic Research (project no. 00-15-96536), and the State Science and Technology Program "Gradient-RRC KI" (grant no. 97, 2002).

REFERENCES

1. S. V. Mirnov and I. B. Semenov, At. Energ. **30** (1), 20 (1971).
2. V. G. Merezhkin, Fiz. Plazmy **4**, 275 (1978) [Sov. J. Plasma Phys. **4**, 152 (1978)].
3. O. Kluber, H. Zohm, H. Bruhns, *et al.*, Nucl. Fusion **31**, 907 (1991).
4. J. S. Kim, D. H. Edgell, J. M. Greene, *et al.*, Plasma Phys. Controlled Fusion **41**, 1399 (1999).
5. T. Dudok de Wit, A.-L. Pecquet, J.-C. Vallet, and R. Lima, Phys. Plasmas **1**, 3288 (1994).
6. D. E. Vakman and L. A. Vaĭnshteĭn, Usp. Fiz. Nauk **123**, 657 (1997) [Phys. Usp. **20**, 1002 (1997)].
7. L. M. Soroko, *Hilbert Optics* (Nauka, Moscow, 1981).

Translated by N.F. Larionova

Plasma Physics Reports, Vol. 29, No. 10, 2003, pp. 831–834. From Fizika Plazmy, Vol. 29, No. 10, 2003, pp. 896–900.

STELLARATORS

The Effect of Hexapole and Vertical Fields on α-Particle Confinement in Heliotron Configurations[1]

M. Yu. Isaev*, K. Y. Watanabe, M. Yokoyama**, and K. Yamazaki****

**Nuclear Fusion Institute, Russian Research Centre Kurchatov Institute, pl. Kurchatova 1, Moscow, 123182 Russia*

***National Institute for Fusion Science, Tokyo, 509-5292, Japan*

Received February 18, 2003

Abstract—Collisionless confinement of monoenergetic α particles in three-dimensional magnetic fields produced by the magnetic coils of the Large Helical Device is calculated. It is found that the inward shift of the magnetic axis due to the vertical field improves the α-particle confinement. In contrast to the vertical field, both large positive and negative hexapole fields do not improve the confinement. The study of the β effect and Mercier criterion calculations for different hexapole fields are also presented. *© 2003 MAIK "Nauka/Interperiodica".*

1. INTRODUCTION

The Large Helical Device (LHD) at the National Institute for Fusion Science (Japan) is the largest active heliotron device. Recent work by Murakami *et al.* [1] concerns the neoclassical transport optimization with respect to the radial shift of the magnetic axis by evaluating the monoenergetic transport coefficient and the effective helical ripple. The optimum configuration is found in which the magnetic axis with a major radius of 3.53 m is shifted by 0.22 m inward from the standard LHD configuration. A strong inward shift of the magnetic axis in the LHD can diminish the neoclassical transport to a level typical of the so-called "advanced stellarators," like Wendelstein 7-X (see, e.g., [2]).

In our previous paper [3], it was shown that a quasi-omnigenous structure of the magnetic field [4, 5] can be achieved by optimizing the conventional inward-shifted LHD-like heliotron configurations with an aspect ratio of 6.5 and $N = 10$ periods. For the $N = 10$ quasi-omnigenous configuration obtained, there are almost no lost α particles during 0.05 s of their collisionless flight. However, in [3], the plasma boundary shape was significantly modified in optimization calculations in order to achieve such a good α-particle confinement. In particular, the largest modification was made for the R_{21} component in the Fourier representation of the plasma boundary shape (here, 2 is the poloidal index and 1 is the toroidal index, which is normalized to N), which corresponds to the increase in the rotating triangularity of the plasma shape. The question arises from these modifications as to whether it is possible to achieve such a significant variation in the plasma boundary shape by the real LHD coil system. In this paper, we explore numerically the possible effect of the relevant magnetic field components on the collisionless α-particle confinement, taking into account mainly the effect of the vertical and hexapole fields produced by the real LHD coil system. We also consider the β effect and the ideal Mercier criterion for the configurations obtained in order to determine the possible optimal combination of the LHD coil fields.

The paper is organized as follows. Section 2 describes the numerical tools used in the calculations. Section 3 presents the relationships between the hexapole and vertical fields and the plasma boundary shape in the LHD. The effect of these fields on α-particle confinement and the Mercier criterion is also examined. The results obtained are reiterated in Summary.

2. NUMERICAL TOOLS

Three-dimensional numerical codes are an essential part of stellarator theoretical achievements in recent years. In this paper, we use KMAG [6], DESCUR [7], VMEC [8], JMC [9], and MCT [10] numerical codes.

The KMAG is a field-line-tracing code with the Biot–Savart law from the given coil geometry. The hexapole and vertical fields are varied in this paper by changing the coil current ratio (mainly currents in the three pairs of poloidal coils).

We obtain the Fourier spectrum of the plasma-boundary magnetic surface from 60 intersections of the magnetic field line with 20 toroidal cross sections using the DESCUR code.

Three-dimensional ideal MHD equilibria for a given fixed boundary are calculated by the VMEC code. The VMEC code solves the 3D MHD ideal inverse equilibrium equations by the gradient method using a representation for the magnetic field that assumes nested flux surfaces. In this paper, we use the 5.20 version of the VMEC code, which is suitable for stellarator systems without net toroidal current. The modification of the

[1] This article was submitted by the authors in English.

1063-780X/03/2910-0831$24.00 © 2003 MAIK "Nauka/Interperiodica"

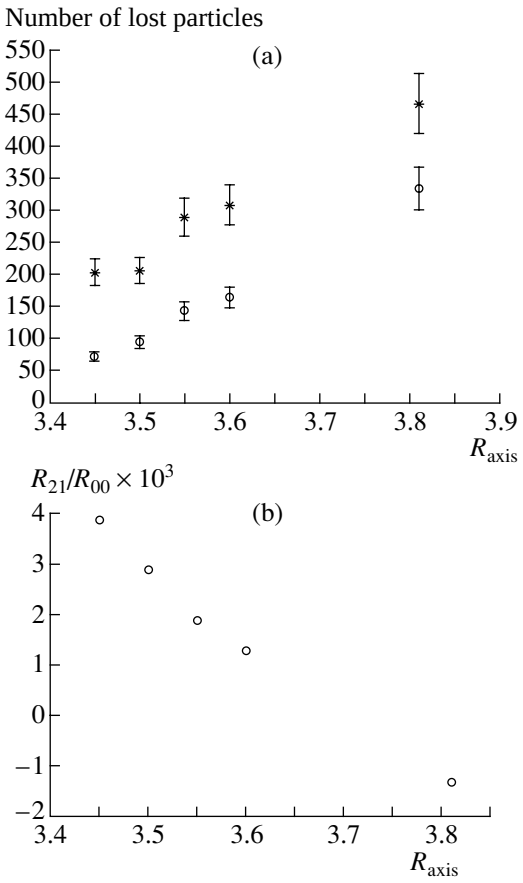

Fig. 1. (a) Numbers of lost α particles in the vacuum LHD configurations vs. magnetic axis position R_{axis}, calculated with the MCT code [10] with launching surfaces $s = 0.0625$ (lower points) and $s = 0.240$ (upper points). The total number of the followed α particles equals 2000. (b) Relationship between R_{axis} and the rotating triangularity.

VMEC code (version VMEC2000-6.80) was recently improved to calculate plasma equilibrium for low-aspect-ratio systems with net toroidal current, like NCSX and QOS [11]. In these equilibrium calculations, 33 flux surfaces and 113 VMEC poloidal and toroidal Fourier components are used for the representation of equilibrium quantities.

The JMC code calculates the magnetic field strength B in Boozer coordinates [12]. The maximal poloidal mode index in our runs is 9, and the maximal toroidal mode index is 8. The transformation from VMEC angular variables to Boozer coordinates is helpful because of the simplicity of the co- and contravariant vector representations of the magnetic field. In this paper, we use 162 magnetic field components obtained from the JMC code in Boozer coordinates. The Mercier criterion [13] is also calculated by the JMC code.

To check the α-particle confinement properties, the MCT code is used, which follows 2000 collisionless drift orbits of monoenergetic (3.52 MeV) α particles during a typical confinement time of 0.05 s for a plasma volume of 1000 m^3 and $B_0 = 5$ T and with a given Boozer spectrum of the magnetic field and given profiles of equilibrium flux quantities.

3. EFFECT OF HEXAPOLE AND VERTICAL FIELDS ON α-PARTICLE CONFINEMENT

We briefly describe the coil system of the LHD [14]. For the flexible currentless plasma operation of the LHD, the magnetic field properties such as the rotational transform, plasma position and shape, and plasma-wall clearance should be controlled by the external coils. For these purposes, the three-layer structure of the helical coils is adopted to adjust the helical pitch parameter and the divertor-wall clearance. The applied vertical magnetic field is produced by helical and poloidal coils. Three pairs of poloidal coils provide the controllability of the system, such as the adjustment of the axis position by the dipole field component, the triangularity by the hexapole field component, etc. The vertical field component B_Z produced by poloidal coils can be represented as the sum of the dipole (B_D), quadrupole (B_Q), and hexapole (B_H) components: $B_Z = B_D + B_Q X + B_H X^2 + \ldots$, where $X = (R - R_{axis})/R_{axis}$ [15].

First, we explore the effect of the vertical magnetic field, which changes the major radius of the magnetic axis R_{axis} and changes the triangularity of the plasma boundary. The basic improvement of α-particle confinement with the more inward shifted magnetic axis is illustrated in Fig. 1a. Here, we present pairs of points that correspond to the number of lost α particles starting from the quarter of plasma radius (the flux surface label $s = 0.0625$, lower points) and from the half of plasma radius (the flux surface label $s = 0.240$, upper points). The error bar shows the accuracy of these MCT calculations based on the Monte Carlo method.

The highest losses of more than 20% are estimated in magnetic configurations with $R_{axis} = 3.81$ m. The lowest losses of just a few percent were found for $R_{axis} = 3.45$ m. The increase in the vertical field also leads to the increase in rotating triangularity of the plasma boundary R_{21} and results in the nonplanar magnetic axis. The R_{21} component is the largest for $R_{axis} = 3.45$ m, in which case $R_{21}/R_{00} = 3.7 \times 10^{-3}$. For the case of $R_{axis} = 3.81$ m, we have $R_{21}/R_{00} = -1.3 \times 10^{-3}$ as is shown in Fig. 1b. Here, the calculations were performed for a low-β currentless regime, where β is the volume-averaged beta value. These results seem to correspond to the tendency for a decrease in neoclassical diffusion due to the inward shift of the magnetic axis revealed numerically in [1] and in the LHD experiments [16]. Here, we have chosen the case with $R_{axis} = 3.60$ m for further investigations of the hexapole fields effect. In general, the hexapole fields do not change the magnetic axis position and the rotating triangularity R_{21}; however, these fields change the so-called constant triangularity of the plasma boundary, which is expressed by the R_{20}

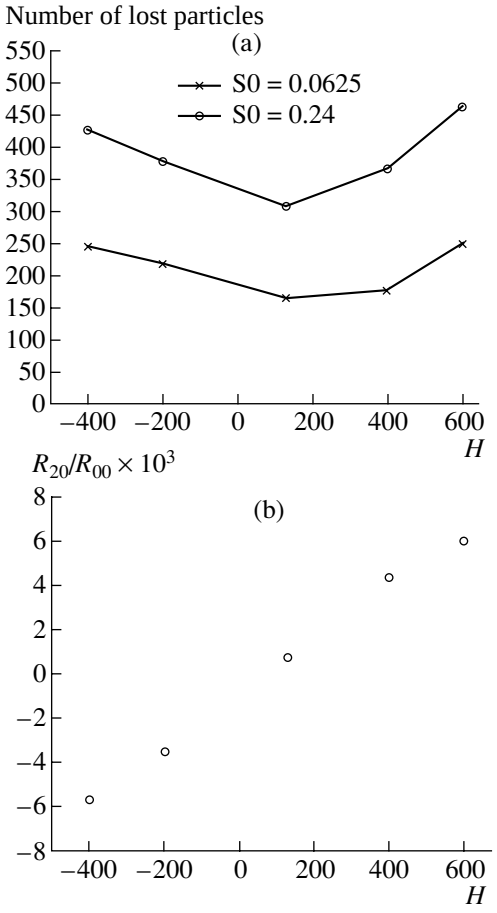

Fig. 2. (a) Numbers of lost α particles vs. hexapole field amplitude for a vacuum configuration with R_{axis} = 3.60 m for the same conditions as in Fig. 1. The lower and upper points correspond to s = 0.0625 and 0.240, respectively. (b) Relationship between the hexapole field amplitude and the triangularity.

component. In our computations, the component R_{10} is related to the minor plasma radius and is nearly constant, the rotating triangularity is proportional to $R_{21}R_{10}$, and the axisymmetric or the constant triangularity is proportional to $R_{20}R_{10}$. All variations in the triangularities are due to the changes of the R_{21} and R_{20} components, respectively.

The effect of the hexapole fields is shown in Fig. 2a. It can be clearly seen that the optimal hexapole field value is H = 129%. Here, H denotes the hexapole component produced by the poloidal coils, which is normalized to the field of the helical coils; i.e., at H = 100%, the total hexapole component is zero and the triangularity is also almost zero. The H = 129% value corresponds to the triangularity with $R_{20}/R_{00} = 7.9 \times 10^{-4}$. Both positive ($H$ = 600% gives $R_{20}/R_{00} = 6.0 \times 10^{-3}$) and negative ($H$ = –400% gives $R_{20}/R_{00} = -5.7 \times 10^{-3}$) changes of the hexapole fields do not improve α-particle confinement. Figure 2b shows the relationship between H and R_{20}/R_{00}.

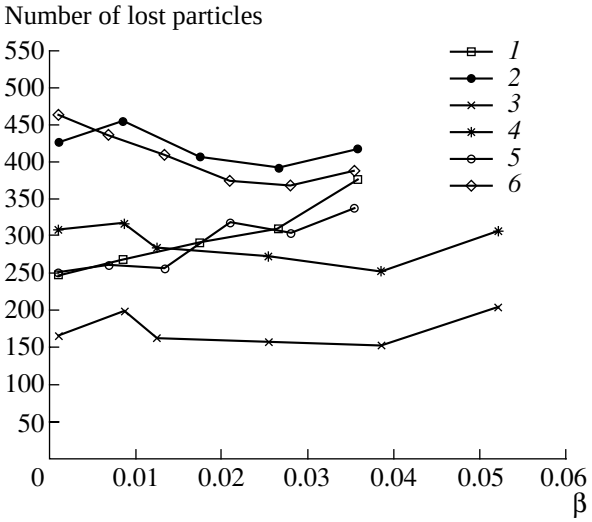

Fig. 3. The β effect on the confinement of α particles launched at the magnetic surfaces s = (*1*, *3*, *5*) 0.0625 and (*2*, *4*, *6*) 0.240 in configurations with R_{axis} = 3.60 m for different hexapole fields: H = (*1*, *2*) –400%, (*3*, *4*) 129%, and (*5*, *6*) 600%. Plasma pressure profile is given by the formula $p(s) = p_0(1 - s)(1 - s^4)$, where s is the flux surface label.

Figure 3 presents the β effect on α-particle confinement in configurations with R_{axis} = 3.60 m for different hexapole fields: H = –400, 129, and 600%. In these calculations, we use the pressure profile given by the formula $p(s) = p_0(1 - s)(1 - s^4)$, where s is the flux surface label. This is a typical profile observed in LHD experiments and is frequently used in the analysis. For the hexapole field value H = 129%, α does not substantially change β-particle confinement. For H = –400%, the fraction of lost particles starting from s = 0.0625 increases with increasing pressure by a factor of almost 1.5, and it is maximum for β = 0.036. For H = 600%, the optimal value of β is approximately equal to 0.027; however, the β effect on the confinement in this case is not so strong. Large positive and large negative hexapole fields decrease the equilibrium β limit; the VMEC equilibrium code has a poor convergence for H = 600% and H = –400% at β values larger than 0.04.

We also performed the calculations of the ideal MHD Mercier stability criterion with the JMC code for R_{axis} = 3.60 m and β = 0.01 to define the optimum value of the hexapole field (Fig. 4). According to this figure, the case of H = 129% is more stable than the cases with both large positive (H = 600%) and negative (H = –400%) hexapole fields.

4. SUMMARY

The effect of the vertical and hexapole fields on the collisionless α-particle confinement and the ideal MHD Mercier stability have been numerically calcu-

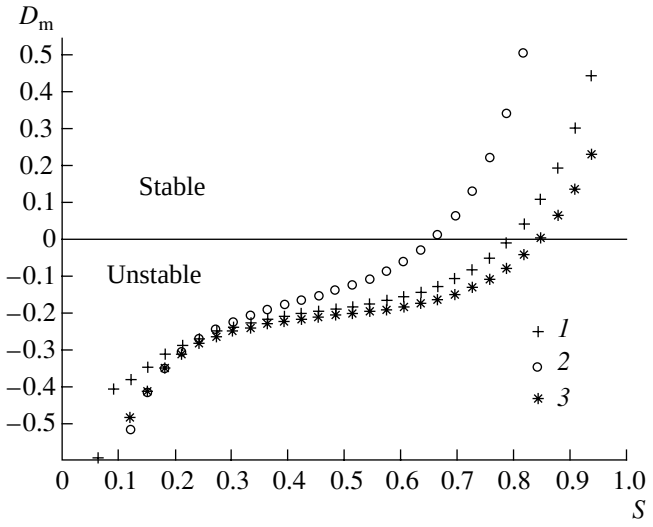

Fig. 4. The Mercier criterion calculated with the JMC code in configurations with R_{axis} = 3.60 m for β = 0.01 and different hexapole fields: H = (*1*) –400%, (*2*) 129%, and (*3*) 600%. The pressure profile is the same as in Fig. 3.

lated for the LHD. A significant improvement of the confinement in a configuration with the inward shifted axis (R_{axis} = 3.45 m) has been found. However, such a configuration is less stable with respect to the Mercier modes. In the configuration with R_{axis} = 3.60 m, the effects of the hexapole fields and β effect have been investigated. It is found that both large positive and large negative hexapole fields do not improve the α-particle confinement and the stability with respect to the Mercier modes. Variations in the β value only slightly affect the confinement in configurations with a small hexapole field. The configurations with strong positive or negative hexapole fields have a lower equilibrium β limit, are more unstable, and have larger α-particle losses. These numerical results should be checked in LHD experiments and also can be taken into account in calculating the new compact 6-period torsatron L-V, the project of which has been designed at the Institute of General Physics (Moscow, Russia) [17].

Large rotating triangularity ($R_{21}/R_{00} \approx 0.1$) can minimize the poloidal variations in the second adiabatic invariant on the magnetic surfaces and significantly decrease α-particle losses. In this study, we could not obtain such a large rotating triangularity of the plasma boundary for the real LHD coil system. Further work (for example, introducing additional coils) can clarify this issue, which is important for future heliotron reactor devices.

ACKNOWLEDGMENTS

This work was performed during the visit of M.Yu. Isaev to the National Institute for Fusion Science (NIFS, Japan). This visit was initiated and supported by Prof. M. Fujiwara (the Director of NIFS) and Prof. C. Namba with a grant-in-aid from the Ministry of Education, Science, Culture, Sports, and Technology (MEXT) of Japan. The authors are grateful to Dr. S.P. Hirshman for providing us with the VMEC and DESCUR codes and to Dr. Y. Nakamura for providing us with the KMAG code. This work was supported by INTAS (grant no. 99-00592), the Russian–German Agreements WTZ RUS 01-581, the Russian Foundation for Basic Research (project no. 00-02-17105), and the Russian Federal Program "Support of the Leading Scientific Schools" (project no. 00-15-96526). The computations were performed on the NEC-SX5 platforms at the Rechenzentrum Garching, Max-Planck-Institut für Plasmaphysik, Germany. This work was also supported by grants-in-aid from the Sumitomo Foundation and a grant-in-aid for young scientists (B) from the MEXT (Japan) to one of authors (M. Yokoyama).

REFERENCES

1. S. Murakami, A. Wakasa, H. Maassberg, *et al.*, Nucl. Fusion **42**, 19 (2002).
2. W. Lotz, J. Nührenberg, and C. Schwab, in *Proceedings of the 13th International Conference on Plasma Physics Controlled Nuclear Fusion Research, Washington, 1990* (IAEA, Vienna, 1991), Vol. 2, p. 603.
3. M. Isaev, J. Nührenberg, M. I. Mikhailov, *et al.*, Submitted to Nucl. Fusion.
4. J. Cary and S. Shasharina, Phys. Rev. Lett. **78**, 674 (1997).
5. D. Spong, S. P. Hirshman, J. C. Whitson, *et al.*, Phys. Plasmas **5**, 1752 (1998).
6. Y. Nakamura, J. Plasma Fusion Res. **69**, 41 (1993).
7. S. P. Hirshman and H. K. Meier, Phys. Fluids **28**, 1387 (1985).
8. S. P. Hirshman and O. Betancourt, J. Comput. Phys. **96**, 99 (1991).
9. J. Nührenberg and R. Zille, in *Proceedings of the International School of Plasma Physics on Theory of Fusion Plasmas, Varenna, 1987* (Editrice Compositori, Bologna, 1988), p. 3.
10. R. H. Fowler, J. A. Rome, and J. F. Lyon, Phys. Fluids **28**, 338 (1985).
11. R. Sanchez, M. Isaev, S. P. Hirshman, *et al.*, Comput. Phys. Commun. **141**, 55 (2001).
12. A. H. Boozer, Phys. Fluids **26**, 496 (1983).
13. C. Mercier, Nucl. Fusion Suppl. **1**, 121 (1962).
14. A. Iiyoshi, A. Komori, A. Ejiri, *et al.*, Nucl. Fusion **39**, 1245 (1999).
15. K. Yamazaki, O. Motojima, and LHD Design Group, in *Proceedings of the 1st International Conference on Plasma Physics and Controlled Nuclear Fusion, Tokyo, 1990*, NIFS-PROC-3, p. 252.
16. H. Yamada, K. Y. Watanabe, K. Yamazaki, *et al.*, Nucl. Fusion **41**, 901 (2001).
17. M. Yu. Isaev, S. E. Grebenshchikov, S. V. Shchepetov, *et al.*, Fiz. Plazmy (in press).

Plasma Physics Reports, Vol. 29, No. 10, 2003, pp. 835–844. Translated from Fizika Plazmy, Vol. 29, No. 10, 2003, pp. 901–910.

PLASMA DIAGNOSTICS

The Effect of Charge Exchange with Neutrals on the Saturation of the Spectral Line Intensities of Multicharged Ions in Plasma

L. A. Bureeva*, V. S. Lisitsa, D. A. Petrov**, D. A. Shuvaev**, F. Rosmej***, and R. Stamm******

**Institute of Spectroscopy, Russian Academy of Sciences, Troitsk, Moscow oblast, 142092 Russia*
***Russian Research Centre Kurchatov Institute, pl. Kurchatova 1, Moscow, 123182 Russia*
****GSI, Planckstr 1, D-64291 Darmstadt, Germany*
*****Université de Provence, Centre St. Jérôme, Case 321, 13397 Marseille Cedex 20, France*
Received March 5, 2003; in final form, May 7, 2003

Abstract—The influence of charge-exchange processes on the spectral line intensities of impurity ions in the edge and core plasmas of fusion devices is considered. It is found that, at a sufficiently high density of neutrals, the rate at which the atomic states are populated through charge exchange becomes independent of the neutral density, which results in the saturation of the spectral line intensities. This effect can substantially limit the efficiency of impurity-ion spectroscopy. Conditions under which the saturation effect manifests itself are examined for both the edge and core plasma regions in the presence of fast neutral beams. The results of calculations for the edge plasma are used to interpret the experimental data from the TORE SUPRA tokamak. It is shown that, in the central plasma region, the intensities of the visible spectral lines associated with the charge exchange of impurity ions in the course of neutral beam injection decrease (rather than increase, as was expected earlier) with increasing ion charge. *© 2003 MAIK "Nauka/Interperiodica".*

1. INTRODUCTION

In recent years, spectroscopic methods based on the observations of radiative transitions between highly excited electronic states of impurity ions have been extensively used in plasma diagnostics. The main mechanism for populating highly excited electronic states of impurity ions in plasmas of magnetic fusion devices is charge exchange with neutrals. This is true both for the edge plasma, in which slow neutrals are inherently present due to the plasma–wall interaction, and for the core plasma under conditions of neutral beam injection (NBI). The advantage of observing the spectral lines associated with transitions between highly excited electronic states of impurity ions is that these lines lie in the visible spectral region.

The specific features of the population of highly excited ion states through charge exchange in the edge plasma are related to the fact that the charge exchange of impurity ions with neutrals occurs not only from the ground state of atoms, but also from the excited states populated via electron collisions. In this case, the charge-exchange processes and the subsequent population of the levels involve a great number of the excited states of both the neutrals (which serve as a population source) and the ions populated through charge exchange. Under these conditions, the population kinetics of a great number of atomic levels can be described using a universal approach [1] that takes into account the contributions from all of the excited states and is based on the universal description of the kinetics of highly excited hydrogen-like states by simple approximating formulas. This approach was used to develop a numerical code for calculating the populations of atomic states and, accordingly, the intensities of atomic transitions of hydrogen-like ions. This code was used to examine the spectral line intensities of hydrogen-like helium ions that were measured near the ergodic divertor of the TORE SUPRA tokamak [2].

For the core plasma, we also have analyzed the possibility of observing the lines of impurity ions in the spectral region corresponding to transitions between highly excited electronic levels under NBI conditions.

In both cases, we have observed the saturation of the line intensities, which substantially limits the efficiency of charge-exchange plasma diagnostics. The reason is that, as the density of neutrals, which are the main source for charge exchange and ion population, reaches a certain level, the density of the ions participating in charge exchange begins to decrease because of the shift in their ionization equilibrium. As a result, both the power of the effective population source and the line intensities arrive at certain steady levels (become saturated), even although the neutral density increases further.

For the edge plasma of the TORE SUPRA tokamak, the way in which charge exchange influences the spec-

1063-780X/03/2910-0835$24.00 © 2003 MAIK "Nauka/Interperiodica"

tral line intensity depends on which of the two experimental regimes is realized: an attached plasma regime, with a relatively low temperature and a high electron density, or a detached plasma regime, with a relatively high temperature and low electron density. Since the relative neutral and electron densities differ in these two regimes, the measured spectral line intensities of the hydrogen-like helium ions used in diagnostics are also different.

For a plasma core under NBI conditions, it is shown that the saturation effect depends on the beam geometry, which affects the degree of saturation of the spectral line intensity in the course of charge exchange.

2. KINETIC MODEL

To calculate the populations of the atomic states in the central region and at the plasma periphery, it is necessary to solve a self-consistent set of kinetic equations and ionization-balance equations. Hereinafter, we use the following notation: σ is the cross section for the process (in cm^2); $\kappa = \langle v\sigma \rangle$ is the rate coefficient of the process (in cm^3/s); $\alpha = N_1\kappa$ is the coefficient of the process; $q = N_2\alpha$ is the source (the number of events in a unit time per unit density); and $N_{1,2}$ are the densities of the colliding particles (in cm^{-3}), which are different for different processes.

In the central region of the plasma column, there are the following main sources for populating the atomic (ionic) states n:

(i) electron-impact excitation from the ground state $q^{exc}(n)$,

(ii) radiative recombination on impurity ions $q^{rr}(n)$,

(iii) polarization recombination on impurity ions $q^{plr}(n)$,

(iv) dielectronic recombination of electrons on ions $q^{dr}(n)$, and

(v) charge exchange from the ground state of neutrals $q^{cx}(n)$.

When estimating the dielectronic recombination rate, it is necessary to take into account the effect of the microfield produced by the surrounding ions, the secondary ionization by electrons, etc. [3]. The process of polarization recombination, which increases the radiative recombination rate for ions that have a composite core, is easy to take into account by introducing the ratio $R(\omega)$ of the polarization-recombination coefficient α^{plr} to the ordinary radiative-recombination coefficient α^{rr} [4]:

$$R(\omega) = \alpha^{prl}/\alpha^{rr} = [N(\omega)/Z(\omega)]^2,$$

where $N(\omega)$ is the effective number of electrons inside the ion core and $Z(\omega)$ is the effective ion charge. Hence, polarization recombination can be taken into account by multiplying the radiative-recombination coefficient α^{rr} by $[1 + R(\omega)]$. The factor $R(\omega)$ is close to unity for the small and moderate Z values that are typical of the existing high-temperature plasma devices. Below, we will only consider radiative recombination, keeping in mind that the correction for the factor $R(\omega)$ has already been made.

In the edge plasma, in addition to the above processes, we should also take into account the charge exchange from the ground and excited states of neutrals, as well as their three-body recombination onto highly excited levels.

When determining the ionization balance of impurities, we take in to account not only the above processes, but also electron-impact ionization.

Let us write the general set of kinetic equations describing the population of the level n of an $A^{+(Z-1)}$ ion. The population source $q(n)$ has the form

$$q(n) = \alpha_n^{ext} N_{A^{+(Z-1)}} + \alpha_n^{rec} N_{A^{+Z}}, \quad (1)$$

where α_n^{exc} is the excitation coefficient and α_n^{rec} is the sum of the coefficients of all the recombination processes (including charge exchange) accompanied by the transition of an electron on to the level n ($\alpha_n^{rec} = \alpha_n^{rr} + \alpha_n^{dr} + \alpha_n^{cx}$).

The population kinetics of the levels of $A^{+(Z-1)}$ ions should be considered simultaneously with the ionization balance equations relating the densities of $A^{+(Z-1)}$ and A^{+Z} ions,

$$-\alpha^{rec} N_{A^{+Z}} + \alpha^{ion} N_{A^{+(Z-1)}} = 0, \quad (2)$$

where α^{rec} is the total (summed over n) recombination coefficient ($\alpha^{rec} = \alpha^{rr} + \alpha^{dr} + \alpha^{cx}$) and α^{ion} is the ionization coefficient.

Population sources (1) should be considered simultaneously with balance equation (2). Determining the density of $A^{+(Z-1)}$ ions from Eq. (2) and substituting it into Eq. (1), we find

$$q(n) = N_{A^{+(Z-1)}}[\alpha_n^{ext} + \alpha^{ion}\alpha_n^{rec}/\alpha^{rec}]. \quad (3)$$

It follows from Eq. (3) that the population source depends on the ratio between the coefficient of recombination α_n^{rec} onto the level n and the total recombination coefficient α^{rec}. The relative contributions from excitation and recombination to the population source depend on the ion structure and plasma conditions. If recombination is dominant, then the source is proportional to the density of $A^{+(Z-1)}$ ions. As the number of recombination channels increases, both the numerator α_n^{rec} (which is responsible for the population of the level n) and the denominator α^{rec} (which is responsible for the ionization balance) in the second term of Eq. (3) increase. These two coefficients are proportional to the density of the particles involved in recombination.

Hence, as the density of the particles involved in recombination increases, the ratio of these coefficients remains unchanged; i.e., the population source does not increase. This means that the recombination-dominated source becomes saturated.

3. POPULATION OF THE ATOMIC STATES AND THE SPECTRAL LINE INTENSITIES IN THE EDGE PLASMA

Let us consider the kinetic model under the edge plasma conditions. We will take into account all the four sources for populating the level n of $A^{+(Z-1)}$ ions (radiative recombination includes polarization recombination): $q(n) = q^{\text{exc}}(n) + q^{rr}(n) + q^{dr}(n) + q^{cx}(n)$.

The first three populating processes are well known [5]. Let us consider in more detail the population due to charge exchange by the example of charge exchange of impurity ions with neutral hydrogen in a certain state n that is typical of the edge plasma conditions.

As an ion and an excited hydrogen atom come within a distance on the order of the Bohr radius of the electron orbit, the probability of an electron overcoming the potential barrier and falling from one potential well to another sharply increases ($\sim n^4$).

At a moderate electron temperature, the process goes in two steps: the electron-impact excitation of neutral hydrogen and the subsequent charge exchange with impurity ions (see Fig. 1). In this case, in spite of the low population of the excited states, charge exchange from these states is a rather efficient process, because, as was mentioned above, the charge-exchange cross section sharply increases with increasing principal quantum number of the atomic level. We note that charge exchange from the excited atomic states is selective in character. The principal quantum number of the initial atom, n_{H} (hereinafter, the subscript H stands for a hydrogen atom), and that of the final ion, n, are related by the formula [6]

$$n \approx Z n_{\text{H}}.$$

Thus, the source of population of the level n via charge exchange can be written in the form

$$q^{cx}(n) = N_{A^{+Z}} N_{\text{H}} \langle v\sigma_n^{cx} \rangle_{A^{+Z}\text{H}} = N_{A^{+Z}} N_{\text{H}} \kappa_n^{cx} = N_{A^{+Z}} \alpha_n^{cx}, \quad (4)$$

where N_{H} and v are the density and velocity of hydrogen atoms in a plasma. Remember that, at low and moderate velocities of hydrogen atoms, charge exchange occurs from both the ground state and the excited states of hydrogen. Hence, in expression (4), N_{H} includes not only the ground state of neutral hydrogen, but also the densities of the excited states, whose populations are determined by the plasma parameters. The kinetics of populating these states can be considered in the conventional radiative–collisional model. Below, however, we will use a faster numerical code based on an analytical representation of the Green function describing the probability of a radiative–collisional transition from one energy range to another within the Rydberg energy spectrum of hydrogen-like atoms [5]. The method is based on changing from a discrete energy spectrum of hydrogen-like ions to a continuous spectrum according to the formula $\varepsilon = 1/n^2$. Thus, the populations $N(\varepsilon)$ are defined by the formula

$$N(\varepsilon) = \int G(\varepsilon, \varepsilon_p) \frac{q(\varepsilon_p) d\varepsilon_p}{2\varepsilon_p^{3/2}}, \quad (5)$$

where $G(\varepsilon, \varepsilon_p)$ is the Green function [1, 7] and $q(\varepsilon_p)$ is the external source responsible for the population of the excited atomic states. Integration in formula (5) is performed from the minimum energy $\varepsilon_{\min}$ (which is determined from the relation $\varepsilon_{\min} = Z^2/n_{\max}^2$, where $n_{\max}$ is the cutoff parameter for charge exchange) to a certain maximum energy $\varepsilon_{\max}$ corresponding to the ground-state energy.

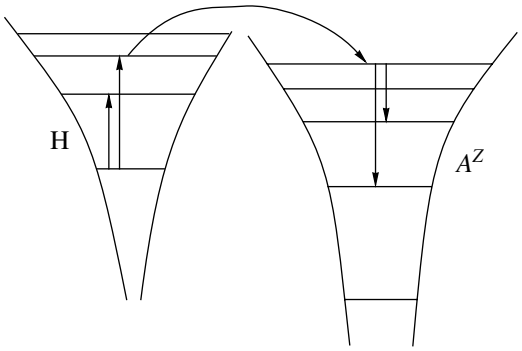

Fig. 1. Scheme of populating the excited levels of a multicharged ion A^{+Z} in the course of charge exchange with a hydrogen atom H.

It follows from the aforesaid that, at low collision frequencies, the source of population of the A^{+Z} ions via charge exchange with neutral hydrogen [see Eq. (4)] may be approximated by the formula

$$q^{cx}(\varepsilon_{A^{+(Z-1)*}}) = N_{A^{+Z}} \sum_{n_{\text{H}}} N_{\text{H}*}(n_{\text{H}}, N_e, T_e) \langle v\sigma(n_{\text{H}}) \rangle_{A^{+Z}\text{H}*}^{cx}, \quad (6)$$

$$\langle v\sigma(n_{\text{H}}) \rangle_{A^{+Z}\text{H}*}^{cx} \sim v_{\text{H}} Z n_{\text{H}}^4 a_0^2,$$

where $N_{A^{+Z}}$ is the density of nuclei, $N_{\text{H}*}(n_{\text{H}}, N_e, T_e)$ are the populations of the excited states of atomic hydrogen H* in a plasma with a temperature T_e and density N_e, $\sigma(n_{\text{H}})$ is the cross section for charge exchange from the level n_{H} of a hydrogen atom H* onto the level n of an

A^{+Z} ion, $n = Zn_H$ (see [5]), v_H is the relative velocity of neutrals and ions, and $\langle v\sigma(n_H)\rangle^{cx}$ is the charge-exchange rate. The populations of the excited states of atomic hydrogen were determined from relation (5), where we used the sum of q^{exc} and q^{rr} as an external source.

The dependence of the charge-exchange cross section on the level number n was assumed to be proportional to n^4 (see [8]), which corresponds to ε_p^{-2} in the energy variables, where ε_p is the dimensionless energy with respect to which integration in formula (5) is performed. It can easily be verified that the integral with respect to ε_p (or with respect to n) in Eq. (5) diverges as $n \longrightarrow \infty$. A similar divergence takes place also when calculating the statistical sum of hydrogen-like systems [9]. Hence, in expression (6), the sum over n_H, which determines the overall probability, should be cut at a certain value n_{max}. This value can be found by two methods: either from the condition of equilibrium with continuum (see [5]) or from the detailed balance between the neutral and charge-particle densities in plasma (see [10]). For example, for the He^+ ion considered below, both methods give nearly the same value, $n_{max} \sim 10$.

The set of equations for calculating the population of the level n of the $A^{+(Z-1)}$ ions should be solved simultaneously with the balance equation relating the densities of the $A^{+(Z-1)}$ and A^{+Z} ions. Indeed, the population sources taken into consideration are related to the particle densities as follows:

$$q^{exc}(n) \sim N_e N_{A^{+(Z-1)}}, \quad q^{rr}(n) \sim N_e N_{A^{+Z}},$$
$$q^{dr}(n) \sim N_e N_{A^{+Z}}, \quad q^{cx}(n) \sim N_H N_{A^{+Z}}. \tag{7}$$

The ratio N_H/N_e is a free parameter of the problem, whereas $N_{A^{+(Z-1)}}$ and $N_{A^{+Z}}$ are related by the ionization balance equation. Using Eqs. (1) and (2) and taking into account Eq. (5), expression (4) for the source associated with charge-exchange can be easily transformed into the following form:

$$q^{cx}(n) = N_{A^{+Z}} \alpha^{ion} N_e \frac{\kappa_n^{cx} N_H/N_e}{\kappa^{rr} + \kappa^{dr} + \kappa^{cx} N_H/N_e}. \tag{8}$$

It can be seen from relation (8) that, at large values of the parameter N_H/N_e, the source $q^{cx}(n)$ is independent of N_H; i.e., the population source saturates. For this reason, even when charge exchange makes a dominant contribution to the population of atomic states, the ratio of spectral line intensities calculated disregarding charge exchange do not differ substantially from the results of more accurate calculations and experiments. However, for most lines, the temperature dependences of the line intensities are rather sensitive to variations in the parameter N_H/N_e.

The basis points of the kinetic model are the following. The full kinetic energy-balance equation for A^{+Z} ions has the form

$$(N_{A^{+(Z-1)}} N_e \langle v\sigma\rangle^{ion} + N^*_{A^{+(Z-1)}} N_{H^+} \langle v\sigma(n)\rangle^{cx}_{A^{+(Z-1)*}H^+})$$
$$- (N_{A^{+Z}} N_H \langle v\sigma\rangle^{cx}_{A^{+Z}H} + N_{A^{+Z}} \alpha^{tbr} + N_{A^{+Z}}(\alpha^{rr} + \alpha^{dr})) = 0, \tag{9}$$

where $\alpha^{tbr} = N_e^2 \kappa^{tbr}$, $\alpha^{rr} = N_e \kappa^{rr}$, $\alpha^{dr} = N_e \kappa^{dr}$, and $N^*_{A^{+(Z-1)}}$ accounts for the charge exchange of the excited impurity ions with protons. The parameter $n^{A^Z}_{max}$, which is the upper limit for the summation, was found from the balance of the neutral and charged particles by analogy to [11]. For the helium ion considered below, we have $n^{He}_{max} = 10$.

Ignoring the three-body recombination coefficient α^{tbr} in Eq. (9), we find the following expression for $N_{A^{+(Z-1)}}$:

$$N_{A^{+Z}} = N_{A^{+(Z-1)}}$$
$$\times \frac{N_e \langle v\sigma\rangle^{ion}_{A^{+(Z-1)}} + \sum_{n\geq 3}^{n^{A^Z}_{max}} \frac{N_{A^{+(Z-1)}}(n)}{N_{A^{+(Z-1)}}(1)} N_{H^+} \langle v\sigma_n\rangle^{cx}_{A^{+(Z-1)*}H^+}}{N_H \langle v\sigma_n\rangle^{cx}_{A^{+Z}H} + \alpha^{rr} + \alpha^{dr}}. \tag{10}$$

The total population rate of the level n is equal to

$$q_{A^{+(Z-1)}}(n) = N_{A^{+(Z-1)}} N_e \langle v\sigma_n\rangle^{ext}$$
$$+ N_{A^{+Z}} N_H \langle v\sigma_n\rangle^{cx}_{A^{+Z}H} + N_{A^{+Z}} \alpha_n^{rr} + N_{A^{+Z}} \alpha_n^{dr}. \tag{11}$$

We express all the quantities in Eq. (11) through the density of the $A^{+(Z-1)}$ ions using ionization balance equation (10) to obtain

$$q_{A^{+(Z-1)}}(n) = N_{A^{+(Z-1)}} N_e \langle v\sigma_n\rangle^{ext}$$
$$+ N_{A^{+(Z-1)}}(N_H(n) \langle v\sigma_n\rangle^{cx}_{A^{+Z}H} + \alpha_n^{rr} + \alpha_n^{dr})$$
$$\times \frac{N_e \langle v\sigma\rangle^{ion}_{A^{+(Z-1)}} + \sum_{n\geq 3}^{n^{He}_{max}} b_{A^{+(Z-1)}}(n) N_{H^+} \langle v\sigma_n\rangle^{cx}_{A^{+(Z-1)*}H^+}}{N_H \langle v\sigma_n\rangle^{cx}_{A^{+Z}H} + \alpha^{rr} + \alpha^{dr}}, \tag{12}$$

where we introduce the relative level population

$$b_{A^{+(Z-1)}}(n) = \frac{N_{A^{+(Z-1)}}(n)}{N_{A^{+(Z-1)}}(1)}. \tag{13}$$

Let us determine the dependences of the population sources on the plasma parameters and the atomic quantum numbers using the approximating formulas [5] for the rate constants of ionization and radiative recombi-

nation (omitting dielectronic recombination for nuclei) as functions of these parameters. The corresponding expressions for the probabilities of elementary processes are given in the Appendix.

Using these dependences, we can describe the population sources as functions of the given parameters in the explicit form

$$q_{A^{+(Z-1)}}(n) = 10^{-8}\frac{N_{A^{+(Z-1)}}N_e}{n^3}\frac{1}{Z^3}G(\beta_1)e^{-\beta_1}\left\{V(\beta_1, n^2)\right.$$

$$\left. + \left[2\beta_1\Pi(\beta_1, n^2) + \left(\frac{N_\mathrm{H}}{N_e}\right)\frac{2\times 10^3}{\beta_1\Lambda(\beta_1)}n^7 b^\mathrm{H}\left(\frac{n}{Z}\right)\right]\right. \quad (14)$$

$$\left. \times \frac{\left[1 + \dfrac{0.4}{\sqrt{\beta_1}G(\beta_1)e^{-\beta_1}}\displaystyle\sum_{n\geq 3}^{n_\mathrm{max}} n^4 b^{A^{+(Z-1)}}(n)\right]}{\left[1 + \left(\dfrac{N_\mathrm{H}}{N_e}\right)\dfrac{2\times 10^3}{\beta_1\Lambda(\beta_1)}\displaystyle\sum_{n\geq 4}^{n_\mathrm{max}} n^4 b^\mathrm{H}\left(\dfrac{n}{Z}\right)\right]}\right\},$$

where the main dependences on the atomic and plasma parameters are separated out and the results of numerical approximations are taken into account by the function $G(\beta)$ and the slowly varying functions V, Π, and Λ, which are defined by relations given in the Appendix.

Let us analyze expression (14) for the case of helium nuclei ($Z = 2$), which is of interest for experimental applications. It can be seen from expression (14) that the population source q depends strongly on the two parameters n_max and N_H/N_e. Figure 2 demonstrates the sensitivity of the calculated relative populations $b(n)$ of the excited levels of helium ions to variations in the parameter N_H/N_e. In the calculations, we used expression (14), in which the parameter N_H/N_e controls the population source related to the charge exchange of helium ions with neutrals. It can be seen that the contribution from charge exchange becomes significant for $N_\mathrm{H}/N_e = 10^{-5}$. However, as the neutral density increases further, the population source related to charge exchange (and, accordingly, the population $b(9)$) does not increase because of the simultaneous shift of the ionization equilibrium; i.e., the population source becomes saturated.

The model described was used to calculate the populations of the excited levels and the spectral line intensities of helium ions in a hydrogen plasma in the TORE SUPRA tokamak. We calculated the intensity ratios for the 5–4, 7–4, and 9–4 helium-ion transitions (which depend on the populations of the 5th 7th, and 9th levels, respectively) and the intensities of the 4–3 transition

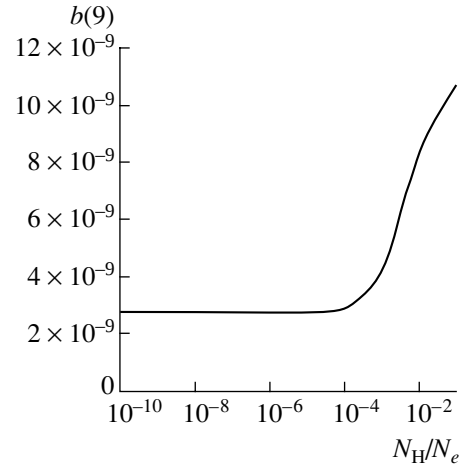

Fig. 2. Relative population b of the level $n = 9$ of helium as a function of the ratio N_H/N_e of the neutral density to the plasma electron density.

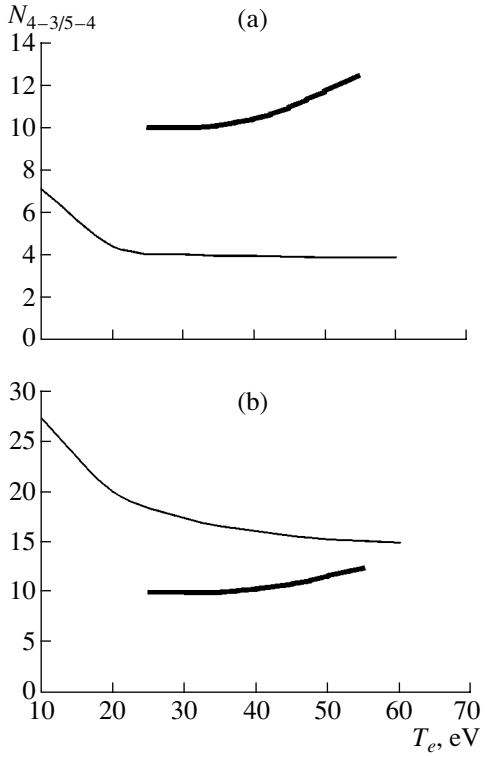

Fig. 3. Temperature dependences of the intensity ratio of the 4–3 and 5–4 transitions: (a) without and (b) with allowance for charge exchange. The solid lines show the measured dependences [2].

(which depends on the population of the 4th level). The calculated intensity ratios are shown in Figs. 3b, 4b, and 5b along with the experimental results. Figures 3a, 4a, and 5a show the corresponding ratios calculated

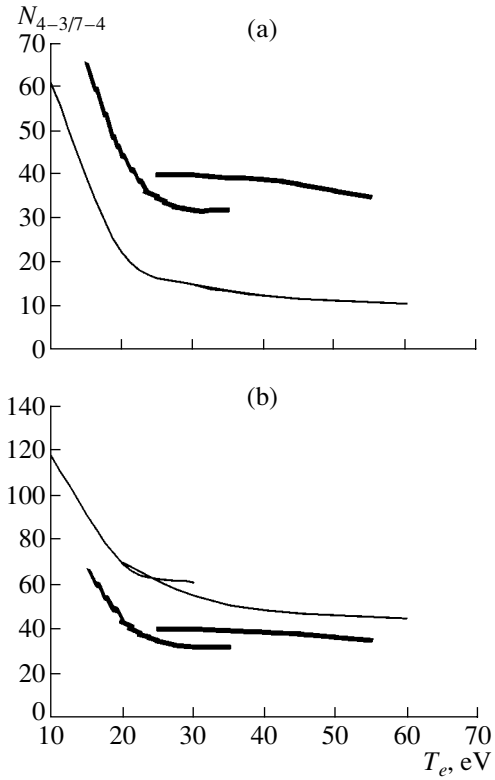

Fig. 4. Same as in Fig. 3 for the intensity ratio of the 4–3 and 7–4 transitions. The theoretical curves for low- and high-temperature regions are calculated with the parameter N_H/N_e best fitted to the experiment.

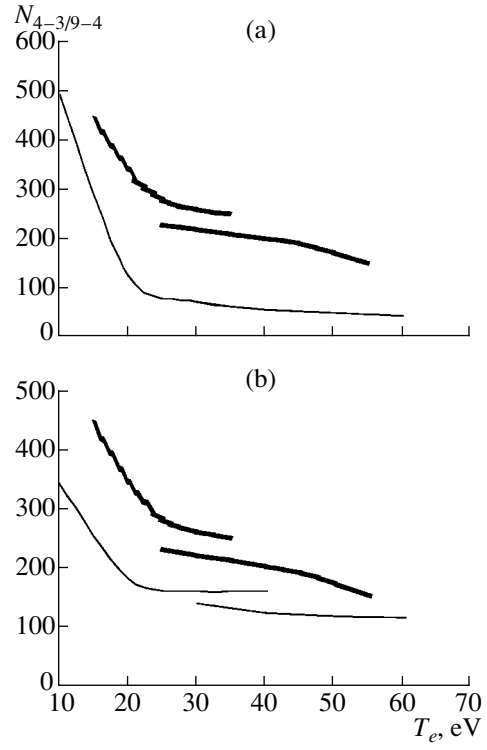

Fig. 5. Same as in Fig. 4 for the intensity ratio of the 4–3 and 9–4 transitions.

without allowance for charge exchange; in this case, electron-impact excitation from the ground state makes the main contribution to the population of the excited states. These results coincide with similar calculations from [2]; however, they do not allow one to distinguish between two different edge plasma regimes (the attached and detached plasma regimes), although the experimental data indicate the existence of these regimes.

Taking into account the charge exchange of ions with neutral hydrogen (see Figs. 3b, 4b, 5b) allows us to capture a certain difference between these regimes. Charge exchange influences the intensity ratio, because the observed transitions correspond to highly excited ion states, for which the population through charge exchange dominates over the electron-impact population.

As is seen from expression (14), the contribution from charge exchange to the total population source of the helium levels is determined by the neutral density, which is characterized by the parameter N_H/N_e. The measured temperature dependence of the electron density is shown in Fig. 6. The neutral density as a function of the temperature was not measured directly; however, in view of the existence of two plasma regimes, we can suppose that the temperature dependence of the parameter N_H/N_e is different for these two regimes.

Within a relatively narrow temperature range (from 10 to 60 eV), the neutral density near the plates of the ergodic divertor of the TORE SUPRA tokamak is primarily determined by neutral fluxes from the wall and, thus, varies more slowly than the electron density. Therefore, the curve $N_H(T)$ should be flatter than the curve $N_e(T)$. It follows from this that, in a region with a low temperature and high plasma density (the attached plasma regime), the value of the parameter N_H/N_e should be smaller than in a region with a high tempera-

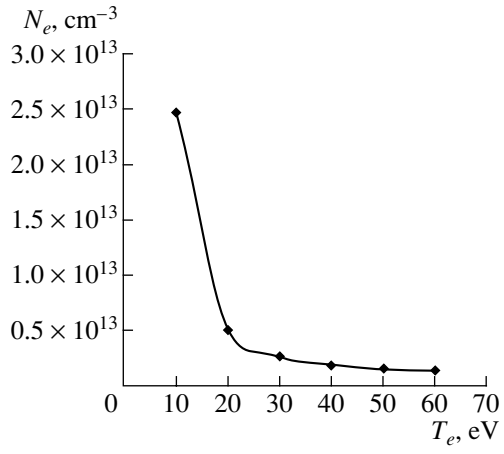

Fig. 6. Measured dependence [2] of the plasma electron density N_e on the temperature T_e.

ture and low density (the detached plasma regime). Hence, the contribution from charge exchange in the detached plasma regime is greater than in the attached plasma regime.

The results of calculations depend on the choice of the free parameter N_H/N_e. However, the value of this parameter must be the same for all of the lines observed, which imposes restrictions on the choice of this parameter. For a particular pair of lines, one can achieve a better fit to the experiment than in Figs. 3b, 4b, and 5b; however, this will result in a significant discrepancy for the other lines. The data presented in Figs. 3b, 4b, and 5b correspond to the optimum choice, which provides the best fit to the experimental data for all of the lines observed. Of course, the scatter in the experimental data is rather wide and, moreover, the neutral density distribution can vary from shot to shot. Nevertheless, such a choice of identical dependences of the relative neutral density N_H/N_e on the temperature enables us to find the neutral density distribution in the edge plasma in the above two regimes. This dependence is presented in Fig. 7 with the corresponding formulas describing the fit curves. One can see that the neutral density decreases more sharply in the attached plasma regime. Unfortunately, there are no experimental data from independent measurements of the hydrogen line intensities with which we could compare the dependences shown in Fig. 7.

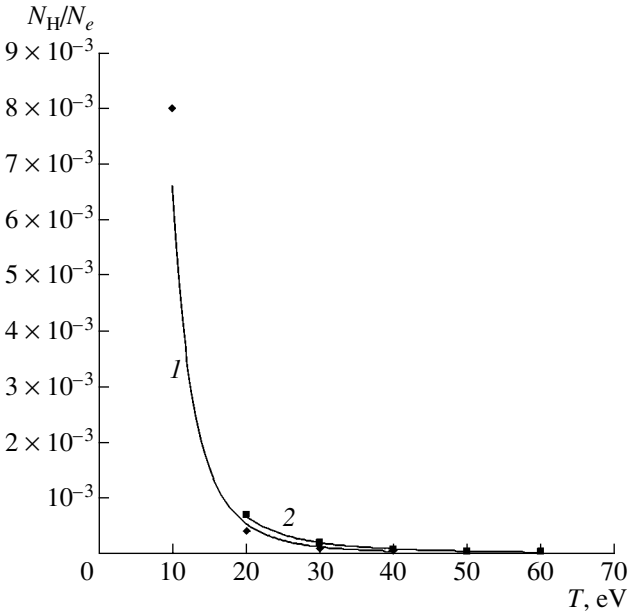

Fig. 7. Approximated temperature dependence of the parameter N_H/N_e. The symbols show the numerical results for the detached (squares) and attached (diamonds) plasma regimes. The solid curves are the analytical fits (*1*) $N_H/N_e = 27.503T^{-3.6196}$ and (*2*) $N_H/N_e = 4.5835T^{-2.9498}$ for the low- and high-temperature ranges, respectively.

We note that the possibility of varying the contribution from charge exchange is substantially limited by the saturation effect. Numerical calculations show that, for the parameter values under consideration, the population source related to charge exchange becomes independent of the neutral density starting from the value $N_H/N_e = 10^{-3}$ (see Fig. 6). Moreover, as can be seen from Fig. 2, charge exchange significantly affects the population of atomic levels and, consequently, the absolute line intensities, whereas its influence on the intensity ratio turns out to be much weaker. Thus, although the level populations calculated with and without allowance for charge exchange are significantly different (see Fig. 2), the intensity ratio is almost the same in both cases. The saturation of the population source makes this effect even more pronounced because it also reduces the influence of charge exchange on the measured line intensity ratio.

4. SOURCES OF THE ION LEVEL POPULATION THROUGH CHARGE EXCHANGE IN THE CORE PLASMA

In a high-temperature core plasma, the charge exchange of fast neutral beams occurs mainly from the ground state. For beam energies of several hundred kiloelectronvolts, the probability of capturing electrons by excited impurity ions is rather low [8].

For the core plasma, we apply the same kinetic model as for the edge plasma and allow for the change in the charge-exchange rate constants at high neutral–impurity ion collision velocities that are characteristic of NBI experiments. At the same time, it is of interest to take into account the beam geometry in expression (5) by introducing a geometric factor $g < 1$ characterizing the plasma region occupied by the beam,

$$q^{cx}(n) \approx N_{A^{+(Z-1)}}\alpha^{\text{ion}}N_e\frac{\kappa_n^{cx}N_H/N_e}{\kappa^{rr} + \kappa^{dr} + g\kappa^{cx}N_H/N_e}. \quad (15)$$

This factor accounts for the fact that the neutral density in the interaction region differs from the averaged (over the entire plasma) neutral density, which determines the shift of the ionization balance (in the previous case, this was unimportant because of the absence of beams).

Using Eq. (15), we write the expression for the population rate or the level n of an $A^{+(Z-1)}$ ion in the form

$$q_{A^{+Z}}(n) = N_{A^{+Z}}N_e\left[\kappa_n^{\text{ext}} + \kappa^{\text{ion}}\frac{\kappa_n^{rr} + \kappa_n^{dr} + \kappa_n^{cx}N_H/N_e}{\kappa^{rr} + \kappa^{dr} + g\kappa^{cx}N_H/N_e}\right]. \quad (16)$$

In expression (16), as in the previous case, the partial values of the rate coefficients enter in the numerator, whereas the total values summed over all n enter in the denominator.

Substituting typical values of the collisional rates from [8] into expression (16), we find the following estimate for the total population source of the excited states of impurity ions:

$$q(n) \approx N_{A^{+(Z-1)}} N_e \left\{ \kappa_n^{\text{ext}} + \kappa^{\text{ion}} \frac{10^{-14}(Z+1)n_1(n_1/n)^3 + (N_{\text{H}}/N_e)\times 10^{-5}(Z+1)^2/25^3}{10^{-14}(Z+1)n_1 + g(N_{\text{H}}/N_e)\times 0.5\times 10^{-5}(Z+1)^3/25^3} \right\}, \quad (17)$$

where n_1 is the principal quantum number of the ground state (below, $n_1 = 1, 2$), and g is the geometric factor determining the contribution of charge exchange to the ionization balance.

Factoring out the ionization cross section and taking into account expressions (15) and (16), we find that

$$q(n)\ [\text{cm}^{-3}\ \text{s}^{-1}] = Bq^*(n), \quad (18)$$

where

$$B = 10^{-8} N_{A^{+(Z-1)}} N_e (Z+1)^{-3} G((Z+1)^2 Ry/n_1^2 T)\exp[-(Z+1)^2 Ry/n_1^2 T)],$$

$$q^*(n) = V\left(\frac{n_1}{n}\right)^3 + \frac{10^{-14}(Z+1)n_1(n_1/n)^3 + (N_{\text{H}}/N_e)\times 10^{-5}(Z+1)^2/25^3}{10^{-14}(Z+1)n_1 + g(N_{\text{H}}/N_e)\times 0.5\times 10^{-5}(Z+1)^3/25^3},$$

and the functions $G(x)$ and V are defined in the Appendix.

For the parameters characteristic of the core plasma, we calculated the influence of the saturation effect on the intensities of the spectral lines of ions with different charges Z at different values of the NBI geometric factor. The saturation effect is clearly demonstrated in Figs. 8 and 9. It can be seen that this effect is more pronounced for high-Z ions. This result correlates with the experimental observations: as the ion charge increases, the role of charge exchange increases, but the intensity of the populated lines decreases because of the saturation effect. Probably, that is why the line emission of low-charge (lithium) ions is only observed in the LHD device (see [12]).

A comparison of Figs. 8 and 9 shows that taking into account the geometric factor g leads to a stronger dependence of the population source on the ratio N_{H}/N_e, which is explained by a smaller shift of the ionization equilibrium in plasma under the action of neutral beams with smaller values of the geometric factor. In the limiting case of an infinitely small geometric factor (which corresponds to narrow diagnostic beams), the local charge-exchange effect increases proportionally to the

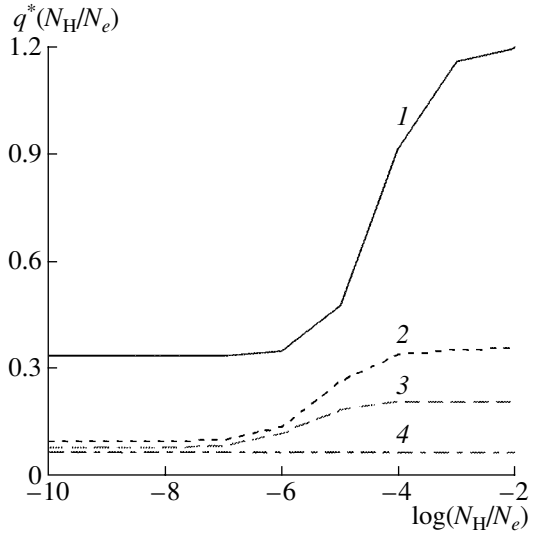

Fig. 8. Dependence of the source $q^*(n)$ on the parameter N_{H}/N_e for $g = 1$ and different values of the ion charge number: $Z =$ (*1*) 2, (*2*) 6, (*3*) 10, and (*4*) 30.

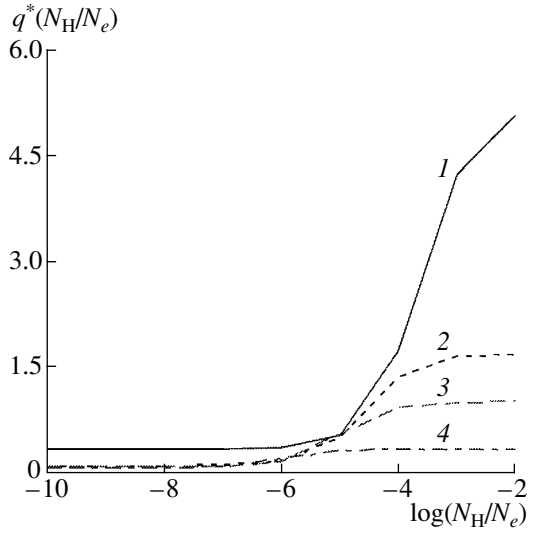

Fig. 9. Same as in Fig. 8 for $g = 0.2$.

neutral beam density without appreciably reducing the number of charge-exchange ions. Of course, the observed signal decreases with decreasing geometric factor. Hence, taking into account the geometric factor is important for analyzing the spectral line intensities of impurity ions in plasma.

5. DISCUSSION AND CONCLUSIONS

The spectral line intensities of impurity ions observed in the edge and central regions of a tokamak plasma have been examined using self-consistent solutions to the equations for the ionization equilibrium and the population kinetics of atomic levels.

It has been shown that the population through charge exchange significantly affects the spectral line intensities of impurity ions in a hydrogen plasma. An expression has been derived for the total population rate of the level n as a function of the electron temperature and the relative neutral density N_H/N_e. It has been found that, at high values of the ratio N_H/N_e, the contribution from charge exchange to the population rate does not depend on the neutral density (the so-called "saturation effect"). The reason is that the line intensities are determined by the product of the neutral density and the density of charge-exchange nuclei. When charge exchange makes the main contribution to recombination, the density of nuclei is inversely proportional to the neutral density, so that their product is independent of the neutral hydrogen density. In other words, the increase in the population and the shift of the ionization equilibrium (both caused by charge exchange) balance each other; as a result, the line intensities become independent of the neutral density in the system. This effect can substantially limit the efficiency of the charge-exchange plasma diagnostics under NBI conditions.

The intensities of the experimentally observed lines associated with transitions between the states of hydrogen-like He^+ atoms in the edge plasma of the TORE SUPRA tokamak have been calculated. Taking into account charge-exchange processes makes it possible to qualitatively explain the experimentally observed fact that the dependences of the intensity ratios of the spectral lines on the temperature are different in different plasma regimes. It has been shown that, in the edge plasma too, the saturation effect can limit the efficiency of charge-exchange diagnostics.

The results obtained allow us to conclude that it makes no sense to increase the neutral density in the device above a certain level in order to more clearly display the effect of charge exchange with neutrals because, after reaching this critical value, the results will not change.

ACKNOWLEDGMENTS

This work was supported in part by the Russian Foundation for Basic Research (project no. 01-02-16305) and the Russian Federal Program for Government Support of Leading Scientific Schools (grant no. 00-15-96526).

APPENDIX

The general expressions for the rates of main atomic processes have the form [5]

$$\langle v\sigma_n\rangle^{\text{ext}} = 10^{-8}\frac{1}{2l_0+1}\left(\frac{Ry}{\Delta E}\frac{E_1}{E_0}\right)^{\frac{3}{2}}G'(\beta)e^{-\beta}, \quad \text{(A. 1)}$$

where

$$G'(Z>1) = \frac{A'\sqrt{\beta}(\beta+1)}{\beta+\chi'},\ \beta = \frac{\Delta E}{T} = Z^2Ry\left(1-\frac{1}{n^2}\right);$$

$$\langle v\sigma_n\rangle^{\text{ion}} = 10^{-8}\frac{1}{2l_0+1}Q_i\left(\frac{Ry}{|E_Z|}\right)^{\frac{3}{2}}G(\beta)e^{-\beta}, \quad \text{(A. 2)}$$

where

$$G(Z>1) = \frac{A\sqrt{\beta}}{\beta+\chi},\quad \beta = \frac{E_Z}{T} = \frac{Z^2Ry}{n^2T};$$

$$\langle v\sigma_n\rangle^{rr} = \frac{32\sqrt{\pi}a_0\hbar}{3\sqrt{3}m(137)^3}Zn_1\beta_1^{\frac{1}{2}} \quad \text{(A. 3)}$$

$$\times\left[\ln(1.78\beta_1) - e^{\beta_1}\text{Ei}(-\beta_1)\left(1+\frac{\beta_1}{n_1}\right)\right] = \mathcal{N}_{0n}^{Kr}\frac{Z^4}{n^3},$$

where $\mathcal{N}_{n0}^{Kr}$ is the Kramers radiative-recombination rate coefficient [1], χ and χ' are numerical factors, $\beta_1 = \frac{Z^2Ry}{n_1^2T}$, and $n_1 = 1$.

The charge-exchange rate with allowance for the relation between quantum numbers of the initial and final states is equal to

$$\langle v_H\sigma_n\rangle^{cx} = v_H\sigma_0^{cx}\frac{n_{He}^4}{16}b^H\left(\frac{n}{2}\right),\quad \sigma_0^{cx} = \pi a_0^2Z. \quad \text{(A. 4)}$$

After substituting all the main dependences, the expression for the total population rate of the level n takes the form

$$q_{A^{+Z-1}}(n) = N_{A^{+Z-1}}N_e\frac{1}{n^3}\left\{(v\sigma_n)^{\text{ext}}n^3\right.$$

$$\left.+\left[\mathcal{N}_{0n}^{Kr}Z^4 + \left(\frac{N_H}{N_e}\right)\frac{\pi a_0^2}{16}2v_Hn^7b^H\left(\frac{n}{2}\right)\right]\right.$$

$$\times \left\{ \frac{\left[\langle v_e \sigma \rangle^{\text{ion}}_{A^{+Z-1}} + v_{\text{H}} \frac{\pi a_0^2}{4} \sum_{n \geq 3}^{n_{\max}} n^4 b^{A^{+Z-1}}(n) \right]}{\left[\langle v_e \sigma \rangle^{RR}_{\text{total}} + \left(\frac{N_{\text{H}}}{N_e} \right) v_{\text{H}} \frac{\pi a_0^2}{16} 2 \sum_{n \geq 4}^{n_{\max}} n^4 b^{\text{H}}\left(\frac{n}{2} \right) \right]} \right\}.$$

The functions *V*, *G*, Π, and Λ, which enter in expressions (14) and (18), have the form

$$V(\beta_1, n^2) = \frac{1}{\left(1 - \frac{1}{n^2}\right)^{\frac{3}{2}}} \frac{G'\left(\beta_1\left(1 - \frac{1}{n^2}\right)\right)}{G(\beta_1)} e^{\frac{\beta_1}{n^2}}; \quad \text{(A. 5)}$$

$$G(\beta_1) = \frac{\sqrt{\beta_1} A}{\beta_1 + \chi}; \quad \Pi(\beta_1, n^2) = -\frac{e^{\frac{\beta_1}{n^2}} \text{Ei}\left(-\frac{\beta_1}{n^2}\right)}{\Lambda(\beta_1)};$$

$$\Lambda(\beta_1) = \ln(1.78\beta_1) - e^{\beta_1} \text{Ei}(-\beta_1)(1 + \beta_1);$$

$$\beta_1 = \frac{Z^2 Ry}{T}.$$

The functions *V*, Π, and Λ are slowly varying functions of the temperature and are on the order of unity.

REFERENCES

1. I. Beigman, in *Proceedings of the Lebedev Physical Institute* (Fiz. Inst. im. P. N. Lebedeva, Akad. Nauk SSSR, Moscow, 1987), Vol. 179, p. 160.
2. R. Guirlet, M. Koubiti, A. Escarguel, *et al.*, Plasma Phys. Controlled Fusion **43**, 177 (2001).
3. L. A. Bureyeva, T. Kato, V. S. Lisitsa, and C. Namba, Phys. Rev. A **65**, 032702 (2002).
4. V. A. Astapenko, L. A. Bureyeva, and V. S. Lisitsa, Usp. Fiz. Nauk **172**, 155 (2002) [Phys. Usp. **45**, 149 (2002)].
5. L. A. Vainstein, I. I. Sobelman, and E. A. Yukov, *Excitation of Atoms and Broadening of Spectral Lines* (Nauka, Moscow, 1979; Springer-Verlag, Berlin, 1981).
6. K. R. Cornelius, K. Wojtkowski, and R. E. Olson, J. Phys. B **33**, 2017 (2000).
7. L. A. Bureyeva and V. S. Lisitsa, *A Perturbed Atom* (Gordon and Breach, 2000).
8. R. K. Janev, L. P. Presnyakov, and V. P. Shevelko, *Physics of Highly Charged Ions* (Springer-Verlag, Berlin, 1985).
9. L. M. Biberman, V. S. Vorob'ev, and I. T. Yakubov, *Kinetics of Nonequilibrium Low-Temperature Plasma* (Nauka, Moscow, 1982; Consultans Bureau, New York, 1987).
10. F. B. Rosmej and V. S. Lisitsa, Phys. Lett. A **244**, 401 (1998).
11. L. A. Bureyeva, T. Kato, V. S. Lisitsa, and C. Namba, J. Phys. B **34**, 1 (2001).
12. http://www-dg.lhd.nifs.ac.jp/layout.html.

Translated by N.F. Larionova

Plasma Physics Reports, Vol. 29, No. 10, 2003, pp. 845–859. Translated from Fizika Plazmy, Vol. 29, No. 10, 2003, pp. 911–925.

PLASMA OSCILLATIONS AND WAVES

Quasilinear Modification of the Spectra of Cyclotron Emission from a Toroidal Plasma near the ECRH Frequency

A. G. Shalashov and E. V. Suvorov

Institute of Applied Physics, Russian Academy of Sciences, ul. Ul'yanova 46, Nizhni Novgorod, 603600 Russia

Received January 28, 2003; in final form, March 27, 2003

Abstract—A study is made of the modification of the spectra of electron cyclotron emission from an ECR heated plasma in a toroidal magnetic confinement system into which the heating radiation is launched from the low-field side. It is shown that, at frequencies close to the heating frequency, cyclotron emission can become more intense because of the deformation of the distribution function of the resonant electrons. This effect can be used to diagnose the slightly pronounced quasilinear perturbations of the electron distribution in the thermal energy range, which are typical of experiments on ECR plasma heating. Results of a qualitative analysis carried out for model electron distribution functions are presented, and examples of three-dimensional numerical simulations of a circular tokamak are described. © *2003 MAIK "Nauka/Interperiodica".*

1. INTRODUCTION

The modification of the electron distribution function during electron cyclotron resonance (ECR) absorption of microwaves in toroidal plasmas is most pronounced in experiments on ECR current drive with high-field-side (HFS) or oblique launch of microwave radiation. In this case, the microwave power is deposited in high-energy suprathermal electrons. In experiments on ECR heating, microwaves are usually launched in a quasi-transverse direction from the low-field side (LFS). In an optically thick plasma column, the microwave power is deposited mainly in the low-energy electrons, whose distribution only slightly deviates from an equilibrium distribution because of the efficient Coulomb collisions between plasma particles. Consequently, under the conditions prevailing in present-day experiments on ECR plasma heating, the perturbation of the distribution function of the resonant electrons leads merely to a slight displacement and expansion of the energy deposition region and does not have any significant influence on the formation of the global density and temperature profiles. Nevertheless, such effects can play a decisive role in auxiliary ECR heating aimed at suppressing MHD instabilities of the plasma column, in which case the position of the energy deposition region should be controlled with a high degree of accuracy.

The interaction of an intense microwave field with the plasma electrons perturbs the electron velocity distribution function and, as a result, modifies the spectra of the electron cyclotron emission (ECE) from the plasma. We can cite the following three main effects responsible for this modification:

(i) The formation of a high-energy tail in the distribution function leads to the appearance of the electrons whose cyclotron emission is weakly absorbed by the plasma because of the relativistic shift of the resonance frequency. This results in a nonthermal feature in the emission spectrum in the frequency range below the heating frequency [1, 2].

(ii) The formation of the so-called quasilinear plateau (i.e., the flattening of the distribution function of the resonant electrons due to their interaction with the microwave field) leads to the degradation of the resonant absorption at frequencies close to the heating frequency. Because of the appearance of a peculiar transparency window in the spectrum of electron cyclotron absorption at the fundamental frequency, the intensity of emission from the plasma layer in the corresponding frequency range becomes higher than the thermal level. It is important to note that the increase in the emission intensity above the thermal level is observed even when the total number of resonant electrons deviates only slightly from the equilibrium value.

(iii) The steep gradients of the electron distribution function that form at the boundaries of the resonance region in velocity space can lead to an effect opposite to effect (ii), specifically, a decrease in the intensity of plasma emission because of an enhanced electron cyclotron absorption of microwaves in a certain narrow frequency range.

In this paper, we discuss the possibility of measuring the quasilinear modification of the electron distribution function during the ECR heating of the main plasma component when microwave energy is deposited in the low-energy thermal electrons. The diagnostic method proposed here is based on measurements of the spectra of cyclotron emission from a toroidal plasma in a range of frequencies that are close to the heating frequency and at which the ECE intensity can increase (regardless of the presence of high-energy electrons in the plasma) because of the deformation of the distribu-

1063-780X/03/2910-0845$24.00

tion function of the resonant electrons. We will focus below on an analysis of effect (ii), which is associated with the quasineutral transparency window and is most pronounced when the fraction of suprathermal electrons is small. Effect (iii) is presumably too weak to be detected by conventional methods. Effects (ii) and (iii) were first noted by Giruzzi [3], who carried out a fairly detailed numerical calculation of the nonequilibrium ECE spectra for experimental conditions close to those in the T-10 tokamak. To the best of our knowledge, it is only recently that the first experimental results in the FTU device have been obtained showing that the peak of the ECE at frequencies close to the heating frequency can be interpreted as being caused by kinetic effect (ii) rather than by the local heating of the microwave power deposition region [4–6].

Conceptually, our study is close to paper [3]. In [7], it was shown, however, that the quasilinear diffusion operator used in that paper is, generally speaking, incorrect. We will use a simpler quasilinear operator obtained from the general expression [7, 8] in the "rectangular magnetic well" approximation. That this approximation is workable was demonstrated, e.g., by Timofeev and Tokman [7], who applied it to the current-drive problem. Using a simplified kinetic model of the microwave heating made it possible to analyze the problem qualitatively and to obtain simple analytic estimates.

The expected maximum increase in the radiation temperature T_r can be roughly estimated by assuming that resonant absorption tends to zero due to quasilinear effects, provided that the number of resonant electrons is essentially unchanged. The result is formally the same as that for an optically thin plasma slab:

$$T_r \approx \tau_0 T_e, \tag{1}$$

where τ_0 is the optical depth of the slab in which the electrons obey a Maxwellian velocity distribution with the temperature T_e. Under the condition that Coulomb collisions do not hinder the formation of a plateau in the electron distribution function, this formula is valid for any value of the parameter τ_0. We can see that the effect in question can be important when the optical depth of the plasma is sufficiently large.

In order to simplify the formulas, we consider the case in which the heating radiation and detected cyclotron emission both propagate strictly transverse to the toroidal magnetic field and correspond to an extraordinary wave at the second cyclotron harmonic. Our paper is organized as follows. In Section 2, we describe the set of quasilinear equations used to determine the electron velocity distribution function at each magnetic surface with allowance for Coulomb collisions and the interaction of resonant electrons with the heating microwave field. In Section 3, we consider the equation of radiation transfer and use this equation to evaluate the perturbations of the ECE spectra in two typical cases: the collisionless distribution function and the distribution function corresponding to perturbations in a narrow resonance region in velocity space. In Section 4, we present examples of numerical calculations of the modified ECE spectra in a circular tokamak. The most laborious analytic manipulations are given in the Appendix.

2. MODEL OF ECR PLASMA HEATING BY MONOCHROMATIC RADIATION IN A TOROIDAL MAGNETIC DEVICE

In order to consider ECR heating of the electron plasma component in a toroidal magnetic device, we formulate a boundary-value problem in which a quasi-steady finite-aperture monochromatic microwave beam is launched into the plasma from the low-field side. Under the assumption that the characteristic time scale of the propagation of perturbations along the magnetic field lines is much shorter than the time scales of the processes that will be considered below, the electron distribution function averaged over high-frequency oscillations in a microwave field can be treated as uniform at each magnetic surface.

Under the combined action of the magnetic field nonuniformity and rotational transform, the nature of the electron cyclotron absorption in a toroidal system changes in a specific manner. When moving over a magnetic surface, an electron repeatedly crosses the microwave beam, the magnetic field strength being different at each crossing. Under ECR conditions, this leads to a finite spread in frequency detunings and eventually results in a stochastization of the interaction of an electron ensemble with monochromatic radiation. If the relative change in the velocity of an electron that has crossed the microwave beam is small, then, after averaging over many revolutions along the torus, we can say that the electrons in velocity space become subject to a kind of Brownian motion, in which case their distribution function is described by a Fokker–Planck diffusion equation. Following [10, 11], we assume that, at each magnetic surface, the process just described is in a sense analogous to electron heating in a homogeneous magnetic field by radiation with a finite-width spectrum. This assumption allows us, first, to work with the variation of the frequency of the external radiation rather than the variation of the gyrofrequency at a certain magnetic surface in the heated region and, second, instead of considering the problem of a toroidal plasma, to consider the problem for a plane slab geometry, in which case the electron distribution function at the surfaces of a constant magnetic field is uniform, but the effective heating radiation has a finite-width noisy (δ-correlated) frequency spectrum because every electron repeatedly crosses the microwave field region with random phases. As a result, the problem can be treated in the standard quasilinear theory describing the dynamics of the electron distribution on time scales much longer than the period of electron oscillations in a microwave field, the period of electron gyration, and

the period of electron drift motion along the magnetic field lines (the bounce period).

When the width of the microwave power deposition region is much smaller than the major radius of the plasma column, we can assume that the magnetic field depends linearly on the coordinate. Let the magnetic field increase linearly in space in a certain direction $\mathbf{z}_0$,

$$\mathbf{H}(z) = (1 + z/L_H)\mathbf{H}_0, \quad \mathbf{H}_0 \perp \mathbf{z}_0 \tag{2}$$

and let the heating radiation propagate in the positive direction of the z axis, which is perpendicular to the magnetic field. In this case, the cyclotron resonance condition, which is determined by the relativistic dependence of the electron mass on energy, also depends on the z coordinate:

$$\begin{aligned}\omega_{\text{res}}(z, v) &= s\omega_H(z)\sqrt{1 - v^2/c^2} \\ &\approx s\omega_H(0)(1 + z/L_H - v^2/2c^2),\end{aligned} \tag{3}$$

where s is the number of the cyclotron harmonic, $\omega_H(z) = eH(z)/m_e c$ is the nonrelativistic electron gyrofrequency, v is the electron velocity, and c is the speed of light in free space. The approximate equality in condition (3) is obtained for $|z|/L_H \ll 1$ and $v/c \ll 1$. The energy of the electrons interacting resonantly with radiation at a fixed frequency increases as the spatial point under consideration is shifted along the z axis in the HFS direction.

The effective spectrum of the heating radiation is determined by the distribution of the electromagnetic field intensity in a microwave beam. To simplify the mathematics, we make the following three assumptions: (i) in the region where the radiation is launched into the chamber, the microwave intensity distribution over the beam cross section (whose plane is perpendicular to the magnetic field) is rectangular; (ii) every time an electron crosses the heated region, it can pass through any point of the cross section of the magnetic surface with equal probability; and (iii) the ray trajectories of the beam are straight and its cross section is large enough that most of its spatial Fourier harmonics propagate almost transverse to the magnetic field. Under these assumptions, the effective spectral radiation intensity at the entrance to the energy deposition region ($z = z_0$) can be described by the following distribution [10, 11]:

$$\begin{aligned}I_\omega^0 &= \begin{cases} I_0\Phi(\omega), & \omega \in (\omega_0, \omega_0 + \Delta\omega) \\ 0, & \omega \notin (\omega_0, \omega_0 + \Delta\omega), \end{cases} \\ I_0 &= \frac{P_{\text{inp}}}{S\Delta\omega},\end{aligned} \tag{4}$$

where P_{inp} is the total input power of the incident microwave radiation and S is the area of the magnetic surface at which the radiation begins to be absorbed. The characteristic frequency of the effective spectrum, $\omega_0 = s\omega_H(1 + z_0/L_H)$, is related to the coordinate z_0 of the starting point of the cyclotron interaction region, and the effective spectrum width $\Delta\omega = s\Delta\omega_H$ is determined by the variation $\Delta\omega_H$ of the resonant electron gyrofrequency at the intersection of the magnetic surface with a finite-aperture quasi-optical microwave beam. The form factor $\Phi(\omega)$ is determined by the geometry of the magnetic surfaces in the heated region. Thus, when a microwave beam launched into the device is symmetric about the equatorial plane and the beam cross section is sufficiently small, so that the circular cross section of the magnetic surface can be regarded as parabolic, we have $\Phi(\omega) \approx \sqrt{\Delta\omega/(\omega - \omega_0)}$, which indicates that the form factor has a singularity because, in the equatorial plane, the electrons cross the microwave beam at an essentially constant magnetic field. When the power deposition region is outside the equatorial plane of the torus and the cross sections of the magnetic surface in the heated region can be regarded as straight lines, we have $\Phi(\omega) \approx 1$. Note that the intensity I_0 of effective spectrum (4) can be obtained from the following simple considerations: since the energy acquired by the electrons in a microwave field is rapidly redistributed over the magnetic surfaces, we can assume that, regardless of the actual cross section of the microwave beam, the total microwave power is uniformly launched through the surface of a certain effective torus of area S.

The evolution of the electron distribution function $f(t, z, \mathbf{v})$ is described by the following set of quasilinear equations:

$$\frac{\partial f}{\partial t} = L_{\text{ql}} f + L_{\text{c}} f, \quad \frac{\partial I_\omega^{\text{eff}}}{\partial z} = -\mu_\omega I_\omega^{\text{eff}}. \tag{5}$$

Here, L_{ql} is the quasilinear diffusion operator determined by the spectral intensity $I_\omega^{\text{eff}}(t, z, \omega)$ of the heating radiation at each spatial point; L_{c} is the Coulomb collision integral; and μ_ω is the electron cyclotron absorption coefficient calculated for the instantaneous distribution function $f(t, z, \mathbf{v})$. The first of Eqs. (5) is the kinetic equation describing the electron distribution function with allowance for ECR heating (in the quasilinear approximation) and the subsequent redistribution of the absorbed energy due to Coulomb collisions between the electrons. The second of Eqs. (5) is the radiation transfer equation, which describes the spatial distribution of the heating radiation intensity, thereby providing the coupling between the solutions to the kinetic equation that correspond to different magnetic surfaces. Since plasma emission is very sensitive to the spatial structure of the plasma slab, it is essential to self-consistently take into account the dynamics of the distribution function and heating radiation when calculating the ECE from the plasma.

Taking into account the fact that, during microwave heating of the electrons, the perturbations of their distribution function are usually not so strong and local-

ized in phase space, we use the linear Coulomb collision operator. Assuming that the collisional relaxation of the perturbed distribution function is governed exclusively by collisions with the bulk electrons, which obey a Maxwellian velocity distribution, and by the angular scattering of the electrons by immobile ions, we can reduce the Landau collision integral to the form [12]

$$L_c f = \frac{1}{u^2}\frac{\partial}{\partial u}u^2\left\{D_c\left(\frac{\partial f}{\partial u} + 2uf\right)\right\} + \nu_c^s\frac{\partial}{\partial s}(1-s^2)\frac{\partial f}{\partial s}, \quad (6)$$

$$D_c(u) = \frac{2\nu_c}{\sqrt{\pi}u^3}\int_0^u x^2 e^{-x^2}dx, \quad (7)$$

$$\nu_c^s = \frac{\nu_c}{u^3}\left\{\frac{1}{2}Z_{\text{eff}} + \frac{1}{\sqrt{\pi}}\left(ue^{-u^2} + (2-u^{-2})\int_0^u x^2 e^{-x^2}dx\right)\right\}. \quad (8)$$

Here, $u = v/v_e$ is the absolute value of the electron velocity normalized to the thermal velocity $v_e = \sqrt{2T_e/m_e}$ of the background electrons, $s = \cos\theta$ is the cosine of the electron pitch angle, $\nu_c = 4\pi e^4 N_e \ln\Lambda_e / m_e^2 v_e^3$ is the effective collision frequency of the thermal electrons, and Z_{eff} is the effective ion charge number. The temperature T_e and density N_e of the background electrons are assumed to be fixed, ensuring that quasilinear equations (5) will have a stationary solution corresponding to a nonzero absorbed microwave power and a given finite energy of the electron plasma component. For simplicity, we assume that the parameters of the background electron distribution are uniform over the region of microwave heating.

When the heating radiation propagates transverse to the external magnetic field, the cyclotron interaction of the electrons with a high-frequency noisy field gives rise to a quasilinear diffusion in the direction of their transverse velocity. In spherical coordinates, the corresponding diffusion operator has the form [13–15]

$$L_{\text{ql}} f = \frac{1}{u^2}\left\{\frac{\partial}{\partial u}\left[u^2(1-s^2)D_{ql}\left(\frac{\partial f}{\partial u} - \frac{s}{u}\frac{\partial f}{\partial s}\right)\right] - \frac{\partial}{\partial s}\left[s^2(1-s^2)D_{ql}\left(\frac{u}{s}\frac{\partial f}{\partial u} - \frac{\partial f}{\partial s}\right)\right]\right\}. \quad (9)$$

The quasilinear diffusion coefficient D_{ql} is proportional to the heating radiation intensity at the resonant frequency, $D_{\text{ql}} \propto I_\omega^{\text{eff}}(t, z, \omega_{\text{res}}(z, u))$. We express the solution to the radiation transfer equation in terms of the optical depth τ to obtain

$$D_{\text{ql}}(t, z, u, s) = \nu_{\text{ql}}\Phi(\omega_{\text{res}})\tilde{D}_{\text{ql}}(u, s)e^{-\tau(t, z, \omega_{\text{res}})}, \quad \tau(t, z, \omega) = \int_{-\infty}^{z}\mu_\omega(t, z', \omega)dz', \quad (10)$$

where ν_{ql} is the characteristic quasilinear frequency and $\tilde{D}_{\text{ql}}$ determines the explicit dependence of the diffusion coefficient on the electron velocity (see, e.g., [16]). Obviously, the quasilinear diffusion coefficient is nonzero only in the local region of the phase space defined by the condition $\omega_{\text{res}}(z, u) \in (\omega_0, \omega_0 + \Delta\omega)$. The interval of resonance energies of the electrons involved in cyclotron interaction is different at different points of the coordinate space. As the point shifts in the HFS direction, this interval shifts toward higher energies.

From the general expression for the absorption coefficient in the case of an arbitrary electron velocity distribution [16], we obtain the following relationship for the case of strictly transverse propagation:

$$\mu_\omega \propto -\int_0^\infty du\int_0^1 ds\left\{u^2(1-s^2)\tilde{D}_{\text{ql}}\left(u\frac{\partial f}{\partial u} - s\frac{\partial f}{\partial s}\right) \times \delta(\omega - \omega_{\text{res}}(z, u))\right\}. \quad (11)$$

Here, the proportionality coefficient can be determined from the condition that, for a Maxwellian distribution, this formula should lead to the known expressions for the optical depth τ_0 of an equilibrium plasma slab in a linearly nonuniform magnetic field [11].

We integrate three-dimensional equations (5) with operators (6) and (9) over the region determined by the inequalities $0 < u < \infty$, $0 < s < 1$, and $z > z_0$. The conditions at the boundaries of this region are as follows:

$$f|_{u=\infty} = 0, \quad \partial f/\partial s|_{s=\infty} = 0, \quad I_\omega^{\text{eff}}\big|_{z=z_0} = I_\omega^0. \quad (12)$$

In deriving these conditions, we took into account the facts that, in the case at hand, the distribution function is even over the electron pitch angle and that the radiation begins to be absorbed resonantly only at a certain boundary z_0 of the interaction region. At the boundaries $u = 0$ and $s = 1$ (which arise because we are working in spherical coordinates), the only requirement is that the derivatives of the distribution function should be finite. The numerical code used in our simulations was devised to solve an initial-value evolutionary problem. However, we are interested here in stationary solutions to Eqs. (5), so that, for our purposes, it is sufficient to prescribe only the electron density N_e at the initial time.

As an example, we present the expressions for ν_{ql}, $D_{ql}^{\sim}$, and τ_0 for two cases that are most important for practical application: heating by an extraordinary wave at the second cyclotron harmonic (an X2 mode) and heating by an ordinary wave at the fundamental cyclotron harmonic (an O1 mode). If we assume that each of these modes propagates transverse to a locally uniform magnetic field, then, for $v/c \ll 1$, we obtain [11, 13]

$$\nu_{ql} = \frac{\pi^2 e^2 \tilde{n}}{c^3 m_e^2}\frac{P_{inp}}{S\Delta\omega}, \quad D_{ql}^{\sim} = u^2\begin{cases}1-s^2 & \text{for the X2 mode}\\ s^2 & \text{for the O1 mode}\end{cases},$$
$$\tau_0 = \frac{\pi}{4}\tilde{n} q \beta_e^2 \frac{\omega_0 L_H}{c}. \tag{13}$$

Here, $q = \omega_p^2/\omega_H^2(0)$, with ω_p the electron plasma frequency, and $\beta_e = v_e/c$. For an ordinary wave, we have $\tilde{n} \approx n$, where n is the refractive index. For an extraordinary wave, the expression for $\tilde{n}$ also includes the mode polarization effect: $\tilde{n} \approx n(3-q/2)^2/(3-q)^2$.

We now qualitatively describe the character of the solutions to Eqs. (5). When the heating radiation is launched from the low-field side, the microwave power begins to be deposited in those regions of the plasma column in which the radiation interacts resonantly with low-energy electrons. Because of the absorption of the microwave field, the distribution of the resonant electrons over transverse energies is smoothed out; as a result, the microwave power absorbed at a given spatial point decreases and the heating radiation penetrates into the region of a stronger magnetic field. During the formation of a quasilinear plateau in the distribution function, the energy deposition region is displaced in space, which corresponds to energy transfer to electrons with increasingly higher energies. In the absence of Coulomb collisions, this process will lead to a specific steady state in which the plasma column becomes fully transparent to microwave radiation and ECR heating terminates. Under the combined action of the resonant field and Coulomb collisions of resonant electrons with nonresonant ones, a quasisteady distribution of the resonant electrons forms that ensures the absorption of a finite (but different from that in equilibrium) fraction of the incident microwave power. Note that the model under consideration is applicable only when the rays forming the microwave beam are not tangent to the magnetic surfaces in the energy deposition region, i.e., when the electrons are heated simultaneously at several neighboring magnetic surfaces.

3. QUALITATIVE THEORY OF THE MODIFICATION OF THE ECE SPECTRA

The quasilinear deformation of the electron distribution function modifies the ECE spectra near the heating frequency and its harmonics. We consider only that ECE component whose polarization and harmonic number coincide with those of the heating radiation, namely, emission at the second harmonic of an extraordinary wave propagating transverse to the magnetic field. In this case, the emission line is broadened due to the relativistic dependence of the mass of an electron on its energy; the Doppler broadening of the line can be ignored when the width of the radiation pattern of a receiving antenna is sufficiently small, $\theta_r \ll \beta_e/n$ [11].

We characterize plasma emission by the effective radiation temperature T_r, which is related to the spectral radiation intensity by the Rayleigh–Jeans formula and is determined from the general equation of radiation transfer along the rays of a microwave beam [17],

$$\frac{dT_r}{dl} = A_\omega - \mu_\omega T_r, \quad T_r = \frac{(2\pi)^3 c^2}{n^2\omega^2} I_\omega^{ECE}. \tag{14}$$

Here, μ_ω is the absorption (reabsorption) coefficient and A_ω is the properly normalized plasma emissivity for a given normal mode,

$$A_\omega \propto 2T_e\int_0^\infty du\int_0^1 ds\{u^4(1-s^2)D_{ql}^{\sim} f\delta(\omega-\omega_{res}(z,u))\}, \tag{15}$$

where the proportionality coefficient is the same as that in relationship (11). Note that for a Maxwellian distribution function, expressions (11) and (15) yield a Kirchhoff's law relating the emissivity A_ω^0 to the absorptivity μ_ω^0 in an equilibrium medium:

$$A_\omega^0 = T_e\mu_\omega^0. \tag{16}$$

The radiation transfer equation for the spontaneous emission from an infinite plasma slab has the solutions

$$\begin{Bmatrix}T_r^+\\ T_r^-\end{Bmatrix} = \int_{-\infty}^{+\infty} A_\omega(z_1)\exp\begin{Bmatrix}\tau(z_1)-\tau(\infty)\\ -\tau(z_1)\end{Bmatrix}dz_1,$$
$$\tau(z_1) = \int_{-\infty}^{z_1}\mu_\omega(z_1')dz_1', \tag{17}$$

where the temperatures T_r^+ and T_r^- characterize radiation propagating in the positive and negative directions of the z_1 axis and $\tau(z_1)$ is the optical depth of a finite plasma slab. For further analysis, we choose the z_1 axis in such a way that T_r^+ and T_r^- are, respectively, the temperatures of radiation propagating in the HFS and LFS directions.

Of course, the detected electron cyclotron radiation from the plasma does not generally propagate along the same geometric optical path as the incident microwave radiation. In this section, however, we assume for sim-

plicity that the z and z_1 axes coincide, which indicates that the emitted radiation propagates along the axis of the heating beam. For estimates, this assumption is quite justified because quasilinear effects have the greatest impact on ECE from the heated region, in which the resonant electrons, whose frequency satisfies the condition $\omega_{res}(z, u) = \omega$, are responsible for both the emission of radiation and absorption of the heating microwave field. For convenience in further calculations, we represent this condition in the dimensionless form:

$$\zeta - \Omega - u^2 \approx 0, \quad \zeta = 2\frac{z - z_0}{\beta_e^2(L_H + z_0)}, \qquad \Omega = 2\frac{\omega - \omega_0}{\beta_e^2\omega_0}, \tag{18}$$

where the variables ζ and Ω are the dimensionless coordinate and dimensionless frequency, respectively. In terms of these variables, the boundaries of the resonance region $\omega_{res}(z, u) \in (\omega_0, \omega_0 + \Delta\omega)$ can be defined as

$$u_1 \le u \le u_2, \quad u_1 = \sqrt{\max(0, \zeta - \Delta\Omega)}, \qquad u_2 = \sqrt{\max(0, \zeta)}, \tag{19}$$

where $\Delta\Omega = 2\Delta\omega/\beta_e^0\omega_0$ is the normalized width of the effective spectrum of the heating radiation.

3.1. Emission from a Collisionless Plasma

For the above-described hypothetical steady-state electron distribution, which is formed as a result of quasilinear relaxation in the absence of Coulomb collisions, the spectrum of ECE at the frequency of the monochromatic heating wave is the easiest to calculate. Let $f(u_\perp, u_\parallel)$ be the electron distribution function over the transverse and longitudinal (with respect to the magnetic field) components of the dimensionless electron velocity. During the collisionless relaxation, the number of resonant electrons with a given longitudinal momentum is conserved:

$$\int\limits_{u_1^2 \le u_\perp^2 + u_\parallel^2 \le u_2^2} f(u_\perp, u_\parallel) du_\perp^2 = \text{const}. \tag{20}$$

In a steady state, the distribution function f_{st} is independent of the transverse electron velocity in the resonance region. The distribution function at the initial time is assumed to be Maxwellian, $f_M = f_M^0 \exp(-u_\perp^2 - u_\parallel^2)$. Consequently, using the law of conservation of the number of resonant electrons, we can see that, over almost the entire resonance region, the electron distribution function is independent of velocity:

$$f_{st} = \kappa f_M^0 e^{-\zeta} \quad \text{for} \quad |u_\parallel| \le u_1, \qquad \kappa = (e^{\Delta\Omega} - 1)/\Delta\Omega. \tag{21}$$

This expression fails to hold for resonant electrons with high longitudinal velocities, $u_1 \le |u_\parallel| \le u_2$; however, when the resonance region is sufficiently narrow, we can ignore emission from these electrons and assume that expression (21) is valid over the entire region of resonant velocities.

Outside the resonance region, the steady-state distribution function remains Maxwellian; consequently, at frequencies $\Omega \notin (0, \Delta\Omega)$ (i.e., $\omega \notin (\omega_0, \omega_0 + \Delta\omega)$), the ECE spectrum is thermal. The spectrum is modified at frequencies $\Omega \in (0, \Delta\Omega)$, at which the emissivity and absorptivity of the medium are determined by the distribution function of the resonant electrons. Substituting distribution function (21) into general formula (15), we can express the emissivity corresponding to this distribution in terms of the equilibrium emissivity:

$$A_\omega = \kappa e^{-\Omega} T_e \mu_\omega^0, \tag{22}$$

where μ_ω^0 is the equilibrium absorptivity. This expression can easily be derived using resonance condition (18) by making the replacement $\zeta \longrightarrow \Omega + u^2$; in this way, the distribution function is expressed in terms of the Maxwellian distribution function multiplied by a frequency-independent coefficient:

$$f_{st} \longrightarrow \kappa e^{-\Omega} f_M. \tag{23}$$

Since, after the formation of a quasilinear plateau, there is no absorption at frequencies corresponding to the perturbed spectrum, the total radiation intensity is deduced by simply integrating expression (22) over the entire plasma slab. As a result, we obtain

$$T_r^{\pm}(\Omega) = \begin{cases} \kappa e^{-\Omega} T_e \tau_0 & \text{for} \quad \Omega \in (0, \Delta\Omega) \\ T_e(1 - e^{-\tau_0}) & \text{for} \quad \Omega \notin (0, \Delta\Omega), \end{cases} \tag{24}$$

where τ_0 is the optical depth of the equilibrium plasma slab. Note that this expression was derived without specifying the type of normal mode and the cyclotron harmonic number (it is only necessary that they be the same for the ECE and the heating radiation). The spectrum obtained is discontinuous at the frequencies $\Omega = 0$ and $\Delta\Omega$ because, in the absence of collisions, the distribution function undergoes jumps at the boundaries of the resonance region.

There are two effects that perturb the ECE: quasilinear weakening of the cyclotron absorption and additional increase in the transverse energy of the electrons in their interaction with the microwave field. In expression (24), the first effect is described by the factor τ_0, and the second effect is accounted for by the factor $\kappa e^{-\Omega}$.

Since, in experiments, even a very low-density plasma is optically thick to the heating radiation, the quasilinear modification of the ECE spectra could be quite readily observable provided that it were possible to achieve a collisionless regime of microwave absorption. Additional acceleration of resonant electrons in the transverse direction is unlikely to play a significant role in the formation of the emission spectrum from the heated region, because, under typical experimental conditions, the spectrum at low electron cyclotron harmonic frequencies is very narrow, $\Delta\Omega \ll 1$, which corresponds to $\kappa e^{-\Omega} \approx 1$.

The emission from nonequilibrium electrons with increased transverse energies manifests itself in a very rare situation when the resonance region is so wide that it is also necessary to take into account the anisotropy of the distribution of the resonant electrons. In this case, the shape of the spectral line is described by fairly complicated expressions involving the polarization of the emitted radiation. However, the final result remains the same: the spectral intensity decreases monotonically over the frequency interval $\Omega \in (0, \Delta\Omega)$. As an example, we present exact expressions for the maximum emission intensity, which is achieved at the frequency $\Omega = 0$:

$$T_r^{\pm} = \tau_0 T_e (1 + \Delta\Omega/2)(1 + \Delta\Omega^2/2 - e^{-\Delta\Omega})/\Delta\Omega \quad \text{for the X2 mode,} \tag{25}$$

$$T_r^{\pm} = \tau_0 T_e (1 + \Delta\Omega^2 - e^{-\Delta\Omega})/\Delta\Omega \quad \text{for the O1 mode.} \tag{26}$$

By comparing these expressions with the estimate $T_r^{\pm} = \kappa\tau_0 T_e$, which was obtained for an isotropic distribution function, we can determine the applicability conditions for expression (24): a deviation of less than 10% from the isotropic distribution corresponds to $\Delta\Omega < 1$ for an extraordinary wave and to $\Delta\Omega < 0.6$ for an ordinary wave.

3.2. Role of Coulomb Collisions

When Coulomb collisions between plasma particles are taken into account, the shape of the spectral line cannot be determined analytically. However, it is possible to estimate the characteristic maximum of the spectral intensity for a sufficiently narrow resonance plasma region. It has been shown above that, in a collisionless plasma, the steady-state distribution function is anisotropic only in a relatively small part of the resonance region; therefore in the case of a narrow resonance region, the emission spectra from a plasma can be calculated without taking into account anisotropy. Coulomb collisions lead to additional isotropization of the distribution function; moreover, this isotropization process can be intensified by elastic collisions between electrons and ions with large charge numbers ($Z_{\text{eff}} \gg 1$). Consequently, we can assume that the perturbed distribution function is isotropic. Under this assumption, the perturbed distribution function at each spatial point can be determined from a one-dimensional kinetic equation obtained by averaging operators (6) and (9) over the electron pitch angles. In the steady-state case, this equation implies that there are no particle fluxes in velocity space:

$$D_c(u)\left(\frac{\partial f}{\partial u} + 2uf\right) + D_{ql}^*(u)\frac{\partial f}{\partial u} = 0,$$
$$D_{ql}^* = \int_0^1 (1 - s^2) D_{ql}\, ds, \tag{27}$$

where D_{ql}^* is the quasilinear diffusion coefficient averaged over pitch angles. During the formation of a quasilinear plateau in a fairly narrow resonance energy range, the electron distribution function changes insignificantly and is close to a Maxwellian function f_M. In contrast, the derivative of the distribution function in the resonance region can change substantially: for $f \approx f_M$, Eq. (27) yields the estimate

$$\frac{\partial f}{\partial u} \approx \frac{1}{1 + D_{ql}^*(u)/D_c(u)} \frac{d f_M}{du}. \tag{28}$$

Accordingly, at frequencies close to the heating frequency, the plasma emissivity is close to its equilibrium value, whereas the absorptivity is lower than the equilibrium absorptivity μ_ω^0:

$$A_\omega \approx T_e \mu_\omega^0, \quad \mu_\omega \approx \frac{1}{1 + D_{ql}^*(u_{res})/D_c(u_{res})} \mu_\omega^0, \tag{29}$$

where $u_{res} = \sqrt{\zeta - \Omega}$. It is easy to see that, if $\Omega \in (0, \Delta\Omega)$, then, by virtue of the resonance condition, the frequency enters into relationships (29) only through the combination $\zeta - \Omega$, which redefines the spatial coordinate. Consequently, as in the equilibrium case, the frequency should drop out of the final formula for the ECE from an infinite plasma slab. Therefore, in the approach at hand, we cannot determine the shape of the spectral line perturbed in a narrow range $\Omega \in (0, \Delta\Omega)$ because, for an arbitrary frequency, the approximate equality $f \approx f_M$ and its consequences—relationships (29)—are valid to first order in $\Delta\Omega$. Thus, at $u = u_{res}$, the steady-state collisionless electron distribution function deviates from a Maxwellian function by the amount $(f_{st} - f_M)/f_M = 1 - \kappa\exp(-\Omega)$; accordingly, we can see that the error is minimum (equal to zero) at a certain fixed frequency $\Omega = \ln\kappa \approx \Delta\Omega/2$ in the vicinity of the center of the spectral line. It is clear that taking collisions into account cannot significantly change this estimate.

At a fixed spatial point, the quasilinear diffusion coefficient depends on the absorption of the heating

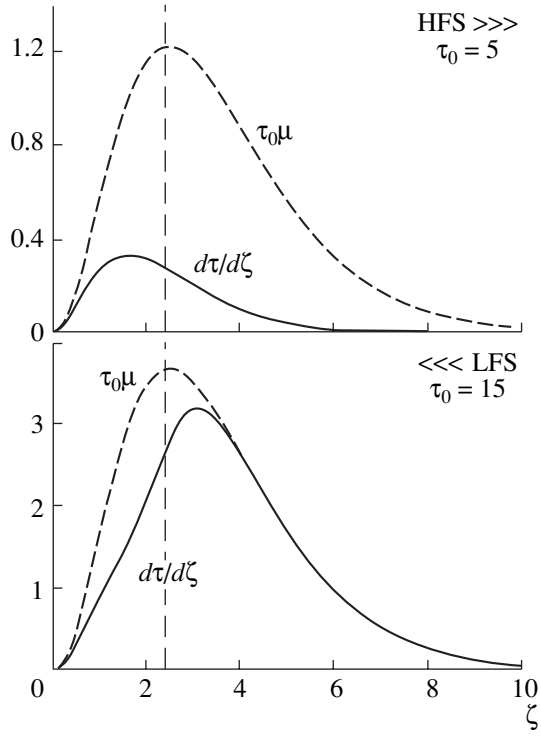

Fig. 1. Steady-state profiles of the plasma absorption coefficient (solid curve) and emissivity (dashed curve) calculated from the solutions to Eq. (30) for the same value of the power parameter ($Q = 0.5$) but for different optical thicknesses $\tau_0 = 5$ (on top) and $\tau_0 = 15$ (on bottom). The profiles are normalized so as to coincide for a Maxwellian plasma.

radiation in the previous regions along the beam. Consequently, in the self-consistent formulation of the problem, the expression for the absorptivity, i.e., the second of expressions (29), yields the following closed equation for the optical depth $\tau(\zeta)$:

$$\frac{d\tau}{d\zeta} = \frac{\tau_0\mu(\zeta)}{1 + Q\phi(\zeta)\exp(-\tau)}, \tag{30}$$

$$\mu(\zeta) = \frac{8}{15\sqrt{\pi}}\zeta^{5/2}e^{-\zeta},$$

$$\phi(\zeta) = \frac{8\sqrt{\pi}}{15}\zeta^{5/2}\left(\int_0^\zeta x^{1/2}e^{-x}dx\right)^{-1}. \tag{31}$$

Here, we have introduced the new parameter $Q = \nu_{ql}/\nu_c$ and the dimensionless functions $\phi(\zeta)$ and $\mu(\zeta)$, which characterize the profiles of the ratio D^*_{ql}/D_c and the absorptivity for a Maxwellian electron distribution. Formulas (31) present the functions ϕ and μ for the extraordinary wave at the second cyclotron harmonic. For the ordinary wave at the fundamental harmonic, the numerical coefficient in the expression for ϕ is equal to $2\sqrt{\pi}/15$, the remaining part of the expression being the same. The formulas were derived under the assumption that the spectrum form factor is equal to unity, $\Phi(\omega) = 1$ (because numerical calculations showed that the ECE spectra are weakly sensitive to the value of the form factor). Substituting the optical depth $\tau(\zeta)$ obtained from Eq. (30) into solutions (17), we can determine how emission from the plasma slab at frequencies close to the heating frequency depends on the parameters τ_0 and Q. For magnetic fusion experiments, the characteristic values of these parameters are $\tau_0 \approx 1$–10 and $Q \leq 1$.

A fairly detailed analysis of Eqs. (17) and (30) is presented in the Appendix. Here, we will outline the results obtained and give their physical interpretation. Depending on the value of the optical depth τ_0, two typical cases can be distinguished. For small values of the optical depth, the power deposition profile is broad and nonthermal radiation is emitted mainly by moderate-energy suprathermal electrons, for which the cyclotron interaction region is shifted in the HFS direction. In this region, the degradation of the absorption coefficient is most pronounced, which is accounted for by the monotonically increasing factor $\phi(\zeta)$ in formula (30). As a result, the total radiation emitted from resonant electrons in the HFS direction is absorbed less intensely than that emitted in the opposite direction (i.e., in the LFS direction). Consequently, the intensity of radiation emitted in the HFS direction is higher. This case is illustrated in the upper plot in Fig. 1, which shows the absorptivity and emissivity profiles corresponding to the solutions to Eq. (30). As the optical depth increases, the peak in the absorption profile shifts toward the starting point of the cyclotron interaction region. In this case, the main contribution to nonthermal radiation comes from the deformation of the electron distribution function in the range of low energies: the factor $e^{-\tau}$ in formula (30) indicates that the transparency region is displaced in the LFS direction, so that the emission in this direction becomes dominant (see the lower plot in Fig. 1). As the optical depth increases further, the region occupied by the microwave field narrows, the energy is deposited in progressively lower-energy electrons, and the role played by Coulomb collisions increases. This is why, as the parameter τ_0 tends to infinity, the level of the emission from the plasma in any optically thick direction approaches the thermal equilibrium level.

Figure 2 shows how the emission intensities in the LFS and HFS directions depend on the equilibrium optical depth at a certain fixed value of the power parameter Q. Note that the actual optical depth of a plasma slab with a perturbed electron distribution function differs from the equilibrium thickness τ_0. However, as is shown in the Appendix, this difference is small for a wide range of parameters of a collision-dominated plasma. For $\tau_0 \longrightarrow 0$, the curves in Fig. 2 asymptotically approach the level corresponding to a collisionless plasma, $T_r^{\pm} \approx \tau_0 T_e$. For $\tau_0 \longrightarrow \infty$, the radiation tem-

perature approaches the local electron temperature, $T_r^{\pm} \longrightarrow T_e$. There exists an optimum value of the parameter τ_0 at which the ECE spectrum in a given direction is perturbed to the greatest extent at a given heating intensity (in Fig. 2, the quantities corresponding to these maxima are marked by the tilde). Because of the asymmetry of the absorption profile (see the previous paragraph), the emission intensities in the LFS and HFS directions depend on the optical depth in different ways: the intensity of radiation emitted in the HFS direction (i.e., the radiation temperature T_r^+) has a larger maximum value, but decreases more sharply as the optical depth increases. In the Appendix, it is shown that the intensity of radiation emitted in the LFS direction approaches the thermal level according to a power law, while the law by which the intensity of radiation emitted in the opposite direction approaches the thermal level is exponential.

The maximum values of the effective radiation temperature, $\tilde{T}_r^{\pm}$, and the values of the optical depth at which these maxima are reached, $\tilde{\tau}_0^{\pm}$, depend linearly with a high degree of accuracy on the second parameter of the problem (the power parameter) over a wide range of its values, $0.1 < Q < \infty$:

$$\begin{aligned} \tilde{T}_r^- &= 1.2 + 3.2Q, \quad \tilde{\tau}_0^- = 2.8 + 6.4Q, \\ \tilde{T}_r^+ &= 1.5 + 5.5Q, \quad \tilde{\tau}_0^+ = 2.8 + 7.9Q. \end{aligned} \tag{32}$$

The coefficients in these expressions were obtained by numerically approximating the solution to Eqs. (17) and (30). An asymptotic analysis presented in the Appendix yields analogous results. Returning to the dimensional plasma parameters, it can be shown that, under the conditions that are most favorable for observations of the effect of quasilinear transparency window, the following relationship between the electron density and temperature should be satisfied:

$$N_e T_e = a + bT_e^{5/2}/(N_e T_e), \tag{33}$$

where the constants a and b are determined by the remaining parameters of the problem. From this relationship, it can be inferred that the optimum density, as a function of temperature, has a minimum, while the product $N_e T_e$ increases monotonically with increasing temperature. The example given in the next section shows that the optimum values of the density and temperature can be achieved in the parameter range characteristic of present-day magnetic fusion experiments.

Above, we have analyzed the limiting case $\Delta\Omega \longrightarrow 0$. To carry out calculations with allowance for the finite width $\Delta\Omega$ of the resonance region and to refine the shape of the perturbed spectral line, it is necessary to numerically solve quasilinear equations (5) and radiation transport equations (14). In the next section, we will present examples of such calculations for a tokamak with circular magnetic surfaces. The method by which the kinetic equation was solved numerically was described in our earlier paper [15].

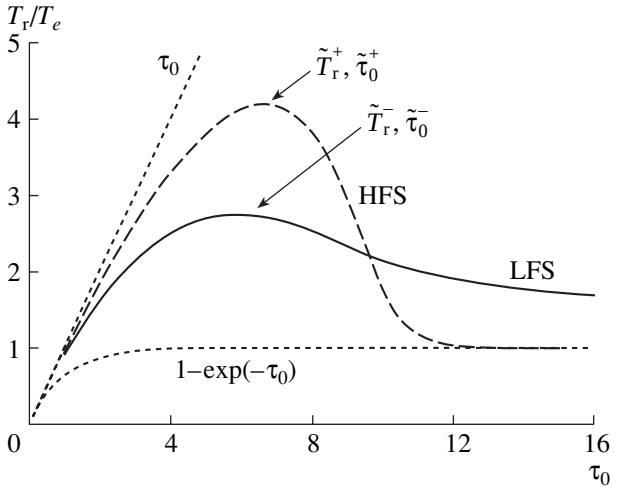

Fig. 2. ECE temperature normalized to the electron temperature as a function of equilibrium optical depth τ_0. The solid curve presents radiation emitted in the LFS direction, and the dashed curve corresponds to radiation emitted in the HFS direction. The curves are obtained from the solutions at $Q = 0.5$ and $\Delta\Omega \longrightarrow 0$.

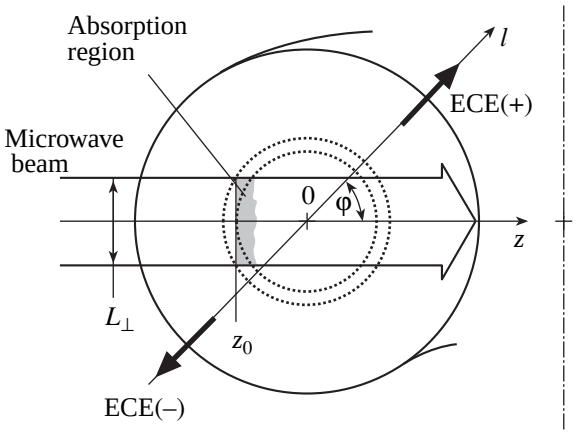

Fig. 3. Schematic view of ECR heating and ECE detecting geometry in a poloidal cross section of a toroidal device.

4. CALCULATION OF THE ECE FROM THE PLASMA OF A CIRCULAR CROSS-SECTION TOKAMAK

The transformation from toroidal geometry to the plane slab model described by Eqs. (5) can be considerably simplified by assuming that the magnetic surfaces in the poloidal cross section of the torus form a system of nested concentric circles (the circular tokamak model without the Shafranov shift). The poloidal

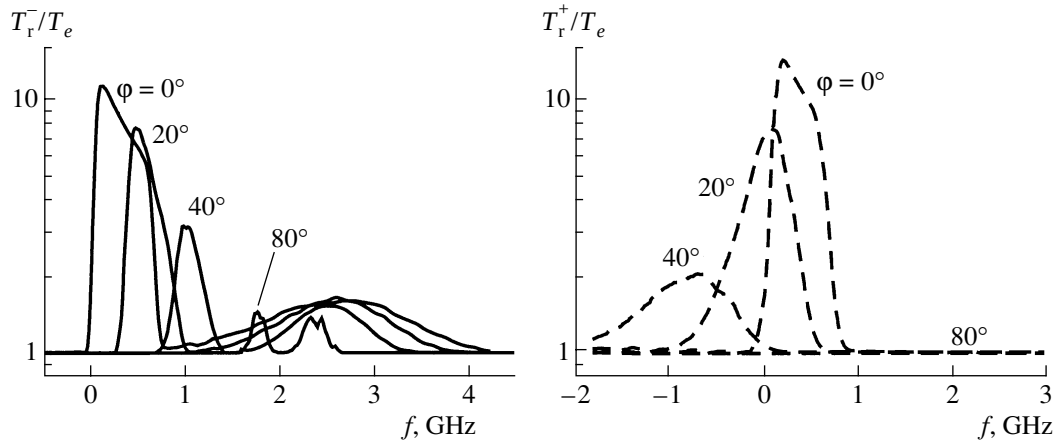

Fig. 4. Steady-state ECE spectra emitted in the LFS (on the left) and HFS (on the right) directions for the detection angles φ = 0, 20, 40, 60, and 80° with respect to the equatorial plane. The absorption region is displaced by $z_0 = -2.5$ cm. The values of the remaining plasma parameters correspond to the basic set of parameter values. The zero of frequency f corresponds to a 140-GHz microwave frequency.

cross section in the ECR heating region in such a device is illustrated schematically in Fig. 3. Let a heating microwave beam be injected into the tokamak plasma symmetrically about the equatorial plane and propagate along a straight line. Let the starting point of the cyclotron interaction region be shifted a distance z_0 from the center of the toroidal chamber along the major radius. Finally, let the basic set of parameter values be typical of experiments on ECR heating of a low-density plasma in the T-10 tokamak:

$$P_{\text{inp}} = 600 \text{ kW}, \quad T_e = 2 \text{ keV},$$

$$N_e = 2 \times 10^{13} \text{ cm}^{-3}, \quad Z_{\text{eff}} = 1,$$

$$\omega_0/2\pi = 140 \text{ GHz}, \quad L_H = R = 150 \text{ cm},$$

$$z_0 = -3.5 \text{ cm}, \quad L_\perp = 3.6 \text{ cm}.$$

The distance z_0 is chosen to satisfy the condition for the applicability of the plane plasma slab model: $|z_0| > \Delta z_{\text{abs}}, L_\perp/2$, where Δz_{abs} is the characteristic length of the absorption region. This length can be considered to be equivalent to the thickness of a plasma slab in which the optical depth increases from zero to unity. Thus, for a Maxwellian electron distribution, we have $\Delta z_{\text{abs}} \approx \beta_e^2 R/\tau_0^{2/7} \approx 0.6$ cm; for the parameter values adopted here, accounting for quasilinear effects increases the absorption length by no more than 15%. For simplicity, we ignore the density and temperature variations in the plasma, in which case the ECE spectra can only be calculated for frequencies very close to the heating frequency (or its harmonics). With the above parameter values, the parameters of a plane plasma slab are equal to $Q \approx 0.9$, $\tau_0 \approx 10$, and $\Delta\Omega \approx L_\perp^2/|4z_0 R\beta_e^2| \approx 0.7$.

The ECE spectra are calculated under the assumption that the emitted radiation propagates along the minor radius of the torus at a certain angle φ to the equatorial plane (Fig. 3); the angle φ = 0° corresponds to the case considered in the previous section. The symmetry of the magnetic surfaces with respect to the equatorial plane implies that $T_r^\pm(\varphi) = T_r^\pm(-\varphi)$. Consequently, it is sufficient to consider the angular range $0° \le \varphi \le 90°$.

Note that the perturbation of the emission spectrum and its variations over the cross section of a quasioptical beam can be of the same order of magnitude. Consequently, the correct calculation of the antenna response requires integration over the set of rays modeling the directional pattern of the receiving antenna. The results that will be presented below were obtained for radiation emitted along the central ray under the assumption that the effects of the finite width of the directional pattern of the receiving antenna do not influence the central ray and lead merely to a slight broadening of the wings of the spectra of the recorded signals [for model spectrum (24), this assumption can be proved rigorously].

Figure 4 illustrates the results of calculating the steady-state ECE spectra detected at different angles φ. The two characteristic peaks in the spectra of radiation emitted in the LFS direction (see the left plot in Fig. 4) result from the fact that, in the model under consideration, there are two diametrically opposite regions where the ray trajectories cross the magnetic surfaces at which the distribution function is perturbed. The spectra of radiation emitted from the absorption region at frequencies close to the heating frequency are seen to be perturbed to the largest extent (in the geometry chosen above, this corresponds to detection angles of $\varphi < 10°$). Moreover, the shape of the central peak coincides approximately with that given by expression (24); this indicates that Coulomb collisions do not lead to any

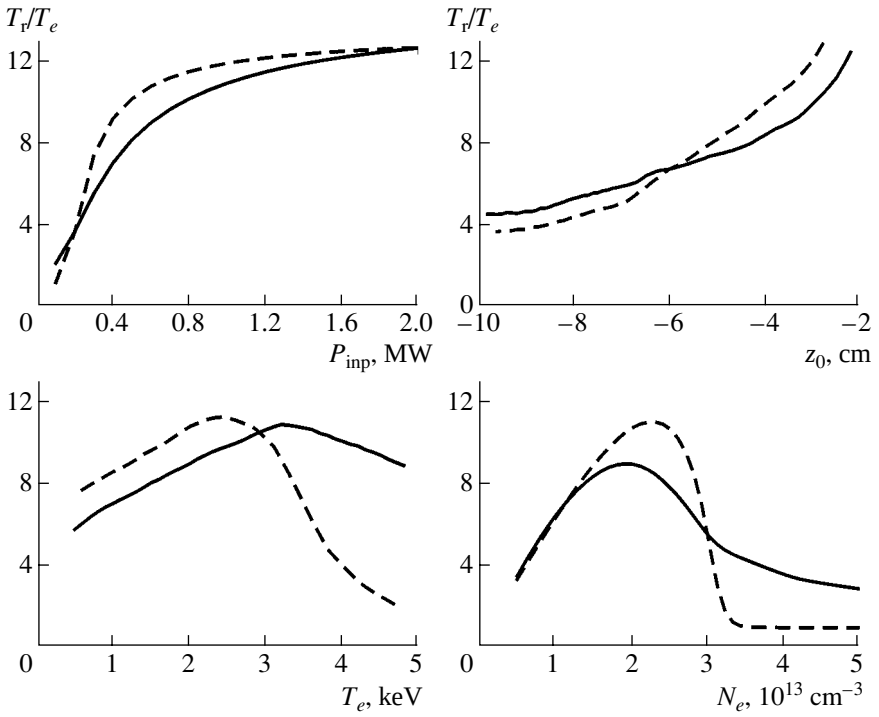

Fig. 5. Maximum spectral intensity of the ECE emitted along the equatorial plane ($\varphi = 0$) in the LFS (solid curves) and HFS (dashed curves) directions as a function of the incident microwave power, the position of the absorption region, the electron temperature, and the plasma density. The values of the parameters that are not varied correspond to the basic set of parameter values.

significant broadening of the spectra. We can see that the larger the detection angle, the larger the shift of the central peak along the frequency axis and the smaller the peak intensity. The peaks in the ECE spectra emitted in the LFS and HFS directions shift in opposite directions along the frequency axis. The additional peak that corresponds to emission from the diametrically opposite zone is barely noticeable and, for $z_0 < 0$, is seen to form only at the spectrum of radiation emitted in the LFS direction.

We now present the results of a parametric study of the perturbation of the ECE spectra at frequencies close to the heating frequency. Figure 5 shows how the maximum spectral intensity of the emitted radiation depends on the main experimental parameters: incident microwave power, position of the absorption region, electron temperature, and plasma density. Variations in these experimental parameters lead to the following variations in the dimensionless parameters of the problem:

variations in the input power give $Q \propto P_{inp}$;

variations in the displacement of the resonance region give $\Delta\Omega \propto z_o^{-1}$;

variations in the electron density give $\tau_0 \propto N_e$ and $Q \propto N_e^{-1}$; and

variations in the electron temperature give $\tau_0 \propto T_e$, $Q \propto T_e^{3/2}$, and $\Delta\Omega \propto T_e^{-1}$.

For the above parameters, quasilinear effects become pronounced when the incident microwave power is between 300 and 400 kW. For an incident power of about 1 MW, the emission intensity saturates and approaches a quasilinear level given by theoretical limit (25). Variations in the emission intensity with the position z_0 of the absorption region are associated solely with a change in the width of the resonance region because the optical depth and the power parameter Q both remain unchanged (the parameter z_0 enters into the expression for Q only through the combination $z_0\Delta\omega \approx$ const). Since the optical depth of the plasma slab is proportional to the product N_eT_e, the profiles of the ECE intensity as functions of temperature and density follow the theoretical profiles $T_r^{\pm}(\tau_0)$, which are plotted in Fig. 2. Up to a certain critical value of the temperature or density, the ECE intensity increases monotonically, in which case the emission intensity in the HFS direction is somewhat larger than that in the LFS direction. However, for higher temperatures or densities, the intensity of emission in the HFS direction falls off sharply. Note that the above basic set of parameter values corresponds to the optical depth for which the emission in the HFS direction dominates. The dependence on the plasma density is stronger than that

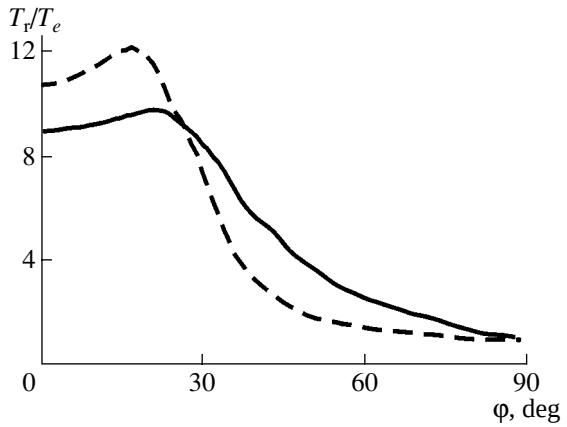

Fig. 6. Maximum spectral intensity of the ECE emitted in the LFS (solid curve) and HFS (dashed curve) directions as a function of the angle at which the radiation is detected. The values of the plasma parameters correspond to the basic set of parameter values.

on the electron temperature because the power parameter decreases with increasing density and increases with increasing temperature, so that the effect of the increase in optical depth is partially canceled.

Figure 6 shows how the spectral intensity depends on the angle φ at which radiation is detected. The change in the detection angle does not change the three parameters Q, τ_0, and $\Delta\Omega$ but changes the resonance condition for the emitting electrons. In terms of dimensionless variables, resonance condition (18) can be represented in the form

$$\varsigma\cos\varphi - \Omega - u^2 = \frac{2z_0}{\beta_e^2 L_H}(1-\cos\varphi) = \text{const}. \quad (34)$$

It is clear that, since the resonance conditions for the heating radiation and the detected emission are different, quasilinear effects are suppressed when $\cos\varphi$ differs considerably from unity. We can show that, when $\cos\varphi$ is close to unity, the main effect is the renormalization of the optical depth, $\tau_0^* = \tau_0/|\cos\varphi|$, which takes into account the increase in the scale on which the magnetic field varies along an obliquely passing ray. In this case, the dependence of the ECE intensity on the renormalized optical depth τ_0^* is qualitatively similar in shape to the curves plotted in Fig. 2. If the value of τ_0^* is at the rising slopes of these curves, then the increase in the optical depth with increasing difference between $\cos\varphi$ and unity compensates for the slipping of the emitting electrons out of resonance with the heating radiation. This effect explains why the emission somewhat intensifies at small values of the angle φ (which can be seen in Fig. 6) and why there is a fairly wide range of values of the angle φ ($\varphi < 40°$) over which quasilinear effects are not suppressed.

Above, we considered the case $z_0 < 0$, in which the absorption region is displaced from the center of the toroidal chamber toward the stronger magnetic field (the case of plasma heating in the outer part of the torus). In the case of plasma heating at the same magnetic surfaces but in the inner (rather than outer) part of the torus (the parameter z_0 changes sign), the central frequencies of the two perturbed lines in the ECE spectrum interchange places, the intensity of the lines and their shapes being unchanged.

Note that radiation from a toroidal plasma possesses the same symmetry properties as the set of magnetic surfaces in a tokamak. Consequently, the ECE receiving system can be shifted in the toroidal direction with respect to the power deposition region (in a tokamak, this shift can be arbitrary while, in a stellarator, the toroidal angle corresponding to this shift should be a multiple of the period of the toroidal magnetic field). It is expected that the most perturbed ECE spectra are those that are emitted at frequencies close to the heating frequency and that come from the power deposition region and the equivalent regions displaced in the toroidal direction. By detecting radiation emitted from the latter regions, it is possible to protect the diagnostic equipment from direct illumination by the heating radiation. If, in this case, the spectral perturbations at frequencies close to the heating frequency are difficult to record because of the presence of intense background radiation at the frequency of the heating radiation, then the plasma can be diagnosed by recording less intense perturbations of the spectra of the ECE from the regions with the shifted electron gyrofrequency. It is clear that, on the one hand, quasilinear effects associated with emissions from such regions manifest themselves at frequencies differing from the heating frequency and, on the other hand, they are suppressed because of the disruption of spatial synchronization between the resonance conditions for the heating radiation and the detected ECE.

To conclude this section, we note that ECE from the plasma is rather sensitive to the quasilinear deformation of the electron distribution function: in the examples considered above, the extent to which the absorption region is modified and the total deposited microwave power is degraded is no larger than 10–15% in comparison with those in an equilibrium plasma. In this case, however, the intensity of perturbations of the ECE spectra is several times or even several tens of times higher than the thermal level.

5. CONCLUSIONS

In this paper, we have considered the perturbations of the ECE and absorption spectra in a toroidal plasma due to the quasilinear modification of the electron distribution function under ECR heating conditions when the heating radiation is launched from the low-field side. This modification shows up as a slight flattening

of the distribution function of the resonant electrons over the velocity component transverse to the magnetic field, in which case the resonant electrons are not accelerated to any significant extent. The distribution function deviates from an equilibrium function only slightly, because the interaction is localized in the thermal energy range in which quasilinear effects are suppressed by Coulomb collisions.

We have shown that, when the plasma column is optically thick to the recorded radiation, the ECE spectrum at frequencies close the heating frequency is highly sensitive to perturbations of the distribution function. For a model situation in which the emissivity profile coincides with the thermal emissivity profile and there is no absorption at a certain frequency, we can obtain the following estimate for the maximum possible amount by which the radiation intensity can exceed the thermal level: $T_r^{\pm} = \tau_0 T_e \gg T_e$ for $\tau_0 \gg 1$. However, the total spontaneous emission from the plasma slab is restricted by reabsorption within the slab. Thus, for an equilibrium slab, we have $T_r^{\pm} = T_e(1 - e^{-\tau_0}) \leq T_e$, because, by Kirchhoff's law, the absorption intensity profile is similar to the emissivity profile. This clearly indicates that, for $\tau_0 \gg 1$, even a small imbalance between the emissivity and absorptivity of a unit plasma volume can substantially change the total emission from the slab; moreover, the larger the optical depth of the plasma, the larger the possible change. On the other hand, the larger the plasma optical depth with respect to the heating beam, the smaller the quasilinear modifications of the radiation transport coefficients, because the energy is transferred to electrons with increasingly lower energies. Nevertheless, our analysis has shown that the perturbation of the ECE spectra is most pronounced in an optically thick plasma slab with $\tau_0 \approx 3$–10.

The perturbations of the ECE spectrum due to modification of the thermal part of the electron distribution function look like one or two spectral spots corresponding to the intersections of the beam with the magnetic surfaces at which the plasma is heated. In principle, such perturbations can be detected by receiving equipment with a sufficiently high spectral resolution in a wide variety of the operating modes of present-day controlled fusion devices with ECR plasma heating.

ACKNOWLEDGMENTS

We are grateful to M.D. Tokman and H. Maassberg for their interest in this study. This work was supported in part by the Russian Foundation for Basic Research, project no 03-02-17466.

APPENDIX

ELECTRON CYCLOTRON EMISSION FROM A PLASMA SLAB WITH ALLOWANCE FOR COULOMB COLLISIONS

Here, we analyze solutions (17) to the radiation transport equation with coefficients (29) by taking into account Eqs. (30) and (31) for the self-consistent optical depth of the plasma slab in different limiting cases.

Asymptotics at Large Q Values

For $Q \longrightarrow \infty$, we can ignore unity in the denominator of expression (30) for the optical depth, in which case the equation obtained has an elementary solution:

$$\tau(\zeta) = -\ln\left(1 - \frac{\tau_0}{Q}\psi(\zeta)\right), \quad \psi(\zeta) = \int_0^{\zeta} \frac{\mu(x)}{\phi(x)} dx. \quad (35)$$

Substituting this solution into Eqs. (17), we find the total intensity of emission from the plasma slab:

$$T_r^-/T_e = \tau_0\left(1 - \frac{\alpha_1\tau_0}{Q}\right), \quad \alpha_1 = \int_0^{\infty} \mu(\zeta)\psi(\zeta)d\zeta; \quad (36)$$

$$T_r^+/T_e = \int_0^{\infty} \tau_0\mu(\zeta)\frac{Q - \tau_0\psi_\infty}{Q - \tau_0\psi(\zeta)}d\zeta,$$
$$\psi_\infty = \psi(+\infty) = \frac{1}{4\sqrt{2\pi}}. \quad (37)$$

Each of these expressions has a maximum with respect to the variable τ_0. At the extreme point, the following equalities are satisfied:

$$\tilde{T}_r^-/T_e = \frac{1}{4\alpha_1}Q, \quad \tilde{\tau}_0^- = \frac{1}{2\alpha_1}Q,$$
$$\tilde{\tau}(\infty) = -\ln\left(1 - \frac{1}{2\alpha_1}\psi_\infty\right); \quad (38)$$

$$\tilde{T}_r^+/T_e = \int_0^{\infty} \alpha_2\mu(\zeta)\frac{1 - \alpha_2\psi_\infty}{1 - \alpha_2\psi(\zeta)}d\zeta Q,$$
$$\tilde{\tau}_0^+ = \alpha_2 Q, \quad \tilde{\tau}(\infty) = -\ln(1 - \alpha_2\psi_\infty), \quad (39)$$

where the constant α_2 is the only nonzero root of the equation

$$\int_0^{\infty} \mu(\zeta)\frac{1 - 2\alpha_2\psi_\infty + \alpha_2^2\psi_\infty\psi(\zeta)}{(1 - \alpha_2\psi(\zeta))^2}d\zeta = 0. \quad (40)$$

The tilde in these equalities indicates the quantities at the extreme point.

Inserting numerical values $\alpha_1 \approx 0.08$ and $\alpha_2 \approx 7.72$ into equalities (38) and (39), we arrive at the following

expressions, which agree well with those obtained from general formula (30):

$$\tilde{T}_r^-/T_e \approx 3.1Q, \quad \tilde{\tau}_0^- \approx 6.2Q, \quad \tilde{\tau}(\infty) \approx 1.0; \qquad (41)$$

$$\tilde{T}_r^+/T_e \approx 5.4Q, \quad \tilde{\tau}_0^+ \approx 7.7Q, \quad \tilde{\tau}(\infty) \approx 1.5. \qquad (42)$$

It should be stressed that these expressions also remain valid in the range $Q \sim 1$, in which all the functions are essentially linear [see expressions (32)]. The approximation considered above is valid in the range $\tau_0 \lesssim \tilde{\tau}_0^{\pm}$ and fails to hold for $\tau_0 \longrightarrow \infty$, when the emission intensity approaches the thermal level.

Asymptotics at $Q \longrightarrow 0$ and at $\tau_0 \longrightarrow \infty$ for a Fixed Q Value

For $Q \longrightarrow 0$, we can develop a perturbation method under the assumption that the optical depth is nearly equilibrium. We set

$$\tau(\zeta) = \tau_M(\zeta) + \Delta\tau(\zeta), \quad \tau_M(\zeta) = \tau_0 \int_0^\zeta \mu(x)dx. \quad (43)$$

Regarding $\Delta\tau$ as a small perturbation, we obtain from Eq. (30) the expression

$$\Delta\tau(\zeta) \approx \tau_0 Q \int_0^\tau \mu(x)\phi(x)e^{-\tau_M(x)}dx. \qquad (44)$$

We expand solutions (17) in powers of $\Delta\tau$ to arrive at the following relationship for radiation emitted in the LFS direction:

$$\begin{aligned} T_r^-/T_e &= -\int_0^\infty e^{-\Delta\tau}\frac{d}{d\zeta}e^{-\tau_M}d\zeta \\ &\approx 1 - e^{-\tau_0} + \tau_0 Q\int_0^\infty \mu\phi e^{-2\tau_M}d\zeta. \end{aligned} \qquad (45)$$

For $\tau_0 \le 10$, the last integral can be replaced with good accuracy by an exponential. To do this, we factor the slowly varying function out of the integral sign and obtain

$$\begin{aligned} &\int_0^\infty \mu\phi e^{-2\tau_M(\zeta)}d\zeta \approx e^{-2\tau_M(\zeta_0)}\int_0^\infty \mu\phi d\zeta \approx \alpha_3 e^{-\alpha_4\tau_0}, \\ &\alpha_3 \approx 40, \quad \alpha_4 \approx 1.6, \end{aligned} \qquad (46)$$

where $\zeta_0 \approx 4.9$ is the value at which the function $\mu\phi$ is maximum. Analogous calculations for radiation emitted in the direction in which the magnetic field increases yield a simpler relationship,

$$T_r^+/T_e \approx 1 - e^{-\tau_0} + \alpha_3\tau_0 e^{-\tau_0}Q. \qquad (47)$$

Formulas (44) and (45) are also valid at $\tau_0 \longrightarrow \infty$ for a fixed value of the parameter Q because, in this limit, the perturbations of the optical depth and radiation spectra are, as before, small. In calculating the asymptotic behavior of the last integral in relationship (45) at $\tau_0 \longrightarrow \infty$, we can see that the main contribution to the integral comes from the point $\zeta = 0$, in the vicinity of which the functions $\mu\phi$ and τ_M can be replaced with the corresponding power series expansions:

$$\begin{aligned} &\int_0^\infty \mu\phi e^{-2\tau_M(\zeta)}d\zeta \approx \int_0^\infty \frac{32}{75}\zeta^{7/2}\exp\left(-\frac{32\tau_0}{105\sqrt{\pi}}\zeta^{7/2}\right)d\zeta \approx \alpha_5\tau_0^{-9/7}, \\ &\alpha_5 \approx 1.1. \end{aligned} \qquad (48)$$

Hence, at $\tau_0 \longrightarrow \infty$, the perturbations of the total optical depth and radiation emitted in the LFS direction both fall off according to a power law:

$$\begin{aligned} T_r^-/T_e &\approx 1 - e^{-\tau_0} + Q/\tau_0^{2/7}, \\ \Delta\tau(\infty) &\approx -2.1Q/(\tau_0/2)^{2/7}. \end{aligned} \qquad (49)$$

In this limit, the perturbation of radiation emitted in the HFS direction is also described by formula (47), which implies that the radiation intensity approaches the thermal level according to an exponential law. The above expressions remain valid only in the range $|\Delta\tau| \ll \tau_0$ or $Q \ll (\tau_0/2)^{9/7}$.

REFERENCES

1. M. Lontano, R. Pozzoli, and E. V. Suvorov, Nuovo Cim. Soc. Ital. Fis. B **63**, 529 (1981).
2. E. V. Suvorov and A. A. Fraiman, in *Proceedings of the All-Russian Meeting on High-Frequency Plasma Heating, Gor'kii, 1982*, Ed. A. G. Litvak (Inst. Prikl. Fiz., Akad. Nauk SSSR, Gor'kii, 1983), p. 371.
3. G. Giruzzi, Nucl. Fusion **28**, 1413 (1988).
4. V. Krivenski, in *Proceedings of the 25th EPS Conference on Controlled Fusion and Plasma Physics, Praha, 1998*; ECA **22C**, 1316 (1998); V. Krivenski, in *Proceedings of the 26th EPS Conference on Controlled Fusion and Plasma Physics, Maastricht, 1999*; ECA **23J**, 385 (1999).
5. O. Tudisco, E. de la Luna, V. Krivenski, *et al.*, in *Proceedings of the 26th EPS Conference on Controlled Fusion and Plasma Physics, Maastricht, 1999*; ECA **23J**, 101 (1999).
6. O. Tudisco, G. Bracco, P. Buratti, *et al.*, in *Proceedings of the 28th EPS Conference on Controlled Fusion and Plasma Physics, Funchal, 2001*; ECA **25A**, 1221 (2001).
7. A. V. Timofeev and M. D. Tokman, Fiz. Plazmy **20**, 376 (1994) [Plasma Phys. Rep. **20**, 336 (1994)].
8. R. W. Harvey and M. G. McCoy, Report No. GA-A20978 (General Atomics, San Diego, CA, 1992).
9. A. Yu. Kuyanov, A. A. Skovoroda, and M. D. Tokman, Eur. Phys. Soc. **16C**, Part 1, 365 (1995).

10. E. V. Suvorov and M. D. Tokman, Plasma Phys. **25**, 723 (1983).
11. V. V. Alikaev, A. G. Litvak, E. V. Suvorov, and A. A. Fraiman, in *Proceedings of the All-Russian Meeting on High-Frequency Plasma Heating, Gor'kii, 1982*, Ed. by A. G. Litvak (Inst. Prikl. Fiz., Akad. Nauk SSSR, 1983), p. 6.
12. Yu. N. Dnestrovskii and D. P. Kostomarov, *Numerical Simulations of Plasmas* (Nauka, Moscow, 1982; Springer-Verlag, New York, 1986).
13. E. V. Suvorov and A. G. Shalashov, Fiz. Plazmy **28**, 51 (2001) [Plasma Phys. Rep. **28**, 46 (2001)].
14. C. F. F. Karney, Comp. Phys. Rep. **4**, 183 (1986).
15. E. V. Suvorov and A. G. Shalashov, Preprint No. 462 (Inst. Prikl. Fiz., Nizhni Novgorod, 1998).
16. A. I. Akhiezer, I. A. Akhiezer, R. V. Polovin, *et al.*, *Plasma Electrodynamics* (Nauka, Moscow, 1974; Pergamon, Oxford, 1975).
17. V. V. Zheleznyakov, *Electromagnetic Waves in Space Plasma* (Nauka, Moscow, 1977).

Translated by I.A. Kalabalyk

Plasma Physics Reports, Vol. 29, No. 10, 2003, pp. 860–866. Translated from Fizika Plazmy, Vol. 29, No. 10, 2003, pp. 926–932.

PLASMA OSCILLATIONS AND WAVES

Excitation of Upper Hybrid Cones in Magnetoactive Plasma

A. V. Kostrov, G. A. Luchinin, and G. V. Permitin

Institute of Applied Physics, Russian Academy of Sciences, ul. Ul'yanova 46, Nizhni Novgorod, 603600 Russia

Received November 13, 2002

Abstract—Results are presented from laboratory studies of the radiation transport from a transmitting to a receiving antenna in a cold magnetoactive plasma in the upper hybrid frequency range. In the low-frequency part of this range, sharp maxima of the transmission coefficient are recorded in the resonant directions. In the high-frequency part, a beamed radiation along the external magnetic field is observed. An analysis of the experiments shows that the Q factor of the angular resonances is primarily limited by the phase effects caused by weak spatial dispersion. *© 2003 MAIK "Nauka/Interperiodica".*

1. INTRODUCTION

It is well known that the propagation of electromagnetic waves in a magnetoactive plasma is characterized by not only frequency resonances, but also directional (or angular) resonances. In certain ranges of the parameters, the refractive index n_m of a dispersion branch can sharply increase as the angle θ between the wave vector $\mathbf{k}$ and the external magnetic field $\mathbf{B}_0$ approaches the resonant value θ_c. When dissipation is neglected, the refractive index in the angular resonance tends to infinity: $n_m(\theta \longrightarrow \theta_c) \longrightarrow \infty$ [1, 2]. It should be noted that, in this case, the components of the permittivity tensor $\varepsilon_{ij}(\omega)$ have no singularities.

This paper is devoted to an experimental study of the radiation transport from a transmitting to a receiving antenna in the upper hybrid (UH) range of parameters, in which the extraordinary mode has an angular resonance. The radiation frequency ω in this range is higher than both the electron plasma and electron cyclotron frequencies (ω_p and ω_H, respectively), but is lower than the upper hybrid resonance frequency

$$\omega_p, \omega_H < \omega < \omega_{UH} = \sqrt{\omega_p^2 + \omega_H^2}.$$

In the plane of dimensionless parameters $u = \omega_H^2/\omega^2$ and $v = \omega_p^2/\omega^2$, the UH range occupies a triangular domain (see Fig. 1) that is bounded from above by the plasma resonance ($v = 1$), from the right by the cyclotron resonance ($u = 1$), and from below by the upper hybrid resonance ($u + v = 1$). The electron and ion temperatures (T_e and T_i) in the experimental device were below 1 eV, and the characteristic parameter of spatial dispersion (the ratio of the electron thermal energy to the electron rest energy) was: $\beta^2 = T_e/m_e c^2 < 10^{-6}$. Such a plasma can be regarded as cold, and its dispersion properties are described by the following equation for the refractive index:

$$An^4 + Bn^2 + C = 0,$$

where

$$\begin{aligned} A &= (1-u)(1-v)\cos^2\theta - (u+v-1)\sin^2\theta, \\ B &= (u+v-1)(1-v)\cos^2\theta \\ &\quad + [v(1-v) + u + v - 1]\sin^2\theta, \\ C &= -(1-v)[v(1-v) + u + v - 1]. \end{aligned} \tag{1.1}$$

If the factor by the highest power of n in Eq. (1.1) tends to zero, then the refractive index of one of the normal modes (for the UH range, this is the extraordinary mode) tends to infinity ($A \longrightarrow 0 \Rightarrow n \longrightarrow \infty$). The value of the angle θ_c at which this resonance occurs is determined from the relationship

$$\tan^2\theta_c = \frac{(1-u)(1-v)}{u+v-1}. \tag{1.2}$$

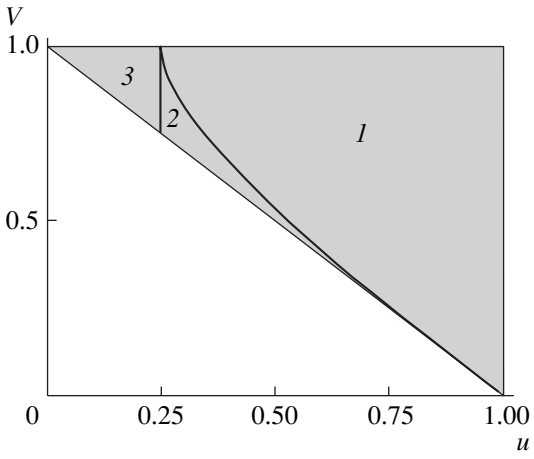

Fig. 1. Upper hybrid range.

1063-780X/03/2910-0860$24.00 © 2003 MAIK "Nauka/Interperiodica"

The sections of the wave-vector surfaces of the ordinary (O) and extraordinary (X) modes are shown in Fig. 2. The closed surface for the O mode has no singularities in the UH range (in what follows, we do not discuss the dispersion properties of these waves).

As the angle θ between the wave vector $\mathbf{k}$ of a plane extraordinary wave and the magnetic field $\mathbf{B}_0$ tends to its resonant value θ_c (or to $\pi - \theta_c$), the group velocity v_g vanishes, whereas the angle Ψ between the unit vector $\mathbf{v}_g/v_g$ and $\mathbf{B}_0$ tends to $\theta_c + \pi/2$ (or to $\pi/2 - \theta_c$). The cone produced by the generatrix inclined at the angle $\Psi_{res} = \pi/2 - \theta_c$ to the magnetic field $\mathbf{B}_0$ is usually called the resonant cone. A plane wave propagating in the resonant direction degenerates to electrostatic oscillations ($\mathbf{E} \longrightarrow E\mathbf{k}/k$, $\mathbf{B} \longrightarrow 0$) that do not transfer energy. However, this is only true for plane waves.

The Green's function (i.e., the radiation field) of an elementary dipole $\mathbf{p}^e \exp(i\omega t)\delta(\mathbf{r})$ (see Fig. 3) has a nonintegrable singularity on the resonant cone [3, 4]. At angles close to the resonant one ($\Delta\Psi = \Psi - \Psi_{res} \ll 1$), the fields E and B, as well as the energy flux density S, depend on the detuning $\Delta\Psi$ as follows:

$$E \sim (\Delta\Psi)^{-3/2}/r, \quad B \sim (\Delta\Psi)^{-1}/r,$$
$$S \sim (\Delta\Psi)^{-5/2}/r^2.$$

Of course, actual currents cannot radiate an infinite power. This means that, in an ideal cold magnetoactive plasma, it is impossible to excite elementary extraneous currents with a finite amplitude in an infinitely small spatial region. On the other hand, the radiation field of an elementary dipole with an infinitely small amplitude is finite on the resonant-cone surface and vanishes outside of it. Such a dipole can be thought of as a supergain antenna with an infinite radiation resistance ($R_{rad} \longrightarrow \infty$).

In real physical systems, there are always factors smoothing out all types of resonances and making their Q factors finite. By analogy to usual frequency resonances, the Q factor of the angular resonance may be defined as the ratio of the total solid angle to the solid angle $\Delta\Omega$ into which one-half of the power is emitted: $Q = 4\pi/\Delta\Omega$. The angular resonance can be smoothing out due to collisional and collisionless energy dissipation, spatial dispersion, finite emitter size, plasma nonuniformity and unsteadiness, thermal fluctuations, finite width of the radiation frequency spectrum, etc. If all these factors are small enough, then the Q factor of the resonance is high ($Q \gg 1$); i.e., the radiation emitted by a small-size source is concentrated within a small solid angle near the resonant (group) cone. Along all other directions, energy transfer is not impossible but is suppressed by the angular resonance. The 3D directivity diagram of a small-size electric dipole with a finite Q factor of the angular resonance is shown in Fig. 4.

These specific features of angular resonances make them attractive for various scientific and technological

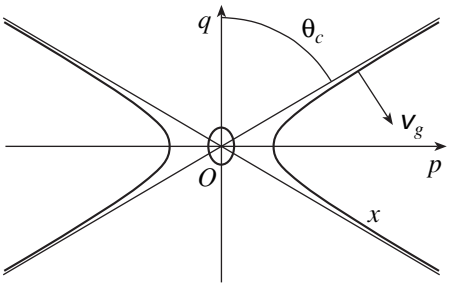

Fig. 2. Wave-vector surfaces ($p = k_\perp/k_0$, $q = k_\parallel/k_0$, $n = \sqrt{p^2 + q^2}$) for $u = 0.32$ and $v = 0.74$.

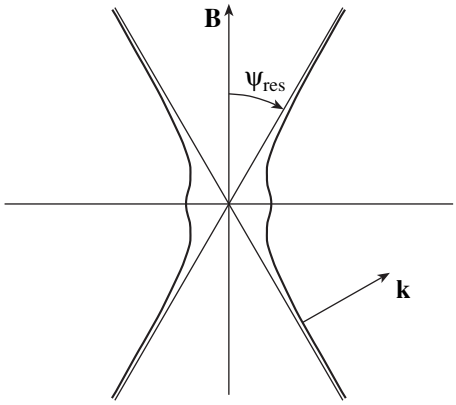

Fig. 3. Section of the directivity diagram of an infinitely small dipole orthogonal to the plane of the figure ($u = 0.32$, $v = 0.74$).

applications, in particular, for directional energy transfer and nonintrusive plasma diagnostics. In addition, waves propagating in the resonant directions have very low phase velocities and can be excited by fast charged-particle beams or, vice versa, can accelerate charged particles. Consequently, these resonances can play a part in the dynamics of plasma turbulence in the Earth's ionosphere and magnetosphere.

It is still very hard to calculate the parameters of actual antennas in a real plasma. Therefore, experimental studies are of especial importance. Among these, we note the space experiment reported in [5]. Two satellites bound with a rope rotated slowly around their common center of mass. When the satellites occurred on the same generatrix of the resonant cone, spikes of the transmission coefficient of electromagnetic radiation were observed. The angular structure of the resonant cones was studied in detail in laboratory experiments [6–9]; however, the excitation efficiency of these cones was very low.

The prime objective of the laboratory experiments described in this paper was to determine the range of

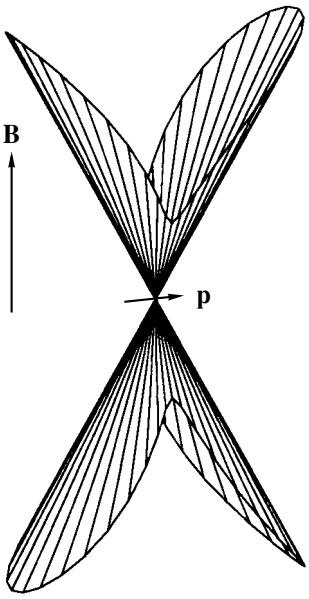

Fig. 4. Directivity diagram of an electric dipole in the case of a high (but finite) Q factor of the angular resonance.

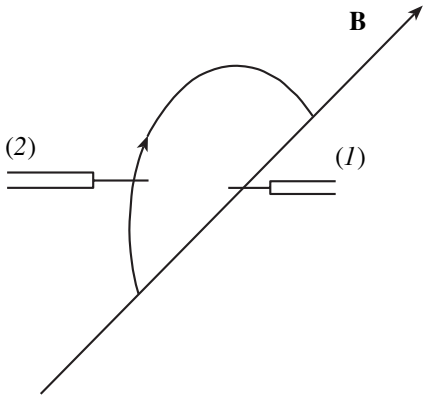

Fig. 5. Positions of the (*1*) transmitting and (*2*) receiving antennas.

plasma parameters within which the angular resonance can reliably be observed. The experiments showed that, in domain *1* in Fig. 1, the Q factor of the resonance is fairly high: the radiation field has a sharp maximum near the resonant cone, whereas it remains at a noise level in other directions. However, this domain does not cover the entire upper hybrid range shown in this figure. As the parameters u and v decrease (domain *2*), the transmission along the resonant directions is suppressed; however, a beamed radiation along the magnetic field is observed in this case. A theoretical analysis has revealed the dominant mechanism for suppressing resonance in our experiments, namely, the phase effects caused by weak spatial dispersion. This was not a priori evident because the characteristic parameter of spatial dispersion seemed to be negligibly small.

2. EXPERIMENTAL LAYOUT

The experiments were carried out in a chamber with the length $L = 1.2$ m and diameter $D = 1$ m. The pumping system maintained the residual gas pressure in the chamber at a level of $P_0 = 10^{-5}$ torr. The working gas was helium.

The magnetic field was produced by three coils with the diameters $D_L = 0.8$ m and lengths $L = 0.35$ m. The length of the region in which the magnetic field was almost uniform ($\Delta B/B_0 < 0.5\%$) was $l_0 = 1.2$ m, and the characteristic time scale on which the magnetic field varied was several hundred milliseconds. The experiments were carried out with the magnetic field in the range from 30 G to 1 kG.

The plasma was created by an inductive discharge (the generator frequency was 5 MHz, and the rf pulse duration was 2 ms). During the discharge, the plasma density reached a value of $\sim 10^{13}$ cm^{-3}. The maximum electron temperature was $T_e \sim 8$ eV. After the inductor was switched off, the electron temperature decreased to the ion temperature $T_i \sim 0.5$ eV in a time of 1.5 ms and then remained constant (the working time interval). The plasma density in the working interval decreased exponentially from 10^{11} to 10^6 cm^{-3}.

The radiation frequency varied in the range from 300 MHz to 3 GHz. The radiation was transmitted and received by two stub antennas with the lengths $l = 8$ mm and diameters $d = 0.2$ mm. The antennas stubs were oriented across the magnetic field and were parallel to each other. The transmitting antenna was immovable, and the receiving antenna was displaced (from shot to shot) in the plane perpendicular to the antenna stubs around a circle of radius 4.3 cm (see Fig. 5). Such an orientation of the antennas was chosen in order for the waves excited along the resonant direction to be as short as possible, the maximum wavenumber being $k_{\max} \sim 1/d$.

Therefore, the radiation directivity was examined within a rather wide range of the plasma parameters:

$$0.06 < u < 1, \quad 1 - u < v < 1, \quad 0.2 < k_{\max}\rho_c < 5,$$

where $\rho_c = V_{Te}/\omega_H$ is the electron gyroradius.

In each shot, we measured the time dependence of the intensity of the received signal $I(t)$ in the working time interval. The high reproducibility of the plasma parameters from shot to shot made it possible to recalculate these parameters to the dependences of the intensities on the angle θ_g between the group velocity of the excited waves and the external magnetic field $\mathbf{B}_0$ at fixed values of u and v.

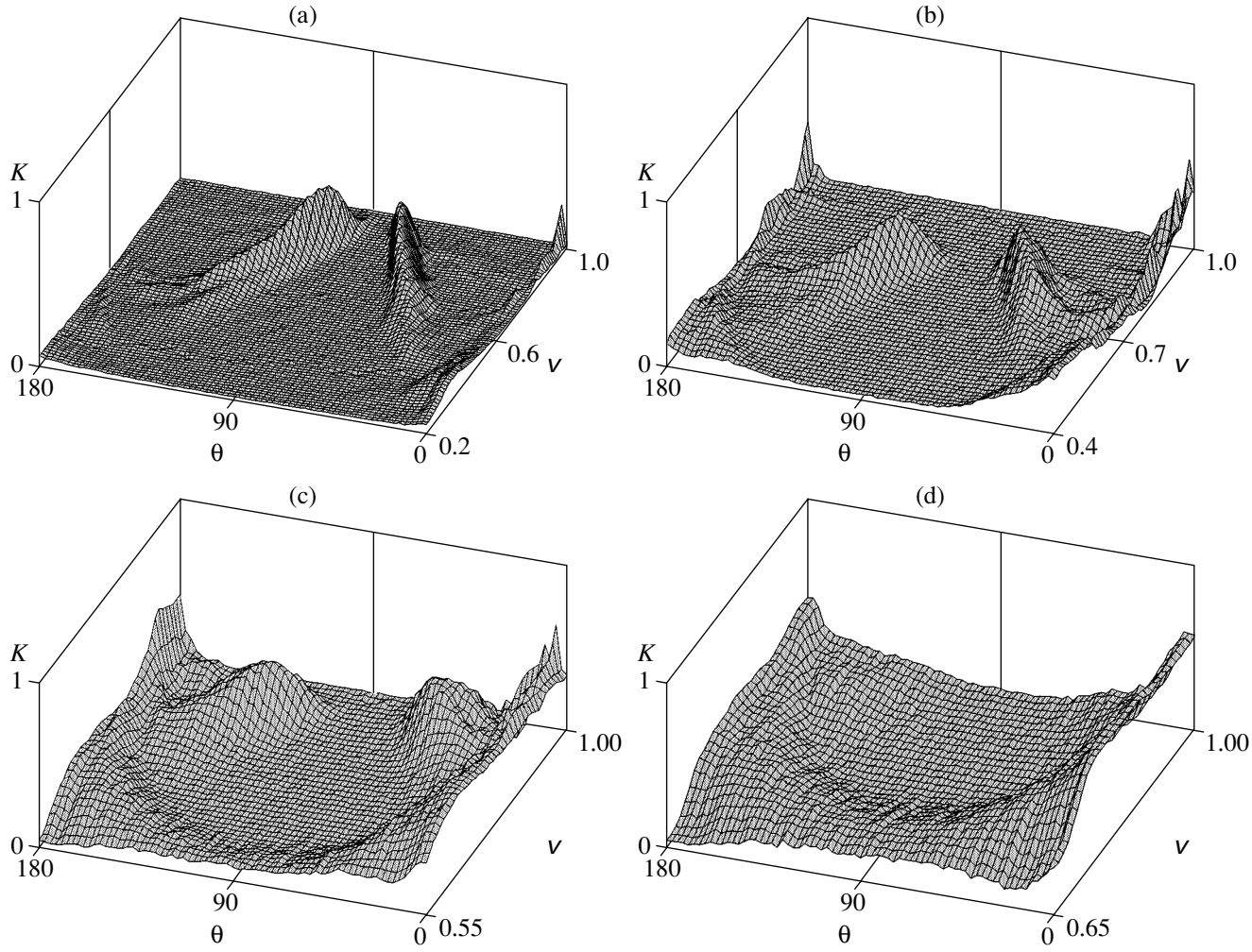

Fig. 6. Transmission coefficient K as a function of the propagation direction and plasma density for different magnetic fields: u = (a) 0.82, (b) 0.59, (c) 0.44, and (d) 0.35.

3. EXPERIMENTAL RESULTS

The experiments clearly demonstrated the excitation of waves propagating along the resonant directions. It was found, however, that these waves were excited only in region *1* in Fig. 1, rather than in the entire range of the parameters u, ν under study.

Figure 6 shows the coefficient of transmission K from the transmitting antenna to the receiving one as a function of the angle $\theta_g \in (0°, 180°)$ and the parameter $\nu \in (1 - u, 1)$ for different magnitudes of the external magnetic field (the parameter u). It can be seen that the waves propagating along the resonant cones are excited only at $u > 0.43$ and in the upper part of the range of the parameter ν (Figs. 6a–6c). In the lower parts of the ranges of the parameters u and ν, one can see another resonant response corresponding to the longitudinal propagation. Since beamed radiation along the magnetic field should not occur in a cold plasma, the experiments indicate the important role of thermal corrections to the dispersion relation, although these corrections would seem to be negligibly small (remember that the characteristic parameter of spatial dispersion in our experiments was on the order of 10^{-6}).

The characteristic domains in the plane of the parameters u and ν in the upper hybrid range are separated in Fig. 1 by the curve. Above the curve (domain *1*), the radiation is concentrated in the vicinity of the resonant cones. Below the curve (domain *2*), we observed beamed radiation along the magnetic field. No angular resonances were observed at frequencies above the second harmonic of the electron cyclotron frequency ($u < 0.25$; domain *3*).

We note that the design of both the receiving and transmitting antennas was not adapted to study the transmission of signals along the magnetic field and at small angles to it. In particular, no measures were taken to suppress currents flowing along the external screen of the coaxial cable. For instance, in Fig. 6a, one can

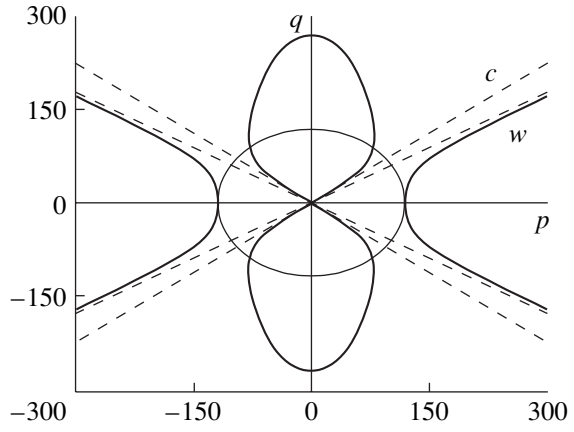

Fig. 7. Wave-vector surfaces in the coordinates $p = k_\perp/k_0$ as abscissa and $q = k_\parallel/k_0$ as ordinate in the case of $\theta_c < \theta_w$ ($u = 0.4$, $v = 0.7$, $T_e = 1$ eV).

see a spike of the transmission coefficient at $\theta \longrightarrow 0$, whereas such a spike is absent at $\theta \longrightarrow 180°$. Therefore, the results concerning the longitudinal propagation call for additional verification.

4. INTERPRETATION OF EXPERIMENTAL DATA

The experimentally observed beamed radiation along the external magnetic field (i.e., within the "shadow" region in the cold plasma approximation) indicates that the Q factor of the angular resonance is limited, first of all, by weak kinetic effects that deform the wave-vector surface. If energy dissipation is ignored, then the dispersion relation with allowance for weak thermal corrections takes the form [2]

$$\delta n^6 + An^4 + Bn^2 + C = 0,$$

where

$$\delta = -\beta^2 v\left\{3(1-u)\cos^4\theta + \frac{6-3u+u^2}{(1-u)^2}\sin^2\theta\cos^2\theta + \frac{3}{1-4u}\sin^4\theta\right\} \quad (4.1)$$

and $\beta^2 = T/m_e c^2$. Equation (4.1) is valid when

$$\frac{\beta^2 n^2 \cos^2\theta}{(1-m\sqrt{u})^2} \ll 1, \quad m = 1, 2, 3, \ldots \quad (4.2)$$

which implies that collective losses of the wave energy are small [2]. Outside the cyclotron resonances at the harmonics of the electron gyrofrequency ($u = 1$, $u = 0.25$), condition (4.2) practically coincides with the requirement $kr_D \ll 1$, where r_D is the Debye radius.

Dispersion relation (4.1) describes three branches: ordinary waves (the warm corrections to n_O are small, so that we will not discuss them); extraordinary waves, which are modified in the vicinity of the angular resonance; and short-wavelength plasma waves. The refractive index of the latter waves n_p outside the "cold" resonant cone ($|A| \sim 1$) is approximately equal to $n_p \approx \sqrt{-A/\delta}$. Obviously, condition (4.2) in this case is not satisfied, and plasma waves are damped at distances on the order of their wavelength. The situation is different in the vicinity of the resonance along the directions at which $A \longrightarrow 0$. In this case, we have $n_p \approx (-B/\delta)^{1/4}$; i.e., $\beta^2 n_p^2 \sim \beta \ll 1$. In the vicinity of the cold resonant cone, the extraordinary and plasma modes form a common weakly damped hybrid branch.

Even very small thermal corrections smooth out the cold resonant cone. However, according to dispersion relation (4.1), a new (warm) resonance cone ($n_p \longrightarrow \infty$) formally appears at $\theta \longrightarrow \theta_w$, where

$$\tan^2\theta_w = \frac{(6-3u+u^2)(4u-1)}{6(1-u)^2} + \sqrt{\left[\frac{(6-3u+u^2)(4u-1)}{6(1-u)^2}\right]^2 + (1-u)(4u-1)}. \quad (4.3)$$

For $u \longrightarrow 1$, we have $\theta_w \longrightarrow \pi/2$, whereas for $u \longrightarrow 0.25$, we have $\theta_w \longrightarrow 0$ (for the group-velocity cone angle, the reverse holds). For $u < 0.25$ (frequencies above the second harmonic of the electron gyrofrequency), the warm resonant cone is absent.

We note that, in our experiments, we did not observe any transmission along the warm resonant cone of plasma waves. This is not surprising, because collective energy losses at this cone are high. However, the topology of the wave-vector surfaces of the observed hybrid electromagnetic–plasma waves substantially depends on the ratio between the cone angles of the cold and warm resonant cones (θ_c and θ_w, respectively).

Figure 7 shows the wave-vector surfaces in the case $\theta_c < \theta_w$. The wave-vector surface of the hybrid branch (which is close to the extraordinary wave in the long-wavelength limit and to the plasma wave in the short-wavelength limit) is closed. The cold resonant cone of the extraordinary waves is transformed into a surface with an inflection line. The wave-vector surface of the plasma waves is open and tends asymptotically to a cone with the angle θ_w. However, this branch is not observed in experiments because of strong absorption due to the Landau damping. A circle depicted by the light line in Fig. 7 corresponds to $kr_D \sim 0.2$. Outside this circle, waves are damped at a distance on the order of their wavelength.

Figure 8 shows a large-scale plot of the weakly damping hybrid dispersion branch, whose wave-vector surface has an inflection line. On such surfaces, there

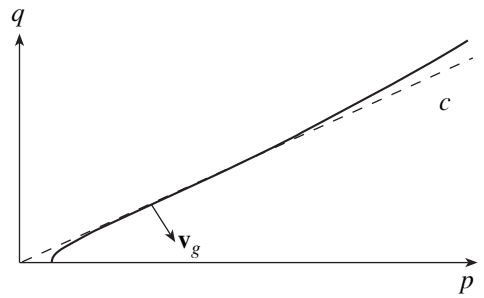

Fig. 8. Hybrid branch with an inflection line ($u = 0.72$, $v = 0.34$, $T_e = 1$ eV).

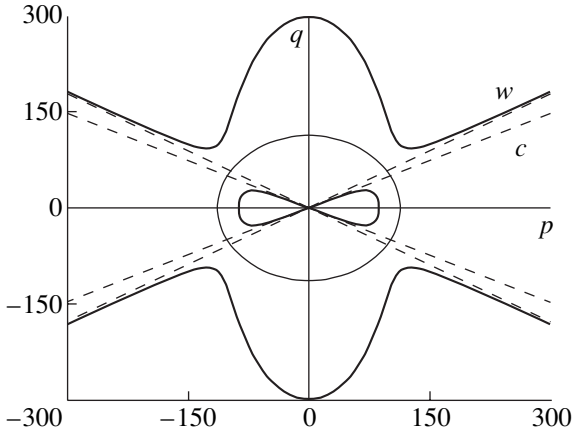

Fig. 9. Wave-vector surfaces in the case of $\theta_c < \theta_w$) ($u = 0.4$, $v = 0.65$, $T_e = 1$ eV).

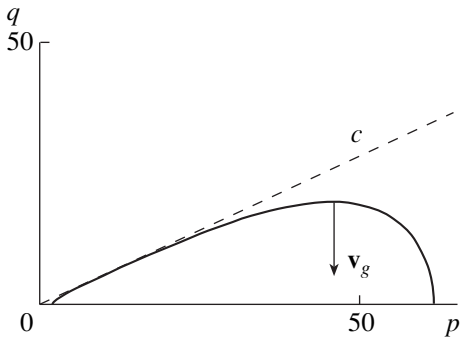

Fig. 10. Toroidal wave-vector surface ($u = 0.32$, $v = 0.74$).

are directions [4] (in our case, the direction making the angle Ψ_{res} with respect to the magnetic field) along which the radiation field falls off as $r^{-5/6}$. The field structure across the resonant cone is described by the Airy function (generally of the complex argument, if one takes absorption into account).

Hence, in the parameter range

$$u > 0.25, \quad v > \frac{1-u}{1-u\cos^2(\theta_w)},$$

(Fig. 1, domain *1*), kinetic processes do not destroy the resonant cones completely. For the radiation field of a short antenna, there is a singularity along the directions making the angle Ψ_{res} with respect to the magnetic field. However, this singularity is integrable; i.e., the power emitted along the resonant cone by an rf current with a given amplitude is finite. The solid angle within which this power is concentrated decreases with distance as $\Delta\Omega \sim 1/r^{1/3}$.

Figure 9 shows the wave-vector surfaces for the opposite case $\theta_c > \theta_w$ (Fig. 1, domain *2*).

The hybrid branch (which is shown on a large scale in Fig. 10) takes the form of a toroidal surface lying under the cold cone (without touching it). A characteristic feature of such surfaces is the presence of modes of internal conical refraction: the entire wave-vector cone corresponds to the same direction of the group velocity, specifically, the direction along the magnetic field. The amplitude of the conical-refraction mode decreases with distance from the source as $1/\sqrt{r}$, and the field structure across it is described by a Bessel function [4].

Another specific feature of the conical-refraction mode, which was (to all appearances) observed in our experiments, is that its group velocity is directed oppositely to the wave vector; i.e., this mode is a backward wave. Since this wave is slow, it can be easily excited by an electron beam whose velocity is somewhat higher than the wave phase velocity. Probably, a sort of such a backward-wave tube can operate in the Earth's ionosphere and magnetosphere. However, to assert this with certainty, it is necessary to perform calculations of the threshold currents and carry out the relevant laboratory experiments.

5. CONCLUSIONS

Our laboratory experiments have demonstrated the efficient transmission of radiation within a narrow solid angle in the vicinity of the resonant cone. However, the parameter range within which such transmission is observed turns out to be somewhat narrower than what follows from the analysis of the dispersion properties of a cold magnetized plasma. Weak spatial dispersion results in the suppression of the angular resonance at $\omega > 1.5\omega_H$. In this frequency range, however, the hybrid mode of the internal conical refraction, which propagates along the magnetic field, is efficiently excited. This mode is a slow backward wave and can be generated by an electron beam synchronous with it. The experimental results presented in this paper can be used to develop active satellite diagnostics of near-Earth plasma [10–12] and reveal the mechanisms for generation of high-frequency ionospheric noise and plasma turbulence.

REFERENCES

1. V. L. Ginzburg, *The Propagation of Electromagnetic Waves in Plasmas* (Nauka, Moscow, 1967; Pergamon Press, Oxford, 1970).
2. Gershman, L. M. Erukhimov, and Yu. Ya. Yashin, *Wave Phenomena in Ionospheric and Space Plasmas* (Nauka, Moscow, 1984).
3. V. F. Aleksin, V. N. Pakhomov, and E. N. Stepanov, Izv. Vyssh. Uchebn. Zaved., Radiofiz. **8**, 1135 (1965).
4. L. Felsen and N. Marcuvitz, *Radiation and Scattering of Waves* (Prentice-Hall, Englewood Cliffs, 1973; Mir, Moscow, 1978), Vol. 1, 2.
5. H. G. James, IEEE Trans. Antennas Propag. **48**, 1340 (2000).
6. T. Ohnuma and B. Lembége, Phys. Fluids **21**, 2339 (1978).
7. J. Thiel and B. Lembége, Phys. Fluids **25**, 551 (1982).
8. T. Ohnuma, T. Watanabe, and H. Sanuki, IEEE Trans. Plasma Sci. **PS-10**, 27 (1982).
9. Th. Pierre and G. Leclert, Plasma Phys. Controlled Fusion **31**, 371 (1989).
10. V. V. Vas'kov and A. V. Gurevich, Geomagn. Aeron. **23**, 544 (1983).
11. S. M. Grach and V. Yu. Trakhtengerts, Izv. Vyssh. Uchebn. Zaved., Radiofiz. **18**, 176 (1975).
12. *Modification of the Ionosphere by High-Power Radio Waves (Proceedings of International Symposium, Suzdal', 1986)* (IZMIRAN, Moscow, 1986).

Translated by N.F. Larionova

Plasma Physics Reports, Vol. 29, No. 10, 2003, pp. 867–873. Translated from Fizika Plazmy, Vol. 29, No. 10, 2003, pp. 933–938.

PLASMA OSCILLATIONS AND WAVES

Absorption of Electromagnetic Surface Waves by Electrons in a Transition Layer between the Plasma and Dielectric

Ya. F. Leleko* and K. N. Stepanov**

**Karazin National University, pl. Svobody 4, Kharkov, 61077 Ukraine*

***National Science Center Kharkov Institute of Physics and Technology, ul. Akademicheskaya 1, Kharkov, 61108 Ukraine*

Received February 3, 2003

Abstract—The effect of the Debye layer on the absorption of an electromagnetic surface wave propagating along the plasma–dielectric interface is considered. The electric field distribution in the Debye layer and the energy absorbed by the plasma electrons in this layer are determined. It is shown that the ratio of the rate at which surface waves are damped due to Cherenkov absorption by the electrons reflected from the electric field potential in the transition layer to their frequency is on the order of the ratio of the electron thermal velocity to the wave phase velocity. *© 2003 MAIK "Nauka/Interperiodica".*

1. Electromagnetic surface waves are widely employed for the creation and heating of plasmas and the amplification of microwaves [1, 2]. The damping of these waves may be caused by such factors as particle collisions, the local enhancement of the electric field in the plasma resonance region, collisionless Landau damping, and collisions of electrons with the wall [1–4].

The absorption of surface waves due to the specular or diffuse reflection of electrons from the wall was studied in [5–7]. In the plasma, surface waves whose amplitude is proportional to $\sim\exp(iky)$ are exponentially damped according to the law $\exp(-\kappa_p x)$ (where $\kappa_p = \sqrt{(-\varepsilon_p/\varepsilon_0)}k$) with increasing distance from the plasma–dielectric interface. Consequently, their Fourier spectrum in x contains harmonics with all possible wavenumbers k_x, including those corresponding to short-wavelength modes whose phase velocities in the x direction are on the order of the electron thermal velocity ($\omega/k_x \sim v_{Te}$). Since such electrons are very numerous, the damping rate of the surface waves is on the order of the ratio of the amplitude of the harmonic with $k_x \sim \omega/v_{Te}$ to the amplitude of the fundamental harmonic with $k_x \sim \kappa_p \sim k$; i.e., $\gamma/\omega \sim v_{Te}/v_{ph}$, where $v_{ph} = \omega/k$.

In this paper, we investigate the absorption of a surface wave due to the interaction of plasma electrons with the electric field of the wave in the transition layer that forms near the plasma–dielectric interface because the electrons escape preferentially from the plasma volume onto the dielectric surface, thereby producing a positive space charge. As a result, the density of the electrons in the transition layer becomes lower than their density n_0 far from the interface. The thickness of the transition layer is on the order of the screening radius r_D (the Debye–Hückel radius). The electrons moving in the space charge electric field are decelerated and are reflected from the turning points when their energy is lower than the wall potential, or from the wall in the opposite case.

In the transition layer, the normal component of the electric field of a surface wave varies on a scale on the order of several screening radii. This indicates that the effective wavenumber in the direction of nonuniformity (the x direction) is about $1/r_D$. If the frequency of the surface wave is on the order of the Langmuir frequency, then the bulk electrons, whose velocity is on the order of the thermal velocity v_{Te}, can efficiently interact with the normal component of the wave electric field, thereby absorbing the wave energy. Since the field of a surface wave is localized in a region with a thickness on the order of $\sim 1/k$ (where k is the wavenumber in the wave propagation direction) and the characteristic frequencies are on the order of $\sim\omega_{pe}$, the fraction of the wave energy carried away by the bulk electrons is about $Q \sim v_{Te}/v_{ph}$, where $v_{ph} = \omega/k$ is the phase velocity of the surface wave. For $v_{Te} \ll v_{ph}$, the thickness of the transition layer is much less than the distance on which the surface wave is damped; so that the quantity Q is low. For $\omega \ll \omega_{pe}$, the wave phase velocity is close to the speed of light and we have $Q \sim v_{Te}/c$, in which case the damping coefficient for the surface wave is of the same order of magnitude as that for a wave that propagates in the dielectric at an angle to the plasma–dielectric interface and is reflected from the plasma [8]. The phase velocity of a surface wave with a frequency near the limiting frequency is much lower than the speed of light; as a result, the wave damping is substantially stronger than that in the previous case.

Below, we will take a kinetic approach to determine the damping of the surface wave due to the absorption of its energy by plasma electrons interacting resonantly with the normal (perpendicular to the plasma–dielectric

1063-780X/03/2910-0867$24.00 © 2003 MAIK "Nauka/Interperiodica"

interface) component of the wave electric field in a transition layer.

2. We consider an electromagnetic surface wave propagating along a plasma–dielectric interface. The half-space $x < 0$ is filled with a dielectric with the permittivity ε_0, and the half-space $x > 0$ is filled with a plasma. The frequency of the electromagnetic surface wave is lower than the critical frequency, $\omega < \omega_{cr} \equiv \omega_{pe}/\sqrt{1+\varepsilon_0}$, where ω_{pe} is the plasma frequency. In the dielectric ($x < 0$), the electric and magnetic fields of the surface wave, $\mathbf{E}_0$ and $\mathbf{B}_0$, have the form

$$\begin{aligned}\mathbf{E}_0(t, x, y) &= \mathbf{E}_0 \exp[\kappa_0 x + i(ky - \omega t)],\\ \mathbf{B}_0(t, x, y) &= \mathbf{B}_0 \exp[\kappa_0 x + i(ky - \omega t)],\end{aligned} \tag{1}$$

where κ_0 is the spatial damping rate of the surface wave in the dielectric. The only nonzero components of the wave electric field are the x and y components, and the wave magnetic field has one nonzero component, directed along the z axis.

Since the plasma electrons are far more mobile than the ions, they are concentrated near the plasma–dielectric interface, forming a layer with a negative potential [9], which is discernibly different from zero at distances from the interface that are on the order of several screening radii $\sim r_D$. Outside the transition layer ($x \geq a$), the plasma is homogeneous and the wave field components decrease exponentially according to the law

$$\begin{aligned}\mathbf{E}_1(t, x, y) &= \mathbf{E}_1 \exp[-\kappa_p x + i(ky - \omega t)],\\ \mathbf{B}_1(t, x, y) &= \mathbf{B}_1 \exp[-\kappa_p x + i(ky - \omega t)].\end{aligned} \tag{2}$$

We represent the wave electromagnetic field in the transition layer $0 \leq x \leq a$ in the form

$$\begin{aligned}\mathbf{E}(t, x, y) &= \mathbf{E}(x) \exp[i(ky - \omega t)],\\ \mathbf{B}(t, x, y) &= \mathbf{B}(x) \exp[i(ky - \omega t)].\end{aligned} \tag{3}$$

For further analysis, we choose the layer thickness a so as to satisfy the inequalities $a \gg r_D$ and $\kappa_p a \ll 1$. In what follows, we will show that, in the layer, the y-component of the wave electric field remains constant to within terms on the order of $\sim v_{Te}/v_{ph} \ll 1$, whereas the x component of the electric field changes substantially.

In the absence of the wave, the velocity distributions of the charged particles are described by the Maxwell–Boltzmann formula $f_{0e,i} \sim \exp(-\varepsilon/T)$, where $\varepsilon \equiv (1/2)m_{e,i}v_x^2 \mp e\varphi(x)$, $m_{e,i}$, and $\mp e$ are the mass and charge of an electron and an ion, respectively; and T is the temperature. In this case, the charged particle densities are equal to $n_{e,i}(x) = n_0 \exp(\pm e\varphi(x)/T)$. The potential $\varphi(x)$ can be found from Poisson's equation $\Delta\varphi(x) = 4\pi e(n_e(x) - n_i(x))$. We introduce the dimensionless variables $\Phi(x) \equiv e\varphi(x)/T$ and $x \longrightarrow x/r_D$ (where $r_D \equiv \sqrt{T/8\pi e^2 n_0}$ is the Debye–Hückel radius) to rewrite Poisson's equation as

$$\frac{d^2\Phi}{dx^2} = \sinh\Phi.$$

Since $d\Phi/dx \longrightarrow 0$ as $\Phi \longrightarrow 0$, we obtain

$$\frac{d\Phi}{dx} = \sqrt{2(\cosh\Phi - 1)}, \quad \ln|\coth(\Phi/4)| = x + C.$$

The integration constant C can be determined from the condition for the electron and ion currents to the wall to be the same. To within a factor on the order of unity within the logarithm, the wall potential is equal to [9]

$$\Phi_0 \cong (1/2)\ln(m_e/m_i). \tag{4}$$

Taking into account secondary electron emission does not change the order of magnitude of the quantity Φ_0 [9]. With allowance for expression (4), we get

$$\Phi(x) = \ln(\tanh^2[(x + C)/2]), \quad C \equiv \ln|\coth(\Phi_0/4)|. \tag{5}$$

The perturbation of the distribution function, $f_1(t, y) \sim \exp(\nu t + i[ky - \omega t])$, is described by the kinetic equation

$$\left\{\frac{\partial}{\partial x} + \frac{e}{mv_x}\frac{\partial\varphi}{\partial x}\frac{\partial}{\partial v_x} - i\frac{\omega_1}{v_x}\right\} f_1(t, \mathbf{r}, \mathbf{v}) = -\frac{2e(\mathbf{vE})}{v_x m v_{Te}^2} f_0, \tag{6}$$

where $\omega_1 \equiv \omega - kv_y + i\nu$, $v_{Te}^2 \equiv (2T/m)$, and ν is the collision frequency ($\nu \longrightarrow +0$). We rewrite Eq. (6) in the form

$$\left\{\frac{d}{dx} - i\frac{\omega_1}{v_x(x)}\right\} f_1(t, x, \mathbf{v}(x)) = -\frac{2e(\mathbf{v}(x)\mathbf{E}(x))}{v_x(x) m v_{Te}^2} f_0, \tag{7}$$

where

$$\frac{d}{dx} \equiv \frac{\partial}{\partial x} + \frac{e}{mv_x}\frac{\partial\varphi}{\partial x}\frac{\partial}{\partial v_x}, \quad \frac{\partial v_x}{\partial x} = \frac{e}{mv_x}\frac{\partial\varphi}{\partial x},$$

$$\varepsilon \equiv \frac{1}{2}mv_x^2 - e\varphi(x).$$

Here, by v_x we mean $v_x(x) = (2/m)\sqrt{\varepsilon + e\varphi(x)}$. The general solution to Eq. (7) can be represented as

$$\begin{aligned} f_1 &= -\frac{2e f_0}{m v_{Te}^2}\int_{x_1}^{x} dx' \frac{\mathbf{v}(x')\mathbf{E}(x')}{v_x(x')}\\ &\times \exp\left\{i\omega_1\left[\int_{x_m}^{x}\frac{dx''}{v_x(x'')} - \int_{x_m}^{x'}\frac{dx''}{v_x(x'')}\right]\right\},\end{aligned} \tag{8}$$

where x_m is determined from the condition $\varepsilon + e\varphi(x_m) = 0$ for electrons with energies $\varepsilon < -e\varphi(0)$. For electrons with energies $\varepsilon > -e\varphi(0)$, we have $x_m = 0$. The integration constant x_1 can be found from the boundary condi-

tions. For particles moving toward the wall ($v_x < 0$), we use the condition that f_1 is finite as $x \longrightarrow \infty$ to obtain

$$f_1^{(-)} = \frac{2ef_0}{mv_{Te}^2}\int_x^\infty dx' \frac{v_x(x')E_x(x') + v_yE_y(x')}{v_x(x')} \times \exp\{i[G(x) - G(x')]\}, \quad (9)$$

where

$$G(x) \equiv \omega_1 \int_{x_m}^x \frac{dx''}{v_x(x'')}. \quad (10)$$

In order to determine x_1 for $v_x > 0$, we use the condition for the reflection from the wall and turning points to be specular,

$$f_1^{(+)}(v_x, v_y, v_z, x = x_m) = f_1^{(-)}(-v_x, v_y, v_z, x = x_m). \quad (11)$$

Using relationships (9) and (11), we arrive at the following correction to the distribution function:

$$f_1^{(+)}(x, v_x(x), v_y) = \frac{2ef_0}{mv_{Te}^2}\left\{\int_{x_m}^\infty dx' \frac{v_x(x')E_x(x') - v_yE_y(x')}{v_x(x')} \times \exp\{i[G(x) + G(x')]\} - \int_{x_m}^x dx' \frac{v_x(x')E_x(x') + v_yE_y(x')}{v_x(x')} \exp\{i[G(x) - G(x')]\}\right\}. \quad (12)$$

The longitudinal current density $j_x = -e\int_{-\infty}^\infty v_x f_1(x, \mathbf{v})d\mathbf{v}$ can be found by integrating over v_y and v_z; passing over to the dimensionless variables $\omega \longrightarrow \omega/\omega_{pe}$, $v \longrightarrow v/v_{Te}$, $\varepsilon \longrightarrow \varepsilon/T$, $E_{x,y} \longrightarrow E_{x,y}/E_{0y}$, $x \longrightarrow x/r_D$, and $\Phi \equiv e\varphi/T$; and making the replacement $v_x \longrightarrow v_x = \sqrt{\varepsilon + \Phi(x)}$:

$$j_x = -\frac{i\omega_{pe}}{4\pi^{3/2}}\int_{|\Phi(x)|}^\infty d\varepsilon e^{-\varepsilon}\left\{\int_x^\infty dx' E_x(x')e^{iG(x')}\sin G(x) + \int_{x_m}^x dx' E_x(x')e^{iG(x)}\sin G(x')\right\}. \quad (13)$$

In the first term in the integrand in expression (13), we integrate over x' from a to infinity (i.e., to distances at which the plasma is homogeneous and the field distribution is known). We introduce the small parameter $v_{Te}/v_{ph} \ll 1$, with respect to which the power series expansions are to be carried out. Ignoring the terms on the order of $\sim v_{Te}/v_{ph}$ and ignoring collisions in expression (13), we change the order of integration over x and ε to obtain the following final expression for the current density component $j_x(x)$ in the transition layer:

$$\frac{4\pi i}{\omega\omega_{pe}}j_x = \frac{1}{\omega\sqrt{\pi}}\left\{\int_x^a dx' E_x(x') \times \int_{|\Phi(x)|}^\infty d\varepsilon e^{-\varepsilon}[\cos G(x')\sin G(x) + i\sin G(x')\sin G(x)] + \int_0^x dx' E_x(x') \times \int_{|\Phi(x')|}^\infty d\varepsilon e^{-\varepsilon}[\sin G(x')\cos G(x) + i\sin G(x')\sin G(x)]\right\} + \frac{2E_x(a)}{\omega^2\sqrt{\pi}}\int_{|\Phi(x)|}^\infty d\varepsilon\sqrt{\varepsilon}e^{-\varepsilon}[-\sin G(a)\sin G(x) + i\cos G(a)\sin G(x)]. \quad (14)$$

The y component of the current density is derived in an analogous way. However, we will not use the current density component $j_y(x)$ (or, more precisely, the electric induction component D_y) to evaluate the field $E_x(x)$, because, as will be seen below, it enters into Maxwell's equations as a product with the small parameter v_{Te}/v_{ph}.

In order to determine the electric field amplitude $\mathbf{E}(x)$ in the transition layer ($0 \le x \le a$) from representations (3), we turn to Maxwell's equations, which imply that $\nabla \times \nabla \times \mathbf{E} - (\omega/c)^2\mathbf{D} = 0$, where $\mathbf{D} \equiv \mathbf{E} + (4\pi i/\omega)\mathbf{j}$ is the electric induction. We thus arrive at the set of equations

$$\left(\frac{\partial}{\partial x}E_y - ikE_x\right) + i\frac{\omega^2}{kc^2}D_x = 0, \quad \frac{\partial}{\partial x}\left(\frac{\partial}{\partial x}E_y - ikE_x\right) + \frac{\omega^2}{k^2}D_y = 0. \quad (15)$$

Integrating the first of Eqs. (15) over dx yields

$$E_y(x) = E_y(0) + ik\int_0^x E_x(x)dx + i\frac{\omega^2}{kc^2}\int_0^x D_x(x)dx. \quad (16)$$

We pass over to the dimensionless variables $x \longrightarrow x/r_D$ and $\omega \longrightarrow \omega/\omega_{pe}$ (where $\omega_{pe}^2 = 4\pi e^2 n_0/m$, $r_D\omega_{pe} = v_{Te}/2$, and $v_{Te} \equiv \sqrt{2T/m_e}$) and normalize the fields to

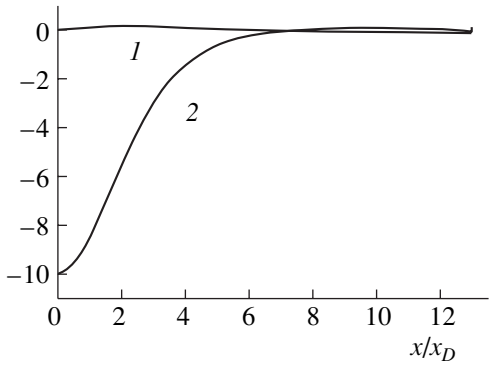

Fig. 1. Dependence of (*1*) $\mathrm{Re}\,E_x(x)/E_{0y}$ and (*2*) $\mathrm{Im}\,E_x(x)/E_{0y}$ on the coordinate x/r_D in the transition layer for $\omega/\omega_{pe} = 0.1$, $\varepsilon_0 = 1 = 1$, and $a = 13r_D$.

the amplitude $E_y(x=0)$ of the y component of the electric field of the surface wave to write

$$E_y(x) = E_y(0) + i\frac{v_T}{v_{ph}}\frac{\omega}{2}\int_0^x E_x(x)dx + i\frac{v_T}{v_{ph}}\frac{\omega(|\varepsilon_p|-\varepsilon_0)}{2\varepsilon_0|\varepsilon_p|}\int_0^x D_x(x)dx. \quad (17)$$

In deriving the third (small) term on the right-hand side of expression (17), we took into account the fact that, in the zeroth approximation (i.e., when the higher order terms are neglected), the wavenumber k and frequency ω are related by the following dispersion relation for the surface wave:

$$k = \frac{\omega}{c}\sqrt{\frac{\varepsilon_0|\varepsilon_p|}{|\varepsilon_p|-\varepsilon_0}}. \quad (18)$$

The first term on the right-hand side of expression (17) is much larger than the second and third terms. An analogous procedure can be applied to the second of Eqs. (15). As a result, we can expand the solution to Eqs. (15) in powers in the small parameter v_{Te}/v_{ph}. In the above dimensionless variables, Eqs. (15) have the form

$$\left(\frac{\partial}{\partial x}E_y - i\frac{v_{Te}}{v_{ph}}\frac{\omega}{2}E_x\right) + i\frac{v_{Te}}{v_{ph}}\frac{\omega(|\varepsilon_p|-\varepsilon_0)}{2\varepsilon_0|\varepsilon_p|}D_x = 0,$$
$$\frac{\partial}{\partial x}\left(\frac{\partial}{\partial x}E_y - i\frac{v_{Te}}{v_{ph}}\frac{\omega}{2}E_x\right) + \frac{v_{Te}^2}{v_{ph}^2}\frac{(|\varepsilon_p|-\varepsilon_0)}{4\varepsilon_0|\varepsilon_p|}D_y = 0. \quad (19)$$

To within terms on the order of $\sim v_{Te}/v_{ph}$, Eqs. (19) yield

$$E_y = A + \frac{v_T}{v_{ph}}i\left(-\frac{\omega(|\varepsilon_p|-\varepsilon_0)}{2\varepsilon_0|\varepsilon_p|}xB + \frac{\omega}{2}\int_0^x E_x(x')dx'\right),$$
$$D_x = B - i\frac{v_T}{v_{ph}}\frac{\omega}{2}\int_0^x D_y(x')dx', \quad (20)$$

where A and B are integration constants. Using the boundary conditions $E_y|_{x=-0}$, $E_y|_{x=+0}$, $D_x|_{x=-0} = D_x|_{x=+0}$, and $E_y|_{x=a-0} = E_y|_{x=a+0}$, $D_x|_{x=a-0} = D_x|_{x=a+0}$ and the relationships between the electric field components in the regions $x < 0$ and $x > a$,

$$E_{0y} = i(\kappa_0/k)E_{0x}, \quad E_{1y} = -i(\kappa_p/k)E_{1x} \quad (21)$$

and omitting terms on the order of $\sim v_{Te}/v_{ph}$ (which corresponds to ignoring the effects associated with the finite thickness of the transition layer), we arrive at dispersion relation (18) for a surface wave in the zeroth approximation. Then, the expressions for κ_0 and κ_p, the formulas for the constants A and B, and the relationships between the wave field amplitudes in the dielectric and in the plasma take the form

$$\kappa_0 = \sqrt{\varepsilon_0/|\varepsilon_p|}k, \quad \kappa_p = \sqrt{|\varepsilon_p|/\varepsilon_0}k, \quad (22)$$

$$A = E_{0y}, \quad B = \varepsilon_p E_{1x}, \quad (23)$$

$$E_{0x} = -i\sqrt{|\varepsilon_p|/\varepsilon_0}E_{0y}, \quad E_{1x} = i\sqrt{\varepsilon_0/|\varepsilon_p|}E_{0y}. \quad (24)$$

The x component of the wave electric field in the region $0 \le x \le a$ can be found from the second of expressions (20) by omitting terms on the order of $\sim v_{Te}/v_{ph}$:

$$D_x(x) = \varepsilon_p E_{1x}. \quad (25)$$

Using expression (25) for $D_x = E_x + (2\pi i/\omega)j_x$ and taking into account expression (14), we obtain the following integral equation for the field distribution E_x in the transition layer:

$$E_x(x) + \int_0^a dx' K(x,x')E_x(x') = R(x), \quad (26)$$

where the kernel $K(x, x')$ has the form

$$K(x,x') = \frac{1}{\omega\sqrt{\pi}}\int_{|\Phi(x)|}^{\infty} d\varepsilon e^{-\varepsilon}[\cos G(x')\sin G(x) + i\sin G(x')\sin G(x)] \quad (x' > x),$$
$$K(x,x') = \frac{1}{\omega\sqrt{\pi}}\int_{|\Phi(x)|}^{\infty} d\varepsilon e^{-\varepsilon}[\sin G(x')\cos G(x) + i\sin G(x')\sin G(x)] \quad (x' < x), \quad (27)$$

and the free term is equal to

$$R(x) = \left\{\varepsilon_p + \frac{2}{\omega\sqrt{\pi}}\int_{|\Phi(x)|}^{\infty} d\varepsilon\sqrt{\varepsilon}e^{-\varepsilon}[\sin G(a)\sin G(x) + i\cos G(a)\sin G(x)]\right\}E_{1x}. \quad (28)$$

Integral equation (26) was solved numerically. For $\kappa_p a \ll 1$ and $r_D \ll a$, the field profile $E_x(x)$ should be independent of the choice of the value of the parameter a. The results of calculations for the parameter values $a = 13r_D$; $\varepsilon_0 = 1$; $T = 10$ eV; and $\omega/\omega_{pe} = 0.1$, 0.3, 0.5, and 0.7 are shown in Figs. 1–4. From these figures, we can see that the field component $E_x(x)$ varies on a scale on the order of several Debye radii and, for $x \sim a$, approaches the value E_{1x} given by expression (24). For $a = 13r_D$, the discrepancy ($\Delta E_x \le 10\%$) stems from the above choice of the approximation for the field component $E_x(x)$ inside the transition layer.

3. Here, we estimate the absorbed electromagnetic wave energy from the change in the energy of the plasma electrons during their reflection from the wall or from the potential barrier. The velocity of an electron has the form

$$v_x(t) = v_x(-\infty) - \frac{e}{m}\int_{-\infty}^{t} dt' E_x(t', x), \qquad (29)$$

and the change in its kinetic energy is equal to

$$\Delta\frac{mv_x^2}{2} = \frac{mv_x^2(+\infty)}{2} - \frac{mv_x^2(-\infty)}{2}. \qquad (30)$$

Averaging expression (30) over the time t_0 and omitting terms on the order of $\sim v_{Te}/v_{ph}$, we obtain

$$\overline{\Delta\frac{mv_x^2}{2}} = \frac{e^2}{4m\omega_{pe}^2}|L(\varepsilon, x)|^2, \qquad (31)$$

where

$$L(\varepsilon, x) \equiv \int_{x_m}^{a} \frac{dxE_x(x)}{\sqrt{\varepsilon + \Phi(x)}}\cos G(\varepsilon, x) - \frac{2E_{1x}}{\omega}\sin G(\varepsilon, x).$$

The quantity $L(\varepsilon, x)$ in expression (31) is represented in the dimensionless variables $x \longrightarrow x/r_D$, $\omega \longrightarrow \omega/\omega_{pe}$, and $\varepsilon \longrightarrow \varepsilon/T$. In order to find the total energy acquired by the plasma electrons per unit area in unit time, we multiply expression (31) by the electron flux through a unit area of the interface and integrate over the entire velocity space. Then, we divide the resulting expression by the period-averaged energy of the surface wave per unit area of the interface and determine the absorption coefficient:

$$Q = \frac{1}{\omega W_S}\int v_x \overline{\Delta\frac{mv_x^2}{2}} f_0(\mathbf{v})d\mathbf{v}, \qquad (32)$$

where

$$W_S = \frac{1}{16\pi}\int_{-\infty}^{+\infty}\left\{\mathbf{E}\cdot\mathbf{E}^*\frac{\partial}{\partial\omega}[\omega\varepsilon(\omega)] + \mathbf{B}\cdot\mathbf{B}^*\right\}dx. \qquad (33)$$

After integration in formula (33), we obtain the following expression for the mean energy of a surface wave per unit area of the plasma–dielectric interface:

$$W_S = \frac{c}{16\pi\omega}\sqrt{|\varepsilon_p| - \varepsilon_0}\left(\frac{|\varepsilon_p|}{\varepsilon_0} + \frac{|\varepsilon_p|^2 + |\varepsilon_p| + \varepsilon_0}{|\varepsilon_p|^2}\right). \qquad (34)$$

The first and second terms in parentheses in expression (34) describe the energy densities of the surface wave in a dielectric ($x < 0$) and in a homogeneous plasma ($x > a$), respectively. The term describing the energy

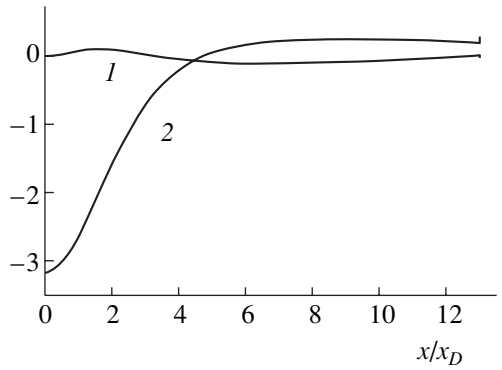

Fig. 2. Same as in Fig. 1, but for $\omega/\omega_{pe} = 0.3$.

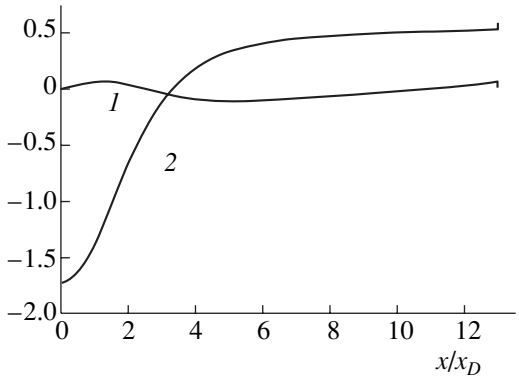

Fig. 3. Same as in Fig. 1, but for $\omega/\omega_{pe} = 0.5$.

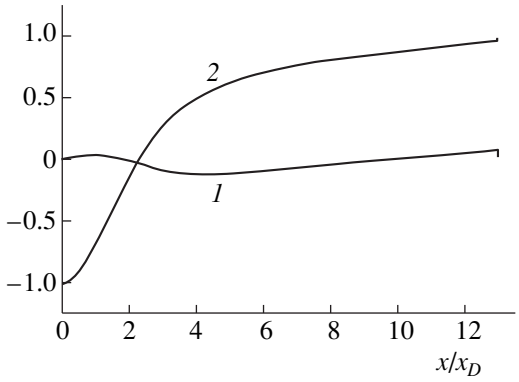

Fig. 4. Same as in Fig. 1, but for $\omega/\omega_{pe} = 0.7$.

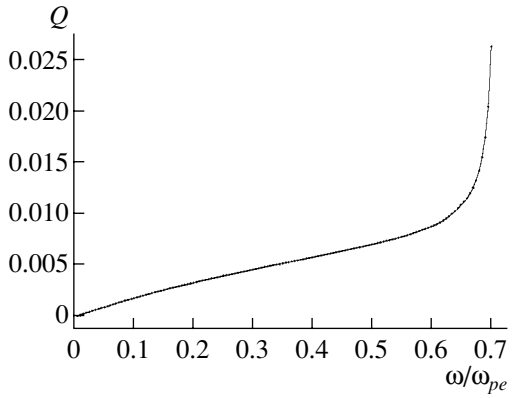

Fig. 5. Absorption coefficient Q vs. frequency ω for $\varepsilon_0 = 1$ and $a = 13r_D$.

density of the surface wave in the region $0 < x < a$ is eliminated because it is as small as v_{Te}/v_{ph} in comparison with the other two. From expression (34), we can see that, for $\omega \longrightarrow \omega_{cr}$, the wave energy density in the plasma is three times higher than that in the dielectric ($\varepsilon_0 = 1$).

Substituting formulas (31) and (34) into expression (32) and changing the order of integration over x and ε yields the following expression for the absorption coefficient in the above dimensionless variables:

$$Q = \frac{v_{Te}}{v_{ph}\sqrt{\pi}}\frac{\sqrt{\varepsilon_0}|\varepsilon_1|^{3/2}}{(|\varepsilon_1| + \varepsilon_0)(|\varepsilon_1|^2 + \varepsilon_0)}M(\omega). \qquad (35)$$

Here,

$$M(\omega) = \left\{\int_0^a dx \int_0^a dx' H(x, x') \int_{|\Phi_{\min}|}^{\infty} d\varepsilon \frac{e^{-\varepsilon}\cos G(x)\cos G(x')}{\sqrt{\varepsilon + \Phi(x)}\sqrt{\varepsilon + \Phi(x')}}\right.$$
$$- \frac{4}{\omega}\int_0^a dx H(x, a) \int_{|\Phi(x)|}^{\infty} d\varepsilon \frac{e^{-\varepsilon}\cos G(x)\sin G(a)}{\sqrt{\varepsilon + \Phi(x)}} \qquad (36)$$
$$\left. + \frac{4}{\omega^2}H(a, a) \int_{|\Phi(a)|}^{\infty} d\varepsilon e^{-\varepsilon}\sin^2 G(a)\right\},$$

where

$$H(x, y) \equiv [\mathrm{Re}\, E_x(x)\mathrm{Re}\, E_x(y) + \mathrm{Im}\, E_x(x)\mathrm{Im}\, E_x(y)],$$

and

$$\Phi_{\min} = \Phi(x) \quad \text{for} \quad x < x',$$
$$\Phi_{\min} = \Phi(x') \quad \text{for} \quad x > x'.$$

Note that the wall potential is high in comparison with the mean electron energy, which is about the temperature ~T. That is why only a few electrons (about 0.31% for a hydrogen plasma) overcome the potential barrier, and, consequently, their role in the absorption of the wave power is insignificant. For the same reason, the electron density at the plasma–dielectric interface ($x = 0$) is exponentially low (about 2.3% of n_0 for a hydrogen plasma). Hence, for plasmas of real gases with $M_i > 10^3 m_e$, it is impossible to pass over to the limit in which $\Phi_0 = 0$ and practically all of the electrons incident on the wall are reflected from it.

The damping coefficient for the surface wave is equal in order of magnitude to $Q \sim v_{Te}/v_{ph}$. The absorption coefficient given by expression (35) was calculated numerically for $\varepsilon_0 = 1$, $a = 13r_D$, and $T = 10$ eV and for different values of the parameter ω/ω_{pe}. The dependence of Q on ω/ω_{pe} is illustrated in Fig. 5. In the frequency range such that $\omega/\omega_{pe} \le 0.6$, the absorption coefficient Q is seen to increase monotonically from about ~10^{-4} to about ~10^{-2}. Near the critical frequency, $\omega_{cr}/\omega_{pe} = 1/\sqrt{2} = 0.7071$, the absorption coefficient Q increases sharply. In the frequency range $\omega/\omega_{pe} = 0$–0.275, the quantity $M(\omega)$ given by expression (36) decreases abruptly from 2×10^5 to 28. In the range $\omega/\omega_{pe} = 0.275$–0.7, this quantity varies in the range 22–28. In the frequency range $\omega/\omega_{pe} = 0$–0.15, the second factor on the right-hand side of expression (35) is small (from 7×10^{-8} to 5×10^{-4}); in the range $\omega/\omega_{pe} = 0.15$–0.7, it increases monotonically from 5×10^{-4} to 0.14. In deriving integral equation (26) for the field component $E_x(x)$, we ignored the changes in $E_y(x)$ and $D_x(x)$ inside the transition layer; in other words, we in fact used the boundary conditions $E_y(0) = E_y(a)$ and $D_x(0) = D_x(a)$. Actually, the quantities $E_y(x)$ and $D_x(x)$ inside the layer vary approximately as $\exp(-\kappa_p x)$. Ignoring this circumstance leads to an error in determining the absorbed wave power. This error is on the order of $2\kappa_p a$ and amounts to 30% for $\omega/\omega_{pe} = 0.7$ and $a = 13r_D$. At the rightmost point $\omega/\omega_{pe} = 0.7$ in Fig. 5, the parameters v_{Te}/v_{ph} and $\kappa_p a$ are quite small ($v_{Te}/v_{ph} = 0.0316 \ll 1$ and $\kappa_p a \approx 0.147 \ll 1$), which justifies the validity of the above assumptions.

4. Our analysis has shown that an electromagnetic surface wave propagating along a plasma–dielectric interface is absorbed by the electrons that are decelerated in a transition layer and are reflected from the potential barrier in the layer or from the interface. In the transition layer, the plasma density decreases from the density n_0 of a homogeneous plasma to a density of about $n_0\exp(\Phi_0) \approx n_0(m_e/m_i)^{1/2}$ and the electric field component in the direction of nonuniformity, $E_x(x)$, changes on a scale of about $\Delta x \sim (2$–$5)r_D$. This indicates that the characteristic wave vector corresponding to the Fourier component $E_x(k_x)$ of the wave electromagnetic field is about $k_x \sim 1/\Delta x$, the wave phase velocity being $\omega/k_x \sim v_{Te}$. Such waves are strongly absorbed by thermal plasma electrons. Since the thickness Δx of this interaction region is small in comparison with the depth $1/\kappa_p$ to which the wave penetrates into the plasma, the

absorption coefficient turns out to be on the order of the ratio of the thickness of the transition layer to the penetration depth, $Q \sim v_{Te}/v_{ph}$.

ACKNOWLEDGMENTS

We are grateful to V.I. Lapshin and V.P. Silin for discussing the results obtained and to I.V. Romenskiĭ for assistance in numerical calculations.

REFERENCES

1. A. N. Kondratenko, *Surface and Bulk Waves in Bounded Plasma* (Énergoatomizdat, Moscow, 1985).
2. N. N. Beletskiĭ, A. A. Bulgakov, S. I. Khankina, and V. M. Yakovenko, *Plasma Instabilities and Nonlinear Phenomena in Semiconductors* (Naukova Dumka, Kiev, 1984).
3. V. P. Silin and A. A. Rukhadze, *Electromagnetic Properties of Plasma and Plasmalike Media* (Atomizdat, Moscow, 1961).
4. A. F. Aleksandrov, L. S. Bogdankevich, and A. A. Rukhadze, *Oscillations and Waves in Plasma Media* (Mosk. Gos. Univ., Moscow, 1990).
5. M. F. Gorbatenko and V. I. Kurilko, Zh. Tekh. Fiz. **34**, 1136 (1964) [Sov. Phys. Tech. Phys. **9**, 884 (1964)].
6. Yu. A. Romanov, Izv. Vyssh. Uchebn. Zaved., Radiofiz. **7**, 242 (1964).
7. Yu. A. Romanov, Izv. Vyssh. Uchebn. Zaved., Radiofiz. **11**, 1533 (1968).
8. Ya. F. Leleko and K. N. Stepanov, Dopov. Natsion. Akad. Nauk Ukr., No. 3, 78 (2000).
9. O. B. Kozlov, *Electrical Probe in Plasma* (Atomizdat, Moscow, 1969).

Translated by I.A. Kalabalyk

Plasma Physics Reports, Vol. 29, No. 10, 2003, pp. 874–882. Translated from Fizika Plazmy, Vol. 29, No. 10, 2003, pp. 939–948.

PLASMA DYNAMICS

Numerical Simulations of a High-Current Plasma Lens

V. N. Gorshkov, A. A. Goncharov, and A. M. Zavalov

Institute of Physics, National Academy of Sciences of Ukraine, pr. Nauki 144, Kiev, 03039 Ukraine

Received January 9, 2003

Abstract—The dynamic processes by which an electrostatic plasma lens with a wide-aperture ion beam and electrons produced from the secondary ion–electron emission relaxes to a steady state is investigated for the first time by the particle-in-cell method. The parameters of a two-dimensional mathematical model were chosen to correspond to those of actual plasma lenses used in experimental studies on the focusing of high-current heavy-ion beams at the Institute of Physics of the National Academy of Sciences of Ukraine (Kiev, Ukraine) and the Lawrence Berkeley National Laboratory (Berkeley, USA). It is revealed that the ion background plays a fundamental role in the formation of a high potential relief in the cross section of a plasma lens. It is established that, in the volume of the plasma lens, a stratified electron structure appears that is governed by the nonuniform distribution of the external potential over the fixing electrodes and the insulating magnetic field. The stratification is very pronounced because of the finite sizes of the cylindrical fixing electrodes of the lens. It is shown that the presence of such a structure limits the maximum compression ratio for an ion beam to values that agree with those observed experimentally. *© 2003 MAIK "Nauka/Interperiodica".*

1. INTRODUCTION

The development of plasma optics as a branch of plasma dynamics was initiated by A.I. Morozov [1], who was the first to formulate the fundamental physical principles for introducing steady-state electric fields into a plasma penetrated by an intense ion beam. These principles are based on the ideas of the magnetic insulation of the electrons neutralizing the beam space charge and the equipotentialization of magnetic field lines. These ideas turned out to be highly fruitful and were soon implemented in a number of experimental works [2–4]. At the same time, it became clear that an adequate analytic theory of plasma lenses (PLs) is very difficult to construct because the set of self-consistent equations describing the processes in the lens is both nonlinear and inhomogeneous. The reason is that none of the parameters of a PL configuration with a curvilinear geometry of the magnetic field lines can be regarded as small. That is why PLs were analyzed theoretically under assumptions that greatly simplify the problem, such as zero electron mass approximation, cylindrical coordinate system, and the ignoring of initial conditions. These restrictions, being consistent with the fundamental principles of plasma optics, provided a good basis for the interpretation of the main experimental results; however, they were too crude to serve as a basis for the elaboration of an algorithm for creating plasma optics systems with specified properties.

With the development of computer technology and the methods of computational physics in the late 1970s, it became possible to numerically model physical processes in plasma optics systems. Volkov and Yakunin [5] proposed a mathematical model of the steady-state processes in an electrostatic PL and computed the equipotential surfaces of the electric field. It was found that the magnetic field lines deviate from these surfaces as the electron temperature increases. This model was non-self-consistent because it did not take into account the distribution of the external electric potential determined by the fixing electrodes of a PL. Of course, the model proposed in [5] reflected the computer's technological level at that time.

Further development of PLs was spurred by advances in the production of wide-aperture repetitive pulsed beams in the ampere range. In the 1980s, such beams found application, first, in injectors for fusion devices and, then, in high-current accelerators of heavy ions and high-dose ion implanters.

A series of experiments carried out at the Institute of Physics of the National Academy of Sciences of Ukraine (IP NASU) revealed new regular features in the behavior of electrostatic PLs during the focusing of such beams [6–8]. It was found that the current of a passing ion beam significantly affects the steady-state and dynamic parameters of the PL. The maximum compression ratio for a slightly divergent laminar beam at the focus is determined by the potential distribution over the fixing electrodes, as well as the strength of the insulating magnetic field and its configuration. It became clear that such high-current PLs are most suitable for focusing and controlling the beams of moderate-energy (10–100 keV) ions of high-Z chemical elements. Optimizing the parameters of the PL at IP NASU made it possible to achieve a maximum compression ratio of 25 at the focus of a copper ion beam with a current of 700 mA, an energy of up to 25 keV, and an initial radius of 5.6 cm [9, 12]. In analogous experiments at the Lawrence Berkeley National Laboratory (LBNL), maximum compression ratios of up to 40 were achieved at the foci of heavy-ion (Ta, Bi, Pb)

1063-780X/03/2910-0874$24.00

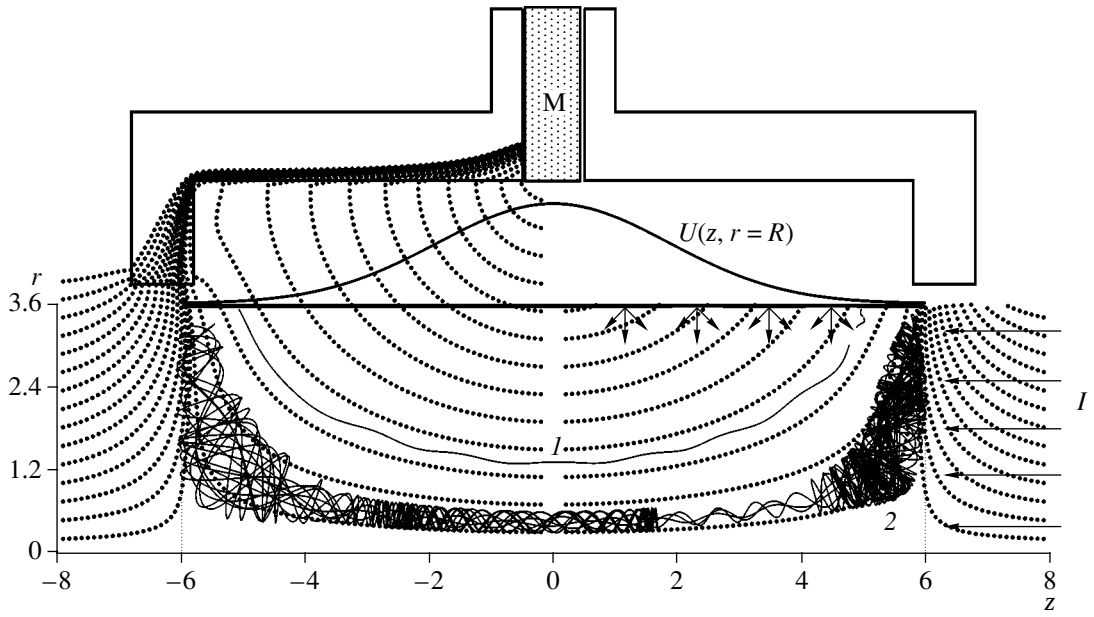

Fig. 1. Schematic of a plasma lens for focusing charge-neutralized ion beams: (*M*) ring magnet with magnetized tips, which produce the magnetic field in the lens; (*I*) ion current (the arrows in the right part of the electrode system indicate electron emission fluxes); and (*1*, *2*) possible trajectories of the secondary electrons. The horizontal arrows in the right part of the electrode show the emission region.

beams with an initial diameter of $d = 10$ cm and energies of up to 50 keV [8, 12].

Estimates of the maximum compression ratio for wide-aperture beams of heavy ions generated by vacuum arcs in cathode-material vapors show that the limitations associated with the beam emittance, the moment aberrations of a PL, and the field of an unneutralized space charge of the beam at the focus may be important for compression ratios of up to 1000.

Further search of the methods for eliminating PL spherical aberrations, which adversely affect the maximum compression ratio of the beam at the focus, and optimizing the PL parameters requires complementary numerical experiments drawing on the resources of modern computational techniques. At this point, it is worth noting that Morozov and Savel'ev [10] were the first to study the self-consistent electron dynamics in a system similar to the plasma optics one, namely, a plasma accelerator with closed electron drift and an extended acceleration region.

In the present paper, we report the results of the first numerical experiments aimed at modeling the relaxation of a high-current PL to a steady state and estimating the effect of this state on the focusing of a wide-aperture PL.

Let us briefly review the principles of operation of a PL, which were first described by Morozov and Lebedev [2]. The lens consists of a system of coaxial cylindrical electrodes of radius R (Fig. 1) held at different electric field potentials. The potential is maximum at the center of the lens and is zero at the outermost electrodes. A given step profile of the potential at the cylindrical surface $r = R$ is symmetric with respect to the $z = 0$ plane and can be approximated by a smooth profile $U(z, r = R)$, as in Fig. 1.

As a function of the variable z, the potential $U(z, r)$ also has a maximum in the central cross section of the lens, in which case, however, we have $U(0, 0) < U(0, R)$. Consequently, in the absence of a magnetic field, we deal with the simplest electrostatic lens. An ion flow entering the lens from the right (Fig. 1) is displaced toward the lens axis by the radial component of the electric field $\mathbf{E} = -\nabla\varphi$. It is assumed that the ion charge density is low and the distribution $U(z, r)$ is distorted insignificantly. However, in actuality, the problem is to focus ion beams with high space charge densities. In this case, the beam charge is neutralized to a great extent by an electron cloud that is trapped by the beam in the stage of its formation and prevents the beam ions from flying apart under the action of Coulomb forces. Such a neutralized ion beam (NIB) is a medium in which the electron conductivity is high and which expels external electric fields from its interior. That is why an NIB cannot be focused by an electrostatic lens.

The above effect of a complete screening of the external electric fields can be eliminated by applying an external magnetic field,[1] the typical configuration of which is shown in Fig. 1. In such a lens, the focusing process can be briefly described as follows. Only a frac-

[1] An azimuthally symmetric magnetic field with the desired line pattern is created by a system of electromagnets or by ring magnets with cylindrical tips of specially shaped cross sections.

tion of the electrons that neutralize the ion beam charge enter the working volume of the lens in the axial region. The remaining beam charge is neutralized by the emission electrons that are knocked out of the electrodes by the beam ions in the so-called "licking" regime (see [2]). Although these secondary electrons neutralize the beam charge, they are incapable of screening the external electric field, because, in a magnetic field in which the electron gyroradius is much less than the electrode radius ($r_L \ll R$), the electron conductivity across the magnetic field is zero. However, the potential distribution over the working volume of the lens will differ from that in the electrostatic analogue described above. The reason is that the electrons move freely along the magnetic field lines and thus tend to smooth out variations in the potential along the lines and to make the lines equipotential. If this is the case, the magnetic field lines that cross the rightmost electrode will transport the zero potential toward the axis of the system. It is in this sense that the electric field within the working volume is nevertheless pushed aside. The penetration depth of the electric field into the working volume is controlled by the magnetic field and is on the order of R. As a result, the potential difference $U(0, R)$–$U(0, 0)$ is higher than that in the purely electrostatic analogue and, accordingly, the compression ratio of an ion beam at the exit from the focusing system is larger.

That the magnetic field lines can be equipotential was asserted by A.I. Morozov in his papers. The equations of the two-fluid hydrodynamic model of a plasma with zero electron temperature and mass in the absence of electron–ion collisions has the stationary solution

$$\mathbf{E} = -\frac{1}{c}[\mathbf{v}_e\mathbf{H}], \tag{1}$$

where $\mathbf{E}$ is the electric field in the plasma and $\mathbf{v}_e$ is the hydrodynamic velocity of the electron gas. Solution (1) implies that there is no component of the electric field in the magnetic field direction and that the electrons drift azimuthally at a rate of about cE/H.

In reality, the gyroradius of the electrons and their temperature are both finite; hence, the magnetic field lines can be expected to be nonequipotential. In addition, the fact that the potential distribution depends on the ion current density (see [6–8]) is not described by solution (1). This is why it is important to carry out a more complete numerical investigation of the relaxation of the plasma to a steady electron state in the lens volume. It is this problem that is the subject of our paper, in which we will use the methods of mathematical modeling of dynamic phenomena in plasma media.

The geometric dimensions of the electrodes and the magnetic field structure in the lens shown in Fig. 1 correspond to those in the plasma lens that was used in experiments at the IP NASU and in which the magnetic field is produced by a constant ring magnet with cylindrical tips. The shape of the tips was chosen so that the outermost magnetic field line that goes through the electrodes held at a zero potential passes at the shortest possible distance from the lens center. This choice was made through a computer simulation of the magnetization of the tips. Another lens version corresponds to the plasma lens that was used in experiments at the LBNL and is based on a 14-cm-long system of electrodes 10 cm in diameter. The numerical results reported below were obtained for these two types of focusing devices.

2. NUMERICAL MODEL

The operating modes of the PL were simulated by the particle-in-cell (PIC) method under the assumption that the plasma is collisionless [11]. The density of the electron emission current from the surfaces of the electrodes was assumed to be uniform and equal to αJ_i (where α is the emission coefficient and J_i is the ion current density at the entrance to the lens). It was assumed that the secondary electrons are emitted in the region $z \geq 1$, whereas, at smaller z, the secondary electrons are not generated because the ion beam begins to be compressed there. It was also assumed that the initial electron energies are distributed uniformly over the interval 6–10 eV and that the angles between the directions in which the secondary electrons are emitted and the normal to the surface of the electrodes range between 0° and 70°. After each time step ΔT (in simulations, it was chosen to be $\Delta T = 7 \times 10^{-11}$ s), N new particles with charge q and mass m (the charge-to-mass ratio being $q/m = e/m_e$, where m_e is the mass of an electron) were injected into the lens. The quantities N, ΔT, and q satisfy the relationship $Nq/\Delta T = \alpha J_i S_e$, where S_e is the area of the surface from which the secondary electrons are emitted. The initial conditions for each of the particles were imposed with the help of a random number generator.

The motion of the electrons (and, thereby, the particles with which the electrons were modeled) in the lens volume was described by the equation

$$m_e\frac{d\mathbf{v}_e}{dt} = -e\left(\mathbf{E} + \frac{1}{c}[\mathbf{v}_e\mathbf{H}]\right), \tag{2}$$

where $\mathbf{E}$ and $\mathbf{H}$ are the electric and magnetic field strengths and $\mathbf{v}_e$ is the electron velocity.

Equation (2) for both the new particles and the particles already present in the lens volume was integrated with a time step $\Delta t \ll \Delta T$. After each time step ΔT, the distribution of the electron space charge density was calculated from the coordinates of all the particles by the PIC method. It was assumed that the distribution of the ion space charge is uniform and correspond to a given ion energy and a given ion current density J_i. This approach is justified in studying the general features of the relaxation of a PL to steady-state operating modes.

The potential $U(z, r)$ was calculated from the distribution of the total space charge density $\rho(z, r)$. Since

the potential in the lens was given only at the electrode surfaces, it was determined using the following procedure. The set of equations

$$U(\mathbf{r}_i) = \iint_S \frac{\sigma(\mathbf{r}')}{|\mathbf{r}_i - \mathbf{r}'|} dS' + \iiint_V \frac{\rho(\mathbf{r}')}{|\mathbf{r}_i - \mathbf{r}'|} dV \qquad (3)$$

(where $U(\mathbf{r}_i)$ are the potentials of the electrodes at the points with the position vectors $\mathbf{r}_i$ and the integrals are taken over the surface of the electrodes and the lens volume) was used to determine the surface change density $\sigma(\mathbf{r})$ at the electrodes in the form of a discrete set σ_k. Then, the right-hand side of Eqs. (3) was calculated at the mesh points $\mathbf{r}_{ik}$ of the spatial grid covering the lens volume. Further, the equations of motion for the particles were again solved but for the corrected electric field. Next, a new group of the emission electrons was injected. This procedure was repeated until the potential in the lens relaxed to a quasi-steady distribution self-consistent with the electron motion. The self-magnetic field of the moving electrons was ignored because their current density is low.

In a steady state, the number of electrons in the lens volume was $(1.5–3) \times 10^6$. The losses of electrons were determined by their escape from the computation region through the ends of the lens and, to a far more substantial extent, toward the electrodes. The electrons can be classified by their trajectories into two types (see Fig. 1; curves *1*, *2*). The motion of the electrons of the first type along the magnetic field lines is regular: on time scales of about $(1–2) \times 10^{-8}$ s, these electrons leave the lens volume. The electrons of the second type are trapped by the magnetic field of the lens and move stochastically between the lens ends for a fairly long time τ_e. It is these electrons that are responsible for the relaxation to a steady-state potential distribution in the lens. A statistical analysis of the electron lifetime τ_e was not carried out. At the same time, calculations of individual test electron trajectories in fixed electric and magnetic fields yielded lifetimes of about $\tau_e \approx (2–8) \times 10^{-7}$ s. Note that, in numerical experiments, the relaxation to steady states occurred on time scales of about 5×10^{-7} s.

Hence, we numerically investigated collective phenomena in a statistical particle–field model. All the applicability conditions of the model were satisfied. In particular, the electric field was recalculated on a time interval ΔT that was much shorter than the plasma period.

3. RESULTS OF COMPUTER SIMULATIONS

Numerical experiments answered a number of questions about the regular features of the formation of space charge within the lens volume.

(i) The important role of the ion background was revealed. Physically, it is clear that the total electron charge in the working volume exceeds the total ion charge. According to experimental estimates [6, 7] and our numerical results, the excess electron charge can amount to 10–14%. However, it is incorrect to assume that the positive and negative charge densities at each point of the lens volume satisfy the relationship $\rho(z, r) = \rho_i(z, r) - \rho_e(z, r) < 0$.[2] If the regions dominated by the positive charge do not form, the lens is insufficiently filled with the emission electrons and numerical experiments are incapable of capturing the potential distributions observed experimentally in the lens volume. When the ion background is taken into account, these distributions become dependent on the beam ion density. In contrast, the traditional approach (the zero temperature approximation) yields the same solution regardless of the magnitude of the ion current density J_i.

(ii) The distribution of the space charge in the radial direction has a stratified structure. The space charge possesses a radially stratified structure even when the potential distribution over the electrodes is smooth (rather than steplike). We carried out simulations for different potential distributions over the lens electrodes. The distributions were modeled by the functions of the form

$$f(z) = U(z, R)/U(0, R).$$

Figure 2 presents the profiles $f(z)$ used to simulate a lens with the geometric parameters given in Fig. 1.

For a given magnetic field structure and a given function $f(z)$, the assumption of precise equipotentialization allows us to readily calculate the potential distribution $\varphi(z, r)$ over the lens volume and the corresponding space charge density $\rho(\mathbf{r})$: $\Delta\varphi = -4\pi\rho$. For a step potential profile at the electrodes (Fig. 2, curve *1*), cylindrical regions with constant potentials U_i appear within the lens. The inner and outer boundaries of each are the surfaces generated by rotating the magnetic field lines that pass through the ends of the *i*th ring electrode about the lens axis. As a consequence, the space charge in the lens volume will be nonzero only within the transition regions between the surfaces with different potentials, thereby forming a pronounced stratified structure in the cross section passing through the lens axis. Such stratified structures are actually observed in numerical experiments for step potential profiles at the lens electrodes. However, they are also captured in simulations with smooth profiles $f(z)$. The reason is that stationary solution (1) is unrealistic. This solution, which is in fact the equipotentiality condition, was obtained without using the boundary conditions and thus cannot clarify the physical reason for a significant difference in the number of electrons moving along different magnetic field lines. In an actual lens, the phases of the electrons moving along the field lines should satisfy certain relationships in order for the electrons to

[2] Such an assumption would allow us to exclude the ion background from consideration and to calculate only the dynamics of the excess electron charge in the lens.

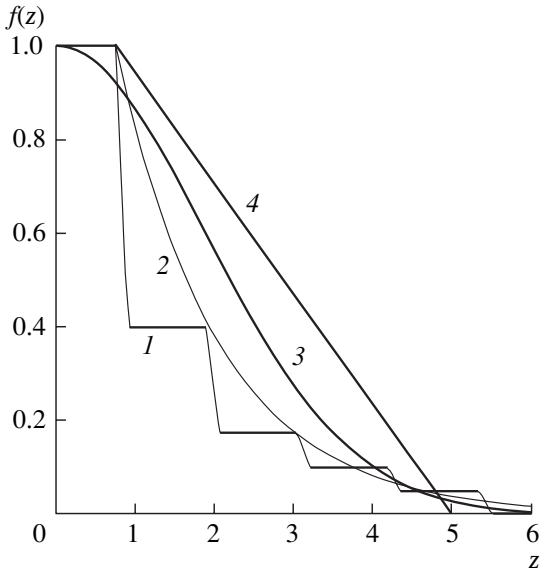

Fig. 2. Potential profiles at the electrodes of the lens that were used in simulations: (*1*) step profile corresponding to the experimental conditions in which the electrodes were separated by a distance of 1.5 mm; (*2*) $f(z) = 1$ for $z < 0.75$ and $\exp(-z/1.3)$ for $z > 0.75$; (*3*) $f(z) = \exp(-z^2/7)$; and (*4*) linear profile over the region $0.75 \le z \le 5$ such that $f(z) = 0$ for $z > 5$.

undergo multiple reflections from the electrode regions. It is only in this case that the space charge of the electrons will be large enough to neutralize the ion beam charge. The only electrons that can be trapped by a self-consistent electric field are those moving along certain magnetic field lines, which explains the stratified structure of the space charge density in the radial direction.

(iii) Efficient ion focusing can be achieved in relatively weak magnetic fields such that the ion gyroradius is comparable to the lens radius. In this case, the space charge distribution is unstratified. In the central region, the radial electric field increases linearly away from the axis. Since the magnetic field is approximately constant over the cross section of the lens, the angular velocity of the azimuthal drift motion depends weakly on the radius. Such an operating mode should be free of instabilities that worsen the parameters of the ion focusing.

We now present numerical results that illustrate the above conclusions. First, we show that the ions play an extremely important role in the dynamics of the formation of both the space charge in the lens and the high potential relief. Assuming that, at each spatial point, the space charge density of the electrons exceeds that of the ions, we can formally set the background ion density equal to zero. In this case, our numerical model will describe only the distribution of the excess electron charge. However, the results of solving the problem as formulated disagree with the experimental data (Fig. 3a). The potential at the center of the lens does not become lower than 600 V/cm even when the secondary emission current is substantially increased. The reason for this lies in the formation of an electron cloud near the emitting electrodes: in the self-consistent steady-state regime, the electrons flow from the cloud into the lens volume and return from the volume to the electrodes. In a dynamic equilibrium state, the total number of electrons within the lens remains essentially the same over a wide range of secondary electron flux densities. As the electrons fill the axial region, they give rise to a retarding potential (Fig. 3a, the vicinity of

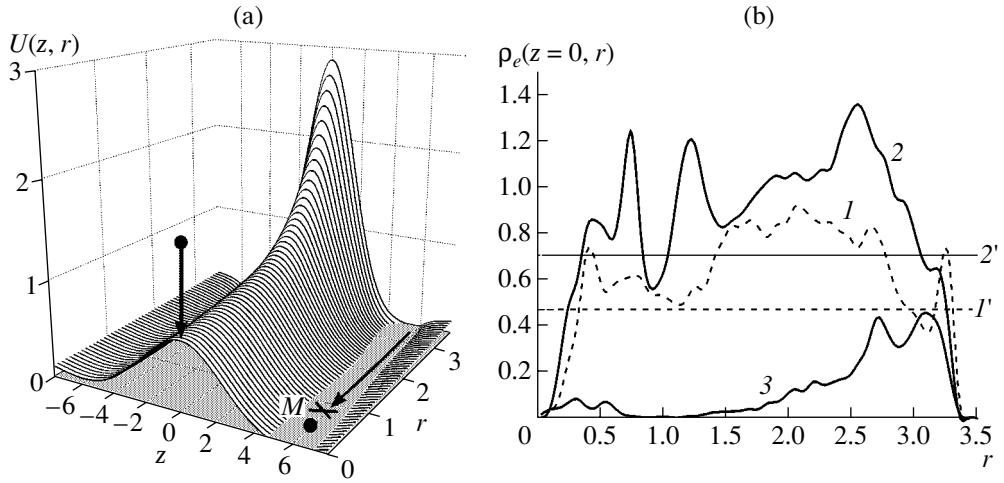

Fig. 3. (a) Spatial distribution of the potential in a plasma lens in the model in which the working volume has an excess of electrons at each point. The calculations were carried out for $U(0, R) = 3$ kV, $H(0, 0) = 360$ Oe, and $f(z) = \exp(-z^2/7)$, the secondary electron emission coefficient being $\alpha = 3$. The emission flux density corresponds to the ion current density $J_i = 3$ mA/cm^2. The arrow at the center indicates a decrease in the potential with respect to its initial value. Point *M* indicates the onset of the retarding potential. (b) Radial profiles of the absolute value of the electron charge density (in electrostatic units) in the central cross section of the lens. Curves *1* and *2* were calculated for $I = 120$ and 180 mA, respectively. Curves *1*' and *2*' show the ion background levels in these two cases. Curve *3* is the radial profile of the absolute value of the electron charge density in the model of Fig. 3a.

point *M*), that prevents the secondary electrons from moving along the magnetic field lines from the outermost electrode toward the axis of the system. If we assume that regions dominated by positive space charge do form in the lens volume and take into account the ion background[3] in the numerical model, then we find that the retarding potential does not arise. The excess negative space charge in the axial region increases, thereby lowering the potential over the entire lens volume and increasing the time during which the electrons move along the magnetic field lines. All these processes occurring in the lens lead to a radical rearrangement of the electron density distribution (Fig. 3b) and an increase in the total excess negative charge in the system. This is in agreement with the experimental data (Fig. 4), according to which the measured potential at the center of the lens is always lower than 50 V. In our model of the lens, we ignore the electrons that enter (together with an ion beam) the axial region, where the radial magnetic field is weak. As a consequence, the axial region in Fig. 3b is dominated by the ion charge; however, the error introduced by this ignoring is unimportant in seeking the optimum modes of the lens operation.

Note that, for all the $f(z)$ profiles shown in Fig. 2, the potential distributions are close to that in a lens version with equipotential magnetic field lines. However, the structure of the space charge distributions differ strongly from that obtained from the classical solution [1, 2]. Thus, for a Gaussian potential profile at the electrodes (Fig. 2, curve *3*), the space charge in the last case will be negative at each point within the lens volume. Although this stationary solution is formally allowed by our task, it is nevertheless unrealistic: if we take into account the boundary conditions, we see that this solution does not correspond to any real situations occurring when the lens is filled by the emission electrodes.

We now discuss the structure of the space charge distribution. Since the equipotentiality condition for the magnetic field lines is satisfied fairly well for a nonzero electron temperature, the stratified nature of the distribution of $\rho(r)$ for a step profile of the function $f(z)$ (Fig. 2) has a physically clear meaning. However, the stratification occurs also for a smooth $f(z)$ profile (Fig. 5). Let us examine this point in more detail.

Since the electrons that undergo a single-pass motion along the magnetic field lines[4] (i.e., along trajectories analogous to curve *1* in Fig. 1) live for only a short time in the lens volume, they cannot produce a significant space charge. The potential distribution over the volume is rearranged by the trapped (long-lived) electrons that move stochastically along the magnetic field lines. The question then naturally arises as to the factors that determine the probability for the electrons to be trapped within the lens volume.

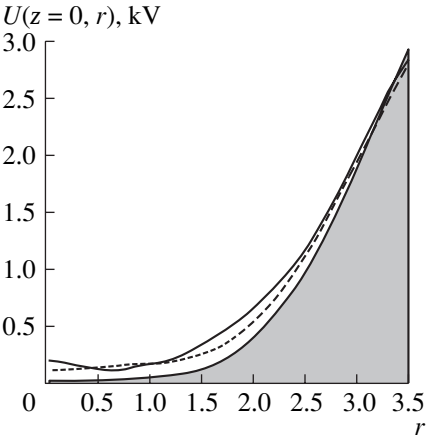

Fig. 4. Radial profiles of the potential at the central cross section of the lens for a Gaussian potential profile at the electrodes. The dashed and solid curves were calculated for $J_i = 3$ and 4.5 mA/cm^2, respectively. The curve that bounds the region shaded in light gray is the solution to the problem with a precise equipotentialization of the magnetic field lines.

The first factor is the presence of regions near the electrodes in which the potential is highly nonuniform. An electron that starts from some point at a certain potential and moves along an orbit with finite Larmor radius will reach the electrodes near the opposite end of the magnetic field line at a point at which the potential differs from that at the starting point. When the gradient of the potential at the electrodes is large, there is a fairly large probability that an electron will enter a region where the potential is lower than that at its starting point and will be reflected by this region. The electrons that are trapped in this manner form the space charge in the bulk of the lens volume. For a step potential profile (Fig. 2, curve *1*), cylindrical layers with an elevated electron density originate and end up at the interelectrode gaps.

The second factor is the presence of regions with nonuniform magnetic fields near the lens ends. Near the outermost electrodes ($z \approx 6$), the electrons move in a magnetic field with an alternating component H_z and a rapidly varying component H_r. The redistribution of energy between the rotational motions (along the orbits with finite Larmor radii) and translational motions results in chaotic reflections of the electrons not only in the regions near the electrodes but also within the lens volume (Fig. 1, trajectory *2*). Trapped electrons of this type, which were taken into account in the classical

[3] For a beam of singly charged copper ions with the current density $J_i = 3$ mA/cm^2 (in which case the total ion current in the lens is 120 mA) and at the potential $U = 12$ kV, the ion density is $n_i = 9.8 \times 10^8$ cm^{-3}, which corresponds to the ion space charge density $\rho_i = 0.47$ esu. For a total ion current of 180 mA, we have $n_i = 1.47 \times 10^9$ cm^{-3} and $\rho_i = 0.7$ esu. Our simulations were carried out precisely for these parameter values.

[4] We mean here the trajectories that lie in the (z, r) plane. In three-dimensional space, the electron motion is also characterized by the drift of the guiding centers of their Larmor orbits in the azimuthal direction.

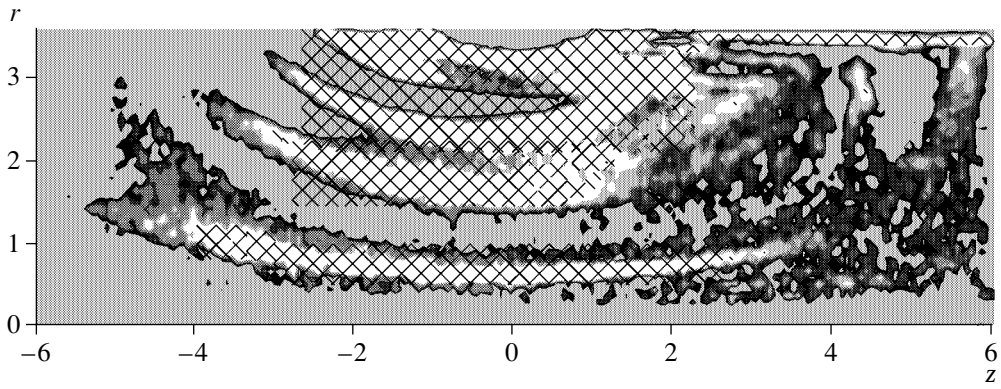

Fig. 5. Structure of the spatial distribution of the electron charge density for an exponential profile of the potential at the electrodes of the lens (Fig. 2, curve *2*). The beam current is $I = 180$ mA. The regions shaded in light gray are those in which the charge density of the ions is higher than that of the electrons. The "islands" in these regions are dominated by electrons. Shades of gray correspond to eight levels of the space charge density, from 0.7 esu for the ion background to an electron charge density equal to 1 esu. The regions where the charge density is higher than 1 esu are hatched.

solution to the problem in the zero temperature approximation [1, 2], produce jumps in the excess electron charge in the axial region (see Figs. 3b, 5), where the space charge density $\rho(z, r)$ should be minimum for the given $f(z)$ profile, provided that the magnetic field lines are equipotential.

In contrast to the situation with a step potential profile, the situation with an exponential profile $f(z)$ (Fig. 2, curve *2*) is more difficult to interpret (Fig. 5). The formation of the outer and inner (axial) space charge layers is consistent with the ideas arising from our model. These effects stem from the distinctive features of the potential distribution over the electrodes (the break in the $f(z)$ profile at $z = 0.75$; see Fig. 2, curve *2*) and the magnetic field near the lens ends (Fig. 1). The formation of two additional space charge layers between the outer and inner layers is due to the effect of the beam ions. It has been pointed out above that the ions play an especially important role in the relaxation to the steady-state operating modes of the lens. The results shown in Fig. 5 illustrate the effect quantitatively. Numerical experiments carried out for smooth $f(z)$ profiles show that the higher the ion current, the more pronounced the stratification and the larger the number of space charge layers. In this case, the electric field penetrates deeper into the working volume and its radial component at the beam periphery becomes weaker, which reduces the focusing efficiency in the regions crossed by the majority of the beam ions.

The above distributions of the space charge in the stratified structure can give rise to various plasma instabilities that may degrade the quality of the focused beam. Low-noise aberration-free focusing regimes should be sought only in the range of weak magnetic fields [13]. Below, we present numerical results obtained for a lens with a radius of 3.6 cm (see Fig. 1), the magnetic field strength at the center being $H_z(0, 0) = 100$ Oe. In simulations, the dependence of $H_z(0, r)$ on the radial coordinate r was approximated by a quadratic parabola such that $H_z(0, R) \approx 170$ Oe. The potential at the central electrode was 3 kV. The values of $f(z)$ at the electrodes are given by curve *1* in Fig. 2. It was assumed that the secondary electrons are emitted only from the region $1 \le z \le 6$ on the surface of the electrodes. The electrons that enter the volume of the lens through its ends were ignored. The ion energy was 12 keV and the beam current was 100 mA, the corresponding ion space charge density being $\rho = 0.394$ esu.

Figure 6 displays the spatial structure of the electron space charge. Because of the increase in the characteristic Larmor radius, the electron space charge density does not possess a pronounced stratified structure in the central part of the working volume. The radial profiles of the potential and electric field in the $z = 0$ plane are almost ideally suited for providing aberration-free beam focusing (see the region between the dashed vertical lines in Fig. 7).

Near the central electrode (i.e., in the region where the magnetic field increases to 170 Oe), the electron density evolves to a highly nonuniform distribution (Fig. 6), which leads to distortions of the linear radial dependence $E_r(0, r)$ shown in Fig. 7a. Of course, the electric field distribution in the central cross section of the lens does not give information about the global electric field structure over the entire lens volume (Fig. 7b), in which case the calculated ion trajectories provide evidence that the focusing is not ideal because of the presence of spherical aberrations. Thus, during the focusing of the ions injected parallel to the lens axis, the maximum mean ion current density at a collector of radius 1 cm is approximately $J_{ic} \approx 34 J_i$ and is reached at a distance of about $|z| \approx 15$ cm from the central cross section of the lens.

The results of numerical experiments carried out based on the model developed here agree well with the

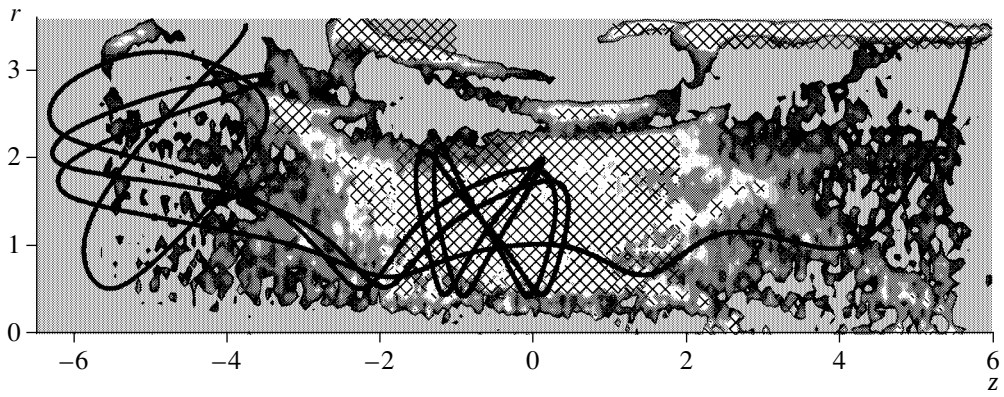

Fig. 6. Distribution of the electron space charge density in a lens with the central magnetic field $H_z(0, 0) = 100$ Oe. In the hatched regions, the space charge of the electrons is higher than that of the ions by a factor of 1.5 and more. The regions where the electron space charge is lower than the ion space charge are shaded in light gray. The solid curve is one of the possible electron trajectories in the lens version in question.

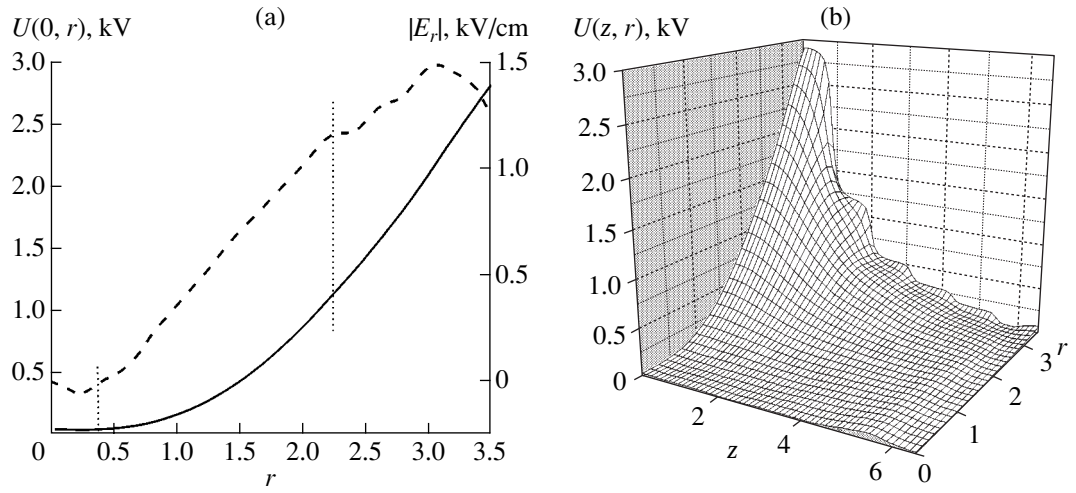

Fig. 7. (a) Radial profiles of the potential (solid curve) and radial electric field (dashed curve) at the central cross section of a lens with $H_z(0, 0) = 100$ Oe. (b) Potential distribution over the volume of a lens with the central potential $\varphi(0, 0) = 24$ V.

data from actual laboratory experiments. This allowed us to employ a specially devised computer code[5] to optimize the parameters of a plasma lens with a 14-cm-long system of electrodes 10 cm in diameter. Such a lens was used in experiments at the LBNL [12]. The magnetic field strength at the lens center was 300 Oe, and the potential at the central electrode was up to 7 kV. We simulated the focusing of a beam of bismuth ions with an energy of 34 keV and a total current of about 200 mA and found a nonmonotonic potential profile at the electrodes (Fig. 8) for which the density of the current to a target 3 mm in diameter reaches a maximum value of 45 mA/cm^2, which corresponds to a beam compression ratio higher than 30.

The results shown in Fig. 8 clearly illustrate a fundamental principle of plasma optics: in the region of the interelectrode gap, the potential profile $f(z \approx 3.6)$ is highly nonuniform; however, the electrons that move along the magnetic field lines passing through this region are not trapped. This conclusion is not surprising, especially in view of the equipotentialization principle for the magnetic field lines. In fact, the charge localized along these magnetic field lines should be positive, because, along the lines, we have $\Delta\varphi(z, r) < 0$ by virtue of a jump in the potential, $\partial f/\partial z > 0$. However, the physical mechanism of the phenomenon under consideration lies in its remarkable capability for self-orga-

[5] In the numerical model, we took into account additional electron fluxes from the lens ends. The radius of the regions from which these fluxes are emitted is 1.5 cm and the starting positions of the electrons at the z axis ($z \approx 6.3$ cm) coincide with those at which the magnetic field component H_z vanishes at the lens ends. The current density of the additional electrons is 0.1 of the ion current density.

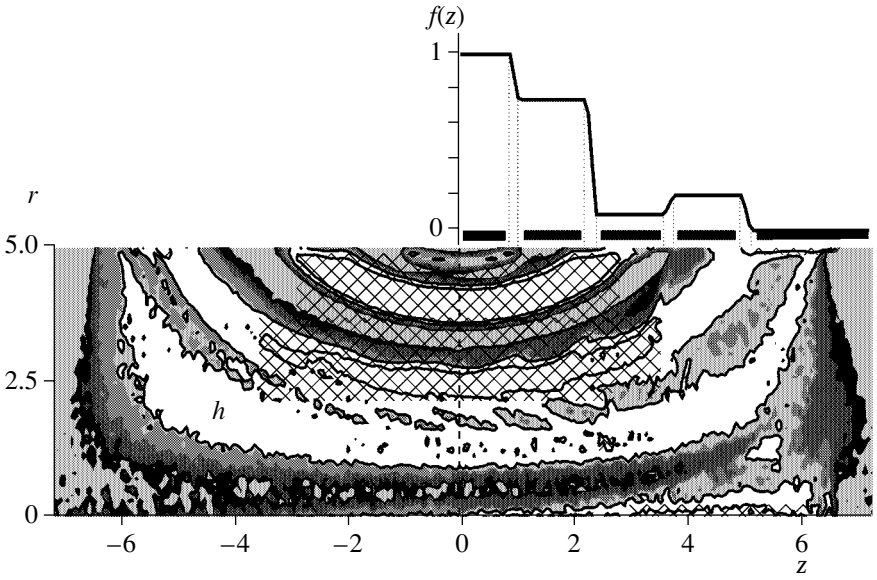

Fig. 8. Structure of the spatial distribution of the electron charge density in a lens in which the height of the steps in the $f(z)$ profile at the electrodes (from the center to the edge) are equal to 1, 0.74, 0.09, 0.2, and 0 (top). The background level of the ion charge density is 0.43 esu. The regions where $\rho_e \geq 0.86$ esu are hatched. In unshaded regions, the electron charge density is higher than the ion charge density. In the regions shaded in light gray, the charge density of the electrons is lower than 10% of that of the ions. The symbol *h* denotes the space charge layer formed by the electrons reflected from the regions of the strong radial magnetic field near the lens ends (see Fig. 1).

nization. Since the pattern of the trajectories of the trapped electrons is consistent with the potential distribution over the lens volume, these electrons cannot be reflected from the electrode regions ($z \approx 3.6$ cm), in which the potential is highly nonuniform.

In conclusion, we note that, on the whole, the potential distribution in the plasma lens corresponds to the equipotentialization principle for the magnetic field lines. In reality, however, the distribution of the electric field strength (the potential gradient) can deviate appreciably from that given by the classical solution, especially when the dependence $f(z)$ is nonmonotonic. That is why it often happens that the "optimal" potential distribution over the electrodes in a prescribed magnetic field obtained by the method of precise equipotentialization is not actually the optimal one.

ACKNOWLEDGMENTS

We are grateful to I.M. Protsenko, A.N. Dobrovol'skiĭ, and S.N. Gubarev, the members of the Gas Electronics Department of the IP NASU, for fruitful discussions and critical comments. This work was supported in part by the Science and Technology Center in Ukraine, grant no. 1596.

REFERENCES

1. A. I. Morozov, Dokl. Akad. Nauk SSSR **163**, 1363 (1965) [Sov. Phys. Dokl. **10**, 775 (1966)].
2. A. I. Morozov and S. V. Lebedev, in *Review of Plasma Physics*, Ed. by M. A. Leontovich (Atomizdat, Moscow, 1974; Consultants Bureau, 1980), Vol. 8.
3. A. A. Goncharov, A. N. Dobrovol'skiĭ, A. N. Kotsarenko, *et al.*, Fiz. Plazmy **20**, 499 (1994) [Plasma Phys. Rep. **20**, 449 (1994)].
4. A. A. Goncharov, Rev. Sci. Instrum. **69**, 1150 (1998).
5. B. I. Volkov and S. A. Yakunin, *Mathematical Problems of Plasmooptics* (Znanie, Moscow, 1982).
6. A. A. Goncharov, A. N. Dobrovolsky, A. Zatuagan, and I. M. Protsenko, IEEE Trans. Plasma Sci. **21**, 573 (1993).
7. A. A. Goncharov, A. Zatuagan, and I. M. Protsenko, IEEE Trans. Plasma Sci. **21**, 578 (1993).
8. A. A. Goncharov, I. M. Protsenko, G. Yushkov, and I. Brown, Appl. Phys. Lett. **75**, 911 (1999).
9. A. A. Goncharov, S. N. Gubarev, A. N. Dobrovol'skii, *et al.*, Fiz. Plazmy **26**, 838 (2000) [Plasma Phys. Rep. **26**, 786 (2000)].
10. A. I. Morozov and V. V. Savel'ev, Fiz. Plazmy **21**, 970 (1995) [Plasma Phys. Rep. **21**, 917 (1995)].
11. D. E. Potter, *Computational Physics* (Wiley, New York, 1973; Mir, Moscow, 1975).
12. A. Goncharov, V. Gorshkov, S. Gubarev, *et al.*, Rev. Sci. Instrum. **73**, 1001 (2002).
13. A. Goncharov, Rev. Sci. Instrum. **73**, 1004 (2002).

Translated by G.V. Shepekina

Plasma Physics Reports, Vol. 29, No. 10, 2003, pp. 883–889. Translated from Fizika Plazmy, Vol. 29, No. 10, 2003, pp. 949–955.

PLASMA DYNAMICS

Elimination of Aberrations in Wide-Aperture Magnetoelectrostatic Plasma Lenses

V. I. Butenko and B. I. Ivanov

National Science Center Kharkov Institute of Physics and Technology, Akademicheskaya ul. 1, Kharkov, 61108 Ukraine

e-mail: butenko@kipt.kharkov.ua; ivanovbi@kipt.kharkov.ua

Received January 22, 2003; in final form, April 14, 2003

Abstract—A computer model is devised for a Morozov plasma lens, in which the magnetic surfaces are equipotential surfaces of the electric field. Results are presented from numerical modeling of the focusing of ions with allowance for their longitudinal, radial, and azimuthal motions. The strengths and spatial distributions of the magnetic and electric fields are optimized. The methods for removing moment, geometric, and chromatic aberrations are analyzed. The effect of a discrete distribution of the potentials on ion focusing is modeled, and the related aberrations are examined. A computer model of an achromatic two-lens system is considered. *© 2003 MAIK "Nauka/Interperiodica".*

1. INTRODUCTION

At present, there is a great need to further develop the physics and technology of intense ions and electron beams (see, e.g., [1–3]). The problems associated with the focusing, transport, and separation of such beams are important for plasma physics, controlled fusion research, nuclear physics, accelerator physics and designs, radiation therapy, isotope separation, and beam technologies. An essential feature of the focusing, transport, and separation of intense ion beams is that, in order to prevent Coulomb instability, the ion space charge should be neutralized by electrons. For these purposes, it is expedient to use plasma-optic focusing devices (lenses) [1, 3], whose development was initiated by A.I. Morozov and his collaborators [3–5] and, in recent years, has been continued by A.A. Goncharov and his group [6–8].

In contrast to vacuum lenses, plasma-optic focusing systems are capable of operating with high ion currents (up to hundreds of amperes or higher) over a wide energy range [3]. Such systems have high focusing power and can both focus and defocus beams. The plasma in the lenses can be created by focused beams as a result of ionization of the residual gas or secondary electron emission from the electrodes and from the wall [6–8]. It can also be created by external sources, which is even better from the standpoint of optimization. In plasma-optic systems, any aberrations can, in principle, be eliminated by properly adjusting the distributions of the magnetic and electric fields.

The main goal of this paper, which is a continuation of [9–11], is to carry out computer simulations aimed at analyzing the possibility of eliminating different types of aberrations in lens systems for focusing wide-aperture (nonparaxial) charge-neutralized ion beams. We will be interested in the following types of aberrations: moment aberrations, which are due to the azimuthal particle motion; geometric aberrations, which depend on the radius and angle at which the ions are injected and also on the spatial distribution of the focusing fields; and chromatic aberrations, which are associated with the longitudinal momentum of the beam particles. The aberrations resulting from the dynamics of the focusing fields (e.g., from their instabilities) are not considered here; the related problems are touched on in [3, 6].

2. FORMULATION OF THE PROBLEM AND BASIC EQUATIONS

Axisymmetric lenses were investigated theoretically and experimentally in [3–11]. In such lenses, the vector potential of the magnetic field has the only azimuthal component A_φ. For theoretical analysis, it is expedient to introduce the so-called magnetic flux function [5]

$$\psi(r, z) = rA_\varphi(r, z), \tag{1}$$

in which case the magnetic surfaces are described by the equation [12]

$$rA_\varphi = \text{const}. \tag{2}$$

For a Morozov lens, the electric field potential $\Phi(r, z)$ is related to the magnetic flux function $\psi(r, z)$ by

$$\Phi(r, z) = F[\psi(r, z)], \tag{3}$$

where the function F is determined by (or is chosen to satisfy) the optimum focusing conditions.

We express the components of the electric and magnetic fields in terms of ψ and F and substitute these components into Newton's equations of particle motion

1063-780X/03/2910-0883$24.00

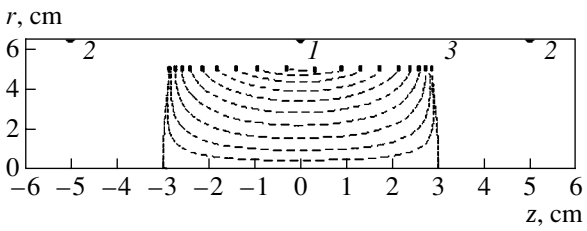

Fig. 1. Schematic of the Morozov lens: (*1*) central current loop, (*2*) side current loops, and (*3*) reference electrodes.

written in cylindrical coordinates. As a result, we obtain the following equations for calculating the particle trajectories in a lens [10]:

$$\frac{dV_r}{dt} = \frac{q}{mr}\frac{\partial\psi}{\partial r}\left(\frac{1}{c}V_\varphi - r\frac{dF}{d\psi}\right) + \frac{V_\varphi^2}{r}, \quad (4)$$

$$\frac{dV_\varphi}{dt} = -\frac{q}{mcr}\left(V_z\frac{\partial\psi}{\partial z} + V_r\frac{d\psi}{dr}\right) - \frac{V_rV_\varphi}{r}, \quad (5)$$

$$\frac{dV_z}{dt} = -\frac{e}{mr}\frac{\partial\psi}{\partial z}\left(r\frac{dF}{d\psi} - \frac{1}{c}V_\varphi\right), \quad (6)$$

where c is the speed of light and q, m, and $\mathbf{V}$ are the charge, mass, and velocity of the focused particles, respectively.

In [6–8], experiments were carried out with a magnetic field configuration produced by three short solenoids carrying opposite currents, which made it possible to localize the so-called reference electrodes (used to apply the electric potentials to the plasma) near the central plane of a lens. In simulations, we modeled this electrode system by three coaxial loops of the same radius; the currents in the side loops were opposite to the current in the central loop. The magnetic field generated by the current J_n in a loop of radius a_c, with its center at the point l_n on the z axis, is described by the azimuthal component of the vector potential (see [12, 13]):

$$A_{\varphi,n} = \frac{4J_n}{ck_n}\sqrt{\frac{a_c}{r}}\left[\left(1-\frac{k_n^2}{2}\right)K(k_n) - E(k_n)\right],$$
$$k_n^2 = \frac{4a_cr}{(a_c+r)^2 + (z-l_n)^2}, \quad (7)$$

where K and E are complete elliptic integrals of the first and second kinds, respectively, and n is the number of the loop. By the superposition principle, the total magnetic field of a solenoid consisting of n current loops is determined by the vector potential $A_\varphi = \sum_n A_{\varphi,n}$.

A schematic of the lens is shown in Fig. 1. The central loop (*1*) is located at $z = 0$, and the side loops (*2*) are placed at $z_s = \pm 5$ cm or at $z_s = \pm 10$ cm. We calculated the magnetic surface topography for different ratios between the opposite currents in the central loop (J_c) and in two side loops (J_s). The numerical results presented below were obtained for $J_c = -1.5J_s$, which makes the magnetic field line topography (shown by the dashed curves in Fig. 1) in the lens volume adequate for our purposes. In modeling the focusing process, we assumed that the lens volume and the region through which an ion beam propagates are filled with a plasma whose density and other parameters are sufficient to neutralize the beam space charge completely and to produce the required focusing fields. (In a sufficiently large volume, a highly homogeneous, high-density plasma with high degree of ionization can be created by a laser, see, e.g., [14].) In the central region (-2.8 cm $< z < 2.8$ cm for $z_s = \pm 5$ cm, or -5.6 cm $< z < 5.6$ cm for $z_s = \pm 10$ cm) of the lens, i.e., in the region between the separatrices (at which the longitudinal magnetic field vanishes), the magnetic surfaces pass through the reference electrodes (*3*) and are held at their potential. The potentials at the magnetic surfaces to the left and right of the central region are assumed to be zero.

Based on Eqs. (4)–(6) and formulas (1)–(3) and (7), we developed a computer model of the Morozov plasma lens. The model makes it possible to trace the particle trajectories and optimize the lens parameters, in particular, to remove different types of aberrations. In the model, Eqs. (4)–(6) are solved by the Adams method of fourth-order accuracy.

3. MOMENT ABERRATIONS

An analysis of the results from the computer modeling of the ion trajectories that was carried out in our earlier paper [10] shows that the moment aberrations increase as the beam injection radius and the magnetic field of a lens increase and as the ion injector is displaced toward the lens. Along the calculated ion trajectories, the conservation laws for the total energy and the moment of the generalized momentum were found to be satisfied to within five significant decimal digits. Here, we are interested not in the trajectories but in the conditions under which the moment aberrations are negligible. Performing the corresponding manipulations with Eq. (5) for the azimuthal ion motion, we can obtain the following conservation law for the moment M_φ of the generalized momentum of an ion with respect to the lens axis:

$$M_\varphi = r(mV_\varphi + qA_\varphi/c) = M_{\varphi 0}. \quad (8)$$

This law implies that the necessary and sufficient condition for the absence of moment aberrations during the focusing of a particle beam is that the initial value $M_{\varphi 0}$ is zero. Since, in experiments, the beam particles are injected at a zero initial azimuthal velocity ($V_{\varphi 0} = 0$), a sufficient condition for the absence of moment aberrations is that the magnetic field in the ion injector be zero, $A_{\varphi 0} = 0$.

4. GEOMETRIC ABERRATIONS IN A LENS WITH A CONTINUOUS DISTRIBUTION OF THE FOCUSING POTENTIAL

4.1. Focusing of the Particles Injected from a Point Source

The particles injected from a point source placed at the lens axis are subject to spherical aberrations, which are a particular case of geometric aberrations. It is well known (see, e.g., [15, 16]) that, in vacuum lenses, spherical aberrations are, in principle, unavoidable. In [3], it was shown theoretically that they can be eliminated in a thin electrostatic plasma lens in the paraxial approximation. Here, we investigate the possibility of removing spherical aberrations in a more general case. Specifically, spherical aberrations in a Morozov plasma lens can be removed by passing the particles to be focused through extraneous charges with a controlled density distribution.

As an example, we present the results from a computer modeling of the focusing of a proton beam for the following parameter values (which are comparable to those in [6]): the proton energy is $W = 20$ keV, the radius of the reference electrodes is 3.7 cm, the radius of the current loops is $a_c = 6.5$ cm, the coordinate of the proton injector is $z_0 = -30$ cm, and the proton beam current is 0.1 A. (In this series of simulations, the magnitude of the proton current is needed merely to determine the compression ratio of the focused beam and is unimportant in other respects because it is assumed that the beam charge is neutralized by the plasma electrons.) The beam divergence angle is 0.1 rad, so that, at the center of the lens, the beam radius is no larger than 3.0 cm. The central loop is placed at $z = 0$, and the side loops are placed at $z_s = \pm 5$ cm.

As in our earlier papers [9–11], the boundary conditions were stated in the form of a radial potential profile in the plane of the central loop, $\Phi(r, 0) = B_1 r^2 + B_2 r^4 + B_3 r^6 + \ldots$, which was optimized by adjusting the values of the dimensional coefficients B_n so as to minimize the aberrations (i.e., to maximize the proton current density at the lens axis in the focal region). When necessary, the radial potential profile could be recalculated into a potential profile $\Phi(R, z)$ over a cylindrical surface. Note that successful optimization of the potential profile requires the use of a high-precision noncontact method for measuring the spatial distribution of the electric field strength in the plasma.

In the lens under consideration, the minimum spherical aberrations are produced by the electric field potential (in electrostatic units) having the following optimized radial profile:

$$\Phi(r, 0) = 1.2r^2 - 0.0180r^4 + 0.000228r^6. \qquad (9)$$

For this profile, we calculated the proton trajectories (in Fig. 2, they are shown in the focal region) and then determined the proton current density in the focal plane (at $z_f = 27.18$ cm), which was found to be 7.5 kA/cm^2, the mean radius of the focal spot being 0.002 cm. Hence, we have demonstrated that the spherical aberrations of a thick plasma lens with nonparaxial beams can be eliminated almost completely.

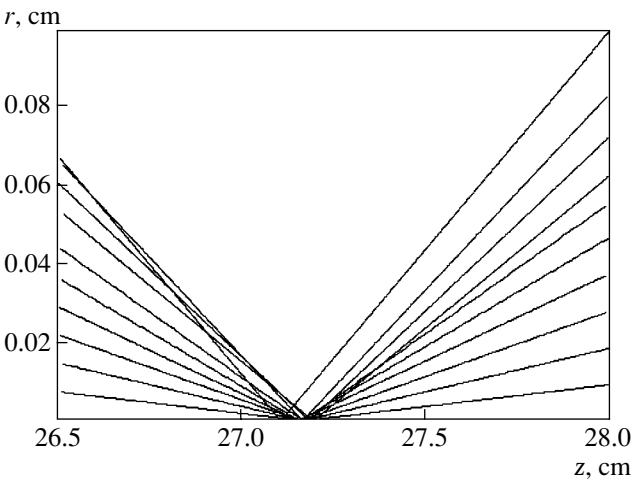

Fig. 2. Trajectories of protons injected from a point source in the focal region.

4.2. Focusing of a Parallel Beam

The ion trajectories during the focusing of a parallel beam were modeled for the following parameter values (which are close to those in the experiments of [8]): the radius of the injected beam of tantalum ions is $r_0 = 5$ cm, the radius of the reference electrodes is 5.1 cm, the radius of the current loops is $a_c = 6.5$ cm, the side loops are placed at $z = \pm 10$ cm, the coordinate of the ion injector is $z_0 = -50$ cm, the potential at the injector is 23 kV, the ion current is 0.5 A, and the energy of the ions with the charge number $Z = 3$ is $W = 69$ keV. It is well known that the focal distance in electrostatic lenses depends on the ratio of the injector potential to the lens potential and is independent of the ion charge (see, e.g., [15, Section 4.7]). In the Morozov lens, the focusing effect of the electric field is much stronger than that of the magnetic field; consequently, it is expedient to choose the charge number of tantalum ions that corresponds to the maximum in their distribution over the charge numbers. In the case at hand, this charge number is $Z = 3$.

We supplement Eqs. (4)–(6) and formulas (1)–(3) and (7) with the boundary conditions describing the injection of a homogeneous monoenergetic ion beam into the lens parallel to its axis:

$$V_z = V_0,\ V_r = V_\varphi = 0,\ z = z_i\ (z_i < 0),\ r = r_i \quad \text{at } t = 0, \qquad (10)$$

where z_i is the coordinate of the end of the injector and the radius r_i at which an ion is injected is varied from zero to a value somewhat smaller than the radius R of

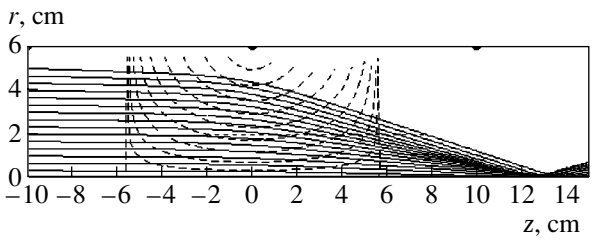

Fig. 3. Trajectories of Ta^{+3} ions in a lens with the potential distribution $\Phi \propto B_z$.

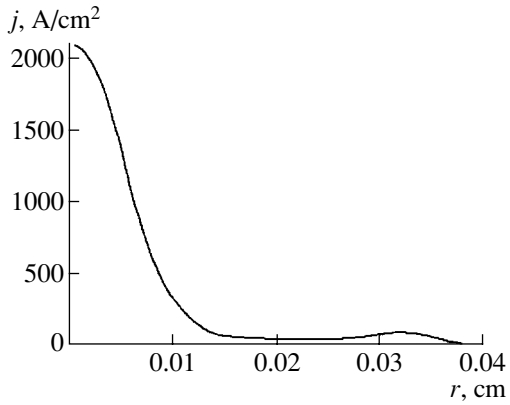

Fig. 4. Radial profile of the ion current density in the focal plane in a lens with an optimized potential profile.

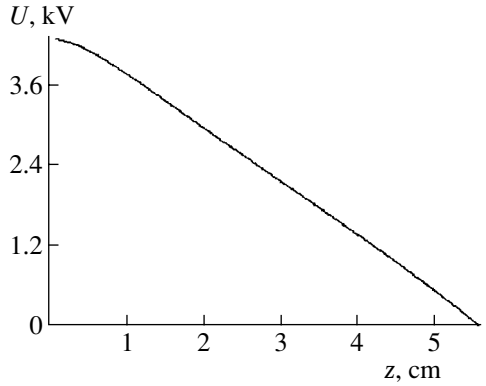

Fig. 5. Optimized potential profile along the lens axis in the region of the reference electrodes.

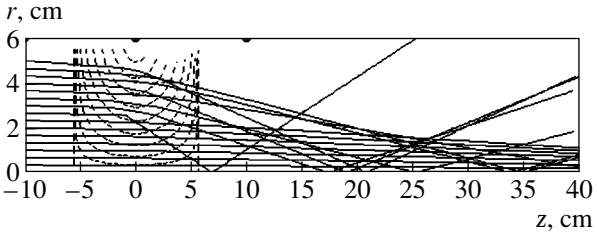

Fig. 6. Trajectories of Ta^{+3} ions in a lens with a smoothed potential profile, the distance between the reference electrodes being 1.6 mm.

the reference electrodes, which, in turn, is smaller than the radius a_c of the current loops.

In [8], the ion beams were best focused (the compression ratio being about 30 at a total ion current of 0.24 A) in experiments in which the potential profile over a cylindrical surface was proportional to the magnetic field strength at the lens axis. For this potential distribution, we numerically traced the ion trajectories (Fig. 3) and computed the radial profile of the ion current density in the focal plane. The current density at the focus was calculated to be $j_{max} = 20$ A/cm^2, the mean beam radius being 0.05 cm and the compression ratio being about 3140. These results are much better than the experimental data but are significantly worse than the optimized results presented below. It should be noted that, in the experiments of [6–8], the potentials were distributed over the reference electrodes in a discrete and stepwise fashion, which substantially degraded the focusing conditions (see below).

In the case in question, the geometric aberrations are minimal when the potential (in electrostatic units) has the optimized radial profile

$$\Phi(r, 0) = 0.6r^2 - 0.002r^4 - 7.5 \times 10^{-5}r^6. \qquad (11)$$

This optimized profile was used to calculate the ion trajectories and the radial profile of the ion current density in the focal region (see Fig. 4). The maximum current density was found to be $j_{max} = 2.1$ kA/cm^2. As a result of the optimization, the beam compression ratio became as large as 3.3×10^5. The optimum potential profile is fairly sensitive to the values of the coefficients. The maximum current density calculated from formula (11), in which the last coefficient was equal to $B_3 = 7.0 \times 10^{-5}$, was found to be $j_{max} = 1.5$ kA/cm^2; the same formula but with $B_3 = 8.0 \times 10^{-5}$ yielded $j_{max} = 1.7$ kA/cm^2.

For convenience in comparing our results with the experimental data, we recalculated radial potential profile (11) in the plane of the central loop into an optimized profile along the cylindrical surface of radius $R = 5.1$ cm, at which the reference electrodes were arranged (see Fig. 5). In this case, the recalculated profile is almost linear, which is favorable for the optimization of the focusing conditions in a lens with a discrete profile of the focusing potentials (see Section 5.2).

5. GEOMETRIC ABERRATIONS OF A LENS WITH A DISCRETE PROFILE OF THE FOCUSING POTENTIALS

5.1. Step Profile of the Focusing Potentials

All numerical results reported above were obtained for a continuous distribution of the focusing potential over the coordinates. However, in the experiments of [6–8], the potentials were applied to the plasma by a finite number (five or nine) of cylindrical electrodes. Here, we consider a lens with nine electrodes. In this

Table

Gap between the electrodes, mm	1.6	3.1	4.3	10
j_{max} at the focus, A/cm^2	0.12	0.14	0.15	0.19

case, it is sufficient to specify six discrete values of the potential within the lens volume such that the sixth value corresponds to a zero potential at the axis. The experiments of [8] were carried out with electrodes of finite length, producing a step potential profile, which was somewhat smoothed out in the plasma. The radius of the electrodes was 51 cm, their length was 12 mm, and the gap between them was 1.5 mm. The total length of the electrode system was 120 mm. In our calculations carried out for the above parameters, the potentials of the electrodes were determined by third-order *B*-splines. In this case, the number of control points was set equal to the number of electrodes times the order $k = 3$ of the *B*-spline, and the potential at each of the three control point was set equal to the potential of the corresponding electrode. In every third interval determining the effective length of the corresponding electrode, there are regions in which this *B*-spline is parallel to the *z* axis. The degree of smoothness was determined by the ratio of the effective lengths of the electrodes to the gaps between them, the total length of the electrode system being unchanged (for information about splines, see, e.g., [17]; for the expediency of using splines to approximate the fields in particle lenses, see [15]). Figure 6 displays ion trajectories calculated for electrodes separated by effective gaps of 1.6 mm (as is the case in [8]) and held at discrete potentials corresponding to the optimum potential profile shown in Fig. 5. The relevant maximum in the radial profile of the ion current density in the focal plane is $j_{max} = 0.13$ A/cm^2 (cf. $j_{max} = 2.1$ kA/cm^2 for the optimum continuous potential profile). From Fig. 6, we can see that, in a potential having a step profile, the ions on the gentle slopes of the steps are underfocused or even are not focused at all, whereas the ions on the steep slopes are overfocused. The reason is that, at the gentle slopes, we have $|\nabla\Phi| \ll E_{opt}$ (where $E_{opt}(r)$ is the optimum electric field strength), while, at the steep slopes, we have $|\nabla\Phi| \gg E_{opt}$. A similar situation takes place when the potential profile along a cylindrical surface is proportional to the strength of the longitudinal magnetic field at the axis (see [8]). Simulations show that the beam focusing depends on the degree to which the steps are smoothed out (see table). It is clear from the table that the quality of beam focusing is poor and depends weakly on the degree of smoothness (and, presumably, on the smoothing method). The half-width of the focal spot (about 1 cm) and the current density (about 0.1 A/cm^2) agree with the experimental data obtained in [8]. Additional information on the subject can be found in [11].

5.2. Piecewise-Linear Profiles of the Focusing Potentials

Here, we discuss the problem of optimizing the focusing potentials in the Morozov lens. We begin by noting that, in such a lens, the trajectories of the electrons moving in crossed electric and magnetic fields in the azimuthal direction are trochoids and the guiding centers of the electrons move along certain magnetic surfaces. The characteristic size of the trochoids is $\delta = V_d/\omega_c = c\nabla\Phi/(\omega_c\sqrt{H_r^2 + H_z^2})$, where V_d is the electron drift velocity and ω_c is the electron gyrofrequency; for typical lens parameters, we have $\delta \sim 0.1$–1 mm. In order for the length Δz of an electrode not to influence the formation of the optimum potential profile (as in Section 5.1), it should be smaller than the cycle of the trochoid ($\Delta z < \delta$) or, in any case, much smaller than the distance between the electrodes ($\Delta z \ll d$).

To optimize the focusing, we consider a piecewise-linear (rather than step) profile of the focusing potentials. A potential having a piecewise-linear profile can be produced by a system of reference electrodes in the form of a set of metal washers with a thickness of about 0.1–1 mm, separated by dielectric bushings. A linear

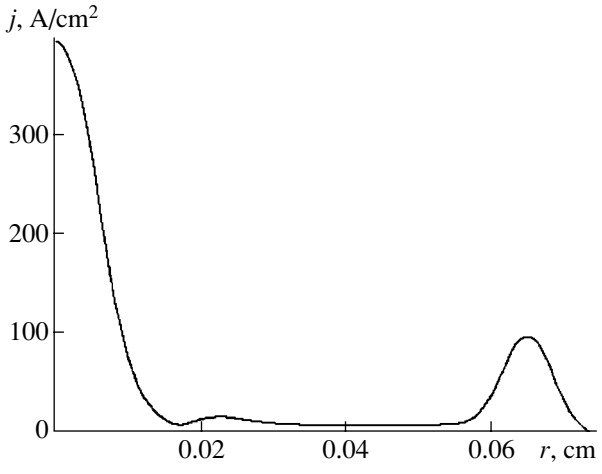

Fig. 7. Radial profile of the current density of Ta^{+3} ions in the focal plane ($z_f = 17.27$ cm) in a lens with nine electrodes in the case of a piecewise-linear approximation to the optimum potential profile in the *z*-direction.

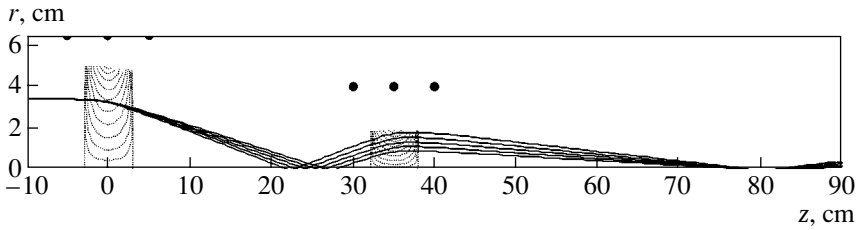

Fig. 8. Scheme for eliminating chromatic aberrations.

potential profile between the neighboring electrodes is ensured by a resistive film deposited onto the inner surfaces of the washers and onto their ends. The inner diameter of this electrode system is sufficient for the beam to pass through.

In the case considered in Section 4.2, the desired potential profile along the *z* axis is almost linear (see Fig. 5), which facilitates the optimization of the focusing. Figure 7 shows the radial profile of the current density of Ta^{+3} ions in a lens with a piecewise-linear *z* profile of the potential of nine electrodes. One can see that, in this case, the ion current density at the focus is as high as 400 A/cm^2, indicating that the focusing is significantly better than that in a lens with a step potential profile. As is expected, a lens with a larger number of electrodes (19 in place of 9) provides even better focusing: the ion current density at the focus amounts to 1.6 kA/cm^2.

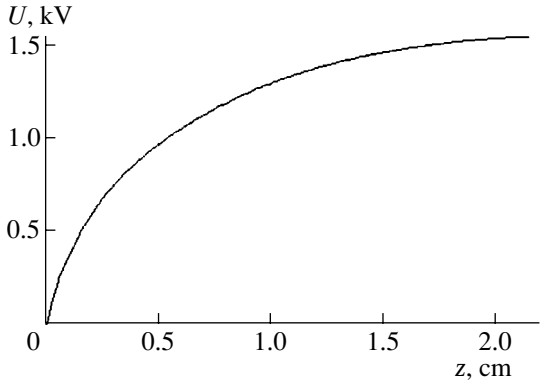

Fig. 9. Optimized longitudinal potential profile in the second lens.

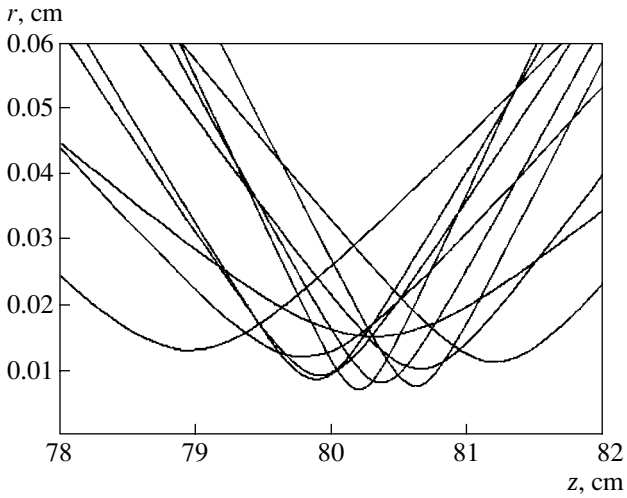

Fig. 10. Proton trajectories in the focal region under the conditions of Fig. 9.

If (as in the case at hand) the desired potential profile along the *z* axis is close to a linear profile, then it is possible to use a small number of electrodes; otherwise, the number of electrodes should be larger in order for the piecewise-linear approximation to the potential profile to give a satisfactory result. It should be emphasized that, in the experimental implementation of the optimization method proposed here, it is necessary to control the optimum distribution of the electric field strength within the lens volume by measuring the electric fields in the plasma with sufficiently high precision.

6. CHROMATIC ABERRATIONS

In axisymmetric vacuum lenses, chromatic aberrations can never be eliminated (see, e.g., [15, 16]). The possibility of removing such aberrations in a system of two electrostatic plasma lenses in the paraxial approximation was shown theoretically by Morozov and Lebedev [5].

Figure 8 illustrates how chromatic aberrations can be eliminated in a system of two Morozov lenses for focusing annular ion beams. The coordinate of the injector is $z = -70$ cm, the initial radius of an annular proton beam being 3.5 cm. The parameters of the first lens, which ensures the radial separation of a nonmonoenergetic beam at the entrance to the second lens, are as follows: the radius of the electrodes is 5 cm, the maximum potential is 2.8 kV, the radius of the current loops is 6.5 cm, the current in the central loop is 30 kA, the coordinate of the central loop is $z = 0$, and the coordinates of the side loops are $z = \pm 5$ cm. The potential distribution within the first lens is unimportant for our purposes: in the case at hand, it is chosen to be Φ [kV] = $2.8\cos(\pi z/5.6)$.

The parameters of the second lens are the following: the radius of the electrodes is 2 cm, the maximum potential is 1.5 kV, the radius of the current loops is 4 cm, the current in the central loop is 30 kA, the coordinate of the central loop is $z = 35$ cm, and the coordinates of the side loops are $z = 35 \pm 5$ cm. Figure 9 shows the potential distribution within the second lens (here, the point $z = 0$ corresponds to the front of the second lens). This distribution was chosen so as to minimize the dependence of the focal distance on the proton energy in the range 16–21 keV. The potential distribution was approximated by third-order *B*-splines with $n = 11$ control points on the left half of the system of the reference electrode. Figure 10 shows proton trajectories in the focal region. We can see that, at a focal distance of 80.2 cm, all protons with energies from 16 to 21 keV (the related energy spread being ±13.5%) are focused into a spot of radius 0.03 cm (the compression ratio in the radial direction being equal to 117).

Hence, we have proposed and analyzed the methods for the almost complete elimination of geometric, moment, and chromatic aberrations in magnetoelectrostatic Morozov plasma lenses for focusing wide-aperture (nonparaxial) charge-neutralized ion beams.

ACKNOWLEDGMENTS

We are grateful to V.I. Karas' for discussing the results of our work and all his useful advice.

REFERENCES

1. M. D. Gabovich, N. V. Pleshivtsev, and N. N. Semashko, *Ionic and Atomic Beams for Controlled Thermonuclear Fusion and Technological Applications* (Énergoatomizdat, Moscow, 1986).
2. *Proc. CERN Accelerator School: Cyclotrons, Linacs and Their Applications*, Ed. by S. Turner, CERN 96-02 (1996).
3. A. I. Morozov, *Encyclopaedia of Low-Temperature Plasma*, Ed. by V. E. Fortov (Nauka, Moscow, 2000), Introduction Vol., Part 3, Chaps. 9.3, 9.4.
4. A. I. Morozov, Dokl. Akad. Nauk SSSR **163**, 1363 (1965) [Sov. Phys. Dokl. **10**, 775 (1966)].
5. A. I. Morozov and S. V. Lebedev, *Reviews of Plasma Physics*, Ed. by M. A. Leontovich (Atomizdat, Moscow, 1974; Consultants Bureau, New York, 1980), Vol. 8.
6. A. A. Goncharov, A. N. Dobrovol'skiĭ, A. N. Kotsarenko, *et al.*, Fiz. Plazmy **20**, 499 (1994) [Plasma Phys. Rep. **20**, 449 (1994)].
7. A. Goncharov, A. Dobrovolskii, I. Litovko, *et al.*, IEEE Trans. Plasma Sci. **25**, 709 (1997).
8. A. A. Goncharov, I. M. Protsenko, G. Yu. Yushkov, and I. G. Brown, Appl. Phys. Lett. **75**, 911 (1999).
9. V. I. Butenko and B. I. Ivanov, Fiz. Plazmy **27**, 540 (2001) [Plasma Phys. Rep. **27**, 511 (2001)].
10. V. I. Butenko and B. I. Ivanov, Fiz. Plazmy **28**, 651 (2002) [Plasma Phys. Rep. **28**, 603 (2002)].
11. V. I. Butenko and B. I. Ivanov, in *Proceedings of the 20th International Symposium on Discharges and Electrical Insulation in Vacuum, Tours, 2002*, p. 182; V. I. Butenko, Probl. At. Sci. Technol., Ser.: Nucl. Phys. Res., No. 3, 74 (2001).
12. A. I. Morozov and L. S. Solov'ev, *Reviews of Plasma Physics*, Ed. by M. A. Leontovich (Gosatomizdat, Moscow, 1963; Consultants Bureau, New York, 1966), Vol. 2.
13. W. Smythe, *Static and Dynamic Electricity* (New York, 1950; Inostrannaya Literatura, Moscow, 1954).
14. M. J. Hogan, R. Assman, F.-J. Decker, *et al.*, Phys. Plasmas **7**, 2241 (2000).
15. M. Szilagui, *Electron and Ion Optics* (Plenum, New York, 1988; Mir, Moscow, 1990).
16. L. A. Baranova and S. Ya. Yavor, *Electrostatic Electron Lenses* (Nauka, Moscow, 1986).
17. C. de Boor, *A Practical Guide to Splines* (Springer-Verlag, New York, 1978; Radio i Svyaz', Moscow, 1985).

Translated by G.V. Shepekina

Plasma Physics Reports, Vol. 29, No. 10, 2003, pp. 890–894. Translated from Fizika Plazmy, Vol. 29, No. 10, 2003, pp. 956–960.

PLASMA INSTABILITY

Electromagnetic Instability of an Anisotropic Relativistic Plasma in the Context of the Evolution of Galactic and Intergalactic High-Energy Particle Sources

A. S. Baranov

Pulkovo Astronomical Observatory, Russian Academy of Sciences, Pulkovskoe shosse 65/1, St. Petersburg, 196140 Russia

Received May 15, 2002; in final form, February 12, 2003

Abstract—The electromagnetic instability of a relativistic space plasma is considered. The instability manifests itself during transverse oscillations in an anisotropic plasma either when the wavelength is sufficiently long and the velocity distribution is fixed or when the plasma is strongly anisotropic and the wavelength is fixed. The critical wavenumber is estimated for a velocity distribution in the form of an oblate ellipsoid of revolution.

1. INTRODUCTION

Over the past decade, theoretical and observational studies have focused much attention on such sources of high-energy particles as active galactic nuclei, quasars, and black holes. Although the accuracy and resolution of modern astronomical observations are becoming increasingly higher, they do not provide detailed and comprehensive information about the structure of such space objects. As for theoretical modeling, one has to choose between plausible physical models [1, 2], keeping in mind that not all of them are entirely realistic because they do not take into account the onset of possible instabilities. The instability of relativistic objects has received insufficient study. This circumstance was pointed out in a recent paper by Heinz and Syunyaev [3], who mentioned only one specific isotropization factor—the instability of two overlapping plasma flows (which hardly exhausts the subject)—and found it necessary to continue research in this field. In particular, the electromagnetic instability of a laboratory plasma due to the anisotropy of the velocity distribution should play a more important role at relativistic plasma velocities. This is why it is desirable to investigate this instability under the conditions encountered in quasars and analogous objects with high energy densities.

The aim of this paper is to study the stability of a homogeneous relativistic plasma with a generally anisotropic velocity distribution. If such a plasma is unstable, then it will rapidly become isotropized even in the absence of collisions. This isotropization should be taken into account in a theoretical analysis of the models of the astrophysical objects mentioned above [4].

To simplify the mathematics, we first consider discrete beams with certain momenta and then turn to a plasma with a continuous velocity distribution. This approach, which, of course, yields the same formulas and conclusions as that based on the initially continuous distributions, is sometimes more efficient, especially in view of the fact that discrete beams can consist of particles of different origin [5–7]. (Note that discrete injected beams find many technical applications [8].)

2. BASIC EQUATIONS

We will work in a model of a homogeneous plasma consisting of the particle flows designated as $i = 1, 2, \ldots, N$, with the corresponding velocity vectors $V_i(u_i, v_i, w_i)$, spatial densities n_i, masses m_i, and charges e_i. The model also assumes a background with a spatial charge density of opposite sign:

$$\gamma = -\sum_i n_i e_i.$$

We consider the propagation of a wave in the linear approximation, assuming that the z axis points along the wave vector $\mathbf{k}$ and all of the linearized perturbed quantities are proportional to the factor $\exp(\lambda t + ikz)$ where t is the time and λ is the growth rate.

If there were no perturbation, each particle would move by inertia, $\mathbf{r} = \mathbf{r}_{0i} + \mathbf{V}_i t$. In order to linearize the equations of motion

$$\frac{d\mathbf{p}_i}{dt} = e_i\left(\mathbf{E} + \frac{\mathbf{V}_i \times \mathbf{H}}{c}\right)$$

(where c is the speed of light), we take into account the algebraic relationships between the velocity and momentum,

$$\mathbf{p} = \frac{m\mathbf{V}}{\beta}, \quad \mathbf{V} = \frac{\mathbf{p}}{\sqrt{m^2 + \frac{p^2}{c^2}}}, \quad \sqrt{m^2 + \frac{p^2}{c^2}} = \frac{m}{\beta} \quad (1)$$

1063-780X/03/2910-0890$24.00

(where $\beta = \sqrt{1 - V^2/c^2}$ and $\beta_i = \sqrt{1 - V_i^2/c^2}$). After some simple manipulations, we arrive at the equations

$$\delta \mathbf{V}_i = \frac{e_i \beta_i}{m_i(\lambda + ikw_i)}\boldsymbol{\nu}, \quad \delta \mathbf{r}_i = \frac{e_i \beta_i}{m_i(\lambda + ikw_i)^2}\boldsymbol{\nu}.$$

Here, we have introduced the notation

$$\boldsymbol{\nu} = \boldsymbol{\varepsilon} + \frac{\mathbf{V}_i \times \mathbf{h}}{c} - \frac{(\mathbf{V}_i \cdot \boldsymbol{\varepsilon})\mathbf{V}_i}{c^2},$$

in which $\boldsymbol{\varepsilon}$ and $\mathbf{h}$ are the perturbations of the electric field $\mathbf{E}$ and magnetic field $\mathbf{H}$, respectively.

Summing the contributions of all the particles, we obtain the linearized current density:

$$\delta \mathbf{j} = \sum_{i=1}^{N} \frac{e_i^2}{m_i} n_i (\boldsymbol{\nu}_i L_i - ik\mathbf{V}_i \nu_{iz} L_i^2)\beta_i \quad (\mathrm{Re}\,\lambda > 0), \quad (2)$$

where $L_i = 1/(\lambda + ikw_i)$. Note that, if the quantities k and λ are of the same order of magnitude, then the current density is inversely proportional to k.

Current densities (2) are substituted into Maxwell's equations to yield

$$\frac{\lambda}{c}h_x = ik\varepsilon_y, \quad \frac{\lambda}{c}h_y = -ik\varepsilon_x,$$
$$ikh_y + \frac{\lambda}{c}\varepsilon_x + \frac{4\pi}{c}\delta j_x = 0, \quad (3)$$
$$-ikh_x + \frac{\lambda}{c}\varepsilon_y + \frac{4\pi}{c}\delta j_y = 0, \quad \frac{\lambda}{c}\varepsilon_z + \frac{4\pi}{c}\delta j_z = 0.$$

3. DERIVATION AND ANALYSIS OF THE DISPERSION RELATION

Here, we are interested in ultrarelativistic space plasmas. In this case, in formulas (3), it is convenient to pass over from the velocities again to the momenta. In order of magnitude, we set

$$k \sim \frac{\lambda}{c} \sim \frac{e^2 n \beta}{\lambda c m},$$

which corresponds to millimeter wavelengths and, as will be shown at the end of the paper, to very short (from an astrophysical point of view) time scales of the instability.

In relationships (1), we neglect the quantity m under the square root symbol in comparison with p/c. We express δj in terms of the particle momenta p_i and also, using formulas (3), express the perturbed magnetic field h in terms of the perturbed electric field ε. We restrict ourselves to considering a particular case in which the particle momentum distribution is symmetric with respect to all three coordinate planes. In this case, some of the sums vanish by symmetry. We single out the x and y components of the electric field to obtain

$$4\pi c \sum_{i=1}^{N} \frac{e_i^2 n_i}{p_i} L_i \left[\varepsilon_x - \frac{icp_z(\boldsymbol{\varepsilon} \times \mathbf{k})_y}{\lambda p} - \frac{(\mathbf{p} \cdot \boldsymbol{\varepsilon})p_x}{p^2} + \frac{ikcp_x p_z (\mathbf{p} \cdot \boldsymbol{\varepsilon})}{p^3} L \right]_i + \frac{\lambda^2 + k^2 c^2}{\lambda} = 0,$$

where the quantity L_i now takes the form

$$L_i = \left(\lambda + ikc\frac{p_{zi}}{p_i}\right)^{-1}.$$

After some explicit cancellations, the equation for the x component becomes

$$4\pi c \sum_{i=1}^{N} \frac{e_i^2 n_i}{p_i} \left[1 - \frac{(\lambda^2 + k^2 c^2)p_x^2}{(p\lambda + ikcp_z)^2} \right]_i + \lambda^2 + k^2 c^2 = 0. \quad (4)$$

The y component of the electric field satisfies an analogous equation. Singling out the z component results in the equation

$$4\pi c \sum_{i=1}^{\infty} \frac{e_i^2 n_i}{p_i} \frac{p_i^2 - p_{zi}^2}{(p_i\lambda + ikcp_{zi})^2} + 1 = 0. \quad (5)$$

As an example, we consider an ellipsoidal velocity distribution,

$$\varphi(p_x, p_y, p_z) = F\left(1 + \frac{p_x^2}{A^2} + \frac{p_y^2}{B^2} + \frac{p_z^2}{C^2}\right),$$

a special case of which, with an exponential function F, is often used in model calculations [9, 10].

In what follows, we will omit the subscript i, assuming that all the particles are of the same species.

We use dispersion relation (4) and introduce the polar coordinates through the relationships

$$\frac{p_x}{p} = \sin\theta\cos\xi, \quad \frac{p_y}{p} = \sin\theta\sin\xi, \quad \frac{p_z}{p} = \cos\theta.$$

In extending the model step by step, we first consider a velocity distribution that is symmetric under the operations of rotations, $A = B$. (It is physically clear that a spherically symmetric distribution is stable.) Switching from summation to integration, using a particular expression of φ, and integrating over p and ξ, we reduce Eq. (4) to

$$2\pi^2 c e^2 \varphi_0 \int_0^{\pi} \left[2 - \frac{(\lambda^2 + k^2 c^2)\sin^2\theta}{(\lambda + ikc\cos\theta)^2} \right] \times \left(\frac{\sin^2\theta}{A^2} + \frac{\cos^2\theta}{C^2}\right)^{-1} \sin\theta\, d\theta + \lambda^2 + k^2 c^2 = 0, \quad (6)$$

where

$$\varphi_0 = \int_0^\infty F(\chi)d\chi.$$

Since the explicit expression for the remaining integral is somewhat involved, we restrict ourselves to calculating the left-hand side of Eq. (6) at $\lambda = 0$:

$$\begin{aligned} &4\pi^2 ce^2\varphi_0 A^2(2\psi\cot 2\psi - 1) \\ &+ k^2c^2\left(C < A, \frac{C}{A} = \cos\psi\right), \\ &4\pi^2 ce^2\varphi_0 A^2(2\tau\coth 2\tau - 1) \\ &+ k^2c^2\left(C > A, \frac{C}{A} = \cosh\tau\right). \end{aligned} \tag{7}$$

As $\lambda \longrightarrow \infty$, the left-hand side approaches $+\infty$. The second of expressions (7) is always positive by virtue of the inequality $2\tau > \tanh 2\tau$. The quantity in parentheses in the first of expressions (7) is negative because $2\psi < \tan 2\psi$; hence, at small k values, we deal with the instability of a velocity distribution in the form of an oblate spheroid, $C < A$. The vanishing of the first of expressions (7) gives the stability boundary. As the deviation of the distribution from a spherical shape decreases (i.e., as ψ reduces) at A = const, this boundary shifts progressively toward smaller values of k (i.e., toward longer wavelengths).

It is of interest to consider the limit $A \longrightarrow \infty$ at constant C. The numerator of the fraction in the integrand in Eq. (6) can be represented as the sum

$$\begin{aligned} &2 + \left\{-\frac{\lambda^2 + k^2c^2}{\lambda^2}\right. \\ &\left. + (\lambda^2 + k^2c^2)\left[\frac{1}{\lambda^2} - \frac{1}{(\lambda + ik\cos\theta)^2}\right]\right\}\sin^2\theta. \end{aligned}$$

After the replacement $\theta \longrightarrow \pi - \theta$ and the corresponding symmetrization in θ at $A = \infty$, the quantities $\cos^2\theta$ cancel each other out, so that the contribution of the last term to the integral can be calculated directly. In the remaining terms, we perform integration and replace $\arccos C/A$ with $\pi/2$ to obtain the approximate dispersion relation

$$\begin{aligned} &2\pi^2 ce^2\varphi_0 C^2\left[\frac{\pi A}{C}\left(1 - \frac{k^2c^2}{\lambda^2}\right)\right. \\ &\left. + \frac{4(\lambda^2 + k^2c^2)kc}{\lambda^3}\arctan\frac{kc}{\lambda}\right] + \lambda^2 + k^2c^2 = 0. \end{aligned}$$

We can readily see that, in the limit $A \longrightarrow \infty$, the solution behaves asymptotically as $\lambda \approx kc$, which indicates instability, in complete agreement with the above analysis. This asymptotic behavior is valid under the conditions $A \gg C$ and

$$AC \gg \frac{k^2c}{e^2\varphi_0},$$

the latter of which implies that the wavelength should be quite long.

In three-dimensional geometry, the mathematics is somewhat more laborious. To integrate over p in the three-dimensional generalization of Eq. (4) is an easy task. In order to determine the sign of the left-hand side at $\lambda \longrightarrow 0$, we integrate by parts over the variable θ. As a result, the singularity in the denominator $(\lambda + ikc\cos\theta)^2$ is removed and $\lambda = 0$ can be inserted directly into the resulting integral. Finally, straightforward integration over ξ in the double integral transforms the dispersion relation into

$$\begin{aligned} &4\pi^2 ce^2\varphi_0\left(\frac{1}{B^2} - \frac{1}{C^2}\right) \\ &\times\int_0^\pi \frac{\sin^3\theta d\theta}{\left(\frac{\sin^2\theta}{A^2} + \frac{\cos^2\theta}{C^2}\right)^{3/2}\left(\frac{\sin^2\theta}{B^2} + \frac{\cos^2\theta}{C^2}\right)^{1/2}} \\ &+ \lambda^2 + k^2c^2 = 0. \end{aligned} \tag{8}$$

For $B > C$, the first term is negative; hence, for sufficiently small k values (writing the relevant exact condition involves fairly complicated elliptic integrals and doing so goes beyond the scope of this paper), the system is unstable. Thus, at long wavelengths, any ellipsoidal velocity distribution is unstable [the only exception to this is a spherical (degenerate) distribution], because the wave vector can always be turned about the axes of the ellipsoid so as to satisfy the condition $B > C$. In this case, however, the instability boundary again shifts toward longer wavelengths as the deviation of the distribution from a spherical shape decreases, and, in the limit $B = C$, the critical wavelength becomes infinitely long. We thus have considered the instability of a velocity distribution having a prolate spheroidal shape ($A = B > C$). This distribution is a particular case of the distribution whose instability has just been analyzed. However, a velocity distribution in the form of an oblate spheroid ($A = B < C$) is also actually unstable, provided that the wave vector has a different orientation (i.e., is perpendicular to the major axis of the ellipsoid of revolution).

In the context of the astrophysical applications in question, we are dealing with ultrarelativistic objects. However, objects with nonrelativistic velocities can also be subject to the same electromagnetic instability [11, 12]. In our case too there is only one instability

region for an anisotropic velocity distribution of nonrelativistic particles, although, in [11], it was pointed out that the instability occurs in two forms. In fact, if, in formula (31.12) from [11], we retain only the electron term and consider exclusively the instability boundary (at which the oscillation frequency is zero, $\omega = 0$), we then obtain

$$k^2c^2 = \omega_L^2\left(\frac{T_\perp}{T_\parallel} - 1\right), \quad (9)$$

where $T_\parallel$ and $T_\perp$ are the longitudinal and transverse temperatures, respectively, and ω_L is the gyrofrequency. As in our case, Eq. (9) yields a unified dependence of the critical wavelength on the anisotropy parameter, provided that the first term in the first of expressions (7) is equated to zero.

We now are left with the problem of analyzing Eq. (5). Substituting the momentum distribution $\varphi(p_x, p_y, p_z)$ adopted above into Eq. (5) yields

$$2\pi ce^2\varphi_0\int_0^\pi \frac{\sin^3\theta d\theta}{(\lambda + ikc\cos\theta)^2\left(\frac{\sin^2\theta}{B^2} + \frac{\cos^2\theta}{C^2}\right)^{1/2}\left(\frac{\sin^2\theta}{A^2} + \frac{\cos^2\theta}{C^2}\right)^{1/2}} + 1 = 0.$$

Integration of this equation by parts puts it into the form

$$\frac{2\pi ce^2\varphi_0}{C^2}\int_0^\pi \frac{\sin\theta\cos^2\theta}{\lambda^2 + k^2c^2\cos^2\theta}\left(\frac{\sin^2\theta}{B^2} + \frac{\cos^2\theta}{C^2}\right)^{-3/2}$$

$$\times\left(\frac{\sin^2\theta}{A^2} + \frac{\cos^2\theta}{C^2}\right)^{-1/2}$$

$$\times\left[\sin^2\theta\left(\frac{1}{A^2} + \frac{1}{B^2}\right) + 2\frac{\cos^2\theta}{C^2}\right]d\theta + 1 = 0.$$

For $\lambda^2 \geq 0$, the left-hand side of this equation is obviously positive, indicating that, at least, aperiodic instability is absent.

Hence, in the case of an anisotropic relativistic velocity distribution, transverse oscillations are subject to an aperiodic instability, in whose development an important role is played by the magnetic field. In contrast, longitudinal Langmuir oscillations are not subject to aperiodic instability, as is the case when the particles do not fall into sharply separated flows (see, e.g., [8] for details).

4. DISCUSSION

We have shown that ultrarelativistic and nonrelativistic plasmas with anisotropic particle velocity distributions are both unstable on short time scales.

In an unstable plasma, the critical wavenumber is determined from dimensionality considerations:

$$k^* \sim e\sqrt{\frac{D}{AC}}, \quad (10)$$

where we have introduced the spatial density of the particles,

$$D = \pi^2A^2C\varphi_0.$$

It should be noted that formula (10) refers to a strongly anisotropic plasma and, as has been said above, when the degree of anisotropy $B/C - 1$ in dispersion relation (8) reduces, the critical wavenumber k decreases to zero (for an isotropic distribution). However, for rough estimates, this circumstance is not so important: in any case, a low degree of anisotropy can neither affect the evolution of the system nor manifest itself in the observational results.

Numerical estimates can be taken from the paper by Nobili *et al.* [13], who theoretically considered the conditions near the accretion disk surrounding a black hole. In that paper, the hydrogen density near the event horizon was estimated to be between 5×10^{-8} and 2.5×10^{-4} cm^{-3} and the hydrogen temperature was estimated as $T \sim 10^{10}$ K. Inserting these values into formula (10) gives a critical wavelength of about one millimeter, the time scale of the instability being about 10^{-13} s. In other words, the instability is local and develops practically instantaneously. This indicates that the plasma evolution cannot lead to any significant degree of anisotropy; consequently, the calculation of the growth rate is important merely from the formal point of view. The evolution of the plasma should be calculated by using an isotropic plasma model (in which the plasma may or may not relax to a Maxwellian distribution). It should also be stressed that, in astrophysical problems, the system is usually large enough for its linear dimensions to be treated as effectively infinite compared to the spatial scales of the electromagnetic instability.

The question about the stability of the systems of cosmic rays, which also belong to the class of relativistic systems, has not received a wholly satisfactory answer because the actual structure of the spatial and angular distributions of rays is very complicated [14]. Note that, in the simplest models we have analyzed above, the perturbations of systems of cosmic rays inevitably interact with interstellar gas and, therefore, are rapidly damped.

ACKNOWLEDGMENTS

I am grateful to V.A. Antonov and to my reviewer for their interest in this work and their valuable remarks.

REFERENCES

1. V. M. Lyutyĭ, *Astrophysics and Space Physics*, Ed. by R. A. Syunyaev (Nauka, Moscow, 1982), p. 318.
2. E. A. Dibai, *Active Nuclei and Stellar Cosmogony*, Ed. by R. A. Syunyaev (Nauka, Moscow, 1987), p. 204.
3. S. Heinz and R. Syunyaev, Astron. Astrophys. **390**, 751 (2002).
4. G. Pelletier and A. Marcowith, Astrophys. J. **502**, 598 (1998).
5. G. Lucek and A. R. Bell, Mon. Not. R. Astron. Soc. **281**, 245 (1996).
6. G. Lucek and A. R. Bell, Mon. Not. R. Astron. Soc. **290**, 327 (1997).
7. J. Bally, C. R. O'Dell, and M. J. McCaughrean, Astron. J. **119**, 2919 (2000).
8. A. A. Ivanov, *Physics of Highly Nonequilibrium Plasma* (Gosatomizdat, Moscow, 1977), p. 347.
9. A. B. Mikhaĭlovskiĭ and A. M. Fridman, Zh. Éksp. Teor. Fiz. **61**, 457 (1971) [Sov. Phys. JETP **34**, 243 (1971)].
10. G. S. Bisnovatyĭ-Kogan, Astron. Zh. **49**, 1238 (1972) [Sov. Astron. **16**, 997 (1973)].
11. A. F. Alexandrov, L. S. Bogdankevich, and A. A. Rukhadze, *Principles of Plasma Electrodynamics* (Vysshaya Shkola, Moscow, 1978; Springer-Verlag, Berlin, 1984).
12. A. B. Mikhaĭlovskiĭ, *Theory of Plasma Instabilities* (Atomizdat, Moscow, 1971; Consultants Bureau, New York, 1974).
13. L. Nobili, R. Rurolla, and L. Zampieri, Astrophys. J. **383**, 250 (1991).
14. M. V. Alaniya and L. I. Dorman, *Spatial Distribution of the Density and Flux of Galactic Cosmic Rays* (Metsniereba, Tbilisi, 1981), p. 119.

Translated by I.A. Kalabalyk